Transport of Oxygen and Light in Model Tumor Systems

by
Michael G. Nichols

Department of Physics and Astronomy
The College
Arts and Sciences

Submitted in Partial Fulfillment
of the
Requirements for the Degree
Doctor of Philosophy

Supervised by
Professor Thomas H. Foster

Department of Radiology
The School of Medicine and Dentistry

University of Rochester
Rochester, New York

1996

To my family,

without whose help

I couldn't have made it to page

ii

Curriculum Vitae

Mike Nichols was born in La Mesa, California on July 6th, 1968. In 1986, he graduated from El Capitan High School, where Mr. Scott Lieberknecht and Mr. James Peabody opened his eyes to the intriguing worlds of mathematics and biology.

Smitten by the sciences, he entered Harvey Mudd College, located in Claremont, California, in the fall of that year with the intention of pursuing a liberal arts degree in engineering and possibly a career as a Biomedical Engineer. At Mudd, his interests turned to the more fundamental aspects of nature and man as he began his studies of physics and philosophy. Through undergraduate research, Dr. Richard Haskell sparked Nichols' interest in optical techniques in biophysics, which Nichols would continue to pursue as a graduate student. While a senior at Mudd, Nichols became enamored of Jennifer Anne Stengel, a freshman chemist at the time whom he would later marry in the summer of 1994. He graduated from Mudd in 1990 with a Bachelor of Science degree in physics and a substantial concentration in philosophy. His undergraduate thesis was entitled *Photon Correlation Spectroscopy of Thickness Fluctionations in Soap Films.* Later that year, he drove cross-country with his faithful cat "Puck" to Rochester, New York where he pursued graduate studies in physics at the University of Rochester.

In his first two years in Rochester, Nichols learned a great deal about teaching from his mentors Dr. Stewart Gazes and Dr. Robert S. Knox and received a Physics Department honorable mention for excellence as a teaching assistant in 1991. In that same year he met Dr. Thomas H. Foster who introduced Nichols to many interesting problems in biological and medical physics pertaining to the detection and treatment of cancer. In 1992, he obtained a Master of Arts degree in physics. He became a doctoral candidate in 1993, and his thesis research was completed under Dr. Foster. In 1996, the eventful final year of his graduate career, Nichols had the privilege of teaching physics at Hobart and William Smith Colleges in Geneva, New York, and his son, Joshua Emerson Nichols, was born on May 11th.

Nichols is a member of American Physical Society and Sigma Xi.

Acknowledgments

The pursuit of knowledge in science is a group effort. While this document represents research which I have pursued, it was made possible by a number of individuals to whom I am gratefully indebted.

During the course of my graduate research, I was supported financially from a number of sources. At times, I was supported by department funds from the department of Radiology, and office and lab space were made available for me as well. I was awarded a grant in aid of research from Sigma Xi which was used to further the oxygen electrode experiments described in Chapters 2 and 3. The research conducted under Dr. Thomas H. Foster was supported by USHPHS grants CA36856 and CA11198, and a grant from the Whitaker Foundation also allowed for the construction of the white-light steady-state diffuse reflectance spectrometer described in Chapter 6. I am grateful for all of this support.

Dr. Russell Hilf and Scott Gibson taught and helped me to understand various issues of the biology and biochemistry that helped to define this research. I am very thankful for their patience in educating yet another physicist in these matters and their generosity in supplying pieces of equipment, materials, and occasionally "junk", which allowed me to explore a variety of creative experimental approaches to a problem. Donna Hartley taught me a great deal about techniques in cell culture and provided invaluable assistance in keeping the multicell tumor spheroids happy and healthy.

Irene Georgakoudi, Ed Hull, and David Rifkin were all students in lab of Dr. Foster during my tenure there, and they directly contributed to the material presen-

ted here on a daily basis. Without their help, progress would have been severely limited and this document would be much less interesting and would contain many fewer pages.

Finally, I am fortunate to be able to say that my development as a research scientist is due to the excellent guidance of Dr. Thomas H. Foster. All of the research presented in this document was conducted under Dr. Foster. Daily discussions with him formed my view of the topics presented herein and directly impacted my approach to this material. It has truly been a pleasure to work with him and learn from his experience. I am especially grateful for his patience with me during the tumultuous final months.

Abstract

Analytic models of oxygen and optical diffusion in biological systems are developed and examined experimentally and through numerical simulations. The predictions made by the models are discussed in relation to singlet oxygen dosimetry in photodynamic therapy (PDT) and non-invasive tumor oximetry.

An *in vitro* dose model is developed for the multicell tumor spheroid. The model determines singlet oxygen dose through calculations of oxygen diffusion with reaction based on the primary photophysical events of PDT. Oxygen microelectrode measurements made within and in the vicinity of a spheroid prior to and during PDT support the model and provide estimates of the model's parameters. These measurements demonstrate that photodynamic oxygen consumption can induce a region of anoxia severe enough to limit photodynamic efficacy in a multicell system. Simulations of PDT are compared with spheroid cell survival data, and a threshold dose of reacting singlet oxygen is determined. Two mechanisms of photosensitizer bleaching are evaluated, and evidence is presented that demonstrates that the porphyrin photosensitizer Photofrin® bleaches *via* a singlet oxygen-mediated mechanism.

To observe photodynamic oxygen consumption *in vivo*, a non-invasive optical technique is developed based on a diffusion model of optical transport in turbid media. Several approaches to the problem of extracting absorption and scattering coefficients from steady-state diffuse reflectance measurements are investigated. A Monte Carlo algorithm is developed to test the accuracy of photo-diffusion model predictions in realistic biological systems.

A white-light diffuse reflectance spectrometer is developed to measure spatially- and wavelength-resolved diffuse reflectance from biological tissue. The system performance is evaluated with tissue-simulating phantoms composed of a scattering emulsion and molecular chromophores. A theoretical comparison of extracted and actual optical properties is made by analyzing Monte Carlo data. Measurements made on phantoms containing red blood cells demonstrate that tissue oxygenation can be assessed at time intervals that are relevant to PDT.

Finally, potential complications to the assessment of oxygenation in small animal tumors are discussed. The impact of the skin layer above a subcutaneous tumor and the curvature of the air-tissue interface are investigated.

Contents

Curriculum Vitae **iv**

Acknowledgments **v**

Abstract **vii**

Table of Contents **ix**

List of Tables **xiii**

List of Figures **xiv**

1 Introduction and Overview **1**

1.1 Photodynamic Dosimetry 1

1.2 Tissue Oximetry 6

2 Oxygen Diffusion in Spheroids **10**

2.1 Introduction 10

2.2 The Oxygen Dependence of PDT 13

2.3 The Multicell Spheroid Model Tumor System 16
2.4 Steady-State Oxygen Diffusion in the Spheroid 18
2.5 Time-Dependent Oxygen Diffusion with Consumption 23
2.6 The Numerical Solution of the Diffusion Equation 25
2.7 Experimental Results and Analysis 32
  2.7.1 Microelectrode Measurements 32
  2.7.2 A Comparison of the Fluence Rate-Dependent Efficacy of PDT in Multicell Tumor Spheroids with Model Calculations 39
2.8 Discussion 50
  2.8.1 Microelectrode Measurements 50
  2.8.2 A Determination of the Threshold Reacting Dose of Singlet Oxygen 56
2.9 Conclusions 63

3 Singlet Oxygen Photobleaching in PDT **65**
3.1 Introduction 65
3.2 The Effect of Singlet Oxygen-Mediated Photobleaching 67
3.3 Verification of Singlet Oxygen-Mediated Photobleaching 73
3.4 Conclusions 81

4 Light Transport in Biological Media **84**
4.1 Introduction 84
4.2 Derivation of the Photo-Diffusion Equation 87
  4.2.1 The Transport Equation 87

4.2.2 The Diffusion (P_1) Approximation 89
4.2.3 Boundary Conditions for Photo-Diffusion 92
4.3 Solution of the Photo-Diffusion Equation 95
4.3.1 The Exact Solution 95
4.3.2 The Dipole Approximation 96
4.4 A Comparison of the Dipole and Exact Reflectance Expressions . 99
4.5 A Comparison of the Extrapolated and Partial-Current Boundary Conditions 104
4.6 Monte Carlo Solution of the Transport Equation 111
4.6.1 Theoretical Tests of the OOMC Algorithm 116

5 Evaluation of Reflectance Expressions 120

5.1 Introduction 120
5.2 Index-Matched Boundary Conditions 123
5.3 Index-Mismatched Boundary Conditions 133
5.4 Conclusions 148

6 The Diffuse Reflectance Spectrometer 151

6.1 Introduction 151
6.2 System Description 154
6.2.1 Instrument 154
6.2.2 Data Reduction 159
6.3 Phantom Studies 161
6.4 Conclusions 175

7 Reflectance Spectroscopy of Hemoglobin **177**

7.1 Introduction 177

7.2 Experimental Methods 180

7.2.1 Phantom Preparation 181

7.2.2 Hemoglobin Oxygen Saturation Measurement 182

7.3 Phantom Oxygenation Status Assessment 183

7.4 The Effects of Additional Chromophores 210

7.5 Conclusions 214

8 Optical Spectroscopy *In Vivo* **216**

8.1 Introduction 216

8.2 Non-Planar Air-Tissue Boundaries 219

8.3 Limited Measurement Sensitivity in Subcutaneous Tumors 231

8.4 Layered Geometries: The Subcutaneous Tumor Model 241

8.5 Conclusions 254

Bibliography **258**

A The Exact Reflectance Expression **274**

B Fluorescence from an Embedded Source **280**

B.1 Introduction 280

B.2 Fluorescence from a Spherical Source 282

B.3 Distributed Fluorescent Fluence Calculation 283

B.4 Fluorescent Diffuse Emittance Calculation 288

List of Tables

2.1 Summary of steady-state electrode measurements 37

2.2 Comparison of steady-state $^3O_2$ diffusion parameters with selected literature values 38

2.3 Summary of spheroid cell survival data with results of model calculations 43

4.1 Verification of OOMC algorithm for an index-matched thin slab . . 117

8.1 Optical properties estimated from index-matched curved surface diffuse reflectance 228

8.2 Optical properties estimated from index-mismatched curved surface diffuse reflectance 229

List of Figures

2.1 Jablonski diagram for type-II photooxygenation 14

2.2 Spatial regions defining $^3O_2$ transport in the spheroid 19

2.3 Spatial lattice used in the numerical solution of the time-dependent diffusion-with-consumption equation 26

2.4 Experimental apparatus for microelectrode measurements of a single spheroid 34

2.5 Steady-state electrode measurements of $^3O_2$ in a spheroid 36

2.6 $^3O_2$ depletion measured at the edge of a single photosensitized EMT6/Ro spheroid 40

2.7 Γ_0 as a function of fluence rate at 514 nm 41

2.8 Spatial and temporal distributions of $^3O_2$ concentration during 25 mW cm^{-2} PDT 45

2.9 Spatial and temporal distributions of $^3O_2$ concentration during 50 mW cm^{-2} PDT 46

2.10 Spatial and temporal distributions of $^3O_2$ concentration during 200 mW cm^{-2} PDT 47

2.11 Net photochemical $^3O_2$ consumption as a function of position in a spheroid . . . 48

2.12 Correlation between the critical and anoxic radii . . . 51

2.13 Estimate of the $^1O_2$ threshold dose . . . 52

2.14 Comparison of consumed $^3O_2$ distribution resulting from PDT when k_p/k_{ot} is increased from 2.8 μM to 13 μM . . . 57

3.1 Time-resolved $^3O_2$ concentration at the edge of a spheroid for several values of the bleaching coefficient, α . . . 74

3.2 Time-resolved $^3O_2$ concentration at the edge of a spheroid for several values of $k_{os}/k_{oa}A$ . . . 75

3.3 Evidence of Photofrin®-photobleaching in $^3O_2$ microelectrode measurements . . . 76

3.4 Fit of $^3O_2$ microelectrode data with a $^1O_2$ -mediated bleaching model 77

3.5 Comparison of $^1O_2$ dose distributions in the presence and absence of bleaching . . . 80

4.1 Radial distribution of diffuse reflectance generated by the exact and dipole reflectance expressions for an index-matched boundary . . . 100

4.2 Radial distribution of diffuse reflectance generated by the exact and dipole reflectance expressions for an index-mismatched boundary . 101

4.3 Diffuse reflectance generated from the exact reflectance expression for several values of the scattering anisotropy . . . 103

4.4 Actual and theoretical extrapolated boundary lengths calculated for the dipole solution and matched boundary conditions 106

4.5 Error in the partial-current boundary condition for the dipole solution and matched boundary conditions 107

4.6 Actual and theoretical extrapolated boundary lengths calculated for the dipole solution and mismatched boundary conditions 109

4.7 The error in the partial-current boundary condition for the dipole solution and mismatched boundary conditions 110

4.8 Flow chart for the OOMC (Object Oriented Monte Carlo) algorithm 114

4.9 Flow chart for the MOVE PHOTON procedure of the OOMC algorithm 115

4.10 Diffuse reflectance from a semi-infinite slab with an index mismatched boundary 119

5.1 Best-fit optical coefficients estimated as a function of the minimum source-detector separation by the dipole reflectance expression . . 125

5.2 Optical coefficients estimated as a function of ρ_{min} by the exact reflectance expression 127

5.3 χ^2_ν goodness of fit parameter for the fits of Figures 5.1 and 5.2 . . 129

5.4 Comparison of the estimated and actual absorption coefficients obtained from fits to Monte Carlo data for several values of the absorption coefficient 131

5.5 Comparison of the estimated and actual transport scattering coefficients obtained from fits to Monte Carlo data for several values of the absorption coefficient 132
5.6 Comparison of the estimated and actual absorption coefficients obtained from fits to Monte Carlo data for several values of the scattering coefficient 134
5.7 Comparison of the estimated and actual scattering coefficients obtained from fits to Monte Carlo data for several values of the scattering coefficient 135
5.8 Optical coefficients estimated as a function of ρ_{min} by dipole fits of mismatched Monte Carlo reflectance data 138
5.9 Optical coefficients estimated as a function of ρ_{min} by exact fits of mismatched reflectance data 139
5.10 Optical coefficients estimated as a function of ρ_{min} by dipole fits of mismatched reflectance data with an erroneously low value of 1.0 for A 141
5.11 Optical coefficients estimated as a function of ρ_{min} by dipole fits of mismatched reflectance data with an erroneously low value of 1.25 for A 142
5.12 Optical coefficients estimated as a function of ρ_{min} by dipole fits of mismatched reflectance data with an erroneously low value of 1.75 for A 143

5.13 χ^2_ν for various fits to index-mismatched Monte Carlo diffuse reflectance data 144

5.14 Dependence of the optical properties on the index of refraction estimated by the dipole reflectance expression 146

5.15 Dependence of the optical properties on the index of refraction estimated by the exact reflectance expression 147

6.1 White-light steady-state spatial-resolved diffuse reflectance spectrometer 155

6.2 Optical probe for detecting spatially-resolved diffuse reflectance . . 157

6.3 Absorption spectra of Liposyn-II®-MnTPPS phantom 163

6.4 Scattering spectra of Liposyn-II®-MnTPPS phantom 164

6.5 Comparison of the actual and predicted MnTPPS concentration . 166

6.6 Polystyrene microsphere scattering spectra (2.79×10^{10} ml^{-1}) . . . 169

6.7 Polystyrene microsphere scattering spectra (2.39×10^{10} ml^{-1}) . . . 170

6.8 Polystyrene microsphere scattering spectra (1.98×10^{10} ml^{-1}) . . . 171

6.9 Polystyrene microsphere scattering spectra (1.58×10^{10} ml^{-1}) . . . 172

6.10 Absorption spectra of Liposyn-II®-Nile Blue A phantoms 174

7.1 Visible absorption spectra of 0.91% Liposyn-II® phantom with human red blood cells 185

7.2 Near-infrared absorption spectra of 0.91% Liposyn-II® phantom with human red blood cells 186

7.3 Visible absorption spectra of oxy- and deoxyhemoglobin 188

7.4 Near-infrared absorption spectra of oxy- and deoxyhemoglobin . . 189

7.5 Hemoglobin concentration determined spectroscopically 190

7.6 Background-subtracted visible absorption spectra obtained from a Liposyn-II®-red blood cell-yeast phantom during deoxygenation . 193

7.7 Background-subtracted near-infrared absorption spectra obtained from a Liposyn-II®-red blood cell-yeast phantom during deoxygenation (4 s integration) 194

7.8 Background-subtracted near-infrared absorption spectra obtained from a Liposyn-II®-red blood cell-yeast phantom during deoxygenation (45 s integration) 195

7.9 Visible scattering spectra obtained from a Liposyn-II®-red blood cell-yeast phantom during deoxygenation 196

7.10 Near-infrared scattering spectra obtained from a Liposyn-II®-red blood cell-yeast phantom during deoxygenation (4 s integration) . 197

7.11 Near-infrared scattering spectra obtained from a Liposyn-II®-red blood cell-yeast phantom during deoxygenation (45 s integration) . 198

7.12 Best-fit visible spectra obtained from an oxygenated and a deoxygenated Liposyn-II®-red blood cell-yeast phantom 200

7.13 Best-fit near-infrared spectra obtained from an oxygenated and a deoxygenated Liposyn-II®-red blood cell-yeast phantom (4 s integration) 201

7.14 Best-fit near-infrared spectra obtained from an oxygenated and a deoxygenated Liposyn-II®-red blood cell-yeast phantom (45 s integration) 202
7.15 Time-dependent oxy- and deoxyhemoglobin concentration in the Liposyn-II®-red blood cell-yeast phantom determined spectroscopically at visible wavelengths 204
7.16 Time-dependent oxy- and deoxyhemoglobin concentration in the Liposyn-II®-red blood cell-yeast phantom determined spectroscopically at near-infrared wavelengths 205
7.17 Oxygen partial pressure measured in the Liposyn-II®-red blood cell-yeast phantom during the experiment depicted in Figure 7.15 206
7.18 Oxygen partial pressure measured in the Liposyn-II®-red blood cell-yeast phantom during the experiment depicted in Figure 7.16 207
7.19 Hill plot obtained from visible steady-state diffuse reflectance spectroscopy of the Liposyn-II®-red blood cell-yeast phantom 208
7.20 Hill plot obtained from near-infrared steady-state diffuse reflectance spectroscopy of the Liposyn-II®-red blood cell-yeast phantom . . 209

8.1 Histological section of an R3230AC tumor from a Fischer rat . . . 221
8.2 Geometric model for simulating light propagation in a subcutaneous tumor. 223
8.3 Diffuse reflectance from an index matched curved surface 225
8.4 Diffuse reflectance from an index mismatched curved surface . . . 226

8.5 Effect of ρ_{max} and μ_s' on absorption sensitivity of reflectance measurements based on the dipole approximation (conservative estimate). 234
8.6 Effect of ρ_{max} and μ_s' on absorption sensitivity of reflectance measurements based on the dipole approximation (liberal estimate). . . 235
8.7 Diffuse reflectance from hemispherical index-matched boundary for several values of μ_a 237
8.8 Diffuse reflectance from hemispherical index-mismatched boundary for several values of μ_a 238
8.9 Summary of estimated absorption coefficients obtained from dipole fits of the reflectance from a 12 mm diameter tumor 239
8.10 Summary of estimated absorption coefficients obtained from fits of 12 mm diameter tumor reflectance using the exact diffusion theory expression 240
8.11 632 nm diffuse reflectance from a 1 cm R3230AC tumor in a Fischer rat 245
8.12 Effect of increasing skin absorption on reflectance from a 12 mm diameter tumor 247
8.13 Effect of increasing skin scattering on reflectance from a 12 mm diameter tumor 249
8.14 Monte Carlo diffuse reflectance from a 12 mm diameter subcutaneous tumor for several tumor absorption coefficients 252
8.15 Effect of normal tissue absorption on Monte Carlo diffuse reflectance from a subcutaneous tumor 253

B.1 Diffuse fluorescent fluence in an infinite turbid medium 285
B.2 Arrangement of fluence point sources used to obtain the radially-resolved diffuse fluorescence emitted from a semi-infinite medium 287

Chapter 1

Introduction and Overview

1.1 Photodynamic Dosimetry

Photodynamic therapy (PDT) is a promising cancer treatment that selectively eradicates cancer cells through the generation of a highly reactive oxygen species by an intermediate photosensitive drug. Selectivity is obtained by the combination of preferential retention of the photosensitizer in the tumor volume and its controlled excitation by optical irradiation. Photofrin®, a commercial photosensitizer, has recently been approved in the United States for PDT of esophageal cancer and has also been approved in Canada, the Netherlands and Japan for a variety of indications including recurrent bladder cancer, early- and late-stage lung cancer, and esophageal cancer. While PDT has been an active area of research for over two decades now, several questions remain regarding the fundamental mechanism of photodynamic action in tumors (Dougherty, 1993).

The conventional measure of photodynamic dose is the product of the drug concentration and the total optical fluence delivered to the tissue. As a result, a great deal of research has been directed toward characterizing the distribution of fluence and photosensitizer in the tumor (van Gemert *et al.*, 1985; Patterson *et al.*, 1990). While it is commonly recognized that singlet oxygen ($^1O_2$), the lowest lying excited state of molecular oxygen ($^3O_2$), mediates cell death (Weishaupt *et al.*, 1976), oxygen has yet to be included in current dose models.

Profio and Doiron (1981) first proposed that the dose rate in tissue would be proportional to the number of $^1O_2$ molecules created per photon absorbed. They indicated that this would be dependent on the tumor oxygenation and recognized that reduced therapeutic effectiveness may occur in treatments of hypoxic tumors. For well oxygenated tissue, their definition of dose is equivalent to the conventional definition, and several investigators have demonstrated that a reciprocal change in the drug concentration and delivered fluence produces equivalent photodynamic efficacy (Cowled and Forbes, 1985; van Gemert *et al.*, 1985; Fingar *et al.*, 1987).

van Gemert *et al.* first introduced the concept of a threshold photodynamic dose when they observed a clear demarcation between necrotic and undamaged cells in a tumor after PDT. They found that the maximum depth of necrosis correlated with the theoretical penetration depth of the incident beam and hypothesized that necrosis did not occur until a threshold dose of absorbed photons was delivered. More recently, Patterson *et al.* (1990) observed a similar demarcation in normal rat liver treated with PDT. They reported that the demarcation occurred at the point where the absorbed dose fell below a threshold value of 3.8×10^{19}

photons cm^{-3}. While both of these studies could successfully predict cell death without considering the local $^3O_2$ concentration, recent evidence suggests that this is not always the case. Over the past six years, evidence has been accumulating that demonstrates a pronounced dependence of photodynamic efficacy on the fluence rate in several animal tumor models and with several different photosensitizers (Feins *et al.*, 1990; Foster *et al.*, 1991; Cincotta *et al.*, 1994; Gibson *et al.*, 1994; Hua *et al.*, 1995). These results suggest that oxygen utilization by PDT may be sufficient to deplete $^3O_2$ in the target tissue, and a mathematical model of the primary photophysical events of PDT supports this hypothesis (Foster *et al.*, 1991).

Foster *et al.* have reported that the regrowth rate of the R3230AC mammary adenocarcinoma in the Fischer rat following PDT exhibits a strong dependence on the incident fluence rate when the drug and light doses are constant. Contrary to the conventional measure of photodynamic dosimetry, the tumor volume doubling time was increased from 6.5 to 16.2 days by reducing the fluence rate from 200 to 50 mW cm^{-2} with a corresponding increase in the irradiation time to ensure an equivalent delivered fluence. Tumor regrowth was shown to be further inhibited by delivering the light with a 50% duty cycle. From these observations it was hypothesized that the reduction in the fluence rate and fractionated light delivery reduced the rate of photodynamic $^3O_2$ consumption which increased the amount of $^3O_2$ that was able to diffuse from the capillary wall to a region remote from the vasculature. This would allow $^1O_2$ to be created in this region and improve photodynamic efficacy.

To explicitly incorporate the oxygen dependence of PDT in a model of photodynamic dosimetry, an oxygen-diffusion-with-consumption model has been developed for the *in vitro* multicell tumor spheroid and is presented in Chapter 2. [Sections of this chapter have been previously published in Nichols and Foster (1994) and joint authorship with T.H Foster is gratefully acknowledged.] The spheroid is an avascular spherical aggregate of tumor cells that captures many of the features of a tumor *in vivo*. Previously, we have reported that photodynamic efficacy in the spheroid also exhibits a pronounced fluence rate dependence (Foster *et al.*, 1993). This, coupled with the spherical symmetry, makes the spheroid an excellent system for the development of an *in vitro* dose model. Starting with the primary photophysical kinetic equations which define PDT, an expression is derived for the photochemical oxygen consumption in a spheroid that is undergoing PDT. This expression is incorporated into a pair of time-dependent $^3O_2$ diffusion equations that describe oxygen transport in the spheroid. A numerical solution of these equations provides the spatial and temporal distribution of $^3O_2$ concentration and $^1O_2$ reaction within the spheroid for a specified treatment protocol. To obtain values for the parameters defined in the model, steady-state and time-dependent microelectrode measurements of $^3O_2$ obtained within and in the vicinity of a photosensitized spheroid prior to and at the onset of photodynamic irradiation are fit with the numerical solution of the diffusion equations. Finally, by comparing the results of model simulations with experimental spheroid cell survival data, the threshold dose model is examined in terms of reacting $^1O_2$. By correlating the fraction of cells which are observed to survive PDT at a given fluence rate with the simulated spatial distribution of $^1O_2$, a consistent threshold dose of reacting $^1O_2$ is obtained for the spheroid.

While this oxygen-based dose model supports the concept of a threshold $^1O_2$ dose, it does not treat the consequences of photobleaching of the sensitizer during therapy. Sensitizer photobleaching has been observed in the treatment of human tumors by monitoring the decay of photosensitizer fluorescence during therapy (Potter *et al.*, 1987). Both exponential and non-exponential decay kinetics have been observed, and constant photobleaching coefficients between 25 and 45 J^{-1} cm^2 have been reported for porphyrin photosensitizers (Moan, 1986; Mang *et al.*, 1987). Since optical fluences in excess of 100 J cm^{-2} are commonly used in PDT, photobleaching can have a profound impact on the delivered dose.

In Chapter 3, the oxygen-diffusion-with-consumption model is modified to account for the loss of photon absorption which accompanies photobleaching. Two different mechanisms are investigated: $^1O_2$ -mediated photobleaching, wherein the photosensitizer is degraded by interactions with $^1O_2$ that has been produced though interactions of $^3O_2$ and the sensitizer; and an oxygen-independent bleaching mechanism characterized by a constant photobleaching coefficient. Theoretical calculations of the modified oxygen-diffusion-with-consumption model indicate that bleaching according to either of these mechanisms would be observable from photochemical oxygen depletion at the edge of a photosensitized spheroid. As the sensitizer is bleached, the rate of photodynamic oxygen consumption within the spheroid is modified in a mechanism-dependent manner and, as a result, the recovery of the $^3O_2$ concentration at the edge of the spheroid as irradiation proceeds is a unique predicator of the bleaching mechanism. Evidence is presented which implicates a $^1O_2$ -mediated bleaching mechanism and the consequences to photodynamic dosimetry are discussed.

Having demonstrated that photochemical oxygen depletion can be significant enough to protect regions of a multicell spheroid from photodynamic action, it remains to be seen whether the fluence rate-dependent response to PDT observed in animal tumor models is due to a similar oxygen depletion. Previously, Tromberg *et al.* (1990) have monitored transcutaneous $^3O_2$ pressure in the normal rabbit ear during PDT. They reported that irreversible hypoxia could be induced at sufficiently high optical fluences; this was attributed to vascular occlusion which would irreversibly alter flood flow. At smaller fluences, however, there was reversible hypoxia with no measurable change in the local flow conditions. These observations seem to support the $^3O_2$ consumption hypothesis.

1.2 Non-Invasive Optical Measurements of Tissue Oximetry

To see if a similar effect can be seen in the rodent tumors that exhibit a fluence rate-dependent response to PDT, a technique for non-invasively measuring tumor oxygenation status *in vivo* has been developed. Oxygen electrode measurements are not practical *in vivo* because they are invasive and difficult to interpret. Furthermore, an electrode measures the $^3O_2$ pressure within a small region of a tumor. While it was possible to use a mathematical model to infer the spatial distribution of $^3O_2$ in the spheroid from an electrode measurement, the heterogeneous tumor vasculature prevents this type of an approach *in vivo*.

Another approach is to make an optical reflectance or a transillumination measurement to ascertain the absorption spectra of endogenous oxygen-dependent chromophores such as hemoglobin and cytochrome aa_3, as first demonstrated by Jöbsis (1977) in the cat brain. The absorption spectra of these molecules change with the local oxygen pressure. Hemoglobin absorption at either visible or near infrared wavelengths reports the oxygenation status of blood, while cytochrome aa_3, present in the mitochondria, reports the cellular oxygenation status. To accurately measure the oxygen saturation in turbid biological tissue, it is necessary to separate the effects of scattering and absorption in the attenuation measurement.

Several types of optical techniques have been developed for a variety of applications of tissue oximetry, such as cerebral oxygen monitoring of infants (Cope and Delpy, 1988; Chance *et al.*, 1988a; Sevick *et al.*, 1991; Ferrari *et al.*, 1995; Liu *et al.*, 1995a). Time- and frequency-domain techniques have been developed that measure various aspects of the diffuse light that is emitted or transmitted from illuminated tissue (Patterson *et al.*, 1989, 1991). Data collected by these techniques are analyzed with photo-diffusion models of light transport in turbid tissue to quantify the tissue scattering and absorption coefficients. Continuous-wave techniques based on a modification of the Beer-Lambert law of absorption have typically been used as trend indicators, though recently Farrell *et al.* (1992) have described a steady-state reflectance technique that provides quantitative measurements of tissue absorption and scattering by analyzing the spatially-resolved diffuse reflectance from an irradiated tissue.

In Chapters 4 and 5, models of light propagation in turbid biological media are discussed, and expressions for the radially-resolved diffuse reflectance from a semi-infinite turbid medium are analyzed. A Monte Carlo model of light propagation in tissue is used to provide idealized reflectance data sets to test the capability of the Farrell *et al.* reflectance expression in determining the scattering and absorption coefficients of tissue over a biologically relevant range. Based on this analysis, a white-light radially-resolved diffuse reflectance spectrometer has been developed and is presented in Chapter 6. [Certain sections from Chapter 5 and the majority of Chapter 6 have been accepted for publication in *Applied Optics*. Joint authorship with E.L. Hull and T.H. Foster is gratefully acknowledged.] This instrument is capable of measuring wavelength- and spatially-resolved reflectance over a variable 160 nm wavelength range. By interpreting the data with Farrell *et al.*'s expression for diffuse reflectance, the transport scattering spectrum and the absorption spectrum of tissue-simulating phantoms consisting of a liquid scattering emulsion and biological chromophores can be accurately determined. Furthermore, data can be acquired at time intervals which are relevant for oxygen diffusion during PDT.

In Chapter 7, the diffuse reflectance spectrometer is tested with tissue-simulating phantoms consisting of human red blood cells, yeast, and a scattering emulsion. Measurements of diffuse reflectance are made periodically as the yeast deoxygenates the phantom. The ${}^3O_2$ partial pressure is measured simultaneously with an oxygen electrode that is placed just below the surface of the phantom. These two measurements are combined to produce Hill plots which indicate the hemoglobin oxygen saturation as a function of the oxygen partial pressure of the phantom.

These studies demonstrate that non-invasive tissue oxygenation measurements are feasible *in vivo*.

While the phantom studies described in Chapters 6 and 7 were conducted with biologically relevant optical properties, they did not attempt to simulate the structural characteristics of tissue. In particular, the interface between the turbid medium and air is flat for the liquid phantoms, while the tumors in which fluence rate effects have been observed have a pronounced curvature. Pogue and Patterson (1994) have investigated the effects of curved boundaries on experimental diffuse reflectance analyzed with frequency-domain spectroscopy. In that report, the curvature of the boundary was shown to lead to an overestimation of the true absorption coefficient of the phantom. Another complication of spectroscopy of tissue *in vivo* is the characteristic heterogeneous layered geometry of tissue. Subcutaneous tumors are located beneath a layer of skin and are surrounded by normal tissue. In principle, all three of these regions could have distinct optical properties. The effects of these biologically relevant characteristics on the analysis of diffuse reflectance data obtained from subcutaneous tumors is considered in Chapter 8.

Chapter 2

Oxygen Diffusion and Reaction Kinetics in Photodynamic Therapy of Multicell Tumor Spheroids

2.1 Introduction

Photodynamic therapy (PDT) is an experimental cancer therapy that seeks to eradicate tumors by initiating cytotoxic photochemistry within an irradiated tissue. Briefly, a photosensitizing drug is administered, typically through systemic injection, and, for reasons still unknown, preferentially accumulates in cancerous tissue. Upon optical excitation in the presence of molecular oxygen ($^3O_2$), this agent produces high yields of singlet oxygen ($^1O_2$), which is known to be harmful to cellular function and is believed to the principal cytotoxic species involved in

PDT. Photofrin®-PDT has recently been approved in the United States for the treatment of esophageal cancer and has also been approved in Canada, the Netherlands, and Japan for the treatment of a variety of indications. Various aspects of this effort have recently been reviewed (Gomer, 1991; Henderson and Dougherty, 1992; Dougherty, 1993; van Hillegersberg *et al.*, 1994).

Over the past several years, research conducted by ourselves and our collaborators has raised questions regarding the general validity of a commonly accepted measure of photodynamic dose, namely, the product of the fluence of the incident radiation and the local photosensitizer concentration (Fingar *et al.*, 1987; Patterson *et al.*, 1990). Studies of tumor response to PDT conducted in three rodent tumor models and with two different photosensitizers indicate a substantial dependence on the incident fluence rate when the product of the total fluence and the photosensitizer concentration is held constant (Feins *et al.*, 1990; Foster *et al.*, 1991; Cincotta *et al.*, 1994; Hua *et al.*, 1995). Similar fluence rate effects have been demonstrated in a study of photodynamic efficacy in multicell tumor spheroids (Foster *et al.*, 1993). While not all tumors exhibit the same pattern of response (Dougherty, 1993; Gibson *et al.*, 1994), it is now clear that the irradiation fluence rate can significantly alter therapeutic outcome in certain situations.

Our interpretation of these experiments has centered on the hypothesis that PDT conducted at high fluence rates can induce an hypoxic region wherein the $^3O_2$ concentration is too low to support the sustained production of $^1O_2$. We have hypothesized that this should occur if the rate of photodynamic $^3O_2$ depletion exceeds the rate at which diffusion can resupply the treatment volume. This hypothesis has been expressed in terms of a mathematical model of PDT induced $^3O_2$ consumption in the vicinity of a pair of capillaries to offer a qualitative explanation of the fluence rate effects observed *in vivo* (Foster and Gao, 1992), and more recently was shown to be consistent with the fluence rate dependence of multicell tumor spheroid response to PDT (Foster *et al.*, 1993). In that recent study, we assumed that the rate of photodynamic $^3O_2$ consumption would be proportional to the incident fluence rate. We then used the solution of the steady-state diffusion-with-consumption equation to determine the constant of proportionality that gave the best agreement between the fraction of cells that survived therapy at a given fluence rate and the spheroid volume fraction predicted to be in an anoxic environment as a result of therapy induced $^3O_2$ depletion. Although we found agreement by assuming that this linear relationship existed, until recently we had not actually measured photodynamic $^3O_2$ depletion.

In this chapter, we describe a series of measurements, made with a Clark-style oxygen microelectrode, that demonstrate photochemical $^3O_2$ depletion in a multicell tumor spheroid undergoing PDT. When analyzed in terms of a time-dependent theory of $^3O_2$ diffusion with consumption, these measurements quantitatively determine the rate of photodynamic $^3O_2$ consumption as a function of the incident fluence rate and several other parameters that describe $^3O_2$ diffusion in this system. With these parameters and a knowledge of the properties of $^1O_2$ in a cellular environment, the $^3O_2$ -diffusion-with-consumption model can be used to calculate the amount and distribution of reacting $^1O_2$ molecules in a multicell tumor spheroid during PDT conducted according to a specific therapeutic protocol. We report the results of a series of such calculations based on our previously reported study of the fluence rate dependence of photodynamic efficacy in multicell spheroids. By comparing the calculations with the results of these experiments, we are able to estimate the threshold dose of reacting $^1O_2$ necessary to kill cells in the EMT6/Ro spheroid.

2.2 The Oxygen Dependence of PDT

It is widely accepted that the principal cytotoxic product of porphyrin photosensitization is $^1O_2$, the lowest lying electronic excited state of $^3O_2$ (Weishaupt *et al.*, 1976). The mechanism of $^1O_2$ production by the optical excitation of a photosensitizer and the subsequent reaction of $^1O_2$ with a biological substrate has been described by Foote as a type II photooxidation (Foote, 1967). This process is depicted in Figure 2.1 as an intermolecular energy level diagram. Light incident on tissue containing a photosensitive porphyrin in its ground state, S_0, will promote the molecule to an excited singlet state, S_1. The majority of these excitations will proceed to the lowest excited triplet state, T_1, through intersystem crossing. T_1 will be quenched through interactions with $^3O_2$, and a fraction of these interactions, S_Δ, will promote $^3O_2$ to $^1O_2$. It has been estimated that $^1O_2$ will diffuse less than 70 nm from its point of origin before reacting with, or being quenched by, a variety of cellular targets denoted, A, in Figure 2.1 (Moan, 1990).

Since $^1O_2$ production is dependent on the availability of $^3O_2$, the rate of $^1O_2$ formation is fundamentally limited by $^3O_2$ supply. As Figure 2.1 indicates, the

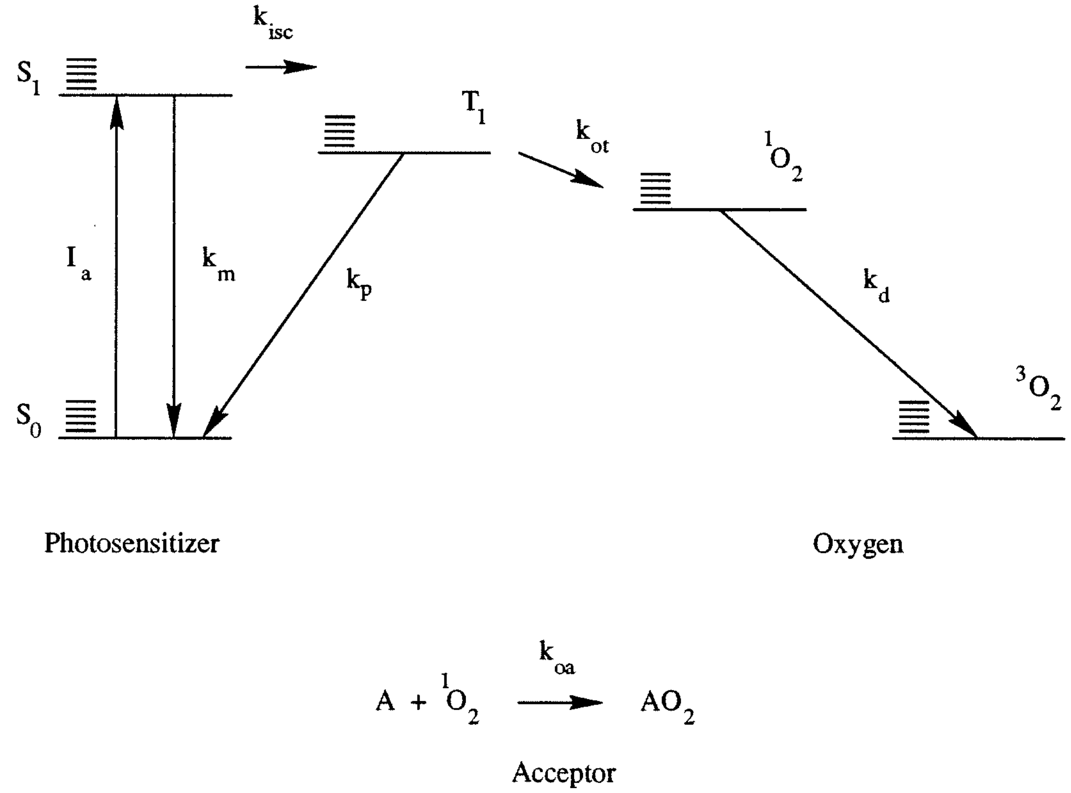
k isc
S1
S0
T1
I a
k m
k p
k ot
1O2
k d
3O2
Photosensitizer
Oxygen
k oa
A + 1O2 → AO2
Acceptor

Figure 2.1: The Jablonski diagram for type-II photooxygenation reactions. The photosensitizer singlet and triplet states are denoted S and T, respectively, while the intracellular targets of $^1O_2$ reaction are denoted A. The kinetic rate constants associated with the fundamental transitions are placed adjacent to arrows depicting the transition.

ratio of the T_1 decay rate, k_p, to the T_1-$^3O_2$ interaction rate, k_{ot}, is the oxygen concentration at which half of the excited sensitizer triplets will be quenched by $^3O_2$, while the remainder decay through radiative and non-radiative pathways independent of $^3O_2$. When the local $^3O_2$ concentration is greater than k_p/k_{ot}, T_1 will be efficiently quenched by $^3O_2$, and consequently the $^1O_2$ production and reaction rates will be maximal. Conversely, if the $^3O_2$ concentration is reduced below k_p/k_{ot} the principal decay route for T_1 will be independent of $^3O_2$ and the rate of $^1O_2$ formation and subsequent reaction will be reduced accordingly. Hence, this ratio dictates the sensitivity of the $^1O_2$ formation rate to the local $^3O_2$ concentration, and in a biological environment where $^3O_2$ supply is limited by diffusion, it can influence the extent of anoxic regions resulting from excessive photodynamic $^3O_2$ consumption.

Since $^1O_2$ reaction with substrate removes $^3O_2$ from the system, $^1O_2$ reaction can be monitored by measuring $^3O_2$ consumption. Kimel *et al.* (1989) have proposed that this principle could be used to screen photosensitizers *in vitro* for desirable photophysical properties. In another study, Tromberg *et al.* (1990) used transcutaneous $^3O_2$ sensors to monitor the $^3O_2$ tension in a tumor during PDT. They reported that $^3O_2$ depletion appeared to be caused by a combination of photochemical $^3O_2$ consumption and changes in the vasculature and suggested that observations such as these may be useful in monitoring the progress of PDT. Although a quantitative assessment of therapy induced $^3O_2$ depletion is complicated by vascular effects *in vivo*, the principle of measuring $^3O_2$ consumption to assess the efficiency of PDT offers an intriguing approach to photodynamic dosimetry.

Given the extremely short diffusion distance of ${}^1O_2$, the spatial distribution of ${}^3O_2$ consumption will correspond to the spatial distribution of ${}^1O_2$ reaction. In a biological system in which the rate of ${}^3O_2$ consumption can be measured, this relationship can be used as a quantitative measure of photodynamic dose, which should be more accurate than estimating ${}^1O_2$ production from photosensitizer absorption. Although this approach may not be feasible *in vivo* due to the sheer complexity of the vascular involvement, the *in vitro* multicell tumor spheroid provides a realistic tumor environment in which ${}^3O_2$ supply and transport are very well understood (Sutherland *et al.*, 1971; Mueller-Klieser, 1984).

2.3 The Multicell Spheroid Model Tumor System

Developed in 1971 by Robert M. Sutherland and co-workers, the multicell spheroid is a spherical aggregate of tumor cells grown in suspension culture to a diameter ranging from 100 μm to greater than 1 mm (Sutherland *et al.*, 1971). The spheroid is intermediate in complexity between cell monolayers or single cell suspensions and intact animal tumors. In contrast with a tumor *in situ*, the spheroid lacks a functioning vasculature and must obtain nutrients for cell growth and function (and eliminate catabolites resulting from these processes) by diffusion from the external medium. Nevertheless, many important features of a tumor system remain: natural cell-cell contact is preserved and typical nutrient gradients can be established by selecting spheroids with a radius typical of capillary separations *in vivo.* Like cells bordering a capillary, cells in the periphery of the spheroid obtain the best nutrient supply and proliferate rapidly. The cells in the center of a spheroid, however, are more quiescent and if the spheroid diameter exceeds a critical radius necrosis can result in this region due to insufficient supply conditions (Franko and Sutherland, 1979). "Spontaneous necrosis" is similarly observed in tumors which grow faster than their vascular capacity.

Multicell tumor spheroids have been used in a variety of studies in which it is desirable to study malignant cells in a tumor-like environment. The relationship between hypoxia, glucose concentration, and the development of necrosis (Mueller-Klieser *et al.*, 1983) as well as the radio-resistance of cells lying in hypoxic regions of a tumor (Durand, 1983) are only two examples of studies for which the spheroid has been shown to be ideally suited. More recently, West (1989) has investigated PDT resistant cells in the multicell tumor model, and König *et al.* (1994) have used a variety of microscopy techniques to observe porphyrin distribution in 5-aminolevulinic acid (ALA)-incubated spheroids as well as intracellular changes resulting from PDT.

The spherical symmetry of the multicell aggregate along with isotropic supply conditions created by the lack of a vascular network make the spheroid a very attractive model system to study the effects of photochemical oxygen consumption during PDT. Furthermore, since the spheroid captures many of the features of a tumor *in situ*, results obtained from this model should also be applicable to more realistic tumor systems.

2.4 Steady-State Oxygen Diffusion with Consumption in the Metabolizing Spheroid

Without a vascular network, the spheroid depends solely on diffusion for nutrient supply. Diffusion of H^+ (protons), ^{3}H-inulin, ^{3}H-thymidine as well as oxygen have been studied under a variety of conditions (Carlsson and Acker, 1988; Freyer and Sutherland, 1983; Mueller-Klieser, 1984). Because of the simple geometry of the spheroid and the possibility for symmetrical supply conditions *in vitro*, the $^3O_2$ distribution can be easily determined by balancing isotropic diffusive supply and metabolic consumption.

Figure 2.2 illustrates the pertinent spatial regions within and exterior to a multicell tumor spheroid suspended in a nutrient rich aqueous medium. $^3O_2$ diffuses into the spheroid from the edge at R_s according to the diffusion coefficient D_s and is consumed *via* oxidative phosphorylation at a volumetric rate given by Γ_{met}. Immediately exterior to the spheroid, $^3O_2$ diffuses in the aqueous medium with a diffusion coefficient D_d. Beyond a critical radius, R_d, we specify that the $^3O_2$ concentration in the bulk medium, C_{bulk}, is uniform. This is done in accordance with our experiments conducted in unstirred media, as well as those of others conducted in flowing media (Mueller-Klieser and Sutherland, 1982) and will be discussed shortly. The $^3O_2$ concentration, $C(r)$, can be quantified by solving the radial part

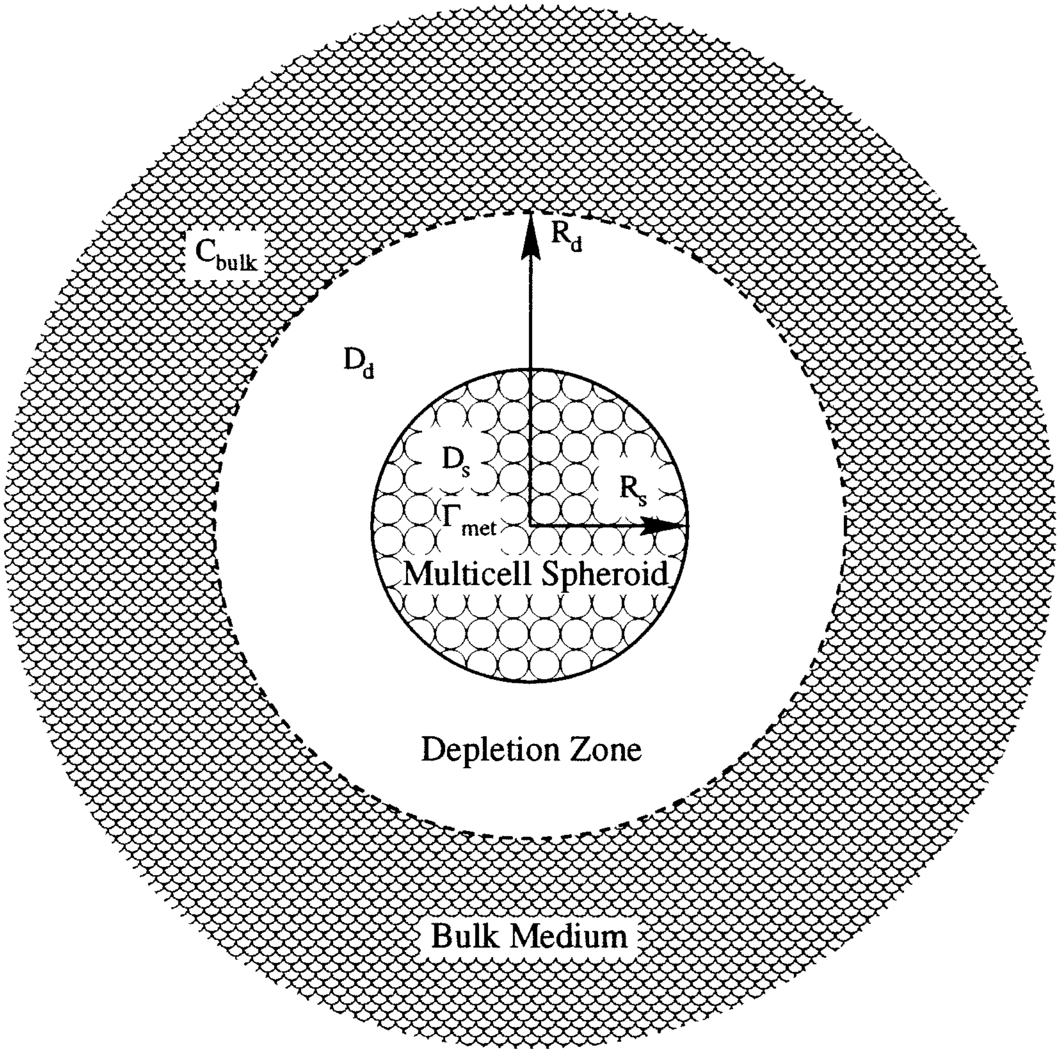
C_bulk
R_d
D_d
D_s
R_s
Γ_met
Multicell Spheroid
Depletion Zone
Bulk Medium

Figure 2.2: The various spatial regions and parameters used to characterize $^3O_2$ transport and consumption in the vicinity of a multicell tumor spheroid. The spheroid radius is specified by R_s, and the diffusion coefficient in the spheroid is D_s. Within the spheroid, oxygen is consumed at a metabolic volumetric rate of Γ_{met}. Immediately exterior to the spheroid, the depletion zone extends a distance R_d, at which point the $^3O_2$ concentration equals that of the bulk medium, C_{bulk}.

of a pair of diffusion–with–consumption equations, given by

$$\begin{aligned}\vec{\nabla}\cdot\left(D_s\vec{\nabla}C(r)\right) &= \Gamma_{met} \qquad (0 < r \leq R_s) \qquad (2.1)\\ \vec{\nabla}\cdot\left(D_d\vec{\nabla}C(r)\right) &= 0 \qquad (R_s < r \leq R_d)\end{aligned}$$

with the appropriate conditions placed upon $C(r)$ at the boundaries. Namely, the $^3O_2$ flux through the center of the spheroid must be zero by symmetry, the $^3O_2$ concentration and the $^3O_2$ flux are continuous at the spheroid edge, and the $^3O_2$ concentration is equal to the bulk $^3O_2$ concentration at the edge of the depletion zone. The following equations express these requirements in terms of the transport parameters of the problem:

$$\begin{aligned} D_s\frac{\partial C(r)}{\partial r}\Big|_0 &= 0, & (2.2)\\ C(R_s^-) &= C(R_s^+), & (2.3)\\ D_s\frac{\partial C(r)}{\partial r}\Big|_{R_s^-} &= D_d\frac{\partial C(r)}{\partial r}\Big|_{R_s^+}, & (2.4)\\ C(r = R_d) &= C_{bulk}, & (2.5)\end{aligned}$$

where the '+' and '-' superscripts indicate that the quantity is to be evaluated just inside the depletion zone or spheroid, respectively. Although it is more generally correct to require the $^3O_2$ partial pressure to be continuous between two regions characterized by differing $^3O_2$ solubilities, we have found insignificant differences between the $^3O_2$ solubilities of the multicell tumor spheroid and the physiological medium which surrounds it. For simplicity we assume that Γ_{met}, D_s, and D_d are all uniform in their respective regions. This may not seem, *a priori*, to be an accurate description of transport within the spheroid which is a heterogeneous cellular aggregate. Indeed, it has been demonstrated that the cellular microenvironment varies radially within the spheroid. For example, Grossmann (1984) has reported that the cell density *decreases* from the edge to the center in spheroids cultured from some cell lines. Furthermore, since the cells at the edge of the spheroid proliferate more rapidly than those in the center, it is not clear that the metabolic activity in these regions will be similar. Nevertheless, Grossmann found little difference between calculated oxygen partial pressure distributions assuming either a constant or a linearly varying oxygen diffusion coefficient and solubility when the variation was based on the local cell density. Mueller-Klieser (1984) and others have made similar assumptions of uniformity with satisfactory results. When these quantities are held constant, the solution to Equation (2.1) is

$$\begin{aligned} C(r) &= C_{bulk} - \frac{\Gamma_{met} R_s^3}{3D_d}\left(\frac{1}{R_s} - \frac{1}{R_d}\right) - \frac{\Gamma_{met}}{6D_s}\left(R_s^2 - r^2\right) \quad (0 < r \leq R_s) \\ &= C_{bulk} - \frac{\Gamma_{met} R_s^3}{3D_d}\left(\frac{1}{r} - \frac{1}{R_d}\right) \quad (R_s < r \leq R_d). \end{aligned} \tag{2.6}$$

This solution is only appropriate for spheroids that have not developed necrosis. For spheroids with necrosis, the $^3O_2$ consumption rate within the necrotic region would be zero, and there would be no net flux of $^3O_2$ in these regions (Mueller-Klieser, 1984). Since we are ultimately interested in quantifying photodynamic damage within the spheroid, we wish to minimize the occurrence of spontaneous necrosis. Consequently, we have chosen to work with EMT6/Ro spheroids approximately 500 μm in diameter which rarely exhibit spontaneous necrosis.

By holding the $^3O_2$ concentration constant beyond the depletion zone (Equation (2.5)), we are implicitly accommodating an external source of ${}^3O_2$. In the experiments that will be described in Section 2.7, this expresses the fact that the measuring chamber is open to the environment. While the metabolizing spheroid consumes ${}^3O_2$ in the medium, ${}^3O_2$ is resupplied from the air such that a steady-state ${}^3O_2$ distribution can be established. The fact that the ${}^3O_2$ gradient is limited to a depletion zone of approximately 1 mm in diameter is an indication that the bulk medium is being stirred. When the experiment is done in an ${}^3O_2$ regulated, sealed chamber with the spheroid in a flowing medium, it has been demonstrated that the depletion zone is limited to an unstirred layer of medium surrounding the spheroid. Oxygen must be supplied from the edge of the depletion zone, R_d, at a rate equal to that at which it is consumed within the spheroid if a steady-state ${}^3O_2$ distribution is to be established. This rate is determined from the ${}^3O_2$ gradient or "kink" in the ${}^3O_2$ concentration at the edge depletion zone. If the depletion zone is static, then the flux into the depletion zone resulting from stirring is given by

$$\vec{J}(R_d) = -\left(\frac{\langle\Gamma\rangle R_s^3}{3R_d^2}\right)\hat{r} \tag{2.7}$$

where $\langle\Gamma\rangle$ is the average rate of ${}^3O_2$ consumption within the spheroid, and $\hat{r}$ is the outwardly directed radial unit vector. If $\langle\Gamma\rangle$ is increased after a (static) depletion zone has been established, then either the gradient in the oxygen concentration must increase or the depletion zone will grow in extent. Which of these two events will occur depends on the rate at which the bulk (stirred) medium can supply oxygen. If the bulk medium is nearly static then one would expect the latter event to occur. In this case, an increase in the net rate of ${}^3O_2$ consumption in the spheroid will cause the boundary to expand at such a rate so as to provide an advective flux into the depletion zone that will balance the increased flux entering the spheroid, assuming bulk equilibrium conditions prevail. The flux at the boundary of the depletion zone would then be specified by

$$\vec{J}(R_d(t)) = -D_d\vec{\nabla}[^3O_2](R_d(t),t) - \vec{v}[^3O_2]_{bulk} \tag{2.8}$$

where $\vec{v}$ is the velocity of the boundary of the depletion zone, and $[^3O_2]_{bulk}$ is the $^3O_2$ concentration in the bulk medium. The movement of the boundary is then explicitly connected to the rate of oxygen consumption within the spheroid by the following differential equation:

$$\frac{dR_d}{dt} = \frac{1}{R_d^2[^3O_2]_m}\left(\frac{\langle\Gamma(t)\rangle\, R_s^3}{3} - D_d\frac{\partial[^3O_2](R_d(t),t)}{\partial r}\right). \tag{2.9}$$

2.5 The Formulation of the Time-Dependent Diffusion-with-Consumption Model

If photodynamic treatment is initiated in a spheroid, photodynamic oxygen consumption can perturb the steady-state $^3O_2$ distribution both within the spheroid and in the depletion zone. We can model this by replacing the metabolic consumption term in Equation (2.1) with the total rate of oxygen consumption, $\Gamma(r,t)$, specified by

$$\Gamma(r,t) = \Gamma_{met} + \Gamma_{PDT}(r,t) \qquad 0 < r < R_s \tag{2.10}$$

where $\Gamma_{PDT}(r,t)$ represents the rate of $^3O_2$ consumption due to PDT, which can vary in both space and time within the spheroid. The functional dependence of

Γ_{PDT} on $^3O_2$ is determined from the kinetic equations that follow from Figure 2.1. Using the instantaneous steady-state solutions for the photosensitizer triplet and $^1O_2$ concentrations, the instantaneous rate of $^3O_2$ consumption by PDT is

$$\Gamma_{PDT} = \Gamma_0 \left(\frac{k_{ot}[^3O_2]}{k_p + k_{ot}[^3O_2]} \right) \tag{2.11}$$

with

$$\Gamma_0 = S_\Delta \phi_t I_a \left(\frac{k_{oa}[A]}{k_d + k_{oa}[A]} \right) \tag{2.12}$$

where I_a denotes the rate of photon absorption, ϕ_t denotes the photosensitizer triplet yield, and S_Δ denotes the fraction of triplet quenching collisions with $^3O_2$ that result in $^1O_2$ formation. Allowing for the fact that the $^1O_2$ acceptor concentration, $[A]$, will be relatively uniform and static in comparison with the $^3O_2$ concentration, Γ_0 will be a constant that is linearly dependent on the incident fluence rate, and the spatial and temporal dependence of $\Gamma_{PDT}(r,t)$ will arise functionally through its dependence on the $^3O_2$ concentration. Therefore, we have

$$\Gamma_{PDT}(r,t) = \Gamma_0 \left(\frac{C(r,t)}{C(r,t) + \frac{k_p}{k_{ot}}} \right) \qquad 0 \le r < R_s \tag{2.13}$$

with

$$\Gamma_0 = \beta_{PDT}\phi \tag{2.14}$$

where β_{PDT} is a constant and ϕ is the incident fluence rate, which is turned on at $t = 0$.

The coupled time-dependent diffusion-with-consumption equations that would then describe the spatial and temporal ${}^3O_2$ distributions are

$$\begin{aligned} D_d\nabla^2 C(r,t) &= \frac{\partial C(r,t)}{\partial t} \qquad R_s < r < R_d \\ D_s\nabla^2 C(r,t) - \Gamma(r,t) &= \frac{\partial C(r,t)}{\partial t} \qquad 0 < r \le R_s \end{aligned} \tag{2.15}$$

where t is the time from initiation of PDT. These equations are solved subject to the boundary conditions at the edge of the spheroid and the edge of the depletion zone as described by Equations (2.2) - (2.5). The initial condition is specified by the solution of the corresponding steady-state diffusion-with-metabolic-consumption Equation (2.6). As discussed previously, when the rate of ${}^3O_2$ consumption is time-dependent the radius of the depletion zone will also be time-dependent. While Equation (2.9) can be solved to determine the location of the depletion zone, for the following theoretical treatment we avoid this complexity and assume that R_d is constant.

2.6 The Numerical Solution of the Time-Dependent Oxygen Diffusion-with-Consumption Equation

The solution of Equation (2.15) with the total rate of oxygen consumption specified by Equation (2.10) does not have a simple analytic form, but it can be solved numerically. To this end, the space and time coordinates are discretized and placed on a radial lattice. The spatial lattice that is employed is shown in Figure 2.3. The space coordinate, r, and the time coordinate, t, are given by

$$r \rightarrow (i-1)\Delta r \qquad i = 1,2,3\ldots \tag{2.16}$$

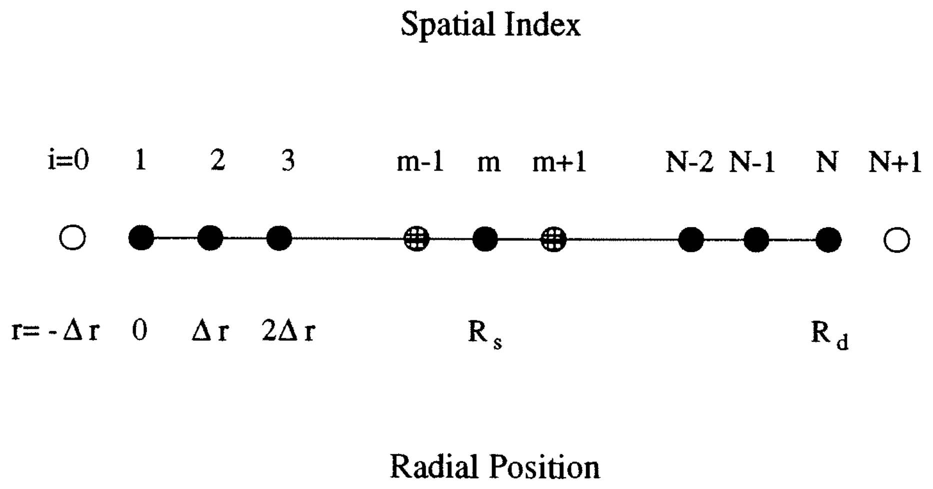

Figure 2.3: The spatial lattice used in the numerical solution of the time-dependent diffusion-with-consumption equation. A uniform grid of lattice points separated by Δr is used within the spheroid and in the depletion zone. The closed circles represent lattice points where the oxygen concentration is evaluated. The open circles represent fictitious spatial locations which are used to obtain a second-order approximation of the boundary conditions. The hatched circles on either side of the spheroid boundary serve a dual purpose. They are used to obtain the one-sided spatial derivatives of $^3O_2$ accurate to second order, but they are also real locations where the oxygen concentration is evaluated.

$$t \rightarrow n\Delta t \qquad n = 0, 1, 2 \ldots \tag{2.17}$$

where i and n represent the spatial and temporal lattice points, and Δr and Δt are the uniform spacings between the spatial and temporal lattice points, respectively. The oxygen concentration is similarly discretized,

$$C(r,t) \rightarrow C_i^n. \tag{2.18}$$

The following second order analogs to the first and second derivative of the oxygen concentration in space are used:

$$\left(\frac{\partial C(r,t)}{\partial r}\right)_i^n = \frac{C_{i+1}^n - C_{i-1}^n}{2\Delta r} \tag{2.19}$$

$$\left(\frac{\partial^2 C(r,t)}{\partial r^2}\right)_i^n = \frac{C_{i+1}^n - 2C_i^n + C_{i-1}^n}{\Delta r^2}, \tag{2.20}$$

while the corresponding second order time derivative is evaluated between grid points to guarantee stability,

$$\left(\frac{\partial C(r,t)}{\partial t}\right)_i^{n+\frac{1}{2}} = \frac{C_i^{n+1} - C_i^n}{\Delta t}. \tag{2.21}$$

To insure that the space and time derivatives are evaluated at the same time point, the following Crank-Nicolson approximation is used:

$$\left(\frac{\partial C(r,t)}{\partial r}\right)_i^{n+\frac{1}{2}} = \frac{1}{2}\left[\left(\frac{\partial C(r,t)}{\partial r}\right)_i^n + \left(\frac{\partial C(r,t)}{\partial r}\right)_i^{n+1}\right] \tag{2.22}$$

$$\left(\frac{\partial^2 C(r,t)}{\partial r^2}\right)_i^{n+\frac{1}{2}} = \frac{1}{2}\left[\left(\frac{\partial^2 C(r,t)}{\partial r^2}\right)_i^n + \left(\frac{\partial^2 C(r,t)}{\partial r^2}\right)_i^{n+1}\right] \tag{2.23}$$

$$\Gamma_i^{n+\frac{1}{2}} = \frac{1}{2}\left(\Gamma_i^n + \Gamma_i^{n+1}\right) \tag{2.24}$$

(Crank, 1975). With these approximations, Equation (2.15) at time index $n + \frac{1}{2}$ and space index i is written:

$$\begin{aligned}
\frac{\bar{C}_i^{n+1} - \bar{C}_i^n}{\Delta\bar{t}} &= \frac{D_s}{2D_d}\left[\frac{\bar{C}_{i+1}^{n+1} - 2\bar{C}_i^{n+1} + \bar{C}_{i-1}^{n+1} + \bar{C}_{i+1}^n - 2\bar{C}_i^n + \bar{C}_{i-1}^n}{\Delta\bar{r}^2}\right. \\
&\left. + \frac{1}{(i-1)\Delta\bar{r}}\left(\frac{\bar{C}_{i+1}^{n+1} - \bar{C}_{i-1}^{n+1} + \bar{C}_{i+1}^n - \bar{C}_{i-1}^n}{\Delta\bar{r}}\right)\right] - \frac{1}{2}\left[\bar{\Gamma}_i^{n+1} + \bar{\Gamma}_i^n\right] \qquad 1 < i < m \\
\frac{\bar{C}_i^{n+1} - \bar{C}_i^n}{\Delta\bar{t}} &= \frac{1}{2}\left[\frac{\bar{C}_{i+1}^{n+1} - 2\bar{C}_i^{n+1} + \bar{C}_{i-1}^{n+1} + \bar{C}_{i+1}^n - 2\bar{C}_i^n + \bar{C}_{i-1}^n}{\Delta\bar{r}^2}\right. \\
&\left. + \frac{1}{(i-1)\Delta\bar{r}}\left(\frac{\bar{C}_{i+1}^{n+1} - \bar{C}_{i-1}^{n+1} + \bar{C}_{i+1}^n - \bar{C}_{i-1}^n}{\Delta\bar{r}}\right)\right] \qquad m \leq i < N.
\end{aligned} \tag{2.25}$$

Here, in anticipation of a numerical solution, a dimensionless set of variables have been chosen and are indicated with barred symbols:

$$\begin{aligned}
\bar{r} &= \frac{r}{R_s} \\
\bar{t} &= \frac{D_d t}{R_s^2} \\
\bar{C} &= \frac{C}{C_{bulk}} \\
\bar{\Gamma} &= \frac{\Gamma R_s^2}{C_{bulk} D_d}
\end{aligned} \tag{2.26}$$

The boundary equations are also discretized and centered at $(i, n + \frac{1}{2})$. To obtain second order accuracy in the boundary conditions, Equation (2.19) requires that the spatial derivatives make use of oxygen concentrations on both sides of the boundary. Since boundary Equations (2.2) - (2.5) must be evaluated on either side of the boundary, the medium is extended by the addition of a fictitious lattice point and the diffusion equation is used to evaluate the corresponding fictitious oxygen concentration. This process is thoroughly described by Crank (1975). The discretized boundary conditions are then

$$\begin{aligned}
2\left(\frac{\bar{C}_m^{n+1}-\bar{C}_m^n}{\Delta\bar{t}}\right) &= \left(\frac{m}{m-1}\right)\frac{\bar{C}_{m+1}^{n+1}-\bar{C}_m^{n+1}+\bar{C}_{m+1}^n-\bar{C}_m^n}{\Delta\bar{r}^2} - \\
&\quad \left(\frac{m-2}{m-1}\right)\left(\frac{D_s}{D_d}\right)\frac{\bar{C}_m^{n+1}-\bar{C}_{m-1}^{n+1}+\bar{C}_m^n-\bar{C}_{m-1}^n}{\Delta\bar{r}^2} - \\
&\quad \frac{1}{2}\left(\frac{m-2}{m-1}\right)\left(\Gamma_m^{n+1}+\Gamma_m^n\right) \qquad (2.27) \\
\frac{\bar{C}_1^{n+1}-\bar{C}_1^n}{\Delta\bar{t}} &= \left(\frac{D_s}{D_d}\right)\frac{\bar{C}_2^{n+1}-\bar{C}_1^{n+1}+\bar{C}_2^n-\bar{C}_1^n}{\Delta\bar{r}^2} - \\
&\quad \frac{1}{2}\left(\Gamma_1^{n+1}+\Gamma_1^n\right) \qquad (2.28) \\
\frac{\bar{C}_N^{n+1}-\bar{C}_N^n}{\Delta\bar{t}} &= \frac{\bar{C}_{N-1}^{n+1}-\bar{C}_N^{n+1}+\bar{C}_{N-1}^n-\bar{C}_N^n}{\Delta\bar{r}^2}. \qquad (2.29)
\end{aligned}$$

As written, Equation (2.25) would form a tridiagonal matrix equation if $\bar{\Gamma}$ is at most linear in the oxygen concentration. However, the kinetic equations that describe photodynamic oxygen consumption indicate that this is not the case. To simplify the problem, either $\bar{\Gamma}$ must be linearized or evaluated only at the past time index, *i.e.*

$$\frac{1}{2}\left(\bar{\Gamma}_i^{n+1}+\bar{\Gamma}_i^n\right) \rightarrow \bar{\Gamma}_i^n \qquad (2.30)$$

By making this substitution, the nonlinearity is removed because the oxygen concentration at time index, $n+1$, will no longer depend on the rate of consumption (and, therefore, nonlinearly on itself by Equation (2.11), at the same time index. Instead, it depends only on the past consumption rate. Practically, this places a time lag of $0.5\Delta t$ on the rate of consumption. The enormous simplification of the problem warrants this kind of linearization. Furthermore, if Δt is taken small enough such that $\bar{\Gamma}$ doesn't change appreciably between two successive time indices, then the resulting error will be slight.

The resulting system of coupled algebraic equations forms a tridiagonal matrix equation that can be solved at each time step to determine the current radial $^3O_2$ distribution in terms of the distribution obtained at the previous step. Through iteration, the complete temporal and radial distribution of $^3O_2$ can be determined for a particular therapeutic protocol given appropriate values for the model parameters. This matrix equation is written

$$\begin{pmatrix} e_1 & f_1 & & & & & & \\ d_2 & e_2 & f_2 & & & & & \\ & & \ddots & & & & & \\ & & d_m & e_m & f_m & & & \\ & & & & \ddots & & & \\ & & & & d_{N-1} & e_{N-1} & f_{N-1} \\ & & & & & d_N & e_N \end{pmatrix} \begin{pmatrix} C_1^{n+1} \\ C_2^{n+1} \\ \vdots \\ C_i^{n+1} \\ \vdots \\ C_{N-1}^{n+1} \\ C_N^{n+1} \end{pmatrix} = \begin{pmatrix} g_1^n \\ g_2^n \\ \vdots \\ g_i^n \\ \vdots \\ g_{N-1}^n \\ g_N^n \end{pmatrix} \tag{2.31}$$

where

$$\begin{array}{llll} & e_1 = 1 + \frac{D_s}{D_d}\alpha & f_1 = -\frac{D_s}{D_d}\alpha & \\ d_i = -\frac{\alpha D_s}{2D_d}\left(\frac{i-2}{i-1}\right) & e_i = 1 + \frac{D_s}{D_d}\alpha & f_i = -\frac{\alpha D_s}{2D_d}\left(\frac{i}{i-1}\right) & (1 < i < m) \\ d_m = -\frac{\alpha D_s}{2D_d}\left(\frac{m-2}{m-1}\right) & e_m = 1 + \frac{\alpha}{2}\left(\frac{m}{m-1}\right) & f_m = -\frac{\alpha}{2}\left(\frac{m}{m-1}\right) & \\ & \quad +\frac{\alpha D_s}{2D_d}\left(\frac{m-2}{m-1}\right) & & \\ d_i = -\frac{\alpha}{2}\left(\frac{i-2}{i-1}\right) & e_i = 1 + \alpha & f_i = -\frac{\alpha}{2}\left(\frac{i}{i-1}\right) & (m < i < N) \\ d_N = -\frac{\alpha}{2}\left(\frac{N-2}{N-1}\right) & e_N = 1 + \alpha & & , \end{array} \tag{2.32}$$

and

$$\begin{aligned}
g_1^n &= \left(1 - \tfrac{\alpha D_s}{D_d}\right) \bar{C}_1^n + \tfrac{\alpha D_s}{D_d} \bar{C}_2^n - \Delta\bar{t}\bar{\Gamma}_1^n \\
g_i^n &= \tfrac{\alpha D_s}{2D_d} \left(\tfrac{i-2}{i-1}\right) \bar{C}_{i-1}^n + \left(1 - \tfrac{\alpha D_s}{D_d}\right) \bar{C}_i^n + \tfrac{\alpha D_s}{2D_d} \left(\tfrac{i}{i-1}\right) \bar{C}_{i+1}^n - \Delta\bar{t}\bar{\Gamma}_i^n \qquad (1 < i < m) \\
g_m^n &= \tfrac{\alpha D_s}{2D_d} \left(\tfrac{m-2}{m-1}\right) \bar{C}_{m-1}^n + \left(1 - \tfrac{\alpha}{2}\left(\tfrac{m}{m-1}\right) - \tfrac{\alpha D_s}{2D_d}\left(\tfrac{m-2}{m-1}\right)\right) \bar{C}_m^n + \\
&\quad \tfrac{\alpha}{2}\left(\tfrac{m}{m-1}\right) \bar{C}_{m+1}^n - \tfrac{\Delta\bar{t}}{2}\left(\tfrac{m-2}{m-1}\right) \bar{\Gamma}_m^n \\
g_i^n &= \tfrac{\alpha}{2}\left(\tfrac{i-2}{i-1}\right) \bar{C}_{i-1}^n + (1-\alpha)\, \bar{C}_i^n + \tfrac{\alpha}{2}\left(\tfrac{i}{i-1}\right) \bar{C}_{i+1}^n \qquad (m < i < N) \\
g_N^n &= \tfrac{\alpha}{2}\left(\tfrac{N-2}{N-1}\right) \bar{C}_{N-1}^n + (1-\alpha)\, \bar{C}_N^n + \alpha\left(\tfrac{N}{N-1}\right) \quad .
\end{aligned} \tag{2.33}$$

In these equations

$$\alpha = \frac{\Delta\bar{t}}{\Delta\bar{r}^2}, \tag{2.34}$$

and, as in Figure 2.3, the index m is the location of the spheroid boundary. All of the elements of the square matrix off the center three diagonals are zero, which indicates that for this second order approximation, the future oxygen concentration at a given lattice point depends only on its nearest neighbor concentrations and the previous oxygen concentration at that point. Numerical algorithms for solving sparse matrix equations such as these are readily available and easily implemented. The algorithm used for the numerical work described here is based on the TRIDAG routine of Press *et al.* (1992). Since the tridiagonal matrix coefficients are dependent only on physical parameters, such as the diffusion coefficient, which are assumed to be constant throughout photodynamic treatment, these need only be evaluated once. The procedure is to evaluate the right hand side vector at each time index using the distribution of ${}^3O_2$ concentration made available by the algorithm at the previous time index. The information for the first evaluation comes from the initial condition. With this, the tridiagonal matrix equation is solved to give the ${}^3O_2$ distribution at the successive time index. The procedure is then repeated to give the complete spatial and temporal distribution of ${}^3O_2$ which results during photodynamic treatment. Note that at each iteration Equation (2.13) is used to determine the photodynamic rate of oxygen consumption within the spheroid.

2.7 Experimental Results and Analysis

2.7.1 Microelectrode Measurements

The experimental apparatus used to spatially and temporally map the radial ${}^3O_2$ distribution is shown in Figure 2.4. For studies of photodynamic oxygen consumption, EMT6/Ro spheroids are incubated in a 100 mm non-tissue culture Petri dish containing 15 ml Eagle's basal medium (Gibco-BRL, Grand Island, NY), 10% fetal calf serum (Gibco-BRL), and 10 μg ml^{-1} Photofrin® (Quadralogic Technologies, Vancouver, British Columbia, Canada) at 37 °C in a humidified 5% CO_2 - 95% air atmosphere for approximately 24 hours. At the completion of incubation, a photosensitized spheroid, approximately 500 μm in diameter, is placed atop a pedestal on an oxygen permeable membrane in an open dish filled with 20 ml Hanks Balanced Salt Solution (Gibco-BRL). The spheroid is held in place on the pedestal with a thin glass pin. A Clark-style oxygen microelectrode (737GC, Diamond General Development Corp., Ann Arbor, MI), with a tip diameter of approximately 5 μm is positioned with the aid of two orthogonal stereo microscopes in such a way that it can be translated with a micropositioning device on a ray that passes through the center of the spheroid. A lensed fiber optic coupled to an argon laser delivers 514 nm light to the surface of the pedestal.

The Clark-style oxygen microelectrode has many advantages over the traditional open-style microelectrode first described by Whalen *et al.* (1967). The membrane material used for open-style microelectrodes does not electrically insulate the cathode from the medium in which the experiment is conducted, since the Ag/AgCl reference electrode must be in electrical contact with the cathode. This interferes with the measurement of the oxygen concentration in the vicinity of a spheroid, because in addition to the oxygen gradient there is a pronounced pH gradient as well (Carlsson and Acker, 1988). Initially, experiments were conducted with the 723 open-style electrode from Diamond General, but we found this electrode to be very sensitive to pH changes and were unable to reliably measure the $^3O_2$ gradient. The Clark-style microelectrode, however, can use membranes which prevent interference from H^+ ions, since both the cathode and the reference electrode are positioned in close proximity behind the oxygen-permeable membrane. Initial experiments demonstrated that the 737GC Clark-style microelectrode was insensitive to pH changes in the range of 4 to 10, and we found it to be both more stable and more reliable than the open-style electrode.

To determine the $^3O_2$ diffusion and consumption parameters appropriate for a multicell tumor spheroid undergoing PDT, two independent measurements are made with the apparatus shown in Figure 2.4. In the absence of irradiation, a steady-state measurement of the radial $^3O_2$ distribution within and in the vicinity

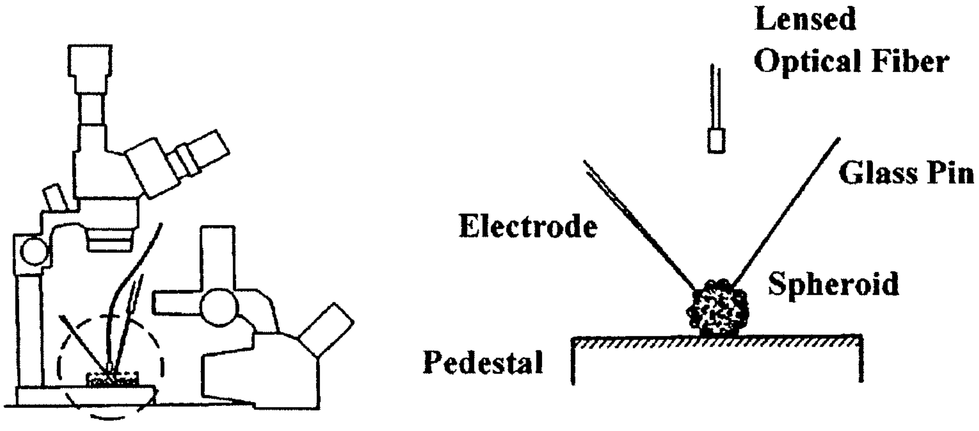
Lensed
Optical Fiber
Glass Pin
Electrode
Spheroid
Pedestal

Figure 2.4: The experimental apparatus for measurements of ${}^3O_2$ consumption in a single spheroid. Two orthogonal stereo-microscopes provide two projections needed to guide the electrode to the edge of the spheroid. The region within the dashed circle is shown expanded in the figure on the right. The pedestal supporting the spheroid is filled with medium and its surface is ${}^3O_2$ permeable.

of the spheroid is made by advancing the microelectrode at 10 μm increments and recording the $^3O_2$ concentration as a function of the radial distance from the center of the spheroid. Equation (2.6) is then fit to the radial $^3O_2$ distribution using a non-linear least-squares fitting algorithm (Press *et al.*, 1992). Assuming literature values for C_{bulk} and D_d and using the measured value of the spheroid radius obtained with a microscope reticle, D_s, Γ_{met} and R_d are optimized to minimize the χ^2 statistic (Bevington and Robinson, 1992). Figure 2.5 shows a representative fit to the measured radial oxygen distribution, and Table 2.1 summarizes the pertinent parameters determined from many of these measurements. On average we find Γ_{met} and D_s are 5.77 μM s^{-1} and 1457 μm^2 s^{-1}, respectively, assuming standard values of 240 μM for C$_{bulk}$ and 2310 μm^2 s^{-1} for D$_d$ (Boag, 1969; St-Denis and Fell, 1971). Table 2.2 compares the ratio of the diffusion coefficients and the metabolic rate of $^3O_2$ consumption determined from these experiments with values from similar experiments conducted by others.

The photodynamic $^3O_2$ consumption parameters, Γ_0 and k_p/k_{ot}, are determined with a time-dependent measurement made by placing the microelectrode at the surface of the spheroid and monitoring $^3O_2$ depletion as a function of time after the onset of irradiation. The numerical solution of Equation (2.15) is fit to the induced $^3O_2$ transient to determine the best values for these parameters. A typical $^3O_2$ transient resulting from PDT conducted at 25 mW cm^{-2} is shown in Figure 2.6 along with the best fit to the data. These measurements have been repeated at four fluence rates to determine the relationship between Γ_0 and the incident fluence rate. Figure 2.7 summarizes the results. A line with a slope of 1.92 ± 0.32

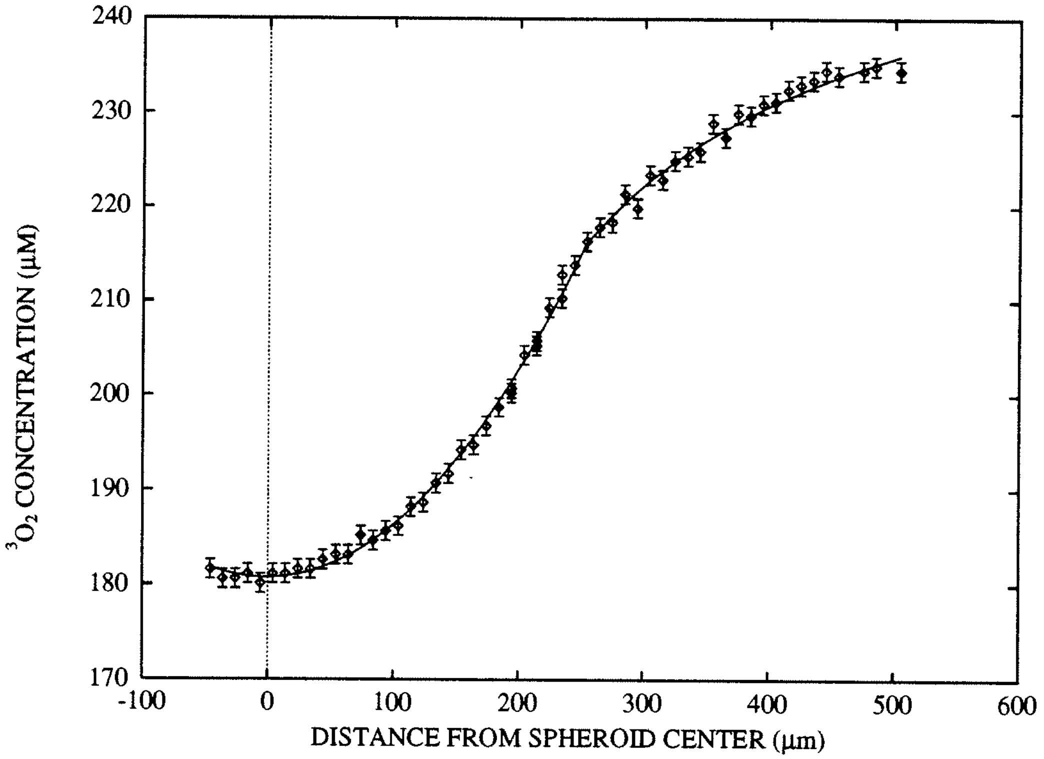

Figure 2.5: Steady-state electrode measurements of the $^3O_2$ concentration in and around a 500 μm diameter spheroid. The solid line is the best fit using Equation (2.6).

R_s (μm)	R_d (μm)	D_s (μm^2 s^{-1})	Γ_{met} (μmol l^{-1} s^{-1})
253 ± 13	534 ± 56	1460 ± 280	5.8 ± 1.5

Table 2.1: A summary of the model parameters determined from steady-state $^3O_2$ microelectrode measurements. The values in the table represent the mean and the standard deviation from experiments conducted on 29 individual spheroids. Each spheroid radius, R_s, was measured with a microscope reticle, and the remaining parameters were determined from fitting Equation (2.6) to the measured steady-state spatial $^3O_2$ distribution.

Investigator	Material	D_s/D_d	Γ_{met} (μmol^{-1} s^{-1})
Mueller-Klieser (1984)	EMT6/Ro spheroid	0.40 ± 0.03	13.8 ± 1.4
Grote *et al.* (1977)	DS-carcinosarcoma tissue	0.53	—
This study	EMT6/Ro spheroid	0.63 ± 0.02	5.77 ± 0.28

Table 2.2: A comparison of steady-state $^3O_2$ diffusion parameters with selected literature values. The values reported are the means and standard error in the means.

μM s^{-1} mW^{-1} cm^2 fits the data very well, indicating that Γ_0 is proportional to the incident fluence rate as expected. This slope yields β_{PDT} of Equation (2.14). As Equation (2.13) indicates, k_p/k_{ot} is also a free parameter of the model. In these experiments it appears that k_p/k_{ot} is significant as a fitting parameter only at the highest two fluence rates. This is consistent with the relatively low value of 2.2 ± 1.7 μM obtained from these measurements.

Since the value of β_{PDT} depends on the concentration of photosensitizer present in the spheroid, we have conducted uptake studies using [^{14}C]polyhaematoporphyrin (Leeds Radioporphyrins, Leeds, UK) to determine the photosensitizer concentration present in the spheroid following incubation. Using a scintillation counting assay (Gibson *et al.*, 1994), we found that a typical 500 μm diameter EMT6/Ro spheroid contains 6.7 ± 1.8 ng of polyhaematoporphyrin, corresponding to a concentration of 66 ± 21 μg ml^{-1}. This is similar to the amount of Photofrin® taken up by WiDR spheroids reported by West (1989).

2.7.2 A Comparison of the Fluence Rate-Dependent Efficacy of PDT in Multicell Tumor Spheroids with Model Calculations

In this section, the $^3O_2$ diffusion-with-consumption model is used to determine the distributions of $^3O_2$ and $^3O_2$ consumption resulting from PDT carried out according to the therapeutic protocols used in our previously published study of the fluence rate-dependent response of EMT6/Ro spheroids. The second column

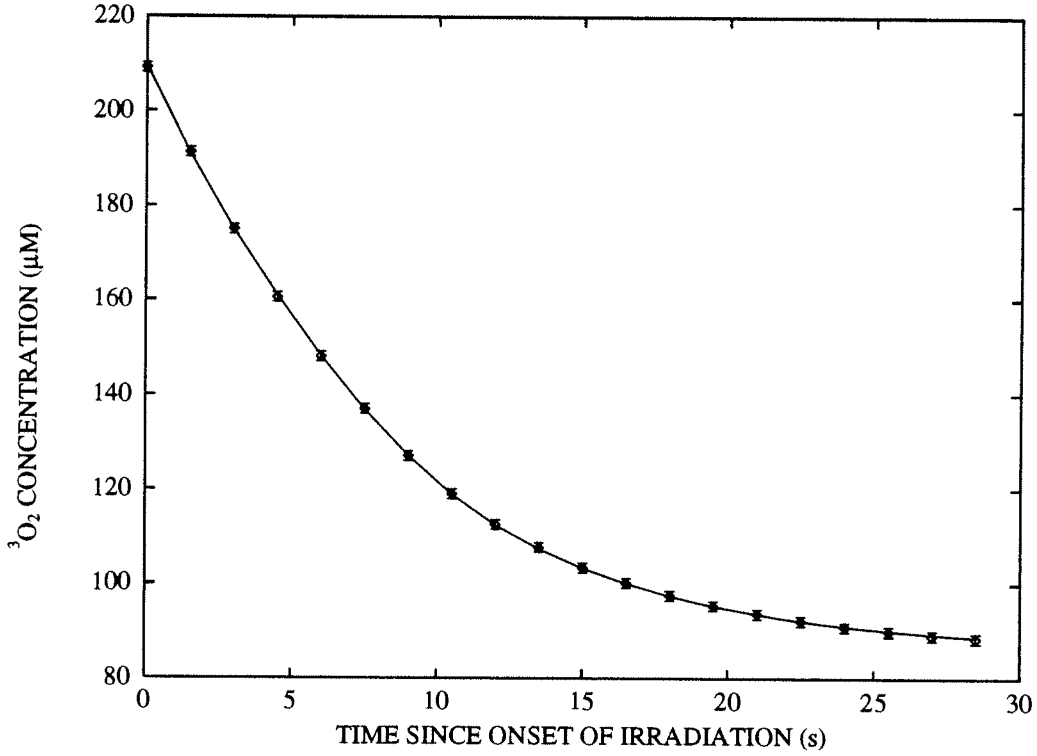

Figure 2.6: The initial $^3O_2$ depletion measured with a microelectrode at the edge of a single photosensitized EMT6/Ro spheroid during laser irradiation (514 nm, 25 mW cm^{-2}). The solid line is the best fit using Equation (2.15). The error bars represent the approximate fluctuation in the electrode current just prior to the onset of irradiation.

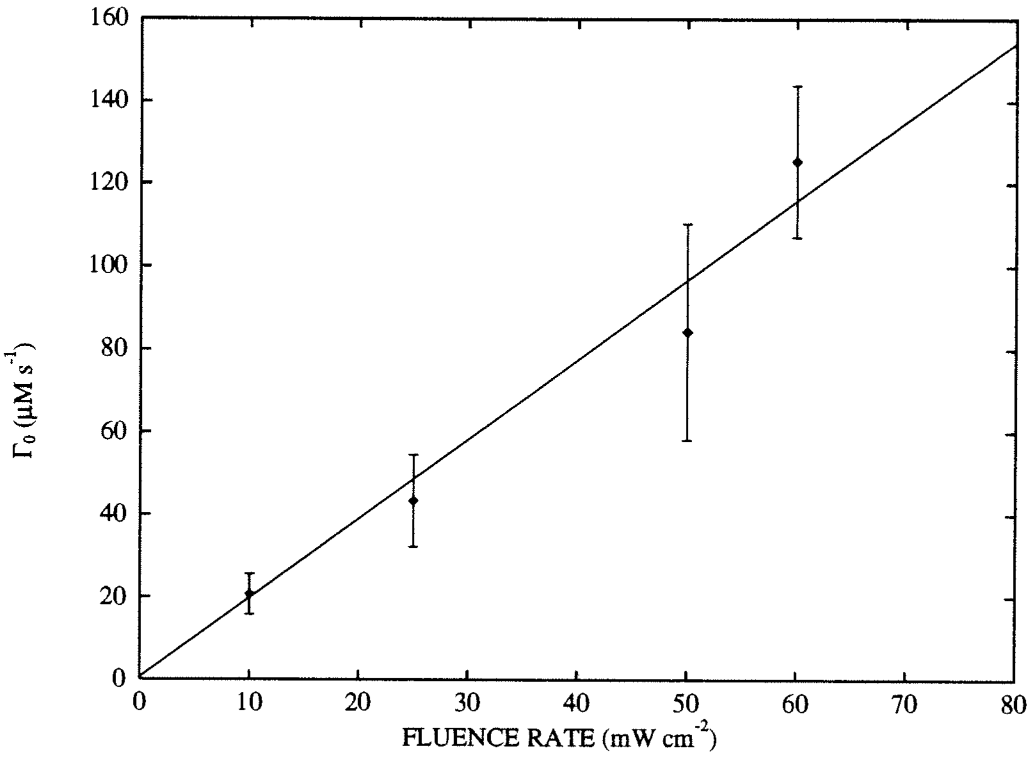

Figure 2.7: The maximal rate of photochemical $^3O_2$ consumption, Γ_0, measured at four 514 nm irradiation fluence rates. The points are the means ± standard deviation determined from six to nine experiments using individual spheroids. The slope of the solid line, 1.92 μM s^{-1} mW^{-1} cm^2, is β_{PDT}(514 nm) of Equation (2.14).

of Table 2.3 lists the fractions of spheroid cells surviving therapy from fourteen separate experiments conducted using identical Photofrin® incubation conditions (10 μg ml^{-1}, 24 h) and total irradiation fluences (60 J cm^{-2}, 630 nm). The incident fluence rate, provided in column one, was varied over the range 25 - 200 mW cm^{-2}. Spheroid diameters were recorded for each experimental group, and these are listed in column three. As previously reported, the mean spheroid cell surviving fractions were 0.07, 0.13 and 0.54 in response to PDT treatments performed at 25, 50 and 200 mW cm^{-2}, respectively.

Given the excellent agreement between the model and the microelectrode measurements, the distribution of $^3O_2$ consumption, $\Gamma(r,t)$, resulting from irradiation at these specific fluence rates can be calculated using the relationship between Γ_0 and the incident fluence rate, shown in Figure 2.7, and the mean values of the parameters gathered in Table 2.1. Although the experiments described herein used 514 nm irradiation to determine β_{PDT} appropriate for that wavelength, it is possible to adjust this value for treatments conducted at 630 nm. Two factors must be considered. First, the Photofrin® extinction coefficient is approximately three–fold higher at 514 nm than it is at 630 nm. Second, while β_{PDT} is expressed in terms of an energy fluence rate, photochemical $^3O_2$ depletion is driven by the photon fluence rate. Therefore, it is also necessary to correct for the fact that at equal energy fluence rates, the photon fluence rate is lower at 514 nm. These two factors combine to yield a correction factor of 2.44 for the ratio of $\beta_{PDT}(514\text{ nm})/\beta_{PDT}(630\text{ nm})$. Hence, we assume a value of 0.79 μM s^{-1} mW^{-1} cm^2 for $\beta_{PDT}(630\text{ nm})$, based on the measured value of 1.92 μM s^{-1} mW^{-1} cm^2 for $\beta_{PDT}(514\text{ nm})$.

Irradiation fluence rate (mW cm^{-2})	Surviving fraction	Average spheroid diameter (μm)	Estimated critical radius (μm)	Calculated radius of anoxia (μm)	Reacting [$^1O_2$] at the critical radius (mmol l^{-1})
25	0.083	497 ± 47	108.3	71.1	3.450
	0.061	558 ± 42	109.5	117.2	0.303
	0.065	626 ± 70	125.8	167.3	0.198
50	0.136	535 ± 62	137.6	164.3	0.239
	0.146	494 ± 82	130.1	141.3	0.320
	0.096	539 ± 49	123.4	174.3	0.208
100	0.349	535 ± 62	188.3	202.4	0.462
	0.264	494 ± 82	158.5	181.3	0.254
200	0.584	497 ± 47	207.7	207.4	0.618
	0.502	558 ± 42	221.7	237.4	0.253
	0.541	626 ± 70	255.0	262.5	0.238
	0.607	535 ± 62	226.5	225.4	0.600
	0.615	494 ± 82	210.1	214.4	0.293
	0.400	539 ± 49	198.6	236.4	0.215

Table 2.3: A summary of spheroid cell survival data described by Foster *et al.* (1993) with results of calculations based on the irradiation protocols used in the individual experiments. The fraction of spheroid cells surviving PDT is given for the individual experiments described in Foster *et al.* (1993). The spheroid radius is the mean for the experimental group which typically consisted of 50 spheroids. The remaining columns are described in detail in Section 2.7.2.

Figures 2.8, 2.9, and 2.10 present the results of calculations of the temporal and spatial distributions of $^3O_2$ in a 540 μm diameter spheroid for the first 90 s of 630 nm irradiation delivered at 25, 50 and 200 mW cm^{-2}, respectively. The corresponding calculations of $\Gamma_{PDT}(r,t)$, the total rate of $^3O_2$ consumption within the spheroid, are depicted as well. If the metabolic rate of consumption is subtracted from $\Gamma(r,t)$ then, in accordance with Equation (2.10), $\Gamma_{PDT}(r,t)$ is obtained. Given the correspondence between photochemical $^3O_2$ consumption and $^1O_2$ reaction, as discussed in Section 2.2, this is equivalent to the spatial and temporal distribution of $^1O_2$ reaction within the spheroid. Hence, these calculations report the reacting $^1O_2$ dose rate distribution for each irradiation protocol. To obtain the total reacting $^1O_2$ dose distribution, $\Gamma_{PDT}(r,t)$ is calculated and integrated over the time required to deliver 60 J cm^{-2} of irradiation. The resulting distribution for each irradiation protocol is given in Figure 2.11.

It is apparent that $^1O_2$ is formed, to varying degree, throughout the spheroid. In each treatment protocol all of the cells of the spheroid are exposed to more than 100 μM of reacting $^1O_2$, yet, as indicated in the first two columns of Table 2.3, the fraction of cells surviving therapy is dependent on the incident fluence rate. This seems to support the threshold dose hypothesis, which contends that a minimum, threshold, dose of $^1O_2$ is necessary to induce necrosis (van Gemert *et al.*, 1985; Patterson *et al.*, 1990). Since the model of $^3O_2$ diffusion with consumption provides a quantitative estimation of the reacting $^1O_2$ dose distribution, the threshold $^1O_2$ dose required for cell killing in this model tumor system can be determined by correlating photodynamic efficacy with the distribution of reacting $^1O_2$ molecules.

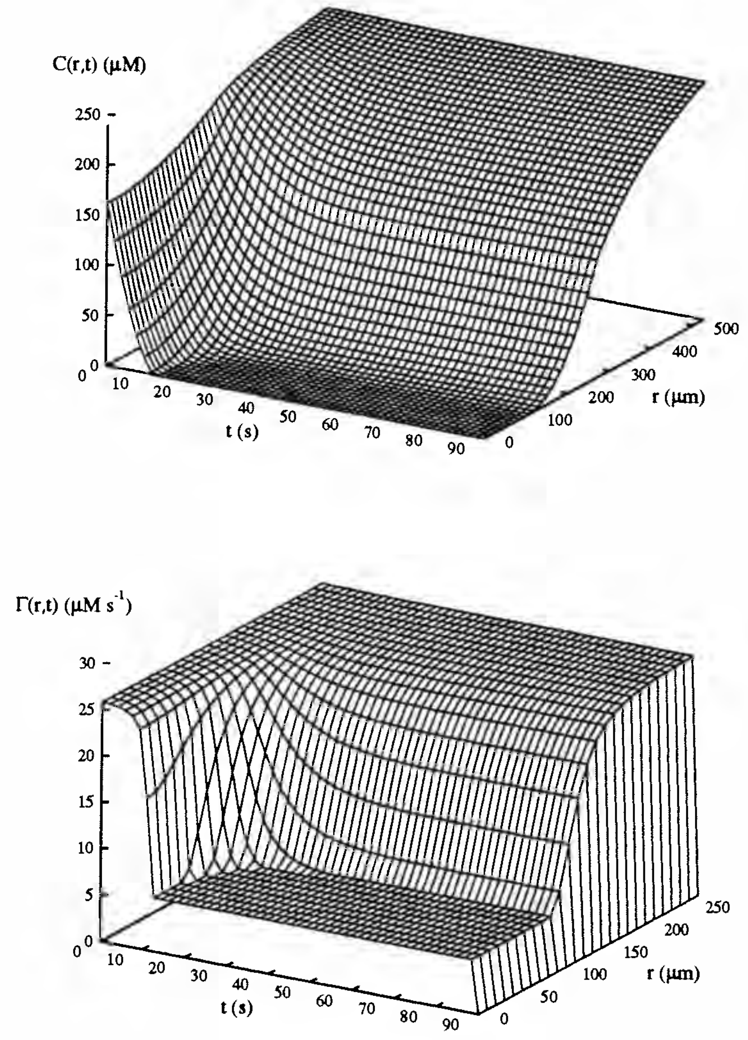

Figure 2.8: The spatial and temporal distribution of $^3O_2$ concentration, $C(r,t)$, and the total rate of $^3O_2$ consumption, $\Gamma(r,t)$, in a 540 μm diameter spheroid during PDT conducted at 25 mW cm^{-2} of 630 nm irradiation. The distributions were calculated by the iterative solution of the matrix equation, Equation (2.31), using parameters determined from microelectrode measurements.

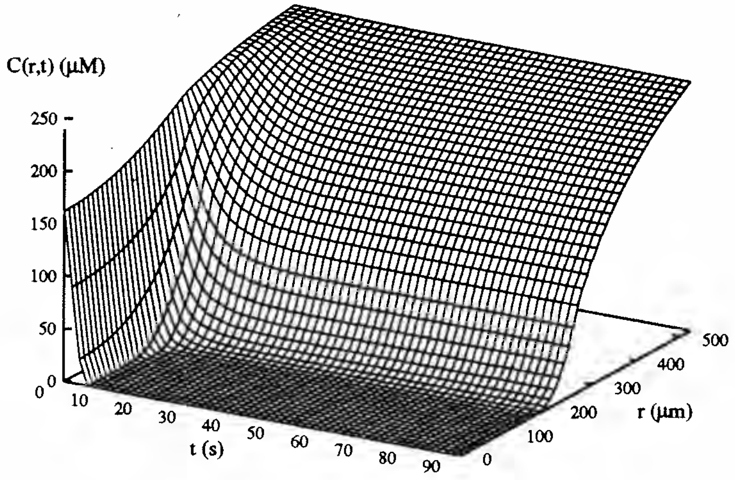

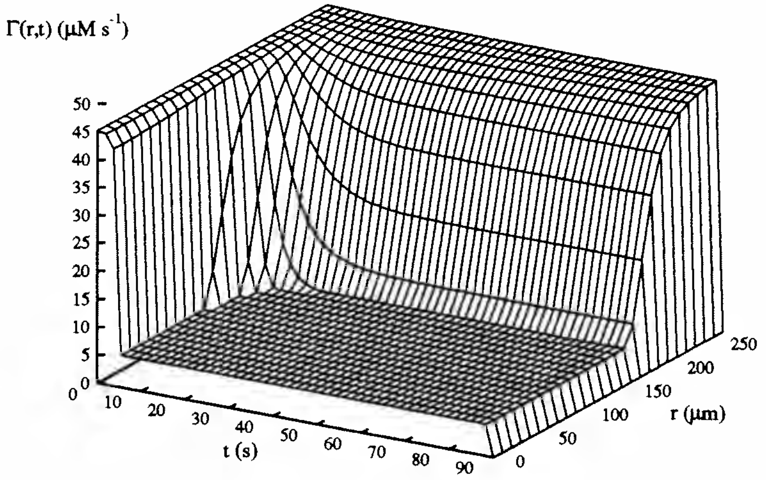

Figure 2.9: The spatial and temporal distribution of $^3O_2$ concentration, $C(r,t)$, and the total rate of $^3O_2$ consumption, $\Gamma(r,t)$, in a 540 μm diameter spheroid during PDT conducted at 50 mW cm^{-2} of 630 nm irradiation, as described in Figure 2.8.

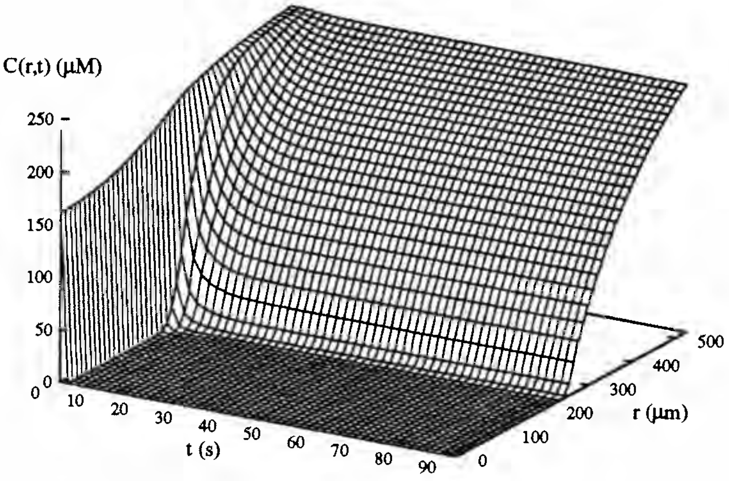

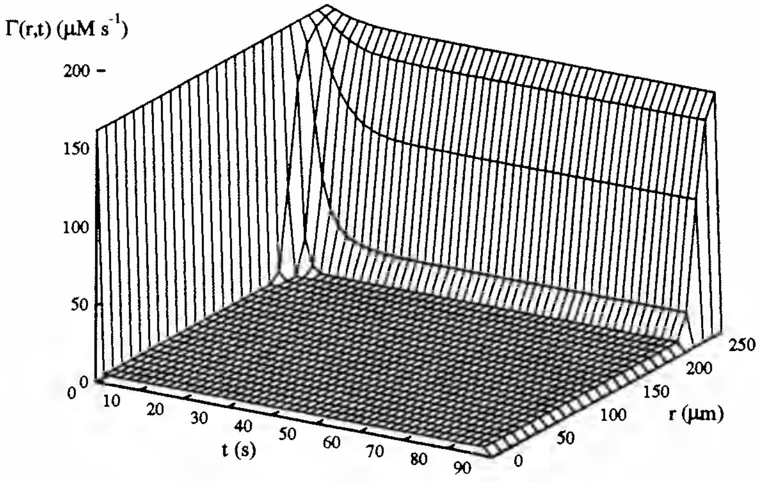

Figure 2.10: The spatial and temporal distribution of $^3O_2$ concentration, $C(r,t)$, and the total rate of $^3O_2$ consumption, $\Gamma(r,t)$, in a 540 μm diameter spheroid during PDT conducted at 200 mW cm^{-2} of 630 nm irradiation, as described in Figure 2.8.

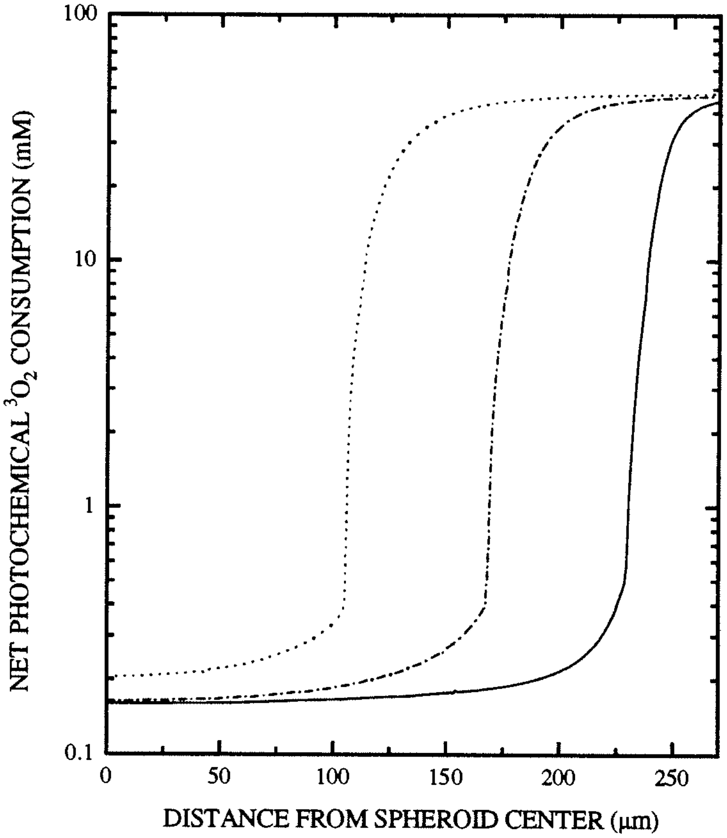

Figure 2.11: The net photochemical $^3O_2$ consumption as a function of the radial position in a spheroid following a fixed dose of 60 J cm^{-2} at 630 nm provided at 25 mW cm^{-2} (···), 50 mW cm^{-2} (- · -), and 200 mW cm^{-2} (—).

A threshold $^1O_2$ dose is assigned to each of the experiments in Table 2.3 by calculating the appropriate reacting $^1O_2$ dose distribution, such as those in Figure 2.11, and determining the dose that occurs at a critical radius. All of the cells that originate within this radius are assumed to survive therapy because an insufficient $^1O_2$ dose is delivered to this region, while the exposure exterior to this region is sufficient for cell killing. If the cell density is approximately constant throughout the spheroid, then the fraction of cells surviving therapy is equivalent to the fraction of the spheroid volume that lies within this critical radius. Therefore, the critical radius can be calculated by determining the radius of the sphere containing a fraction of the spheroid volume equivalent to the fraction of cells that are observed to survive therapy for the protocol being evaluated. Column 4 of Table 2.3 indicates the critical radius for each experiment, computed from the surviving fraction and the mean radius of the experimental group.

The reacting $^1O_2$ dose distributions were calculated in the same manner as in Figures 2.8-2.11, with the mean radius of the experimental group used as the spheroid radius. Each calculation was carried out over a time interval equivalent to the irradiation time necessary to administer 60 J cm^{-2} of fluence. Column 5 indicates the radius of the anoxic region induced by PDT as determined from the calculated $^3O_2$ distribution at the completion of therapy. Figure 2.12 depicts the close correspondence between the critical radius and the radius of the anoxic region. This is a clear indication of the connection between a lack of photodynamic efficacy and anoxia induced by PDT. The final column of Table 2.3 indicates the reacting $^1O_2$ dose at the critical radius. These values are plotted in Figure 2.13

as a function of the fluence rate. With the exception of one outlying point, all of the calculated values are clustered in the range of 200 – 600 μM, which is strongly supportive of a well defined threshold $^1O_2$ dose. From these calculations, we obtain an average reacting $^1O_2$ threshold dose of 323 ± 38 μM (mean ± SEM).

2.8 Discussion

2.8.1 Microelectrode Measurements

The quality of fits such as those shown in Figures 2.5 and 2.6 indicates that the theoretical treatment of $^3O_2$ diffusion with consumption adequately describes photochemical $^3O_2$ depletion in a multicell tumor spheroid during therapy. Since many parameters must be determined to fully characterize the distributions of $^3O_2$ and the rate of photodynamic $^3O_2$ consumption, two independent measurements were necessary to uniquely determine the relevant parameters: a steady-state measurement of the radial $^3O_2$ distribution in the absence of photodynamic irradiation and a time-dependent measurement of the $^3O_2$ transient that occurs at the onset of PDT. The steady-state measurement enables us to isolate Γ_{met}, D_s, and R_d, which are present in both the steady-state and the time-dependent $^3O_2$ diffusion-with-consumption equations. Therefore, by determining them with the steady-state measurement they become known quantities for the time-dependent measurements. This allows the parameters Γ_0 and k_p/k_{ot} to be uniquely determined from a measurement of the $^3O_2$ transient.

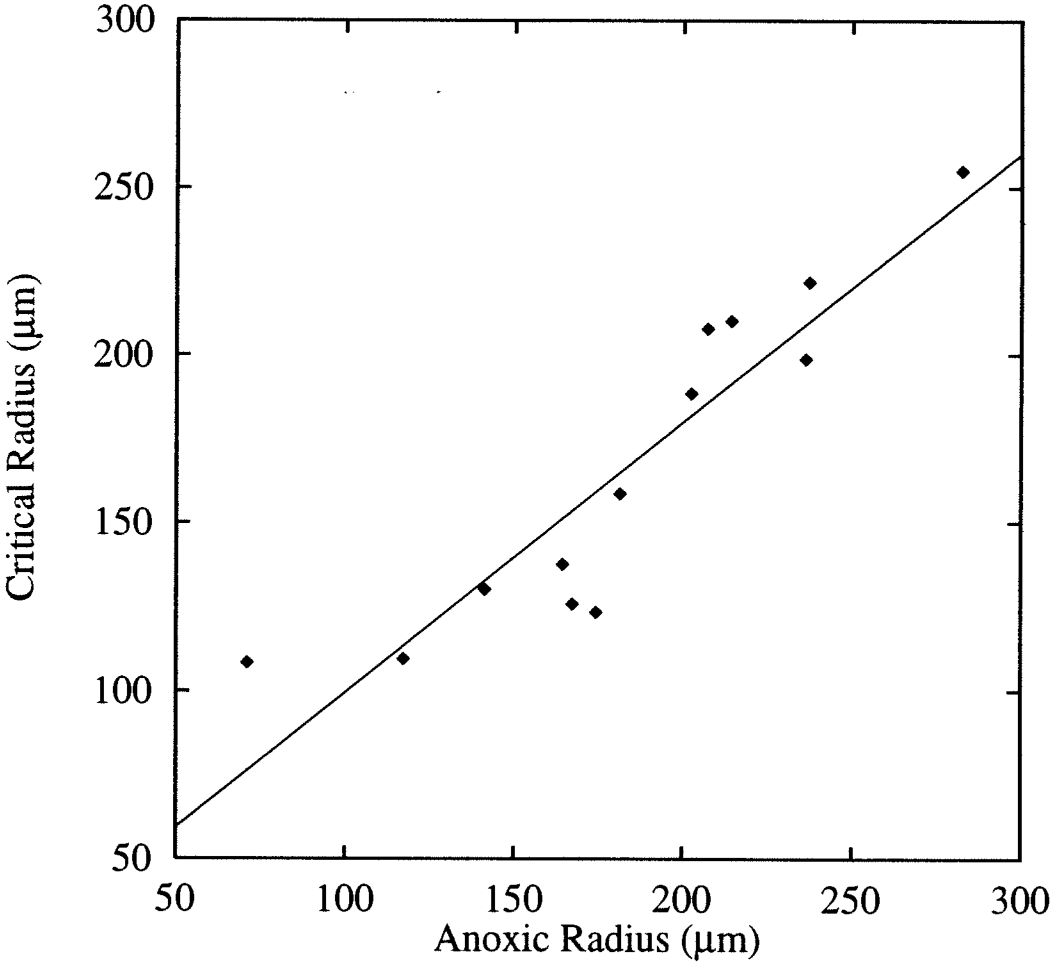

Figure 2.12: The correlation between the critical radii determined from spheroid cell surviving fractions and the anoxic radii calculated using $^3O_2$ consumption data obtained from microelectrode measurements. The data points were taken from columns four and five of Table 2.3. The solid line is the best two-parameter linear fit (correlation coefficient = 0.92).

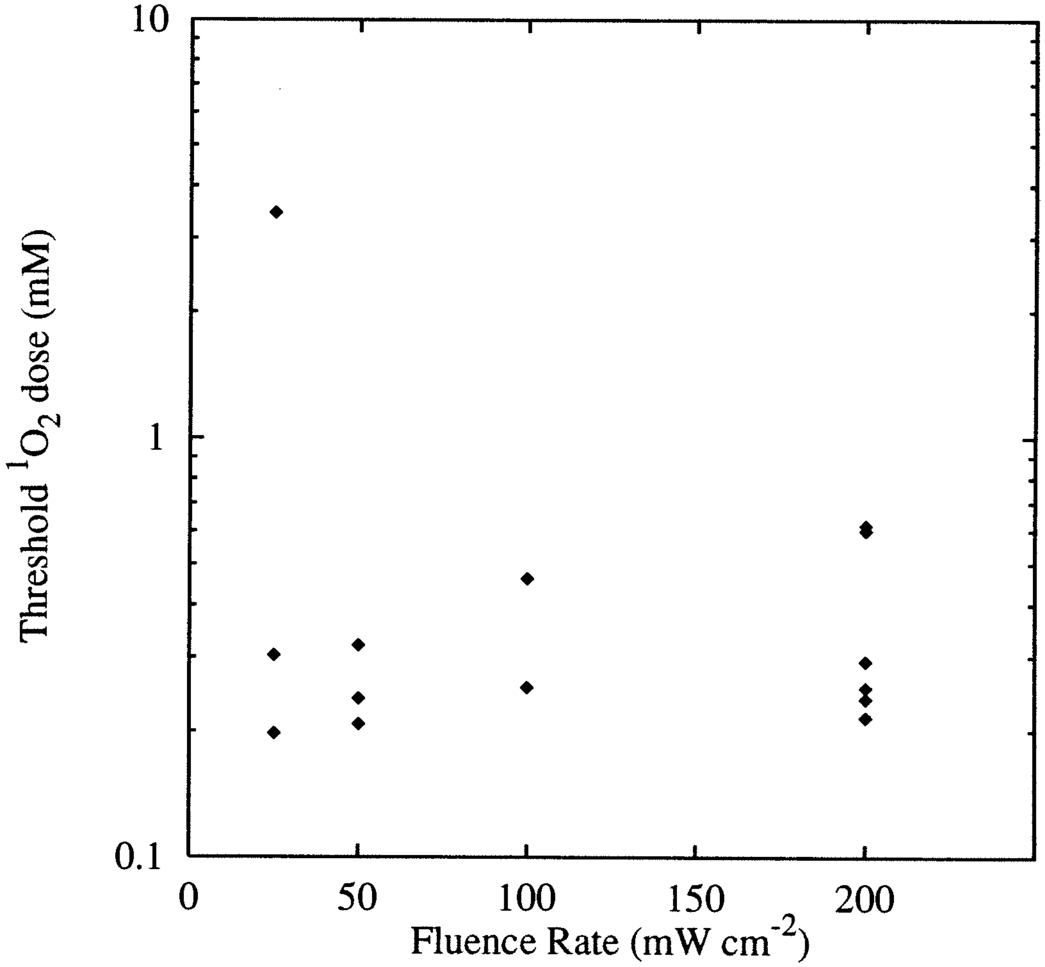

Figure 2.13: Estimates of the threshold dose of reacting $^1O_2$ determined in fourteen separate experiments conducted at four 630 nm fluence rates. Threshold values are the net $^3O_2$ consumed at the critical radius, which was determined from spheroid cell survival data (see Table 2.3). The predicted threshold dose is 323 ± 38 μM (mean ± SEM).

Mueller-Klieser's experiment most closely resembles the steady-state experiments that we describe, yet the ratios of the diffusion coefficients differ considerably. Similarly, our value of the metabolic $^3O_2$ consumption rate is smaller than that reported by Mueller-Klieser. These differences are probably a result of the two experimental environments that were used. While our experiments were conducted at room temperature in static culture media, Mueller-Klieser's were conducted in flowing culture media at 37 °C to mimic growth conditions. One would expect the rate of metabolism at 25 °C to be considerably slower than that at 37 °C. This may also partly explain the discrepancy in the diffusion coefficients. Since the diffusion coefficient depends upon the composition of the spheroid, the higher ratio that we observe may be an indication of a compositional or structural difference in the spheroid attributed to experimental conditions. For example, an increased water content at 25 °C compared to 37 °C would result in a larger diffusion coefficient for $^3O_2$ in the spheroid. For our purposes, it is sufficient that the diffusion parameters are truly representative of the spheroid in an environment that closely resembles that of experiments described previously (Foster *et al.*, 1993). The differences between this study and Mueller-Klieser notwithstanding, it is interesting to note that there is a better agreement between the diffusion coefficient reported here and that reported by Grote *et al.* (1977) for DS-carcinosarcoma tissue.

The fluence rate dependence of Γ_0 is linear over the range investigated with a slope, β_{PDT}(514 nm), of 1.92 ± 0.32 μM s^{-1} mW^{-1} cm^2. In general, β_{PDT} depends upon the photosensitizer extinction coefficient at the irradiation wavelength, the concentration of the photosensitizer in the spheroid, the $^1O_2$ quantum yield, and the probability of $^1O_2$ reaction with a cellular target. Using the correction factor described in Section 2.7.2, the corresponding value for β_{PDT} at 630 nm is 0.79 μM s^{-1} mW^{-1} cm^2. From the fluence-rate dependence of cell survival data obtained from PDT-treated EMT6/Ro spheroids, we had previously estimated β_{PDT} (630 nm) to be 0.14 ± 0.02 μM s^{-1} mW^{-1} cm^2 by using a simplified form of the steady-state diffusion-with-consumption model. The sixfold discrepancy between this earlier value and that determined from the present study is likely a result of the approximations used in the simplified model, since at that time, we had not measured the appropriate diffusion parameters for the spheroid system. The value of 0.79 μM s^{-1} mW^{-1} cm^2 is derived directly from microelectrode measurements and is therefore the more reliable estimate.

Another important parameter that we have been able to estimate is the concentration given by the ratio k_p/k_{ot}. This concentration is a measure of the therapy's sensitivity to the local $^3O_2$ concentration. Previously, we have assumed for simplicity that this value is approximately zero, allowing for $^1O_2$ to be produced at the maximal rate in regions containing arbitrarily small amounts of $^3O_2$. Here, k_p/k_{ot} appears as a fitting parameter in the theoretical function that is fit to the observed $^3O_2$ transient. Since k_p/k_{ot} appears relative to the local $^3O_2$ concentration in the expression for Γ_{PDT}(r,t) (Equation (2.13)), this parameter becomes significant only when a substantial volume of the spheroid is reduced to an $^3O_2$ concentration comparable to the actual value of k_p/k_{ot}. This is understandable considering that this ratio is ultimately responsible for regulating the rate at which $^3O_2$ is consumed by PDT. If $^3O_2$ is abundant, as would be expected for low rates of photon absorption, then $\Gamma_{PDT}(r,t)$ would not be constrained and k_p/k_{ot} would not influence the $^3O_2$ transient.

The results of these measurements indicate that k_p/k_{ot} is significant as a fitting parameter only for the highest fluence rates used in this study. It is from these measurements that our estimate of 2.2 ± 1.7 μM is determined. To improve upon this estimate, additional experiments were conducted at fluence rates in the range of 40 - 80 mW cm^{-2}. At higher fluence rates a more significant fraction of the spheroid is reduced to an oxygen concentration less than that of k_p/k_{ot} and the significance of this parameter is increased. The difference in the estimate of k_p/k_{ot} was insignificant, but with the additional data an improved estimate would be 2.8 ± 1.5 μM.

This value can be compared to an estimate of 13 μM made by Moan and Sommer (1985) who calculated the quantum yield of $^1O_2$ formation based on the $^3O_2$ dependence of the photo-inactivation of NHIK 3025 cells sensitized with hematoporphyrin derivative (HpD). While Moan and Sommer's value is larger than the value that we report, this may be due to real differences between HpD and Photofrin®. It would be interesting to use $^3O_2$ transient measurements to determine k_p/k_{ot} for the various photosensitizers currently under investigation for PDT. This ratio is likely to have a considerable impact on photodynamic efficacy, at least as far as direct cell effects are concerned.

Since the ratio k_p/k_{ot} regulates the $^1O_2$ reaction rate, in a biological system where $^3O_2$ supply is limited by diffusion, all other things being equal, a photosensitizer characterized by a low ratio is likely to induce larger anoxic regions in the tumor volume and, consequently, may be a less effective direct cell sensitizer than a photosensitizer characterized by a higher ratio. This can be seen by comparing the distribution of $^3O_2$ consumed by PDT using the value of 2.8 μM found from this study and Moan and Sommer's value of 13 μM. This comparison is shown in Figure 2.14. From the standpoint of maximizing direct cell killing, the overall reduced but sustainable rate of $^1O_2$ reaction characterized by a higher ratio is preferable to the formation of large anoxic regions in which the rate of $^1O_2$ reaction is precisely zero. Furthermore, while a primary concern in the design of photosensitive compounds is a high singlet oxygen yield, achieving a balance between photochemical oxygen consumption and the supply of oxygen to the tissue appears to be a more important concern for dosimetry.

2.8.2 A Determination of the Threshold Reacting Dose of Singlet Oxygen

Calculations of the $^3O_2$ distribution during PDT, based on diffusion and consumption parameters determined from microelectrode measurements, clearly establish that photochemical $^3O_2$ depletion can be significant in a Photofrin®-sensitized multicell tumor spheroid even at a modest fluence rate of 25 mW cm^{-2} of 630 nm light. As shown in Figures 2.8-2.10 a region of anoxia is established within seconds of initiating PDT in all three of the therapeutic protocols investigated, and the extent of this region is dependent on the incident fluence rate. Because $^3O_2$ consumption is dependent on the local $^3O_2$ concentration, photochemical $^3O_2$

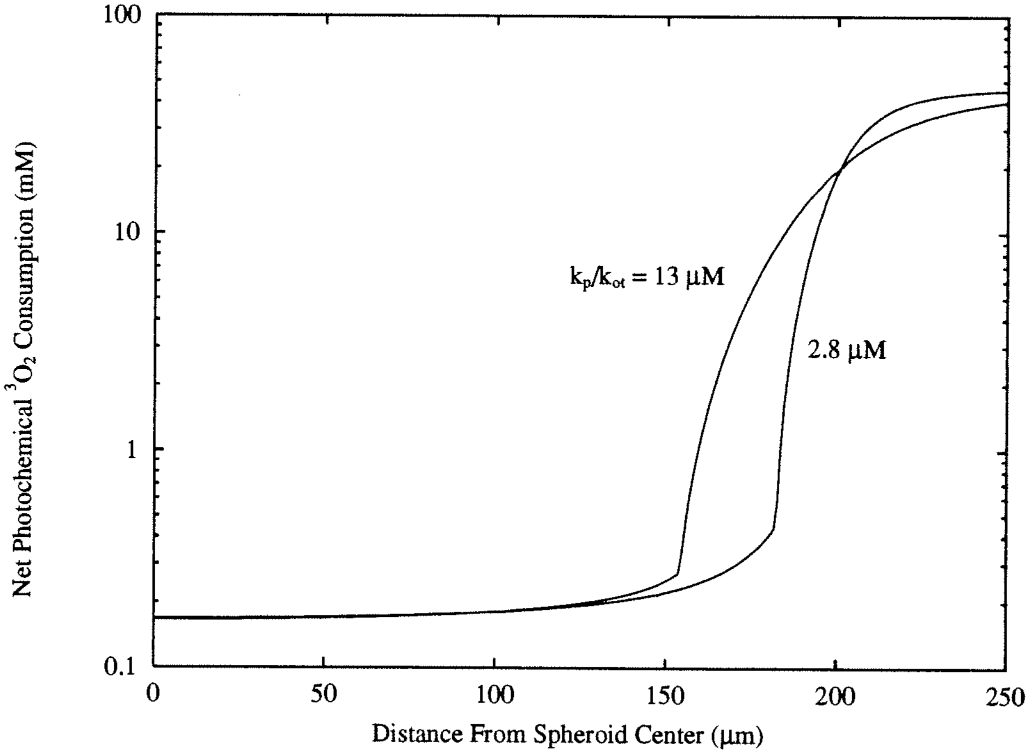

Figure 2.14: A comparison of the calculated radial distributions of photochemical oxygen consumption in a sensitized, 500 μm diameter spheroid which would result from a photodynamic dose of 60 J cm^{-2} (630 nm) at 100 mW cm^{-2} for two values of the oxygen sensitivity parameter k_p/k_{ot}.

consumption ceases within the anoxic region shortly after the onset of PDT. This is evident from the figures as $\Gamma(r,t)$ appears to decay from a maximal value of approximately $\Gamma_{met} + \Gamma_0$ to a minimum value of Γ_{met} in the center of the spheroid in each of the three protocols. Because photodynamic $^3O_2$ consumption ceases in the anoxic region, $^1O_2$ formation occurs in this region only during the first few seconds of the $^3O_2$ transient when the $^3O_2$ concentration is large compared to the ratio k_p/k_{ot}.

The situation is most severe for the 200 mW cm^{-2} protocol, where, as shown in Figure 2.11, the maximal dose of approximately 45 mM of $^1O_2$ is formed only in the outermost layer of cells. The majority of the cells in the spheroid receive less than 300 μM of reacting $^1O_2$ under this protocol. However, as the fluence rate is reduced to 50 mW cm^{-2}, $^1O_2$ formation extends further into the spheroid, delivering a substantial dose to a greater fraction of cells. This trend continues as the fluence rate is further reduced to 25 mW cm^{-2} due to the corresponding reduction in the extent of anoxia.

Since the $^3O_2$ -diffusion-with-consumption model offers a quantitative means of assessing photodynamic dose for specific irradiation protocols, we have reanalyzed previously published spheroid cell survival data in order to determine if the observed fluence rate dependent efficacy can be understood in terms of our $^3O_2$ depletion hypothesis. As indicated in Figure 2.12, there is good correlation between the fraction of cells surviving therapy and the fraction of the spheroid volume that becomes anoxic shortly after PDT is initiated. Furthermore, if it is assumed that the subpopulation of cells surviving PDT originates within the center of the spheroid, then, as indicated in Figure 2.13, the reacting $^1O_2$ concentration necessary for cell killing is narrowly distributed about a mean value of 323 μM. This is consistent with the threshold dose hypothesis described by Patterson *et al.* (1990). Taken together, these observations strongly support the hypothesis that PDT carried out at high fluence rates can undermine the efficiency of PDT by inducing anoxic volumes in which cells are protected from direct $^1O_2$ mediated damage.

Figures 2.8 - 2.11 can also be used to investigate alternative irradiation protocols that might improve photodynamic efficacy. For each fluence rate it appears that between 150 and 200 μM of reacting $^1O_2$ is administered during the $^3O_2$ transient before the new quasi steady-state $^3O_2$ distribution is established. This is essentially all of the available $^3O_2$ present at the time irradiation is begun. After the quasi steady-state $^3O_2$ distribution is established, $^1O_2$ formation only occurs in the oxygenated region of the spheroid, and no additional $^1O_2$ is formed in the anoxic region. For the 60 J cm^{-2} fluence protocols depicted in Figure 2.11, the total amount of $^1O_2$ produced in the spheroid far exceeds the photodynamic threshold, but, due to the nonuniform spatial distribution of $^1O_2$ formation, a region of the spheroid is undertreated in each case. Thus, this analysis predicts that, once the threshold dose has been achieved at a particular fluence rate, no improvement in cell killing will occur if the total fluence is increased. We have in fact demonstrated this experimentally in spheroids (Foster *et al.*, 1993). It is clear that in order to significantly influence therapeutic response, strategies must be devised that deposit a threshold dose of $^1O_2$ throughout the entire spheroid.

There are approaches other than fluence rate reduction that could be employed to accomplish this. Perhaps, the most direct involves increasing the ambient $^3O_2$ concentration in such a way as to insure that the minimum amount of $^3O_2$ present in the spheroid at the onset of irradiation is greater than the required threshold dose of $^1O_2$. In this way, even if the ambient $^3O_2$ concentration is not sufficient to prevent the photochemical induction of anoxia, a threshold dose will be delivered during the $^3O_2$ transient. While this method requires the ability to regulate the ambient $^3O_2$ supply, the same result can be achieved by punctuating continuous irradiation with dark intervals. Once the quasi steady-state $^3O_2$ distribution is established, irradiation could be interrupted for a period of time to allow $^3O_2$ to replenish the anoxic regions. Irradiation could then be resumed, until, once again, anoxic regions begin to form. While we have not pursued these experiments in the spheroid, it has been demonstrated that a 30s light / 30 s dark, fractionated irradiation protocol greatly improved photodynamic efficacy in the R3230AC mammary adenocarcinoma in the Fischer rat (Foster *et al.*, 1991).

There are very few values of the threshold $^1O_2$ dose in the literature. Patterson *et al.* (1990) have investigated the depth of necrosis in normal rat liver as a function of the absorbed photon dose resulting from PDT using aluminum chlorosulphonated phthalocyanine (AlSPC). They found that a threshold absorbed photon dose of $3.8 \pm 0.2 \times 10^{19}$ photons cm^{-3} was necessary to induce necrosis when the photosensitizer concentration was below 20 mg g^{-1}. Using the $^1O_2$ yield for this photosensitizer in aqueous solution, these authors estimated a threshold dose of 22 mM. Following the approach of Patterson *et al.*, Farrell *et al.* (1991)

conducted a study using Photofrin® in the normal rat liver. They found a ten-fold smaller absorbed threshold dose of $3.4 \pm 0.4 \times 10^{18}$ photons cm^{-3} when the injected photosensitizer concentration was below 15 mg kg^{-1}. Using the Dougherty *et al.* (1976) estimate of 0.16 for the $^1O_2$ yield for hematoporphyrin derivative, the unpurified precursor to Photofrin®, in mouse mammary carcinoma cells, Farrell *et al.*'s threshold $^1O_2$ dose is approximately 0.9 mmol l^{-1}. This is within a factor of three of the results presented in this chapter. The treatments of photodynamic dosimetry by Patterson *et al.* and Farrell *et al.* are complementary to the treatment presented here in many respects. In these reports, it was assumed that the $^3O_2$ concentration was uniform and static during PDT, and the threshold absorbed photon dose was determined from a consideration of the penetration of light in tissue. By measuring the appropriate optical properties, they were able to calculate the fluence distribution as a function of depth in the liver along the axis of the irradiation beam. This distribution was used to determine the fluence that was delivered at the depth of necrosis, the demarcation between viable and non-viable cells as determined from histology. In our study, given the small size of the spheroid, light penetration was considered to be uniform, and the threshold $^1O_2$ dose was calculated by correlating the spatial distribution of $^1O_2$ reaction with biological response. While the two approaches differ, both support the concept of a single, well defined value for the threshold $^1O_2$ dose necessary for direct cell killing. The significant difference in the thresholds predicted by Patterson *et al.* and Farrell *et al.* indicates the likelihood that the threshold dose is sensitizer dependent.

While our estimate of the threshold dose appears low relative to Farrell *et al.*'s, it is important to realize that our estimate is of the reacting dose, while Farrell *et al.*'s is of the total dose delivered. Microelectrode measurements of $^3O_2$ consumption are insensitive to $^1O_2$ molecules that are produced but eventually return to $^3O_2$. Hence, the threshold reported by Farrell *et al.* will necessarily be greater than the reacting threshold that we report. With a knowledge of the probability that a $^1O_2$ molecule will react once created, the two values could be directly compared, but this quantity is difficult to assess. Still, it is unlikely that this probability is low enough to bring the two estimates into agreement. There are a number of possible explanations for this discrepancy. In the spirit of this analysis, it is possible that Farrell *et al.*'s estimate may be high because it assumes that $^3O_2$ is not limiting $^1O_2$ production. If $^3O_2$ was being depleted appreciably at the depth of necrosis, then $^1O_2$ production would be greatly reduced. In Farrell *et al.*'s treatment, this would manifest itself in diminished $^1O_2$ yield with respect to the aqueous value. A more likely possibility is that by neglecting the possibility of sensitizer photobleaching during the experiment, we have underestimated the threshold dose of reacting singlet oxygen. This will be addressed at length in Chapter 3, where the photochemical rate of oxygen consumption, Γ_{PDT}, is rederived to properly account for $^1O_2$ -mediated photobleaching.

2.9 Conclusions

In this chapter, a model of $^3O_2$ diffusion with consumption appropriate for a multicell spheroid undergoing PDT has been presented. $^3O_2$ microelectrode measurements have established the validity of the model and provided values for the parameters that constitute it. This model has enabled us to calculate the distribution of reacting $^1O_2$ molecules within a spheroid resulting from PDT conducted according to specific irradiation protocols. By computing the $^1O_2$ distribution for a series of experiments conducted with identical drug and light doses but with different incident fluence rates, we found that the magnitude of the spheroid cell surviving fraction was correlated to the extent of anoxia induced by the therapy. The spheroid cell survival data are consistent with the threshold dose model if the threshold is interpreted as the dose of reacting $^1O_2$ molecules necessary to induce necrosis. In this system, the threshold of reacting $^1O_2$ is 323 $\pm$ 38 μM.

Although this model establishes a means of quantifying $^1O_2$ dose in a multicell tumor spheroid *in vitro*, many of the features of the model apply equally to PDT *in vivo*. The diffusion distances established in a multicell tumor spheroid are characteristic of intercapillary distances in tumors. Furthermore, the diffusion coefficient that we have measured for EMT6/Ro spheroids compares favorably to that measured by Grote *et al.* (1977) for tumor tissue. Experimentally, we have directly established a quantitative relationship between the rate of photochemical $^3O_2$ consumption and the irradiation fluence rate. For Photofrin® and 630 nm irradiation, the value of β_{PDT} in the spheroid system is approximately

0.79 μM s^{-1} mW^{-1} cm^2. In the experimental rodent tumor model that we have reported on previously, Photofrin® concentrations are approximately ten-fold lower than in the EMT6 spheroids (4-10 μg ml^{-1} in R3230AC mammary tumors vs. 66 μg ml^{-1} in spheroids). Correcting for this difference, the rate of photochemical $^3O_2$ depletion *in vivo* would be approximately 4 μM s^{-1} at a fluence rate of 50 mW cm^{-2}. This value is within a factor of two of the calculated estimate of Foster *et al.* (1991).

It should be emphasized that the model presented here does not address the important consequences of photosensitizer bleaching. A number of studies have examined the effect that bleaching during therapy has on optical dosimetry in PDT, especially the possibility of increased penetration depth that is afforded by the decreased sensitizer absorption. In terms of singlet oxygen production, photosensitizer destruction could possibly improve photodynamic efficacy when photochemical oxygen depletion has limited the distribution of $^1O_2$ reaction. The microelectrode data presented here did not exhibit any of the features that would be present when photobleaching was significant, but this is due to the limited irradiation times ($<$ 1 minute, $<$ 1.2 J) that were used. It is likely that photobleaching was significant, however, in the survival data presented by Foster *et al.* (1993), which had total optical doses of 60 J, and evidence for this will be presented in Chapter 3. Since the simulations that were used to estimate the threshold dose of $^1O_2$ reaction in these experiments did not properly account for photobleaching, it is likely to be significantly low.

Chapter 3

Evidence for a Singlet Oxygen-Mediated Photobleaching Mechanism in Photofrin-PDT

3.1 Introduction

In Chapter 2, an oxygen-based *in vitro* photodynamic dosimetry model for the multicell tumor spheroid was presented. The predictions of this model support the concept of a threshold dose and provide a numerical estimate of the concentration of reacting $^1O_2$ necessary to kill cells in this tumor model. Although it correctly implements the oxygen dependence of PDT, the numerical predictions will only be valid if photobleaching of the photosensitizer is not appreciable during PDT. The degree to which a sensitizer degrades during therapy depends upon a variety of factors, and there has been a great deal of research that has investigated the photobleaching kinetics of a number of potential photosensitizers for PDT (Potter *et al.*, 1987; Mang *et al.*, 1987; Spikes, 1992; Svaasand *et al.*, 1996). Reasons for this interest include the possible use of photobleaching to reduce phototoxic damage to surrounding normal tissue during treatment and skin photosensitivity after treatment (Boyle and Potter, 1987; Kennedy and Pottier, 1992). It can also be desirable to have the photosensitizer bleach during therapy to increase the depth of optical penetration when the absorption of the photosensitizer is appreciable. For these reasons, it is important that a quantitative dose model properly reflect the photobleaching kinetics of the photosensitizer.

In this chapter, photobleaching is incorporated into the oxygen-diffusion-with-consumption model. In terms of an oxygen-based model, photobleaching would reduce the rate of photon absorption and, consequently, $^1O_2$ reaction. Therefore, the photodynamic rate of oxygen consumption, Γ_{PDT} (Equation (2.13)), must be modified to reflect a decreased absorption. Two mechanisms of photobleaching are considered. Since PDT inactivates cells through the creation and subsequent reaction of $^1O_2$, it is natural to consider the possibility that the photosensitizer itself is inactivated by interactions with $^1O_2$. This self-sensitization mechanism is contrasted with an oxygen-independent mechanism characterized by a constant bleaching coefficient. Finally, the predictions of the photobleaching models are tested experimentally by observing $^3O_2$ consumption in the vicinity of a Photofrin®-sensitized spheroid during prolonged irradiations. The results indicate that photobleaching can be monitored with oxygen electrodes, and evidence is presented that implicates a $^1O_2$ -mediated bleaching mechanism.

3.2 The Effect of Singlet Oxygen-Mediated Photobleaching on the Rate of Photochemical Oxygen Consumption

In the derivation of Γ_{PDT} presented in Chapter 2, it was assumed that the sensitizer ground-state excitation rate, I_a, would be constant and uniform throughout the spheroid in the absence of photobleaching. The uniformity was justified because the spheroid is small compared to transport scattering and absorption length scales typical of biological tissues (approximately 1 mm and 100 mm, respectively), and broad irradiation beams (approximately 1 cm^2) are used for treatment. When photosensitizer molecules become inactivated through the chemical modification of the chromophore, I_a will decay with time and, depending on the mechanism, may become non-uniformly distributed throughout the spheroid volume. Since $^1O_2$ is known to be highly reactive, it is possible that the $^1O_2$ distribution in the spheroid during treatment may determine the bleaching pattern of certain photosensitizers. If this is the case, photobleaching will initially be restricted to the outer few cell layers in the spheroid where the $^3O_2$ consumption rate was shown to be high (Figures 2.8 - 2.10). As the sensitizer is degraded, however, the rate of $^3O_2$ consumption will decrease, resulting in an increased oxygenation of the spheroid interior. This would allow for an increased photobleaching rate in this region, and, therefore, photobleaching would be observed to proceed radially inward. In contrast, an oxygen-independent bleaching mechanism would bleach uniformly throughout the spheroid.

To incorporate self-sensitization into Equation (2.13), we begin with the assumption that $^1O_2$ reacts only with the ground-state of the photosensitizer. This seems likely since the population of ground-state sensitizer molecules is much greater than the excited singlet- and triplet-state populations under continuous-wave irradiation. Furthermore, as illustrated in Figure 2.1, the energy transfer from the sensitizer triplet state to $^3O_2$ leaves the photosensitizer molecule in the ground-state in close proximity to a $^1O_2$ molecule. Hence, the probability of $^1O_2$ encountering a photosensitizer in its ground-state is much more likely than for an excited-state photosensitizer molecule. This does not address the more fundamental issue of whether $^1O_2$ can, in fact, react with the ground-state of the photosensitizer, but it is a reasonable starting point.

With this assumption, a bleaching path is added for the sensitizer ground-state of the Jablonski diagram (Figure 2.1) and the resulting kinetic equation for the ground-state sensitizer concentration, $[S_0]$, is written,

$$\frac{d[S_0]}{dt} = -I_a + k_m[S_1] + k_p[T] + k_{ot}[T][^3O_2\ ] - k_{os}[S_0][^1O_2\ ] \qquad (3.1)$$

where k_{os} is the bimolecular rate constant for $^1O_2$ reaction with ground-state photosensitizer, and the remaining terms have been defined in Chapter 2. Experiments reported by Potter *et al.* (1987) have indicated that hematoporphyrin derivative (HpD) degradation is very slow relative to the rates of the primary photochemistry. They have estimated the e-folding light dose to be approximately 29 J cm^{-2}, which corresponds to a time of 145 s if the dose is delivered at 200 mW cm^{-2}. In contrast, typical monomolecular decay of the sensitizer singlets may occur in approximately 10 ns, while triplet lifetimes in aqueous media may be as long as 1 ms. Therefore, it is reasonable to assume that the various excited-state species, including singlet oxygen, are in equilibrium with the ground-state photosensitizer population. The population would therefore decay according to

$$\frac{d[S_0]}{dt} = -k_{os}[S_0][{}^1O_2\ ], \tag{3.2}$$

which is readily solved to yield

$$[S_0](t) = [S_0](0)\exp\left(-k_{os}\int_0^t [{}^1O_2\ ](t')dt'\right). \tag{3.3}$$

With these assumptions, the same expression would be obtained if ${}^1O_2$ reacted with *any* of the photosensitizer excited-states, since Equation (3.3) simply states that the overall sensitizer population will decay according to the net ${}^1O_2$ reaction with the sensitizer during the treatment. Because ${}^1O_2$ will quickly equilibrate with $[S_0](t)$, the $[{}^1O_2\ ]$ term in the integrand of Equation (3.3) may be replaced by the steady-state solution to the appropriate rate equation evaluated at a given time, t. This solution is written,

$$[{}^1O_2\ ](t) = S_\Delta \phi_t I_a(t)\left(\frac{k_{ot}[{}^3O_2\ ](t)}{k_{ot}[{}^3O_2\ ](t)+k_p}\right)\left(\frac{1}{k_d + k_{oa}[A] + k_{os}[S_0](t)}\right). \tag{3.4}$$

In Equation (3.4), $k_{os}[S_0]$ will generally be much smaller than $k_{oa}[A]$ since the primary reaction pathway is assumed to be with abundant cellular targets. Therefore, this term may be neglected to obtain an analytic expression for ${}^1O_2$. We also assume that $[A]$ will be static. With these assumptions, the time dependence of Equation (3.4) occurs functionally through ${}^3O_2$ and I_a. Substituting this equation into Equation (3.3) yields

$$[S_0](t) = [S_0](0)\exp\left(-\frac{k_{os}}{k_{oa}[A]}\int_0^t S_\Delta \phi_t I_a(t')\left(\frac{k_{ot}[^3O_2](t')}{k_{ot}[^3O_2\ ](t') + k_p}\right)\left(\frac{k_{oa}[A]}{k_d + k_{oa}[A]}\right)dt'\right) \tag{3.5}$$

for the time dependent concentration of ground-state sensitizer molecules. Again, making use of the fast equilibrium of the primary photochemistry relative to the slow photobleaching process, the kinetic equations associated with Figure 2.1 can be solved to find Γ_{PDT}:

$$\Gamma_{PDT}(t) = S_\Delta k_{ot}[^3O_2\ ](t)[T](t) - k_d[^1O_2\ ](t) \tag{3.6}$$

where

$$[T_1](t) = \frac{k_{isc}[S_1](t)}{k_p + k_{ot}[^3O_2\ ](t)}, \tag{3.7}$$

$$[S_1](t) = \frac{I_a(t)}{k_{isc} + k_m}, \tag{3.8}$$

and, according to Equation (3.5),

$$I_a(t) = I_a(0)\exp\left(-\frac{k_{os}}{k_{oa}[A]}\int_0^t S_\Delta \phi_t I_a(t')\left(\frac{k_{ot}[^3O_2](t')}{k_{ot}[^3O_2\ ](t') + k_p}\right)\left(\frac{k_{oa}[A]}{k_d + k_{oa}[A]}\right)dt'\right). \tag{3.9}$$

Substituting Equations (3.7) - (3.9) into Equation (3.6), one obtains

$$\Gamma_{PDT}(t) = \Gamma_0\left(\frac{k_{ot}[^3O_2](t)}{k_{ot}[^3O_2](t) + k_p}\right)\exp\left(-\frac{k_{os}}{k_{oa}[A]}\int_0^t \Gamma_{PDT}(t')dt'\right) \tag{3.10}$$

where Γ_0 is $S_\Delta \phi_t I_a(0)\,(k_{oa}[A]/(k_d + k_{oa}[A]))$.

This is a straightforward extension of Equation (2.11) with an exponential decay resulting from photosensitizer bleaching given by Equation (3.9). It is a unique perspective on this subject, however, since we have incorporated photobleaching into the primary photochemical kinetics which govern PDT. The fluence rate and distribution of $^1O_2$ directly impacts the photosensitizer distribution. Previous empirical studies of bleaching have used an expression analogous to Equation (3.9) but invoked from a distinctly different mechanism (Potter *et al.*, 1987; Patterson and Wilson, 1994). Reports of sensitizer fluorescence or absorption decaying exponentially with delivered fluence has given rise to the analogous photobleaching expression,

$$I_a(t) = I_a(0)\exp\left(-\alpha\phi t\right) \tag{3.11}$$

where α is a constant bleaching coefficient and ϕt is the total fluence administered in time t. Simple exponential decay such as this implicitly assumes that α is unrelated to the sensitizer concentration, such that

$$\frac{d[S_0]}{dt} = -\alpha[S_0]. \tag{3.12}$$

Bleaching following this kinetic equation could result from direct inactivation as a result of photon absorption, or the reaction of an environmental bleaching agent with the sensitizer. It is fundamentally different than the $^1O_2$ bleaching mechanism described by Equation (3.2), because with $^1O_2$ -mediated photobleaching the bleaching agent is produced by the photosensitizer which is itself bleached. Hence, as the sensitizer degrades, the rate of production of the bleaching agent is also diminished. The corresponding expression for Γ_{PDT} is simply Equation (2.11) modified according to Equation (3.11),

$$\Gamma_{PDT}(t) = S_\Delta\phi_t I_a(0)\exp\left(-\alpha\phi t\right)\left(\frac{k_d}{k_d + k_{oa}[A]}\right)\left(\frac{k_{ot}[^3O_2](t)}{k_{ot}[^3O_2](t) + k_p}\right). \tag{3.13}$$

While photobleaching is typically monitored optically, the fact that Photofrin®-PDT relies on $^1O_2$ reaction with cellular targets allows for the possibility of monitoring photobleaching with $^3O_2$ microelectrodes. This is demonstrated in Figures 3.1 and 3.2. These figures depict the timecourse of the $^3O_2$ concentration at the edge of a Photofrin®-sensitized spheroid resulting from 100 mW cm^{-2} of 630 nm irradiation. Either a $^1O_2$ -mediated bleaching mechanism (Figure 3.2) or a mechanism characterized by a constant bleaching coefficient, α, (Figure 3.1) is assumed. Several possible values for $k_{os}/k_{oa}[A]$ or α are shown to illustrate the range of $^3O_2$ transients which could theoretically be observed. With the onset of irradiation, the $^3O_2$ concentration drops rapidly as photodynamic oxygen consumption depletes the $^3O_2$ in the spheroid and in the nearby culture medium. In the absence of bleaching, the $^3O_2$ concentration reaches a new steady-state value, dictated by the sum of the metabolic and photodynamic rates of oxygen consumption. This situation is depicted in the bottom-most curves of Figures 3.1 and 3.2. The effect of bleaching is to reduce sensitizer absorption and, consequently, the rate of photodynamic oxygen consumption, Γ_{PDT}. This allows the oxygen concentration to recover as irradiation proceeds. In both models, the respective bleaching coefficients influence the rate and the magnitude of this recovery. The highest bleaching coefficients can even influence the extent of the initial transient depletion. While these general features are shared by both theoretical descriptions, a comparison of Figures 3.1 and 3.2 clearly reveals that the two families of curves are quite distinct. Thus, for situations where photobleaching is significant, these calculations suggest that microelectrode measurements of $^3O_2$ at the edge of a spheroid undergoing

PDT would be sensitive to bleaching and may also provide information regarding the photobleaching mechanism.

3.3 Experimental Verification of the Singlet Oxygen-Mediated Photobleaching Mechanism

Figures 3.3 and 3.4 show data obtained from a representative microelectrode experiment and the best fits to the data using a diffusion-with-reaction model incorporating either a constant bleaching coefficient (Figure 3.3) or the ${}^1O_2$ -mediated bleaching (Figure 3.4) form of Γ_{PDT} (Equation (3.13) or (3.10), respectively). The experimental data were obtained with an oxygen-sensitive electrode with a 10 μm diameter tip positioned at the surface of a 500 μm diameter EMT6 multicell spheroid that had been incubated with 10 μg ml^{-1} Photofrin® for 24 h. The spheroid was irradiated with 514 nm light from an argon-ion laser (50 mW cm^{-2}), and the ${}^3O_2$ concentration at the surface of the spheroid was monitored continuously as a function of time after the onset of irradiation. The recovery from bleaching takes a considerable amount of time. The concentration of ${}^3O_2$ is half the initial value after a 40 J cm^{-2} fluence has been delivered. This justifies the assumption that the photobleaching rate is slow relative to the primary photochemistry.

While fitting the data, it became apparent that a good fit could only be obtained if the edge of the depletion zone was allowed to move away from its steady-state position. This is likely to be representative of a real phenomena. Since the ex-

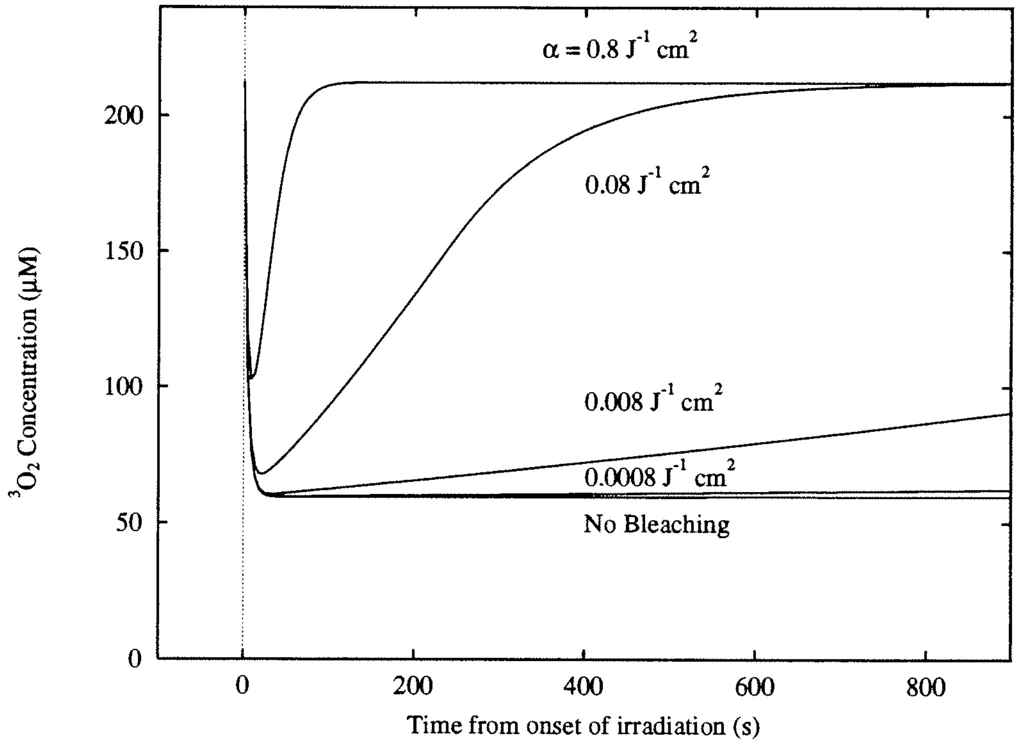

Figure 3.1: Calculations of $^3O_2$ concentration as a function of irradiation time assuming a constant photobleaching coefficient, α, as expressed in Equation (3.13). The curves represent the oxygen transient at the edge of a Photofrin®-sensitized spheroid resulting from PDT conducted at a fluence rate of 100 mW cm^{-2} of 630 nm irradiation. The bleaching coefficients used in the calculation are shown near the corresponding curve. The dashed line at t=0 indicates the initiation of PDT.

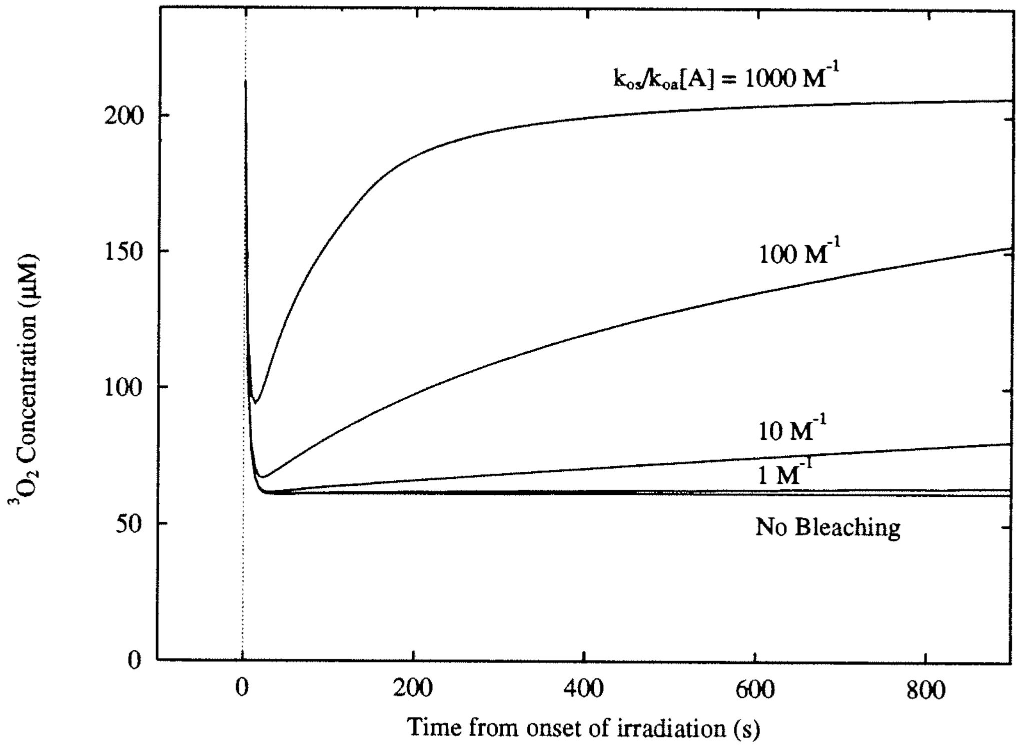

Figure 3.2: Calculations of the oxygen transient resulting from PDT when a $^1O_2$ -mediated bleaching mechanism is assumed (Equation (3.10)). The various curves depict the $^3O_2$ concentration obtained under irradiation conditions identical to those of Figure 3.1, using a range of values for the parameter $k_{os}/k_{oa}[A]$, as shown near the corresponding curves.

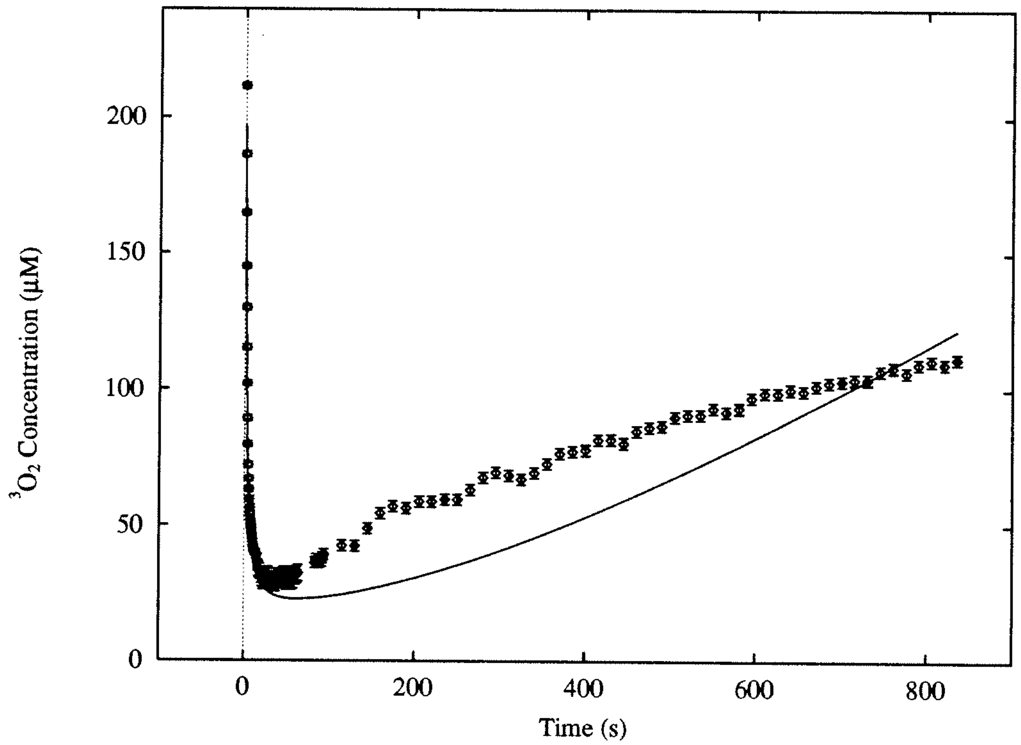

Figure 3.3: A microelectrode measurement of $^3O_2$ concentration at the edge of a Photofrin®-sensitized spheroid during PDT. The points represent a discrete sampling of the microelectrode current, and the error bars represent the approximate fluctuation in the current prior to the onset of irradiation at 0 s. The solid line is the best segmented fit to the data assuming a constant bleaching coefficient.

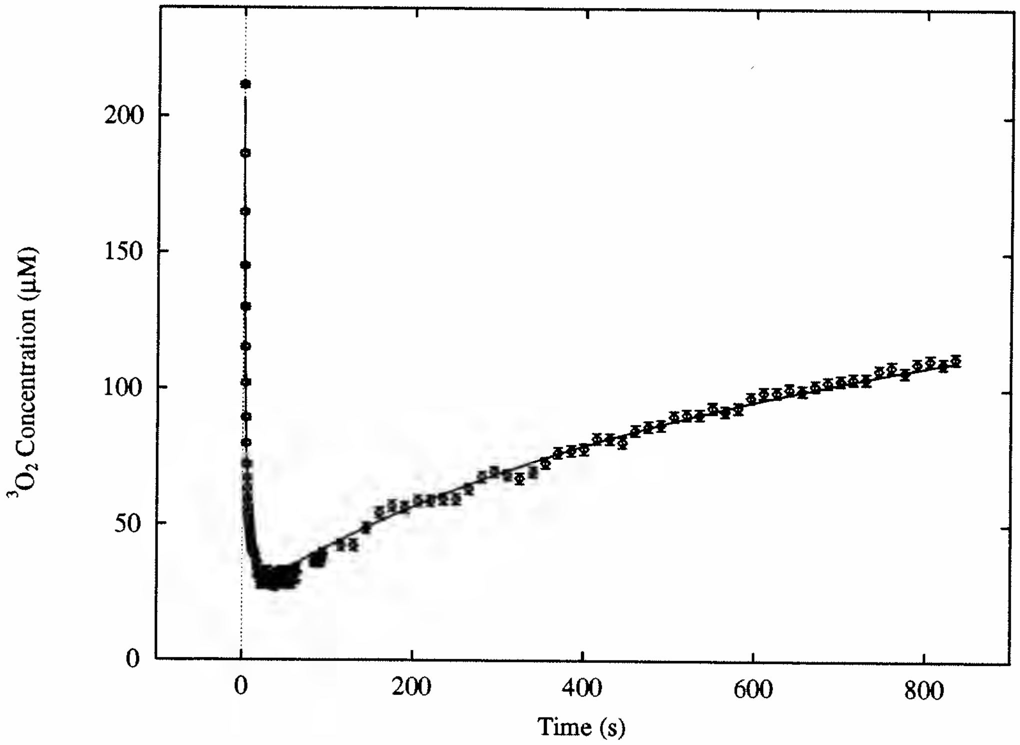

Figure 3.4: A microelectrode measurement of $^3O_2$ concentration at the edge of a Photofrin®-sensitized spheroid during PDT. The data in this figure are the same as in Figure 3.3, but the solid line represents the best segmented fit obtained using Equation (3.10) which incorporates a $^1O_2$ -mediated bleaching mechanism. The best fit value for $k_{os}/k_{oa}[A]$ is 93.7 ± 1.1 M^{-1}.

perimental medium is open to the atmosphere, an equilibrium distribution will eventually be obtained. The edge of the depletion zone will be determined by the net oxygen consumption within the spheroid, as discussed in Chapter 2. At the onset of PDT, the large increase in Γ_{PDT} is expected to cause an increase in the radius of the depletion zone, but the model explicitly fixes this radius *via* Equation (2.5). This simplification appeared to be satisfactory for short irradiation times, but upon closer inspection the quality of the fits described in Chapter 2 was probably due to inappropriate coupling of the oxygen sensitivity parameter, k_p/k_{ot}, with the effect of a moving boundary. This will be discussed in Section 3.4. To obtain a preliminary fit of the data of Figure 3.2, the early (< 40 s) and late (> 40 s) data were fit separately.

In the early data, k_p/k_{ot} and Γ_0 were used as fitting parameters and the respective bleaching coefficients were set to zero. The depletion zone radius, R_d, was held fixed at its steady-state value. The returned values for these fitting coefficients were then used to fit the later data, using either α (Figure 3.3) or $k_{os}/k_{oa}[A]$ (Figure 3.4) and R_d as fitting parameters. With either model, R_d was observed to increase substantially (typically 100 μm or greater) from its steady-state value. Although segmenting the data set allowed the data to be fit, the returned values for the fitting parameters must be treated cautiously since the boundary condition is clearly not correct.

The initial transient decay is described equally well by either model, but details of the photobleaching mechanism distinctly determine the shape of the long-term oxygen recovery. A comparison of the two fits indicates that the $^1O_2$ -mediated bleaching mechanism captures all of the features of the experimental data, while the mechanism that employed a constant photobleaching coefficient cannot. In a multicell system, such as the spheroid, where diffusion establishes a spatial gradient of oxygen during irradiation, the extent of Photofrin®bleaching will be spatially dependent on the distribution of singlet oxygen dose.

Finally, we consider the consequences of an oxygen-dependent bleaching process on the net photodynamic dose delivered throughout a spheroid. Qualitatively, it is apparent that for a given fluence rate bleaching must reduce the maximal dose of $^1O_2$. By reducing the total rate of photodynamic oxygen consumption, however, photobleaching will also extend the oxygenated region as the treatment proceeds. These effects are depicted in the curves of Figure 3.5, which show the net photodynamic doses in a spheroid treated with 60 J cm^{-2} delivered at 100 mW cm^{-2}. One curve illustrates the dose distribution obtained when bleaching does not occur, while the other indicates the effect of $^1O_2$ -mediated photobleaching occurring at a rate determined from the average value of $k_{os}/k_{oa}[A]$ obtained from several fits to microelectrode data such as that shown in Figure 3.4. Again, the exact numerical estimates must be treated cautiously. To obtain accurate numerical results, a moving boundary condition such as that described in Chapter 2 must be implemented and investigated. At this time, only the analysis indicates that the depletion zone is likely to be increasing with irradiation time. Experimental tests of Equation (2.9) should be conducted to verify that the equilibrium approach discussed in Chapter 2 is justified.

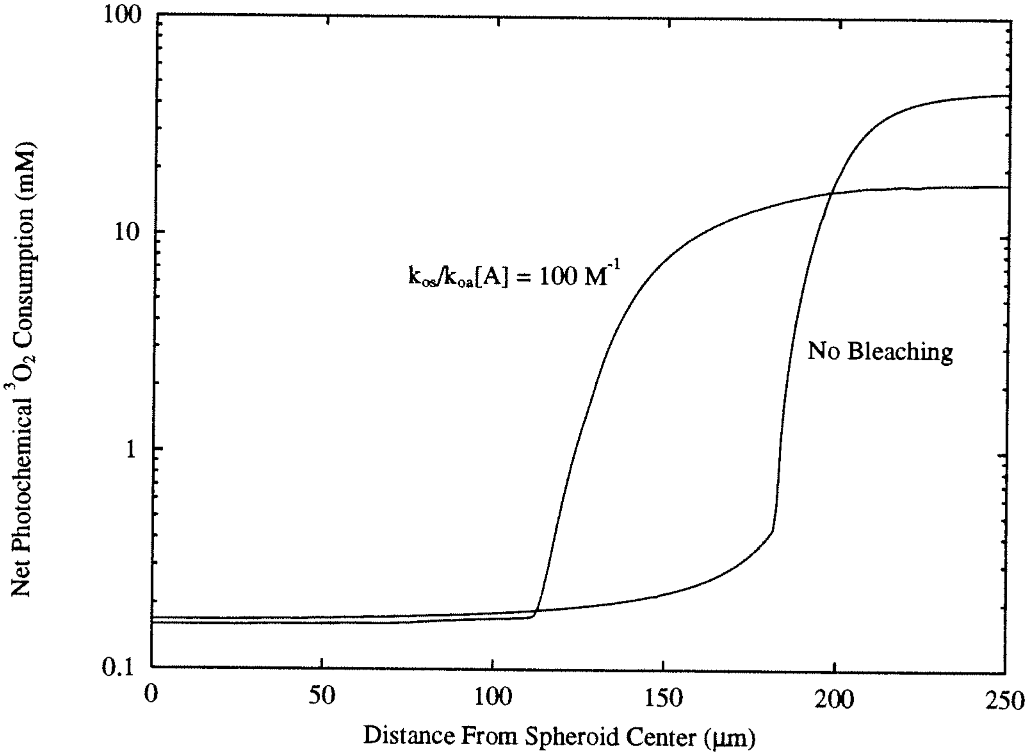

Figure 3.5: A comparison of the calculated $^1O_2$ dose distributions in a 500 μm diameter spheroid following PDT (60 J cm^{-2}, 100 mW cm^{-2}, 630 nm) in the presence and absence of photosensitizer bleaching. The bleaching rate ($k_{os}/k_{oa}[A]$ = 100 M^{-1}) was determined by averaging the results of several best fits to data such as that shown in Figure 3.4.

3.4 Conclusions

Microelectrode measurements of $^3O_2$ are clearly sensitive to the presence of photobleaching during the PDT of spheroids. With increased light dose, reduced photosensitizer absorption reduces the rate of photodynamic oxygen consumption in the spheroid, and this is detected as an increased electrode current. We have introduced and evaluated two theoretical approaches to the interpretation of bleaching in the context of our model of oxygen diffusion with reaction. Preliminary fits of these two models to experimental data indicate that the mechanism of Photofrin® photobleaching is mediated by $^1O_2$. The self-sensitization mechanism is distinct from a mechanism characterized by a constant bleaching coefficient because of the fact that the sensitizer itself is responsible for the bleaching agent. As the sensitizer degrades, the photobleaching coefficient must be diminished. A mechanism employing a constant photobleaching coefficient could, and probably does, exist for other photosensitizers. This could result from direct degradation of the chromophore upon optical excitation, or deactivation due to the reaction of the photosensitizer with an unrelated bleaching agent that is present in the biological milieu. Examination of the effects of bleaching on the time-resolved $^3O_2$ concentration can readily distinguish between these two mechanisms. On the basis of calculations presented here, it is clear that photobleaching can have a profound impact on the distribution of photodynamic dose.

This extension of the oxygen-diffusion-with-consumption model to include bleaching effects should be regarded as preliminary. The experimental measurements described probe photobleaching indirectly by observing the effect on the local $^3O_2$ concentration. We have not yet measured the photosensitizer concentration directly by observing the spatial distribution of photosensitizer fluorescence, for example. Preliminary work on the development of a confocal laser scanning optical system necessary to make these optical measurements with a microscope has begun. This will provide a means to directly verify the pattern of sensitizer bleaching predicted by these models. It is also important to note that the boundary condition used in the modeling, as described in Chapter 2, is clearly inadequate. To overcome this problem, it was possible to break the data set into temporal segments and to fit them somewhat separately. It was necessary to allow the radius of the oxygen depletion zone to move outward during the longer irradiations in order to accommodate bulk oxygen depletion of the medium.

Recently Georgakoudi *et al.* (1996) have implemented the moving boundary condition described in Chapter 2. This resulted in an improved estimate of k_p/k_{ot} of 11.9 ± 2.2 μM, an improved estimate of $k_{os}/k_{oa}[A]$ of 76 ± 12 M^{-1}, and a revised estimate of the threshold dose of $^1O_2$ of 12.1 ± 1.2 mM. The underestimate of k_p/k_{ot} reported in Chapter 2 is likely to be a direct result of an inadequate static boundary condition implemented at the edge of the depletion zone. When the radius was held constant, the fitting algorithm optimized the fit by reducing the value of k_p/k_{ot}. A decrease in this parameter results in a decreased $^3O_2$ sensitivity and allows $^3O_2$ consumption to proceed under hypoxic conditions. As a consequence, the decay of the oxygen transient occurs more quickly. The same kind of effect can be obtained by simultaneously moving the source of $^3O_2$ away from the spheroid, *i.e.* increasing the depletion zone radius. This coupling may have been apparent in data reported in Chapter 2. In this data, k_p/k_{ot} was observed to have a fluence rate dependence, varying from approximately 15 to 2 μM, as the fluence rate was increased from 10 to 60 mW cm^{-2} (514 nm). The returned error in this parameter also decreased substantially with increasing fluence rate. This was initially interpreted as being an indication of a lack of significance in the k_p/k_{ot} fitting parameter at low fluence rates. But improvements to the model to include the moving boundary condition resulted in a consistent value of 11.9 ± 2.2 μM for fluence rates ranging from 40 - 100 mW cm^{-2}. As reported by Georgakoudi *et al.*, this estimate is within uncertainty of that reported by Moan and Sommer (1985) for HpD.

Finally, the proper attention to photobleaching results in a substantially higher estimate of the $^1O_2$ threshold dose, though the model continues to support the fluence rate effects observed in the PDT of spheroids (Foster *et al.*, 1993). This is due to the improved distribution of $^1O_2$ in the interior of the spheroid resulting from the decreased rate of photochemical $^3O_2$ consumption that accompanies photobleaching. To account for the fluence rate dependence of spheroid cell survival, the recalculated threshold dose is increased substantially over our previous estimate which did not account for $^1O_2$ -mediated photobleaching.

Chapter 4

Light Transport in Turbid Biological Media

4.1 Introduction

Light propagation in turbid media has been studied for a variety of materials in the past. Examples include atmospheric optics, scattering of light by interstellar media, and oceanic optics. Recently, a variety of biophysical and biomedical applications involving transport of light in biological tissue has led to a resurgence of research on this topic. Optical dosimetry in photodynamic therapy, for example, requires an accurate knowledge of the distribution of optical fluence in a tumor irradiated with laser light. Similarly, tissue spectroscopy, which seeks to monitor physiological status by absorption, fluorescence, or phosphorescence of endogenous or exogenous chromophores, must interpret measured spectra with a model of light propagation in turbid media to properly account for the effects of scattering. As a result, a variety of theories and measurement techniques have been developed that seek to accurately determine the scattering and absorption characteristics of tissue.

There are two broad classifications of theories appropriate for light propagation in turbid biological materials: analytic theories, based on the fundamental optical fields; and radiative transport theories, based on the flow of optical energy. Analytic theories attempt to treat the electric and magnetic fields in tissue and model absorption and scattering through a spatially varying complex electrical permittivity. Though mathematically rigorous, these approaches require detailed knowledge of the material medium which is complex and difficult to specify. Consequently, many assumptions and simplifications are inevitably made (see for example Twersky, 1979). Radiation transport is an empirical theory which balances radiative energy gains and losses in order to specify the specific intensity at all points in the medium. It seems clear that there should be a correspondence between these two approaches, but this has proven to be elusive (see for example Wolf, 1976; Fante, 1981). By far radiative transport has proven to be the more fruitful approach in the last two decades, and we will deal exclusively with it here.

In a turbid biological medium, a beam of light is rapidly attenuated by scattering and absorption. Scattering tends to dominate absorption in tissue because of the density, size, and index of refraction changes characteristic of biological structures. In the near-infrared, extracellular fluid has an index of refraction in the range of 1.348-1.352, while the index of refraction for membranes and protein aggregates can be as high as 1.46 (Maier *et al.*, 1994). Primary scattering structures range in size from nanometers (simple molecules) to tens of microns (cells, red blood cells, *etc.*). Given this range of particle sizes, one can expect the scattering cross section to vary with wavelength through a complicated combination of Rayleigh and Mie scattering regimes (Saidi *et al.*, 1995). This is well illustrated by the scattering properties of dental hard tissues. Dental enamel is considered to be a disordered array of 30 - 40 nm crystals surrounded by a matrix composed of water, lipids and proteins. Scattering in this tissue has been shown to vary approximately as λ^{-3}, while for dentin, characterized by 1-2 μm cylindrical tubules, no significant variation in the scattering cross section is seen through the visible and near-infrared (Fried *et al.*, 1995). In Intralipid, a tissue-simulating fat emulsion, the scattering coefficient varies approximately as $\lambda^{-2.4}$. An investigation of the particle size distribution and index of refraction of this medium led to the conclusion that Mie theory was an appropriate description (van Staveren *et al.*, 1991). It has been suggested that the dominant contributers to scattering in soft tissues are mitochondria, which are approximately 0.5 μm in diameter (Beauvoit *et al.*, 1995). Due to the fact that these scatterers are approximately one wavelength of visible light in diameter, scattering is strongly forward directed.

In contrast to scattering, absorption by tissue chromophores contributes much less to the total optical attenuation in the visible and near-infrared. The experimental evidence suggests that the ratio of scattering to absorption cross sections in tissue ranges from 10 to 1000 (Duck, 1990; Cheong *et al.*, 1990; Wilson and Jacques, 1990). As examples, human Caucasian skin at 633 nm is characterized by a scattering to absorption ratio of approximately 70, while human uterus appears to have a ratio of over 800 at the same wavelength. It should be mentioned, however, that the majority of the literature values for optical properties cited above are from measurements conducted *in vitro* and consequently are subject to large variability due to sample preparation. When scattering dominates absorption, as it does at visible and near-infrared wavelengths, it is possible to derive a photo-diffusion equation from the radiative transport equation. The diffusion approximation of radiative transfer is derived in detail in a number of texts (Ishimaru, 1978). Here, only a sketch of the derivation will be given to facilitate discussion of the application of diffusion theory to light propagation in biological media.

4.2 Derivation of the Photo-Diffusion Equation

4.2.1 The Transport Equation

The fundamental quantity of interest in radiative transfer theory is the specific intensity at a field point, $\vec{\mathbf{r}}$, along a direction, $\hat{s}$. It is defined by its relationship to the power flux density through the following expression

$$dP = I(\vec{\mathbf{r}}, \hat{s}) \cos\theta \; da \; dw \; d\nu \tag{4.1}$$

where dP is the differential power flowing through the surface element $da\hat{s_0}$ ($\hat{s_0} \cdot \hat{s} = \cos\theta$), within a unit frequency band $d\nu$ and solid angle dw (Chandrasekhar, 1960). Since all real photodetectors have a specified bandwidth and acceptance angle, all physically measurable quantities will consequently involve integrals of the specific intensity over these parameters. The equation of transport states that the specific intensity $I(\vec{\mathbf{r}}, \hat{s})$ can decrease due to scattering out of $\hat{s}$ as well as absorption at $\vec{\mathbf{r}}$. In addition, the specific intensity can increase due to specific intensity $I(\vec{\mathbf{r}}, \hat{s}')$ scattering from $\hat{s}'$ into $\hat{s}$. After separating the diffuse specific intensity from the incident specific intensity, one obtains the equation of transport

$$\left(\hat{s} \cdot \vec{\nabla}\right) I_d(\vec{\mathbf{r}}, \hat{s}) = -(\rho\sigma_t) I_d(\vec{\mathbf{r}}, \hat{s}) + \rho\sigma_s \int\limits_{4\pi} p(\hat{s}, \hat{s}') I_d(\vec{\mathbf{r}}, \hat{s}') dw' + \epsilon_{ri}(\vec{\mathbf{r}}, \hat{s}) \tag{4.2}$$

where ρ is the particle density, σ_t, the total interaction cross section, is the sum of the single particle scattering, σ_s, and absorption, σ_a, cross sections, $\epsilon_{ri}(\vec{\mathbf{r}}, \hat{s})$ is a source term generated by the reduced incident intensity, and $p(\hat{s}, \hat{s}')$ is the normalized phase function, or scattering kernel, governing the probability per unit solid angle that specific intensity along $\hat{s}'$ will scatter into $\hat{s}$. The phase function is dependent on the characteristics of the scatterers, and several appropriate forms have been used in the literature (Henyey and Greenstein, 1941; Reynolds *et al.*, 1975; Groenhuis *et al.*, 1983a; Yoon *et al.*, 1989; Cheong *et al.*, 1990). As this function is difficult to measure experimentally and is likely to vary according to the type of tissue, the appropriate form is often unknown. The first two moments, however, are easily specified to be

$$\int\limits_{4\pi} p(\hat{s}, \hat{s}') dw' = 1 \tag{4.3}$$

and

$$\hat{s} \cdot \int\limits_{4\pi} p(\hat{s}, \hat{s}') \hat{s}' dw' = g, \tag{4.4}$$

where g, the mean cosine of the scattering angle, is the scattering anisotropy. Values of g of $-1, 0$, and 1 indicate strong back-, isotropic and strong forward-scattering, respectively. In tissue, due to the size of the most efficient scatterers, the scattering anisotropy can range from 0.7 to 1.0, though it is typically greater than 0.9. Specifying Equations (4.3) and (4.4) is actually sufficient for the derivation of the diffusion approximation. While it is possible to have sources of diffuse specific intensity within the medium as well (*e.g.,* fluorescence), this term has been neglected in Equation (4.2) to simplify the discussion. A variety of techniques have been developed for solving Equation (4.2), which is essentially the linearized Boltzmann transport equation (see Naqvi *et al.*, 1992, Introduction and references therein). Here we will discuss the P_1 solution, or diffusion approximation, and the Monte Carlo simulation of this equation.

4.2.2 The Diffusion (P_1) Approximation

When the cross section for scattering dominates the interaction cross section, the diffuse energy flux will be small compared to the average optical energy density. In this case, the angular dependence of the specific intensity can be written as a series of Legendre polynomials in the scattering angle,

$$I_d(\vec{\mathbf{r}}, \hat{s}) = \sum_{l=0}^{\infty} A_l P_l(\hat{s'} \cdot \hat{s}), \tag{4.5}$$

where $\hat{s'} \cdot \hat{s} = \cos\theta$ describes the angular distribution of scattering. The coefficients, A_l, can be determined by making use of the orthogonality relations for Legendre polynomials. One finds that

$$A_0 = \frac{1}{4\pi} \int_{4\pi} I_d(\vec{\mathbf{r}}, \hat{s}')dw', \tag{4.6}$$

$$A_1 = \frac{3}{4\pi} \hat{s} \cdot \int_{4\pi} I_d(\vec{\mathbf{r}}, \hat{s}')\hat{s}'dw', \tag{4.7}$$

and

$$A_2 = \frac{5}{4\pi} \int_{4\pi} I_d(\vec{\mathbf{r}}, \hat{s}')(0.5(3(\hat{s}' \cdot \hat{s})^2 - 1))dw'. \tag{4.8}$$

Here we see that A_0 is specified by the average diffuse intensity, or fluence rate, given by

$$\phi(\vec{\mathbf{r}}) = \int_{4\pi} I_d(\vec{\mathbf{r}}, \hat{s}')dw', \tag{4.9}$$

and A_1 involves the diffuse flux,

$$\vec{\mathbf{j}}(\vec{\mathbf{r}}) = \int_{4\pi} I_d(\vec{\mathbf{r}}, \hat{s}')\hat{s}'dw'. \tag{4.10}$$

When $\left|\vec{\mathbf{j}}(\vec{\mathbf{r}})\right| \ll \phi(\vec{\mathbf{r}})$, the sum in Equation (4.5) can be terminated with the second term and the diffuse specific intensity written

$$I_d(\vec{\mathbf{r}}, \hat{s}) = \frac{1}{4\pi}\phi(\vec{\mathbf{r}}) + \frac{3}{4\pi}\vec{\mathbf{j}}(\vec{\mathbf{r}}) \cdot \hat{s}. \tag{4.11}$$

Upon integrating Equation (4.2) over all solid angles and making use of Equation (4.11), a steady-state diffusion equation in the fluence rate, $\phi(\vec{\mathbf{r}})$, can be derived. This equation takes the form

$$D\nabla^2\phi(\vec{\mathbf{r}}) - \mu_a\phi(\vec{\mathbf{r}}) = -S_0(\vec{\mathbf{r}}) + 3D\vec{\nabla} \cdot \vec{\mathbf{S_1}}(\vec{\mathbf{r}}), \tag{4.12}$$

where

$$D = \frac{1}{3(\mu_s(1-g) + \mu_a)}, \tag{4.13}$$

is identified as the photo-diffusion coefficient, $\mu_a = \rho\sigma_a$ is the absorption coefficient, $\mu_s = \rho\sigma_s$ is the scattering coefficient, and $S_0(\vec{\mathbf{r}})$ and $\vec{\mathbf{S_1}}(\vec{\mathbf{r}})$ are isotropic and linearly anisotropic source terms, respectively, that depend on the characteristics of the illuminating beam. Furthermore, the continuity relationship for optical diffusion is found to be

$$\vec{\mathbf{j}}(\vec{\mathbf{r}}) = -D\vec{\nabla}\phi(\vec{\mathbf{r}}), \tag{4.14}$$

which is analogous to Fick's law. Note that since the diffusing quantity is itself a flux, the diffusion coefficient has units of length. Since the diffuse radiant energy density, $u_d(\vec{\mathbf{r}})$, is related to the fluence rate by the speed of light in the medium,

$$\phi(\vec{\mathbf{r}}) = \frac{c}{n}u_d(\vec{\mathbf{r}}), \tag{4.15}$$

Equation (4.14) could be rewritten in the form

$$\vec{\mathbf{j}}(\vec{\mathbf{r}}) = -D^*\vec{\nabla}u_d(\vec{\mathbf{r}}), \tag{4.16}$$

where

$$D^* = \frac{c}{n}D \tag{4.17}$$

is the diffusion coefficient for optical energy within the medium. Equation (4.16) clearly indicates that under appropriate circumstances, a radiant current results from a gradient in the optical energy density. For reference, using typical tissue values of $\mu_s = 100$ cm^{-1}, $\mu_a = 0.1$ cm^{-1}, $g = 0.9$, and $n = 1.4$, the diffusion coefficient for optical energy, $D^* \approx 7.1 \times 10^8$ cm^2 s^{-1}. By analogy with Equations (4.12) and (4.14), when a time-varying irradiance is incident on an optically turbid material, the fluence rate in the medium can be specified by the time-dependent photo-diffusion equation,

$$\frac{n}{c}\frac{\partial\phi(\vec{\mathbf{r}})}{\partial t} = D\nabla^2\phi(\vec{\mathbf{r}}) - \mu_a\phi(\vec{\mathbf{r}}) + S_0(\vec{\mathbf{r}}) - 3D\vec{\nabla}\cdot\ \vec{\mathbf{S}_1}(\vec{\mathbf{r}}), \tag{4.18}$$

and the photocurrent would be given by

$$\vec{\mathbf{j}}(\vec{\mathbf{r}}) = -\frac{n}{c}\frac{d\phi(\vec{\mathbf{r}})}{dt} - D\vec{\nabla}\phi(\vec{\mathbf{r}}). \tag{4.19}$$

4.2.3 Boundary Conditions for Photo-Diffusion

To implement Equations (4.12) and (4.18) to determine the distribution of optical fluence in turbid media, appropriate boundary conditions must be specified. Since these equations describe the *diffuse* fluence rate in the medium, the appropriate condition to implement at an air-tissue interface would be that no diffuse fluence enters the interface from the air half-space. An exception is made in the case of reflecting boundaries. When the turbid medium has an index of refraction which differs from air, it is possible to have diffuse fluence appear to enter the boundary *via* reflection. In terms of the specific intensity, the boundary condition for non-reflecting boundaries is

$$I_d(\vec{\mathbf{r}},\hat{s}) = 0 \qquad\qquad \hat{s}\cdot\hat{n} < 0 \tag{4.20}$$

where $\hat{n}$ specifies the interface normal directed toward the air half-space. This prescription, however, cannot be implemented consistently with the diffusion approximation, Equation (4.11), since it would require that both the fluence rate and the flux vanish for all $\hat{s}\cdot\hat{n} < 0$ at the boundary. This overspecification is a result of truncating the Legendre series after two terms. There have been several approximate diffusion theory boundary conditions which have been employed in the past (Case and Zweifel, 1967). The most common boundary condition to be implemented is the lowest order Marshak boundary condition,

$$\int_{\hat{s}\cdot\hat{n}<0} I_d(\vec{\mathbf{r}},\hat{s})(\hat{s}\cdot\hat{n})^l dw = 0, \qquad l = 1, 3, \ldots \tag{4.21}$$

with $l = 1$, which specifies that the net diffuse flux entering the turbid medium will be zero on average. In the case of an index mismatch at the interface, the inwardly directed flux will be a fraction of the outbound flux,

$$\hat{n}\cdot\int_{\hat{s}\cdot\hat{n}<0} I_d(\vec{\mathbf{r}},\hat{s})\hat{s}dw = (-\hat{n})\cdot\int_{\hat{s}\cdot\hat{n}>0} R(\hat{s}\cdot(-\hat{n}))I_d(\vec{\mathbf{r}},\hat{s})\hat{s}dw, \tag{4.22}$$

where $R(\hat{s}\cdot(-\hat{n}))$ represents the usual Fresnel reflectance from the interface. Substituting Equation (4.11) into (4.22) reveals the *partial-current boundary condition*,

$$\phi(\vec{\mathbf{r}}) + 2A\hat{n}\cdot\vec{\mathbf{j}}(\vec{\mathbf{r}}) = 0, \tag{4.23}$$

where A is determined from the reflectivity of the boundary and may be found from a numerical integration of functions involving the Fresnel reflectance, as described by Yoon *et al.* (1989). For index-matched boundary conditions $A = 1$, while for a typical air-tissue index mismatch of 1.4, $A = 3.25$ (Farrell *et al.*, 1992).

It is interesting to review the implications of Equation (4.23). Neither the fluence rate at the boundary nor the photocurrent leaving the boundary is zero, as expected. Furthermore, since the diffuse flux is related to the gradient of the fluence rate, Equation (4.23) indicates that the fluence rate interior to the medium will be greater than that at the surface. This is understandable if absorption is negligible compared to scattering since the backscattered fluence will add to the incident fluence just inside the boundary. It is also clear that the assumption upon which diffusion theory is based, namely that the diffuse flux be small compared to the fluence rate, is only marginally satisfied at the boundary, given that

$$\frac{\phi(\vec{\mathbf{r}})}{\left|\vec{\mathbf{j}}(\vec{\mathbf{r}})\right|} = 2A, \tag{4.24}$$

though it should be improved by increased reflectivity. Finally, If one linearly extrapolates the fluence rate beyond the physical boundary, Equation (4.23) indicates that it will extrapolate to zero at a distance of $2AD$. For the case of a non-reflecting boundary and a non-absorbing medium with a unity scattering coefficient, this extrapolation distance can be compared to the Milne problem of neutron emission from a deeply buried source. While the extrapolation length has been shown to be 0.7104 for the exact solution of the transport equation for this medium, the partial-current solution leads to an extrapolation length of 0.6667. This gives an indication that diffusion theory results are, in fact, approximate.

The degree to which diffusion theory applies to light propagation in biological media when the transport equation is assumed to be valid will be evaluated in Chapter 5. We begin by reviewing steady-state approaches to the diffusion equation that have been developed to describe optical transport in tissue. These solutions will then be compared with Monte Carlo solutions of the transport equation to estimate the systematic deviations which may occur due to the approximations which have been made. In Chapters 6 and 7, experiments conducted in well characterized tissue-simulating phantoms will be used to validate analysis based on photo-diffusion theory.

4.3 Solution of the Photo-Diffusion Equation

4.3.1 The Exact Solution

The exact solution of the steady-state diffusion equation in a semi-infinite planar medium with matched and mismatched boundary conditions can be found by the method of Green's functions. The solution for a finite slab has been presented by Reynolds *et al.* (1975), and the extension of this solution to a semi-infinite geometry is presented in Appendix A. The only means of rigorously satisfying the partial-current boundary conditions for a slab is through an infinite series of harmonic functions. In the limit that one boundary is removed to infinity, the eigenvalue spectrum becomes continuous and the infinite series can be represented by an integral. The result of this derivation is that the fluence rate at any point in the medium due to an infinitesimal collimated beam of irradiation is given by

$$\phi(\rho, z) = \frac{\mu_s}{\pi^2}\left(\frac{1}{D} + 3g\mu_t\right)(1 + 2AD\mu_t)\int_0^\infty \frac{k\left(\sin kz + 2AD\cos kz\right)K_0\left(\sqrt{k^2 + \frac{\mu_a}{D}}\,\rho\right)}{\left(1 + (2ADk)^2\right)\left(\mu_t^2 + k^2\right)}dk, \tag{4.25}$$

where ρ is the radial distance from the incident beam, z is the axial distance below the boundary, K_0 is the zeroth order modified Bessel function, and $\mu_t = \mu_s + \mu_a$. The diffuse reflectance at the planar interface at $z = 0$ is given by

$$R_d(\rho) = \frac{\mu_s}{2\pi^2}(1 + 3g\mu_t D)(1 + A)(1 + 2AD\mu_t)\int_0^\infty \frac{k^2 K_0\left(\sqrt{k^2 + \frac{\mu_a}{D}}\,\rho\right)}{\left(1 + (2ADk)^2\right)\left(\mu_t^2 + k^2\right)}dk. \tag{4.26}$$

While this solution exactly satisfies the photo-diffusion equation and the partial-current boundary conditions, its complicated form hinders its application. Nevertheless, this solution can be used to deduce the optical properties of a turbid medium from the diffuse reflectance measured at several values of ρ. To facilitate this, Equation (4.26) has been developed as a merit function in a non-linear least-squares (Levenberg-Marquardt) fitting algorithm (Press *et al.*, 1992). This algorithm will be used in Chapter 5 to deduce the optical properties from simulated radially-resolved diffuse reflectance data sets.

4.3.2 The Dipole Approximation

Another promising approach to the steady-state photo-diffusion equation has recently been presented by Farrell *et al.* (1992), who refined the original work of Patterson *et al.* (1989). Instead of satisfying the partial-current boundary condition exactly, these solutions utilize the extrapolated boundary condition to solve the diffusion equation by a superposition of well placed fluence point sources. In an infinite medium, the Green's function of Equation (4.12) is readily shown to be

$$\phi(r) = \frac{1}{4\pi D}\frac{e^{-\mu_{eff} r}}{r}, \tag{4.27}$$

where r is the distance from the point source to the field point, and

$$\mu_{eff} = \sqrt{3\mu_a\,(\mu_s' + \mu_a)}, \tag{4.28}$$

with

$$\mu_s' = \mu_s(1-g). \tag{4.29}$$

Since the fluence rate extrapolates to zero beyond the physical boundary of a semi-infinite medium, Farrell *et al.* proposed the use of an ensemble of sources placed on either side of the physical boundary to force the resulting fluence rate to zero on an extrapolated boundary. They found that by placing a positive source at an approximate depth, z_0, of one transport mean free path (1 mfp$' \equiv (\mu_s' + \mu_a)^{-1}$) below the boundary within the medium and a negative source at an appropriate distance above the boundary, $z_0 + 2z_b$, on axis with the positive source, the extrapolated boundary condition could be satisfied. The resulting fluence rate in the medium is

$$\phi(\rho, z) = \frac{1}{4\pi D}\left(\frac{e^{-\mu_{eff} r_1(\rho,z)}}{r_1(\rho, z)} - \frac{e^{-\mu_{eff} r_2(\rho,z)}}{r_2(\rho, z)}\right) \tag{4.30}$$

where

$$r_1(\rho, z) = \sqrt{\rho^2 + (z - z_0)^2} \tag{4.31}$$

and

$$r_2(\rho, z) = \sqrt{\rho^2 + (z + 2z_b + z_0)^2} \tag{4.32}$$

are the distances from the field point to the source and image charges, respectively, and z_b is the distance from the physical boundary to the extrapolated boundary. As discussed earlier, the partial-current boundary condition indicates that $z_b = 2AD$. Calculating the diffuse reflectance using Equation (4.14) reveals that

$$\begin{aligned} R_d(\rho) \;=\; & \frac{a'}{4\pi}\left(\frac{1}{\mu_{t'}}\left(\mu_{eff} + \frac{1}{r_1(\rho, 0)}\right)\frac{e^{-\mu_{eff} r_1(\rho,0)}}{r_1^2(\rho, 0)} + \right. \\ & \left. (z_0 + 2z_b)\left(\mu_{eff} + \frac{1}{r_2(\rho, 0)}\right)\frac{e^{-\mu_{eff} r_2(\rho,0)}}{r_2^2(\rho, 0)}\right), \end{aligned} \tag{4.33}$$

where $\mu_t' = (\mu_s' + \mu_a)$ and $a' = \mu_s'/\mu_t'$. Upon inspection it is clear that Equation (4.33) is a much simpler function than that given by the rigorous solution of the partial-current boundary condition. Nevertheless, when compared to diffuse reflectance data sets generated from Monte Carlo simulations of the transport equation, excellent agreement was found for $\rho > 1$ mfp′ (Farrell *et al.*, 1992). This critical distance is reasonable since diffusion theory is expected to be valid only after several scattering events. Perhaps most surprising of the results presented by Farrell *et al.* was the fact that the dipole solution gave better results than an extended source model, constructed by summing an infinite line of sources with an exponentially decreasing weight factor, suggested by Equation (A.13). The lack of agreement between Monte Carlo and the extended source model was thought to be due to the influence of heavily weighted diffuse sources near the surface, whereas the exact solution of the transport equation would result in non-diffuse sources in this region. Haskell *et al.* (1994) have recently shown that the dipole configuration of fluence sources yields the same dipole and quadrapole moments of the fluence rate at the boundary as the rigorous solution under the partial-current boundary condition. Evidently, some aspect of the octupole and higher moments, which could only be significant near the irradiation beam, is contributing to the disagreement with the rigorous solution. This is consistent with the analysis of Farrell *et al.*. Fluorescence from a turbid medium is briefly considered in the context of the dipole approximation in Appendix B.

4.4 A Comparison of the Dipole and Exact Reflectance Expressions

The diffuse reflectance obtained from the exact solution of the photo-diffusion equation and the dipole approximation are shown for a biological range of absorption coefficients in Figures 4.1 and 4.2. Index-matched ($A = 1$) boundary conditions were used to create the curves in Figure 4.1, while the diffuse reflectance that results from the same optical properties excepting a mismatch in the index of refraction of 1.4 is illustrated in Figure 4.2. The exact reflectance curves (solid lines) were obtained by numerical calculations of the integral of Equation (4.26) with $\mu_s = 1.00$ mm^{-1}, $g = 0.0$ and μ_a ranging from 0.001 to 0.1 mm^{-1}. This provides the best agreement with the dipole reflectance curves (dashed lines) obtained with a μ_s' of 1.00 mm^{-1} and the same range of absorption coefficients.

For both matched and mismatched conditions, the greatest disagreement occurs in the vicinity of the beam at $\rho = 0$ mm, although significant deviations occur for the entire range of distances examined. The presence of diffuse sources located just inside the interface leads to a logarithmically-diverging reflectance at $\rho = 0$ for the exact solution, while the dipole reflectance has a well-defined maximum. Beyond approximately 1 mfp$'$ from the beam, however, the two solutions are in better agreement when matched boundary conditions are used. The presence of a mismatch in the index of refraction results in an increase in the fluence rate and the reflectance far from the source for both solutions, but the exact solution predicts a larger increase in both of these quantities. In terms of the dipole ap-

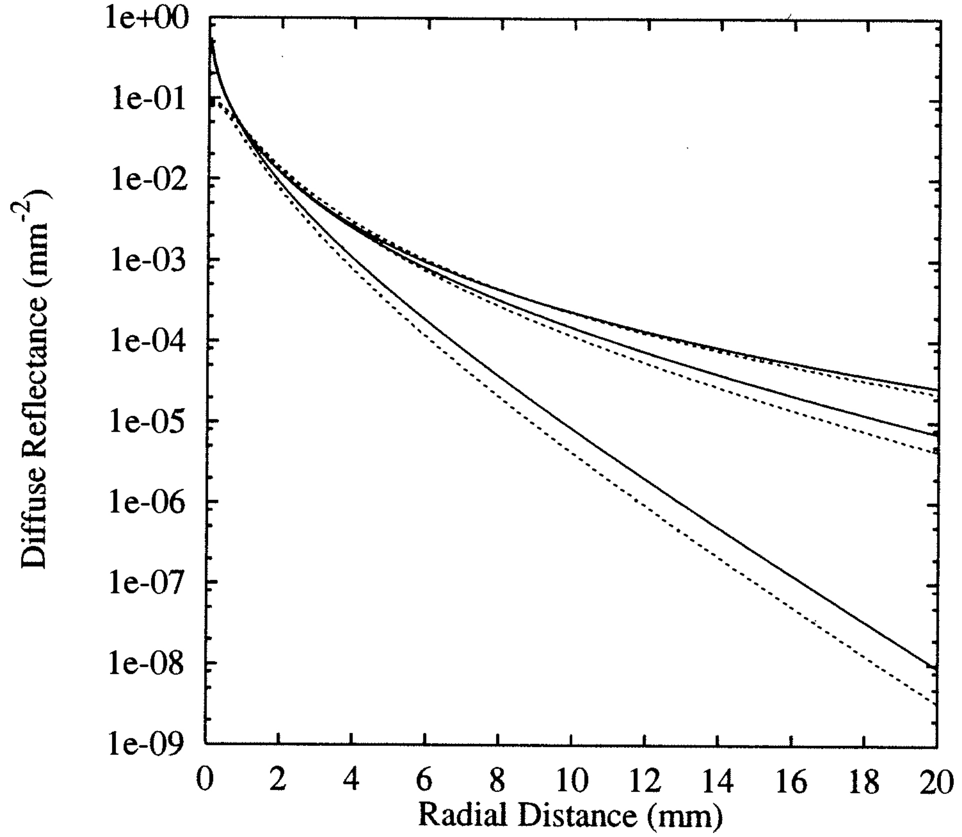

Figure 4.1: The radial distribution of diffuse reflectance generated by the exact (solid lines) and dipole (dashed lines) reflectance expressions for an index-matched boundary. Reflectance for three values of the absorption coefficient are shown for each expression: 0.1 (bottom), 0.01 (middle) and 0.001 (top) mm^{-1}. The transport scattering coefficient, μ_s', is 1.0 mm^{-1} for both expressions, and isotropic scattering was assumed for the exact reflectance expression for best comparison.

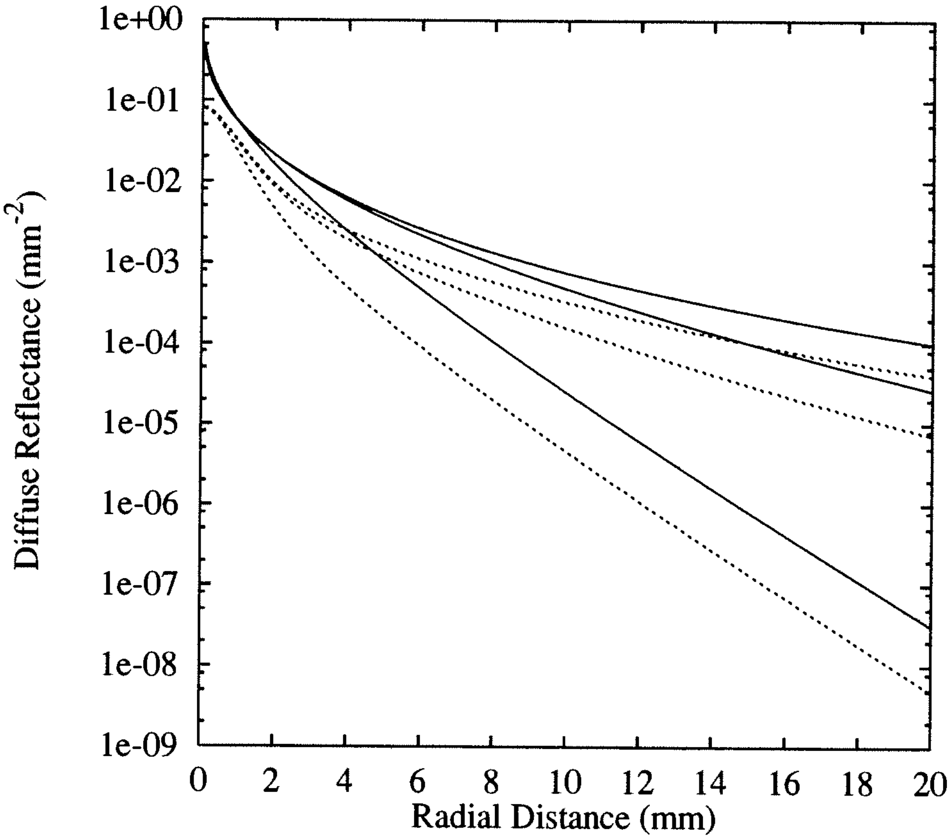

Figure 4.2: The radial distribution of diffuse reflectance generated by the exact (solid lines) and dipole (dashed lines) reflectance expressions for an index-mismatched boundary. The optical properties used to generate the curves were the same as those used in Figure 4.1 except that an index mismatch of 1.4 ($A = 3.25$) was used.

proximation, the negative image source is moved further away from the boundary with an index mismatch, so its impact is reduced while the effect of the positive source is unchanged.

Since the dipole approximation reduces the photo-diffusion equation to a pair of isotropic fluence sources, μ_s is always found multiplied by $(1-g)$, *i.e.* in the form of the transport scattering coefficient, μ_s'. Hence, reciprocal changes in these two quantities will result in equivalent diffuse fluence rates. Equation (4.26) reveals that this is not true for the exact solution of the photo-diffusion equation. When g is increased from 0.0 to 0.9 and μ_s is adjusted to keep μ_s' constant, the diffuse reflectance is seen to increase with the scattering anisotropy. This is shown for four values of g in Figure 4.3. A greater increase occurs in the vicinity of the source, but the curves are actually very similar in shape. Therefore, if the shape of the diffuse reflectance curve is to be used experimentally to discern the optical properties of the medium, the exact expression will be more sensitive to μ_s' than μ_s. Scaling the curves indicates subtle differences in reflectance near the source, but diffusion theory is not expected to model the reflectance in this region very well. It is unlikely that this difference could be exploited to obtain μ_s and g independently through measurements of the radially-resolved diffuse reflectance.

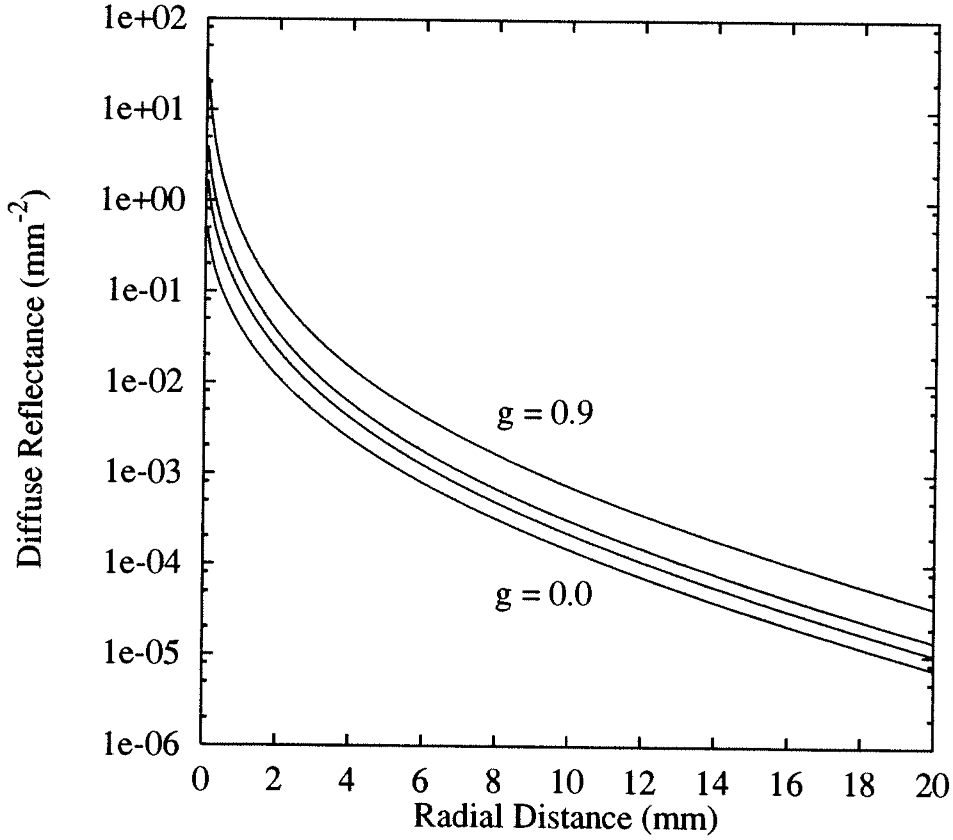

Figure 4.3: The radial distribution of diffuse reflectance generated by the exact reflectance expression for several values of the scattering anisotropy. Reflectance increases with the anisotropy for each of the four values shown: 0.0 (bottom), 0.5, 0.7 and 0.9 (top). For each curve the scattering coefficient, μ_s, was adjusted to ensure that $\mu_s' = \mu_s(1-g)$ was 1.0 mm^{-1}, the absorption coefficient is 0.01 mm^{-1} and the internal reflectance parameter, A, is 1.0 (matched).

4.5 A Comparison of the Extrapolated and Partial-Current Boundary Conditions

Equation (4.30) was constructed in such a way as to force the fluence rate to zero at a specified distance from the physical boundary, *i.e.*

$$\phi(\rho, z_b) = 0 \tag{4.34}$$

where z_b is the axial distance to the so-called extrapolated boundary. In general, this extrapolated boundary condition will not be consistent with the partial-current condition (Equation (4.23)) for small ρ, though for large ρ ($\rho \gg {\mu'_t}^{-1}$) it is expected be a better approximation. The characteristics of the dipole solution at the boundary can be evaluated relative to a solution obeying the partial-current condition by carrying out the extrapolation for both cases. This is shown graphically in Figure 4.4 for a specified set of optical properties and an index-matched boundary. For a planar boundary in the x-y plane, the gradient of the fluence rate along the boundary normal is simply the slope of the fluence rate along the z-axis. Given this slope, linearly extrapolating the fluence rate into the air-region from the interface gives

$$\phi(\rho, z) = \left(\frac{\partial \phi(\rho, z)}{\partial z}\Big|_{z=0}\right) z + \phi(\rho, 0) \qquad z < 0. \tag{4.35}$$

According to the partial-current boundary condition, the slope at the boundary is

$$\frac{\partial \phi(\rho, z)}{\partial z}\Big|_{z=0} = \frac{\phi(\rho, 0)}{2AD}, \tag{4.36}$$

hence

$$\phi(\rho, z) = \phi(\rho, 0)\left(\frac{z}{2AD} + 1\right) \qquad z < 0. \tag{4.37}$$

Clearly, the fluence rate should extrapolate to zero at $z = -2AD$. The solid line in Figure 4.4 is the solution of Equation (4.30) obtained when $\mu_s' = 1.00$ mm^{-1}, $\mu_a = 0.001$ mm^{-1}, $\rho = 0$ mm and $A = 1.0$ (matched). These particular values have been chosen to provide a concrete illustration of the disagreement between the extrapolated boundary condition and the partial-current boundary condition, but the general results do not depend on these values. Inserting the value of the fluence rate at the origin into Equation (4.37), and using the appropriate optical properties to calculate the diffusion coefficient, the dotted line in the figure is obtained. This line depicts the extrapolated fluence rate that would result from a solution that satisfies the partial-current boundary condition. Notice that the dipole solution is forced to zero on the extrapolated boundary, but the slope of the fluence rate at the physical boundary is too great. The actual extrapolation of the dipole fluence rate from the boundary is shown by the dash-dotted line and it results in a shorter extrapolation length than would be obtained from a solution satisfying the partial-current boundary condition. If the dipole solution satisfied the partial-current condition exactly, the dotted and dash-dotted lines would have the same slope.

The error in the fluence rate at the boundary that results from the dipole approximation is simply

$$error = \phi(\rho, z) - 2AD\hat{\mathbf{n}} \cdot \vec{\nabla}\phi(\rho, z), \tag{4.38}$$

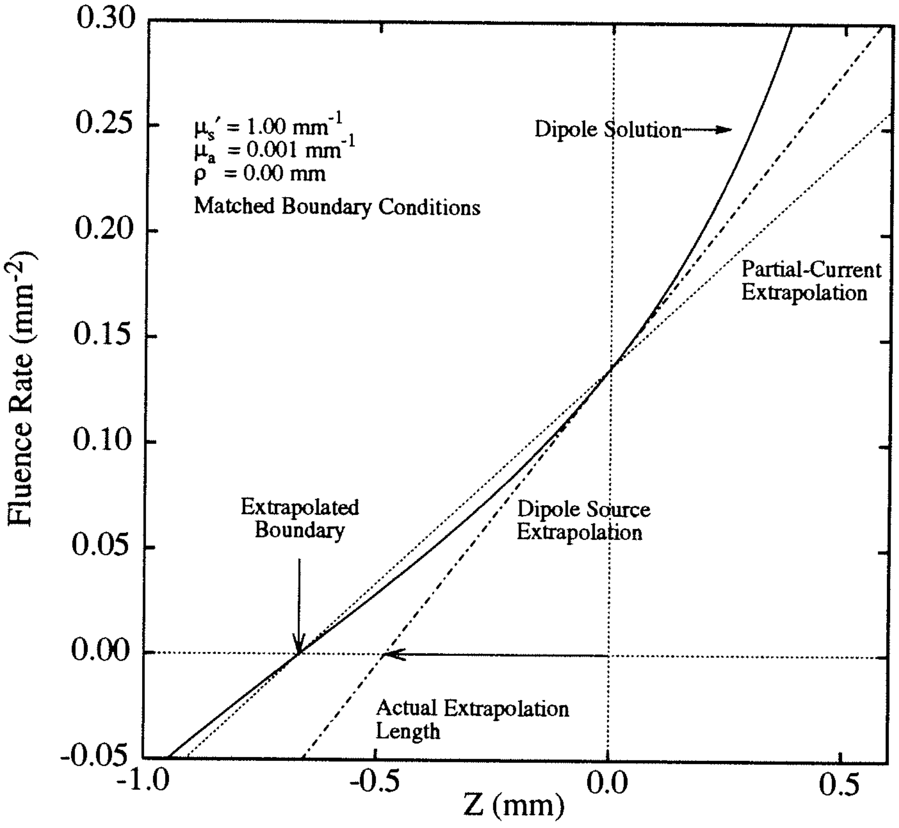

Figure 4.4: Graphical comparison of the actual and theoretical extrapolation lengths for the dipole approximation of Farrell *et al.*. The solid line represents the fluence rate from a dipole source configuration as calculated by Equation (4.30). The extrapolated boundary used by Farrell *et al.* is the axial distance where the fluence rate goes to zero. This corresponds to the theoretical extrapolation length specified by the partial-current boundary condition (Equation (4.23)). The dash-dotted line represents an extrapolation based on the slope of the fluence rate at the physical boundary (Z=0), while the dotted line indicates what would be obtained if the partial-current boundary condition was exactly satisfied.

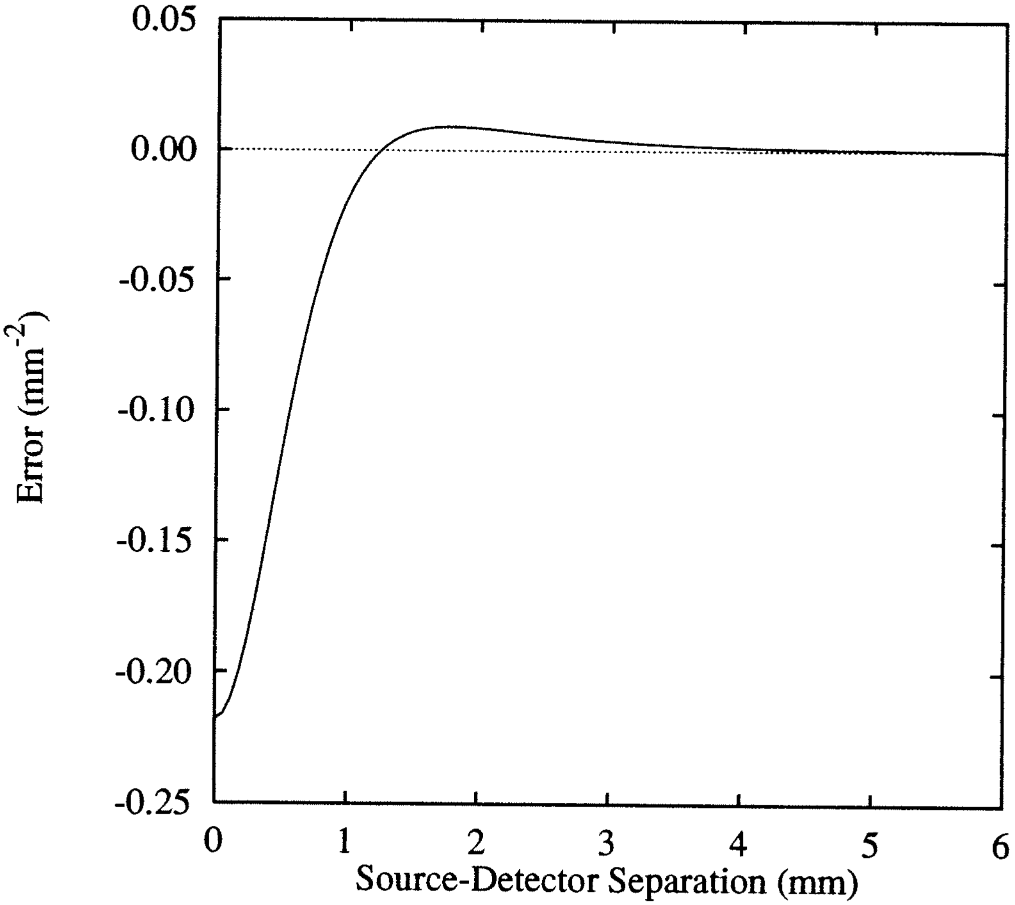

Figure 4.5: The error in the partial-current boundary condition, as defined by Equation (4.38). The optical properties correspond to those used in Figure 4.4.

evaluated on the boundary with $\phi(\rho, z)$ given by Equation (4.30). Figure 4.5 indicates the dependence of the error on the radial distance along the boundary. The largest discrepancy occurs in the vicinity of the point source. For radial distances larger than approximately one transport mean free path, however, the error rapidly approaches zero. Negative error simply indicates that the ratio of the flux to the fluence rate at the boundary is greater for the dipole approximation than for that specified by the partial-current condition, as depicted in Figure 4.4.

A similar analysis was performed when the index of refraction of the turbid medium was different than that of air. Farrell *et al.*'s solution of the photo-diffusion equation accounts for a mismatch in the index of refraction by adjusting the location of the image fluence source to force the resulting fluence rate to zero at $z = -2AD$. This location is dependent on the index mismatch through the internal reflectance parameter, A. Figures 4.6 and 4.7 depict the fluence rate at $\rho = 0$ and the error in the partial-current boundary equation for a value of the internal reflection parameter of 3.25. While the theoretical extrapolation length increases by a factor of 3.25, once again the dipole-source approximation has an actual extrapolation distance of less than half of that specified by theory. The consequential increase in the flux at the boundary relative to the fluence rate results in a more pronounced error than in the index-matched case considered previously. But as indicated in Figure 4.7, once again this error rapidly approaches zero with increasing ρ. For both matched and mismatched boundaries, the error is truly negligible after approximately 10 mfp′.

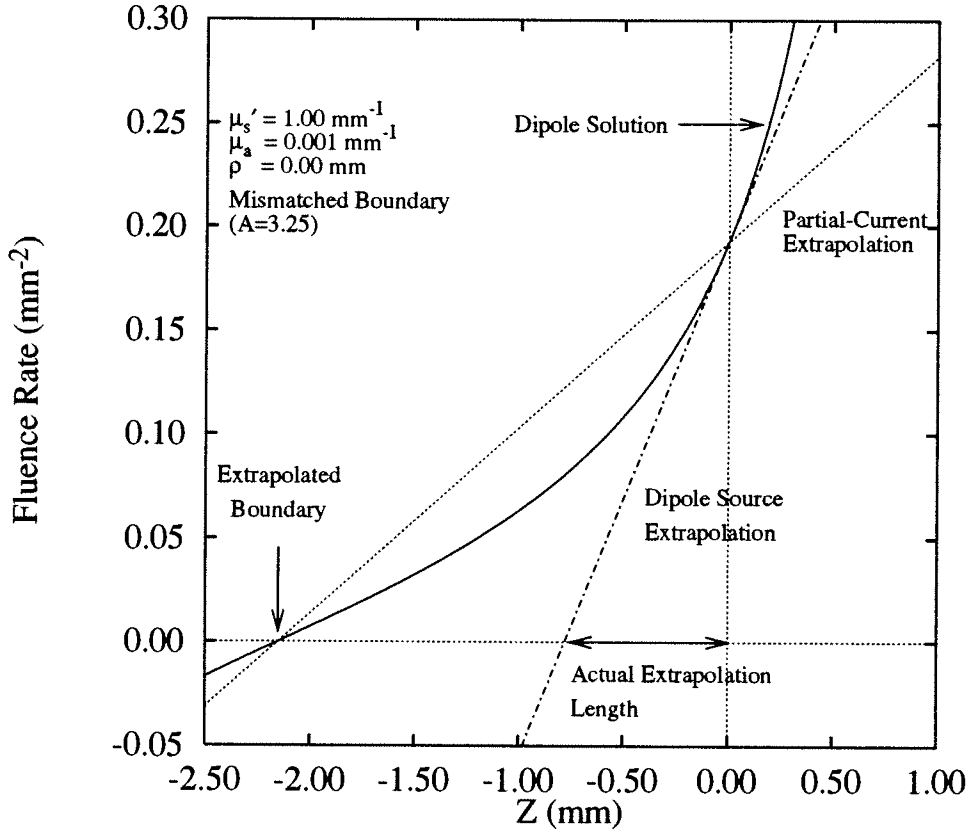

Figure 4.6: Graphical determination of the actual and theoretical extrapolation lengths for the dipole approximation with an index mismatched boundary condition. The analysis is the same as that described in Figure 4.4, but an index mismatch of 1.4 ($A = 3.25$) between air and the turbid medium was used.

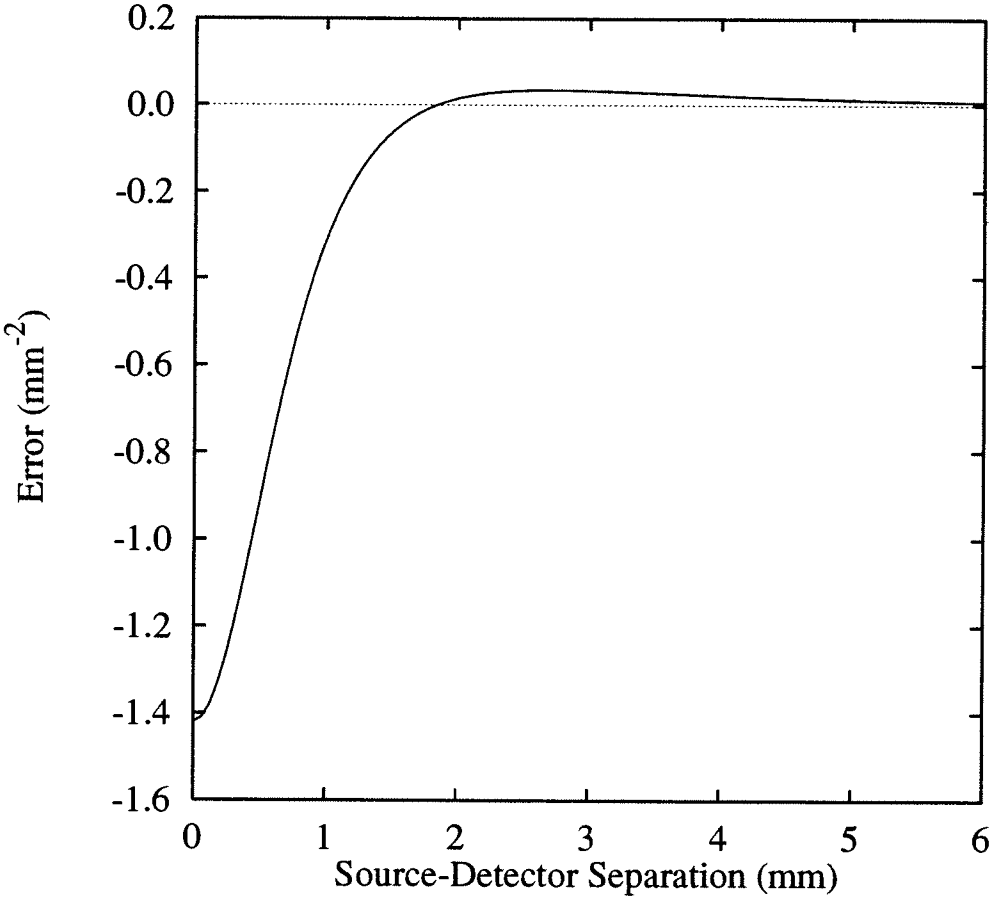

Figure 4.7: The error in the partial-current boundary condition, as defined by Equation (4.38), is plotted as a function of ρ, the source-detector separation. Index-mismatched conditions were used, and the optical properties were the same as those used in Figure 4.6. Both the magnitude of the error and the asymptotic recovery are more extreme for mismatched conditions than for matched conditions (Figure 4.5).

4.6 Monte Carlo Solution of the Transport Equation

Monte Carlo techniques offer another powerful method of solving the equation of transport (Kalos and Whitlock, 1986). A number of Monte Carlo algorithms have been written explicitly to simulate light propagation in biological tissue (Wilson and Adam, 1983; Prahl *et al.*, 1989; Taitelbaum *et al.*, 1989; Wang and Jacques, 1992; Arridge *et al.*, 1995). Briefly, the equation of transport is solved statistically by tracing many "photon" trajectories through a turbid medium. By randomly sampling appropriate probability density functions, the frequency of scattering and absorption events can be chosen to represent the desired optical properties of tissue. When elastic scattering occurs, the angular distribution is chosen to satisfy an appropriate phase function. Physical quantities such as the fluence rate and diffuse reflectance are obtained statistically by summing the number of observed interactions occurring in a region. Hence, the accuracy of Monte Carlo simulation is dependent on the number of observed interactions. While Monte Carlo algorithms can accurately simulate the transport equation under complicated geometrical configurations and in regions where the diffusion approximation is clearly violated, these algorithms are computationally intensive, often requiring several days of CPU time on a workstation. Recently, Wang and Jacques (1993) have described a hybrid Monte Carlo-diffusion theory technique to improve the speed of computation while retaining the accuracy of Monte Carlo. Depending on the optical properties used for the simulation, this technique can lead to a reduction in computation time by more than a factor of ten, yet the direct application is limited to relatively simplistic boundaries.

To accurately model light propagation in complex biological systems such as a subcutaneous tumor undergoing PDT, an object oriented Monte Carlo (OOMC) simulation was written in the C++ programming language. While Monte Carlo algorithms can be used with any geometrical configuration of air-tissue boundaries, in function-oriented languages it is exceedingly difficult to write abstract code which can be used in a variety of situations. Hence, it is customary to rewrite Monte Carlo code specific to each application. Object oriented programming languages provide a number of abstraction features that make it possible to write a single Monte Carlo routine that can easily be configured for a variety of applications (Barton and Nackman, 1994).

The core of the Monte Carlo algorithm, OOMC, is depicted in a flow chart in Figures 4.8 and 4.9. A photon is launched into a turbid region according to the characteristics of the specified source. A variable stepsize is chosen by sampling the probability density function for interaction after traveling a distance s,

$$p(s) = \mu_t e^{-\mu_t s} \tag{4.39}$$

as described by Prahl *et al.* (1989). On the first step, the photon trajectory in the turbid region is determined by the source which launched the photon. The photon is moved along this trajectory a distance, s, given by

$$s = \frac{-\ln \xi}{\mu_t} \tag{4.40}$$

where ξ is a pseudo-random number between 0 and 1. If a boundary is encountered anywhere along this step, the photon is moved to the boundary. In the literature, it is customary to use specular boundaries, where the probability of reflection and the reflection trajectory is dependent on the incident angle. While this may be true of glassy or liquid phantoms, it is less likely that this will be an accurate description of biological tissues such as skin. For a situation such as this, perfectly diffusing boundaries that scatter isotropically may be more appropriate. A random number is then compared with the probability for reflection to determine if the photon is reflected or refracted at the intersection point. Depending on the type of surface encountered, a new trajectory for the photon is determined, and the remaining stepsize is taken in the new direction. If the photon is refracted into a region with a different interaction coefficient, the stepsize is updated as required by the continuity relationship. This process is repeated if a boundary is encountered while finishing the step until the entire step has been taken. Upon completing the step, a weight of either μ_t^{-1} or 1 is deposited in a three dimensional spatial grid at the interaction site for interior or surface coordinates, respectively. Although the random walk is continuous, discrete bins are used to collect statistics. At the completion of a step, a random number is compared with the albedo of the current region to determine if the photon is scattered or absorbed at the interaction site. If the photon is scattered, a specified phase function for the medium, such as the Henyey-Greenstein phase function (Henyey and Greenstein, 1941), is sampled to obtain the random scattering angle, and a new photon trajectory is computed. If the photon is absorbed, the random walk is terminated and another photon is launched.

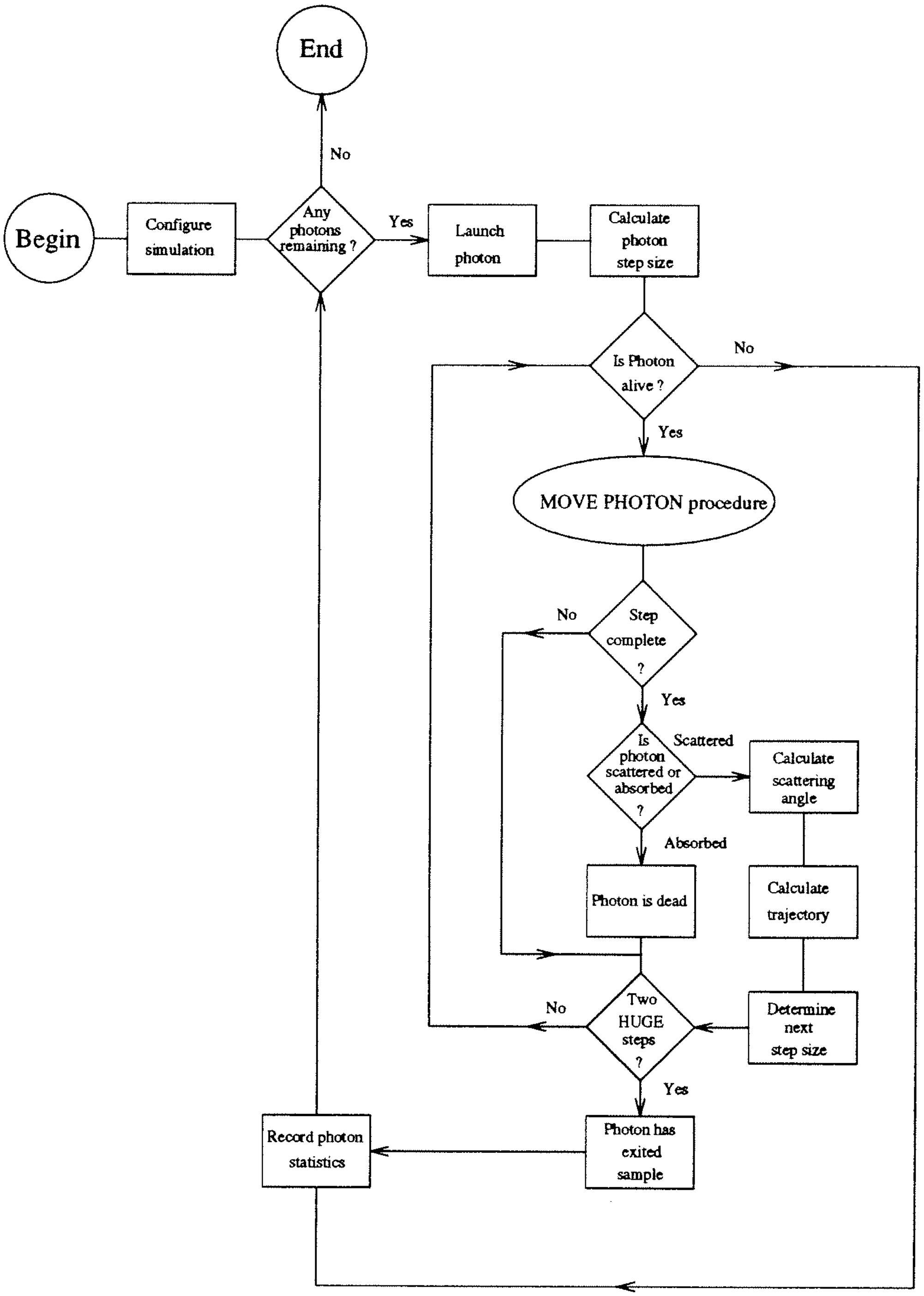
End
No
Begin
Configure simulation
Any photons remaining ?
Yes
Launch photon
Calculate photon step size
Is Photon alive ?
No
Yes
MOVE PHOTON procedure
Step complete ?
No
Yes
Is photon scattered or absorbed ?
Scattered
Calculate scattering angle
Absorbed
Photon is dead
Calculate trajectory
Two HUGE steps ?
No
Determine next step size
Yes
Record photon statistics
Photon has exited sample

Figure 4.8: Flow chart for the OOMC (Object Oriented Monte Carlo) algorithm

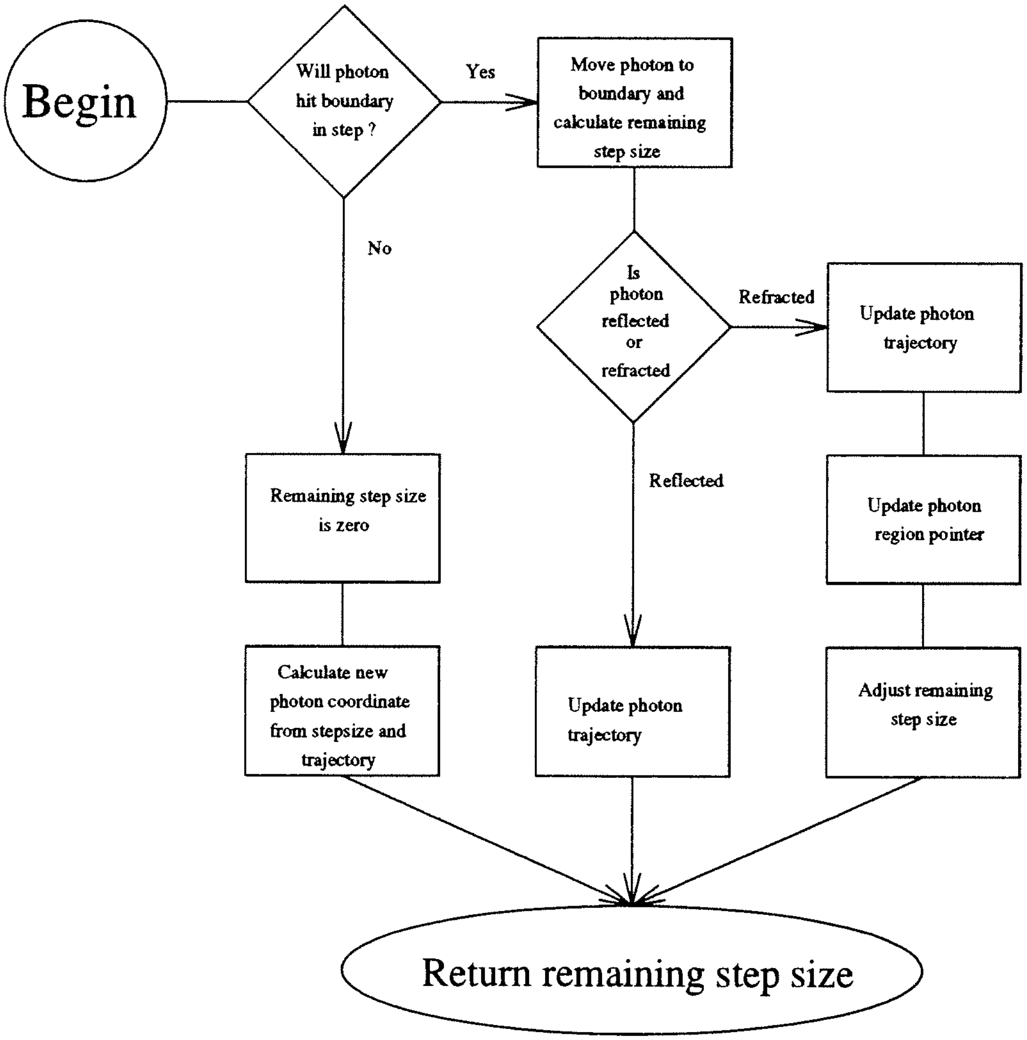
Begin
Will photon hit boundary in step ?
Yes
Move photon to boundary and calculate remaining step size
No
Is photon reflected or refracted
Refracted
Update photon trajectory
Reflected
Remaining step size is zero
Update photon region pointer
Calculate new photon coordinate from stepsize and trajectory
Update photon trajectory
Adjust remaining step size
Return remaining step size

Figure 4.9: Flow chart for the MOVE PHOTON procedure of the OOMC algorithm

At the completion of the simulation, the weighted interactions deposited in the spatial grid are used to estimate the fluence (interior bins) or diffuse reflectance (surface bins). The total number of interactions, $N_{i,j}$, occurring within the ith radial bin and jth axial bin, is given by

$$N_{i,j} = \psi_{i,j}\mu_t V_{i,j}, \tag{4.41}$$

where $V_{i,j}$ is the volume of the bin used to collect statistics and $\psi_{i,j}$ is the fluence. Similarly the number of photons emitted from the ith surface bin, N_i, is given by

$$N_i = R_i A_i, \tag{4.42}$$

where A_i is the area of the bin used to collect statistics and R_i is the diffuse reflectance. Hence, the weight deposited in an interior bin divided by the volume of the bin yields the fluence, while the reflectance is simply the weight deposited in a surface bin divided by the surface area of the bin.

4.6.1 Theoretical Tests of the oomc Algorithm

To test the OOMC algorithm, two configurations were prepared and simulations were compared with literature results. van de Hulst (1980) reports numerical results for total reflectance and transmittance for an index matched slab of albedo 0.9 and scattering anisotropy of 0.75 that is two interaction lengths in thickness. The average results of ten OOMC simulations with this configuration are collected in Table 4.1 along with those of other Monte Carlo results based on variance-reduction techniques which have been reported in the literature. Both the diffuse reflectance

Reference	Total Reflectance	Unscattered Transmittance	Total Transmittance
van de Hulst (1980)	0.09739	0.13534	0.66096
Prahl *et al.* (1989)	0.09711(33)	–	0.66159(49)
Wang and Jacques (1992)	0.09734(35)	–	0.66096(20)
OOMC	0.09733(49)	0.13542(47)	0.66030(74)

Table 4.1: A comparison of the OOMC algorithm with literature results. The average results of ten OOMC simulations of reflectance and transmittance for an index matched slab that is two interaction lengths thick are shown along with numerical results by van de Hulst and variance reduction Monte Carlo results of Wang and Jacques and Prahl *et al.*. The numbers in parentheses are the standard errors in the mean. The OOMC algorithm is in excellent agreement with the literature for this test configuration.

and total transmittance are in good agreement with the literature values. As expected, the standard deviation of the reflectance and transmittance were found to be in good agreement with the statistical uncertainty in these quantities. In addition, the unscattered transmittance, determined from the number of photons which had no interactions within the slab, was found to be in good agreement with the theoretical expectation for a slab two interaction lengths in thickness.

Simulations based on the configurations used by Giovanelli (1955) were conducted to verify the validity of the OOMC algorithm for a semi-infinite slab geometry with mismatched boundary conditions. In these simulations, an index mismatch of 1.5 and isotropic scattering were assumed as the albedo was varied from 0 (pure absorber) to 0.999. Figure 4.10 depicts the total diffuse reflectance as a function of the albedo. The points are the average result of three Monte Carlo simulations and the line is the result of Giovanelli (Giovanelli, 1955, see Table 5). For an albedo of zero, the reflectance is due entirely to specular reflection, while for increasing albedo, diffuse reflectance becomes the dominant component. Once again, the OOMC algorithm is in excellent agreement with the literature. While OOMC can be used to simulate light propagation in the vicinity of non-planar boundaries, analytic calculations for these configurations are extremely difficult. Consequently, a direct verification of more elaborate constructions is not yet possible.

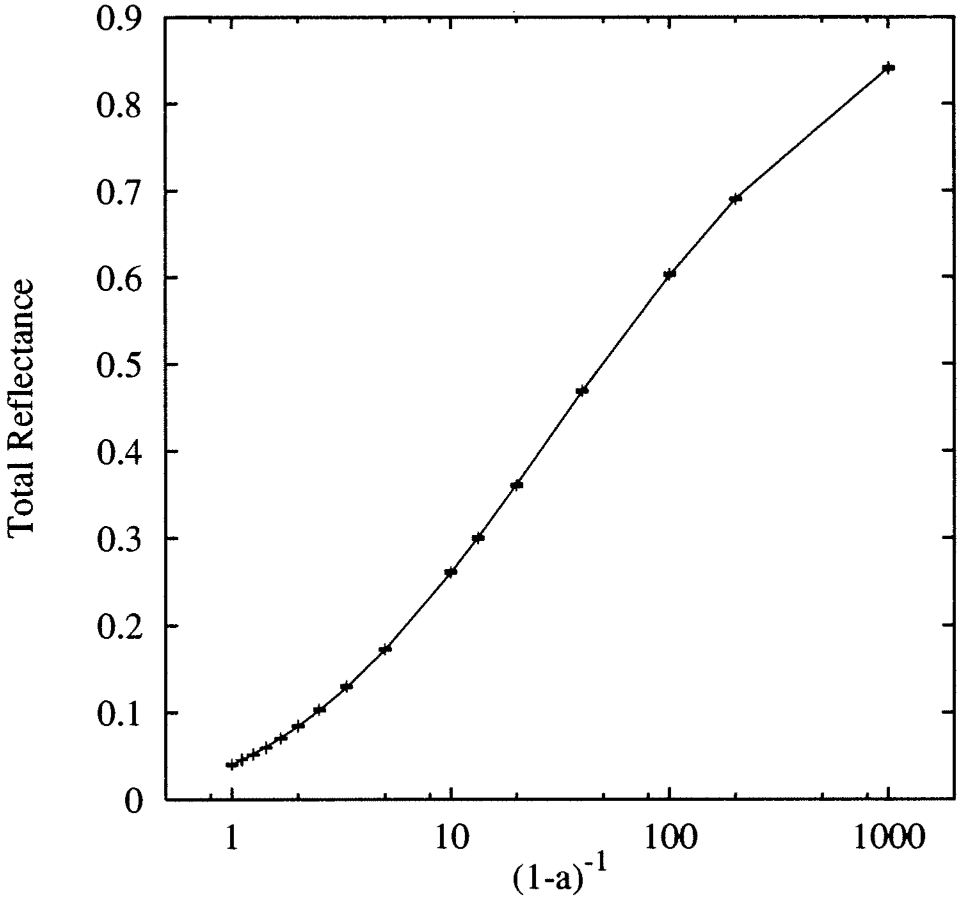

Figure 4.10: Simulation results of diffuse reflectance from a semi-infinite slab with an index mismatch of 1.5 assuming isotropic scattering. The data points represent the average of three Monte Carlo simulations and are plotted as a function of the albedo, a. The function $(1-a)^{-1}$ was chosen to scale the plot for best display. The line represents the results of Giovanelli (1955). The error bars are the standard deviation obtained from the three runs and are consistent with the statistical error of an individual simulation of 50,000 photons.

Chapter 5

Monte Carlo Evaluation of the Dipole Approximation and Exact Photo-Diffusion Expressions for the Diffuse Reflectance From a Planar Boundary

5.1 Introduction

The dipole approximation offers an attractive approach to modeling light transport in optically turbid media. The derivation of the diffuse reflectance based on this approximation is described in detail in Chapter 4. According to this solution, the shape of the spatially-resolved diffuse reflectance is characterized by the transport scattering coefficient, μ_s', and the absorption coefficient, μ_a, provided the internal reflection parameter, A, is known. For small distances from the incident beam (ρ on the order of a few transport mean free pathlengths) the magnitude of the diffuse reflectance is determined primarily by μ_s'. This is because the short optical pathlengths involved do not allow for appreciable absorption since $\mu_a \ll \mu_s'$. For large distances ($\rho \gg \mu_t'$) the radial reflectance curve is determined primarily by μ_{eff}. Since this parameter involves the product of the optical coefficients, it is not sufficient for a unique determination of μ_s' and μ_a. For these reasons, experimental data sets containing the diffuse reflectance measured at both small and large radial distances from the incident beam are required to uniquely separate the two optical coefficients.

A comparison of the diffuse reflectance expressions for the exact solution of the photo-diffusion equation (Equation (4.26)) and the dipole expression (Equation (4.33)) indicates the considerable simplification afforded by the approximation. However, it remains to be seen whether the dipole approximation can be used to accurately extract tissue optical properties from diffuse reflectance data. Farrell *et al.* (1992) originally derived the the dipole expression and demonstrated that the approximation was in excellent agreement with Monte Carlo diffuse reflectance. In comparing the two it was found that the residuals showed no systematic error for reflectance greater than 0.5 transport mean free paths (mfp′) from the beam. Furthermore, the approximate solution seemed to outperform the "extended source model" wherein a suitably weighted infinite line of fluence sources and their respective images was used instead of a single dipole pair. Since this model should be a more faithful representation of photo-diffusion from an irradiation beam, it appears that the non-diffuse nature of reflectance near the beam may be the reason for this counterintuitive result. Phantom studies indicated that the optical coefficients determined from reflectance measurements analyzed with the dipole expression was within 5 - 10% of that predicted by another technique, and the matched boundary condition provided better agreement with the data.

To reproduce and extend Farrell *et al.*'s results, in this chapter we present a thorough analysis of the predictive capabilities of the dipole expression. Monte Carlo simulations provide idealized diffuse reflectance data sets with known optical properties. By analyzing these data sets with an analytical model such as the dipole approximation, the predicted optical properties obtained from the fitting parameters can be directly compared with the optical properties that were used in the simulation. While Equation (4.26) or (4.33) can be used to analyze diffuse reflectance data, it is convenient to normalize the data to the diffuse reflectance measured at a known distance, ρ_{norm}, from the incident beam. We therefore fit the expression

$$R_{dn}(\rho) = \frac{R_d(\rho)}{R_d(\rho_{norm})} \tag{5.1}$$

to the experimental data. This eliminates the need for an arbitrary amplitude scaling parameter that would be dependent on such experimental details as the incident fluence rate and the characteristics of the detectors.

Equation (5.1) is fit to radially-resolved Monte Carlo diffuse reflectance data using a Levenberg-Marquardt non-linear least-squares fitting algorithm to obtain best-fit estimates of the optical properties μ_s' and μ_a (Press *et al.*, 1992). Neither expression is expected to accurately account for non-diffuse reflectance near the source, but, in general, the accuracy should improve as the distance between the source and the detected reflectance is increased. To determine the optimal minimum distance between a source and detector fiber for the experimental determination of the optical properties of small tissue volumes, the data sets are censored to exclude reflectance within a specified distance, ρ_{min}, from the source, and the accuracy of the estimated optical properties is obtained as a function of this distance. Finally, since the index of refraction for turbid biological media is typically close to 1.4, index-mismatched boundary conditions are examined in addition to index-matched.

5.2 Index-Matched Boundary Conditions

Figure 5.1 illustrates the absorption and transport scattering coefficients obtained from a dipole fit to Monte Carlo diffuse reflectance data generated by OOMC using matched boundary conditions and values of 10.00 mm^{-1}, 0.01 mm^{-1} and 0.9 for μ_s, μ_a and g, respectively. Eleven different fits of the Monte Carlo data were performed. In these fits, the minimum source-detector separation was varied from 0.27 mm to 4.2 mm. The maximum source-detector separation for each fit was approximately 20 mm. Fitting to data sets containing the smallest source-detector separations resulted in the greatest error in both the absorption and transport scattering coefficients. The returned absorption coefficient is systematically lower than the actual value used in the Monte Carlo simulation, and the transport scattering coefficient is returned systematically high. It is probable that diffusion theory is unable to account for the non-diffuse component of the reflectance that is encountered for these small source-detector separations. As the minimum source-detector separation (ρ_{min}) is increased, the fractional error in the returned optical properties rapidly decreases, reaching a minimum near zero for $\rho_{min} = 0.75$ mm (0.75 mfp′) where the two curves cross. For minimum source-detector separations from 1 mm to 3 mm (1.0 to 3.0 mfp′), the error in the returned optical properties is relatively constant and much smaller than the error encountered with the smallest source-detector separations. For this range of ρ_{min}, the transport scattering coefficient is consistently underestimated by approximately 8% and the absorption coefficient overestimated by approximately 13%. The symmetry in the curves of the returned optical properties indicates that these errors are highly correlated; when the returned transport scattering coefficient is underestimated, the absorption coefficient is overestimated so that the overall estimate for μ_{eff} is preserved. Plots similar to the one shown in Figure 5.1 were created for Monte Carlo simulations conducted over a wide range of transport scattering coefficients. Each plot of the returned optical properties was similar in structure to Figure 5.1. In each case, the curves representing the returned values of μ_s' and μ_a crossed near a value of zero at a minimum source-detector separation of approximately 0.75 - 1.0 mfp′.

It is important to note that increasing the minimum source-detector separation (ρ_{min}) results in correspondingly larger uncertainty in the estimation of the trans-

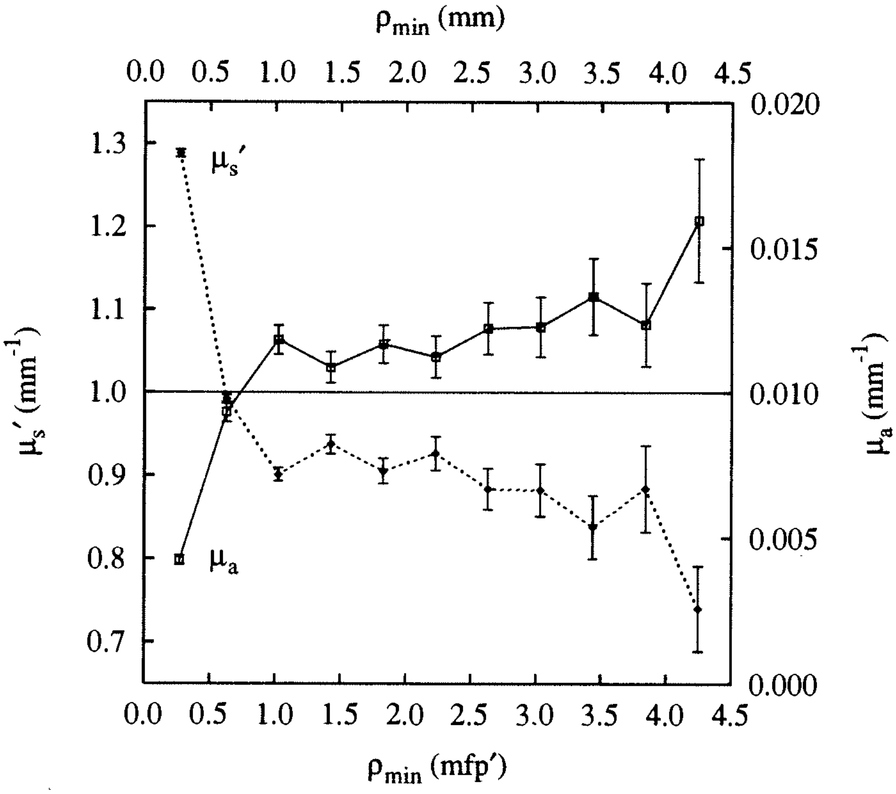

Figure 5.1: The transport scattering coefficient, μ_s' (solid diamonds), and absorption coefficient, μ_a (open squares), estimated by fitting Monte Carlo radially-resolved diffuse reflectance data. Simulations were conducted in a semi-infinite turbid medium with matched boundary conditions and optical properties of $\mu_s = 10.0$ mm^{-1}, $\mu_a = 0.01$ mm^{-1} and $g = 0.90$. Eleven dipole fits were made to the same Monte Carlo data while the radial distance between the source and the first included Monte Carlo data point (ρ_{min}) was varied from 0.27 mm to 4.2 mm. The error bars represent the standard deviation of the fitted values obtained from using the statistical error associated with each diffuse reflectance data point as a measure of its uncertainty.

port scattering coefficient and increased coupling between the returned absorption and scattering coefficients. While the values returned for the optical coefficients in Figure 5.1 are relatively constant for ρ_{min} between 1.0 and 3.0 mm, the uncertainties increase with increasing ρ_{min} since the effects of absorption on the diffuse reflectance become increasingly significant as the distance from the source increases. If all of the detectors are situated at radial distances from the source where absorption is significant, the ability to independently obtain μ_s' is impaired, resulting in poor discrimination between μ_a and μ_s'.

This can also be seen in Figure 5.2 wherein the same data set was fit with the exact reflectance expression. As in the case of the dipole approximation, using a minimum source detector separation that is less than a mean free path results in a systematic error in the returned optical properties. It is interesting to note that for matched boundary conditions the dipole approximation appears to be a better predictor of the true optical properties when small source detector separations are used. However, if the data set contains reflectance starting at several transport mean free paths from the source, the exact expression is the more reliable predictor, although in this case the uncertainty in the estimation is larger for the exact solution due to the more complicated dependency on the optical properties.

Figure 5.3 indicates the returned χ_ν^2 goodness of fit statistic for fits obtained with the minimum source-detector separations shown in Figures 5.1 and 5.2. The dipole fits for data sets with a minimum source-detector separation less than approximately 0.75 - 1.0 transport mean free paths were poor due to the presence of non-diffuse reflectance emitted from the surface near the source fiber. Censoring

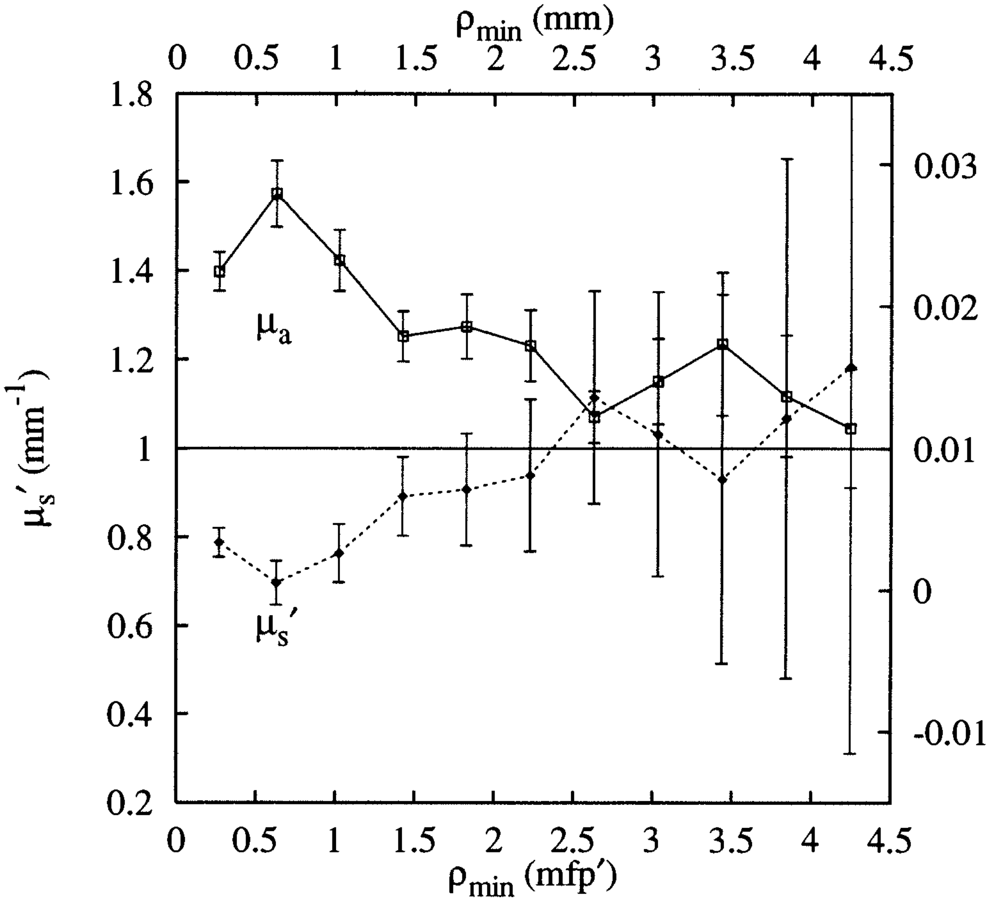

Figure 5.2: The optical coefficients μ_s' (solid diamonds) and μ_a (open squares) estimated by fitting Monte Carlo diffuse reflectance data sets that have been censored to various degree to exclude reflectance near the source. The analysis is the same as described in Figure 5.1, but the exact expression for the diffuse reflectance from a semi-infinite medium, Equation (4.26), was used as the merit function for the non-linear least-squares fit.

Monte Carlo data obtained at points within this distance resulted in a significantly better fit. This is in accordance with the findings of Farrell *et al.* (1992) who reported that the residuals were well-distributed for source-detector separations larger than approximately 0.5 transport mean free paths. The exact fits have a better χ_ν^2 near the source, though a systematic error is still present. Like the dipole fits, the exact fits improve with increasing minimum source-detector separation, but the improvement is more gradual.

The agreement between the absorption coefficients used in Monte Carlo simulations and those returned from fits of the two fitting expressions are illustrated in Figure 5.4. While the absorption coefficient was varied over approximately 4 orders of magnitude, the transport scattering coefficient was fixed at 1.50 mm^{-1} for each of these simulations. The minimum source-detector separation used in fitting the data was 1.0 mm, which is comparable to one transport mean free path and is the minimum source-detector separation available in our current experimental probe (Chapter 6). The dipole approximation clearly results in a better prediction of the true absorption coefficient under these conditions. The smallest absorption coefficient used in the Monte Carlo simulations was 0.0001 mm^{-1}. For this simulation, the fitted value from the dipole model was overestimated by approximately 63%, with a returned standard deviation of 58%. This may be an indication of the lowest absorption coefficient measurable with this probe. For a given detection probe the smallest value of μ_a that can be measured is dependent on the largest available source-detector separation (See Section 8.3). Excellent results were obtained for absorption coefficients ranging from 0.0005 mm^{-1} to 0.0025

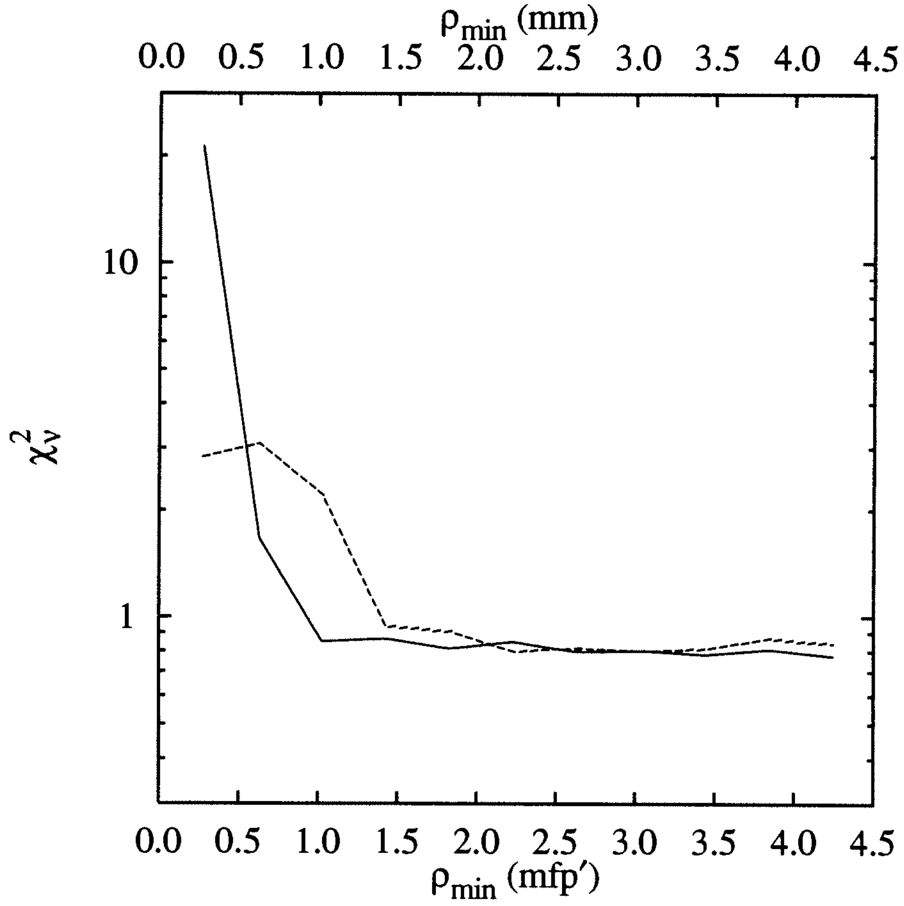

Figure 5.3: The χ^2_ν goodness of fit parameter for the fits shown in Figures 5.1 and 5.2. The solid and dashed lines are the results for reflectance fits obtained using the dipole expression and the exact photo-diffusion expression, respectively. The data corresponds to the fits described in Figures 5.1 and 5.2.

mm^{-1}, corresponding to transport albedos ranging from 0.9997 to 0.9983. In this region, the returned value for μ_a is consistently within 10% of the actual value. For more highly absorbing materials the measured absorption coefficient is more significantly overestimated, although in this range the transport albedo begins to reach values that are sufficiently low that the validity of diffusion theory itself is questionable. For example, the transport albedo corresponding to the simulation with the greatest absorption coefficient is 0.75.

In contrast to the dipole model, the fit results acquired with the exact reflectance expression are far less accurate. As expected from Figure 5.2, the returned absorption coefficients are systematically high when a minimum source-detector separation of 1 mfp′ is used. For values ranging from 0.0025 mm^{-1} to 0.5 mm^{-1} the returned absorption coefficient is overestimated by 100%. Another interesting result is the lack of sensitivity to small absorption coefficients. It appears that absorption coefficients less than 0.001 mm^{-1} cannot be accurately predicted. This was not seen when the same data sets were analyzed with the dipole model.

Figure 5.5 indicates that the transport scattering coefficients obtained from the two models are very similar. They are typically underestimated by approximately 7%, with more substantial inaccuracy associated with the highly absorbing materials for which the transport albedo is quite low. The dipole fit estimates are slightly better than the exact fit estimates at the highest absorption coefficients simulated, but these high values will rarely be encountered in biological tissues *in vivo*.

A second series of Monte Carlo simulations was conducted to determine how

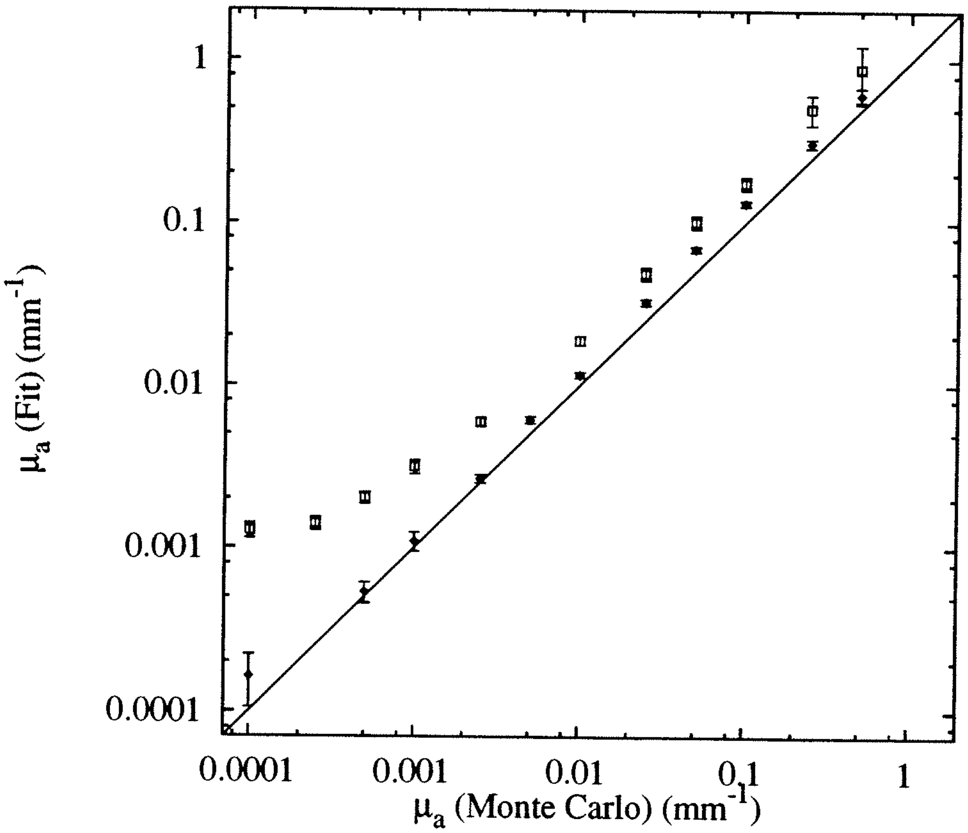

Figure 5.4: The absorption coefficients determined from dipole fits (closed diamonds) and fits using the exact diffusion theory reflectance expression (open squares) are plotted as a function of the actual absorption coefficient used in the Monte Carlo simulations (line). In the simulations, the absorption coefficients were varied from 0.0001 mm^{-1} to 0.5 mm^{-1} while the transport scattering coefficients were held constant at 1.5 mm^{-1}. The minimum source-detector separation was held constant at 1.0 mm in all the simulations. The transport albedo ranges from 0.9999 ($\mu_a = 0.0001$ mm^{-1}) to 0.75 ($\mu_a = 0.5$ mm^{-1})

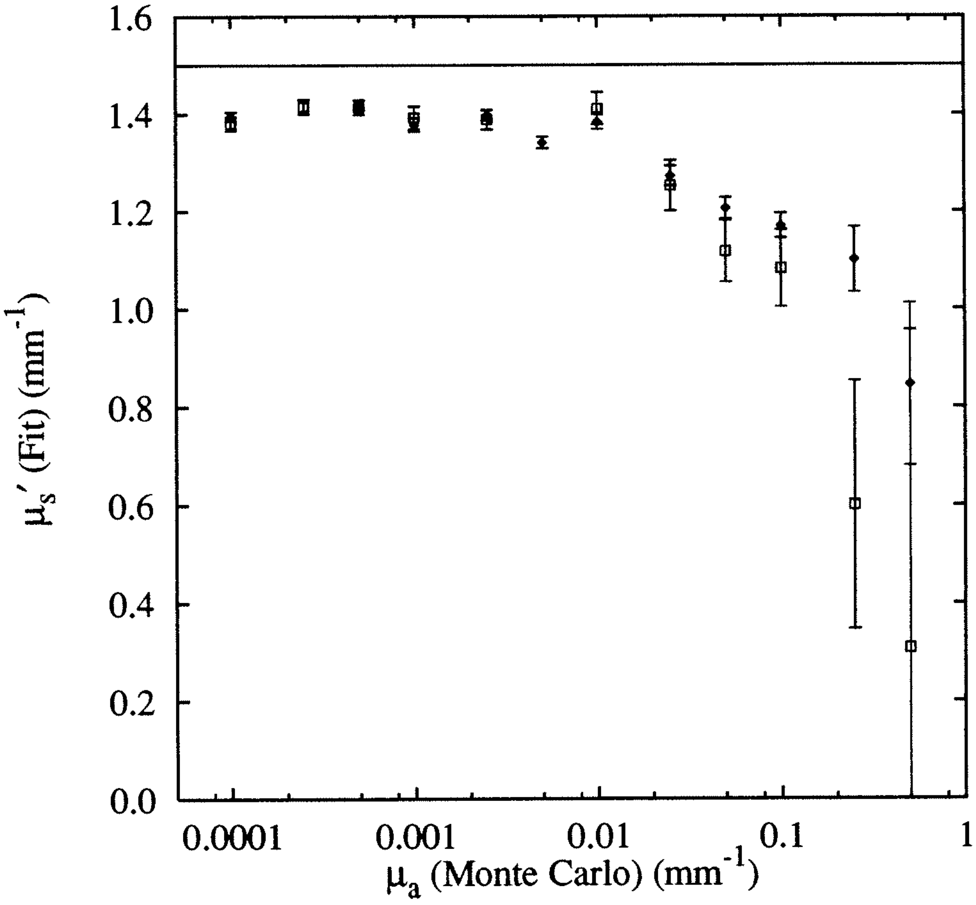

Figure 5.5: The transport scattering coefficients determined from dipole (closed diamonds) and exact diffusion theory fits (open squares) of the reflectance data described in Figure 5.4. The horizontal line indicates the true transport scattering coefficient used in the Monte Carlo simulations.

the accuracy of the fits depends on the scattering coefficient of the medium. In these simulations the absorption coefficient was held constant at 0.01 mm^{-1} while the transport scattering coefficient was varied from 0.5 to 2.25 mm^{-1}. ρ_{min} was 1.0 mm in all of the simulations. Figure 5.6 illustrates the agreement between the absorption coefficient used in the Monte Carlo calculations and that returned by the fitting algorithm when either of the two models is used to analyze these data sets. Again the dipole model provides the best agreement, typically estimating the absorption coefficient to within 10% of the true value. This appears to be true for all but the lowest of albedos tested, and no definite trends are observed with the transport scattering coefficient. The exact expression for the diffuse reflectance provides much less reliable results than the dipole expression, but improves as the scattering coefficient is increased. This is reasonable considering that the diffusion approximation is best justified for albedos approaching unity. Figure 5.7 indicates that the scattering coefficient is typically underestimated by approximately 10% when obtained from a dipole fit, while this error is somewhat improved for scattering coefficients less than approximately 1 mm^{-1}. The results for the exact fit seem to follow a slight quadratic relationship rather than a linear one.

5.3 Index-Mismatched Boundary Conditions

When the index of refraction of the turbid medium is assigned a biologically realistic value, it is anticipated that diffusion theory should be better justified. This is because the mismatch in the index of refraction should result in an increase

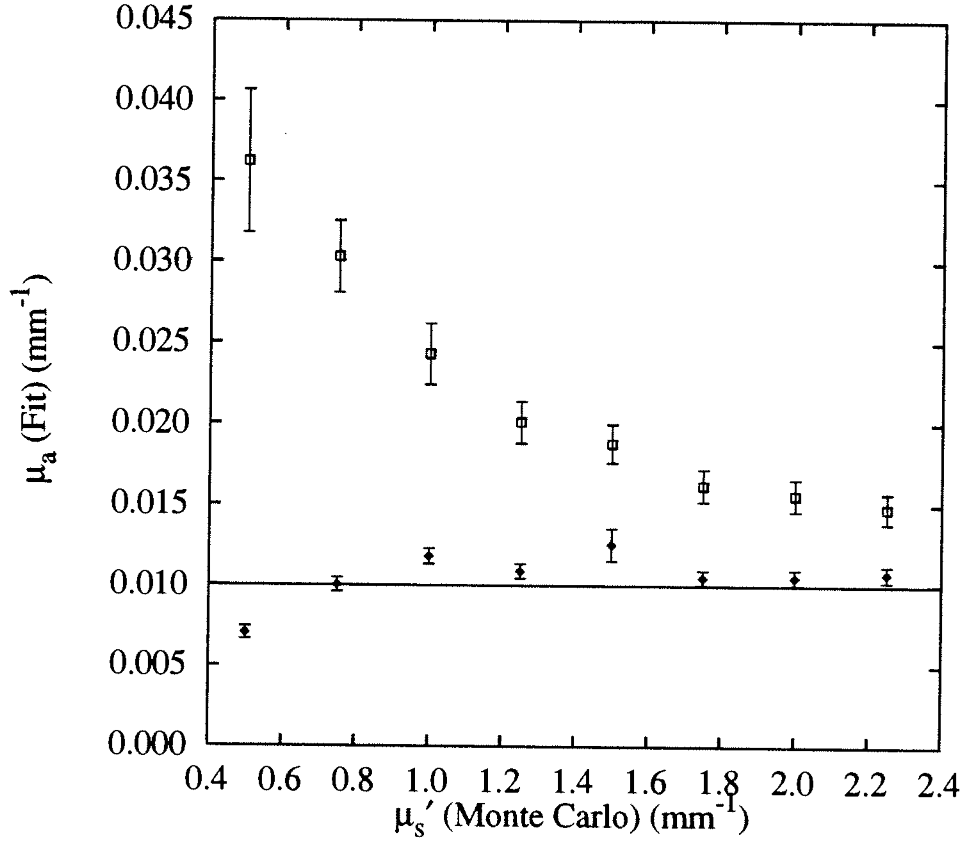

Figure 5.6: The absorption coefficients estimated by dipole fits (solid diamonds) and fits using the exact reflectance expression (open squares) are plotted as a function of the actual scattering coefficients used in the Monte Carlo simulations (line). In the simulations, the absorption coefficients were held constant at 0.01 mm^{-1} while the transport scattering coefficients were varied from 0.5 mm^{-1} to 2.25 mm^{-1}. The minimum source-detector separation was held constant at 1.0 mm. The transport albedo ranges from 0.980 ($\mu_s' = 0.5$ mm^{-1}) to 0.996 ($\mu_s' =$ 2.25 mm^{-1}).

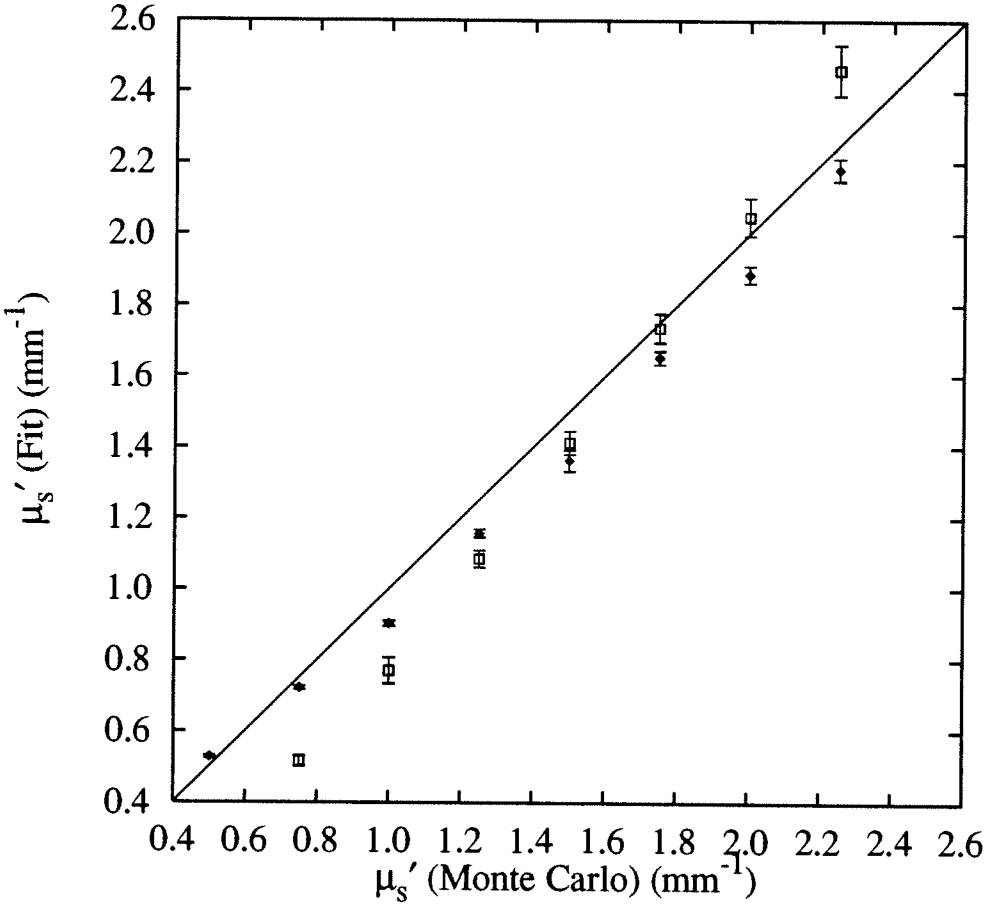

Figure 5.7: The scattering coefficients estimated by dipole fits (solid diamonds) and fits using the exact reflectance expression (open squares) to analyze Monte Carlo diffuse reflectance are compared to the true value (line). The optical properties used in the simulations are described in Figure 5.6.

in the fluence near the boundary due to internal reflection and consequently reduce the ratio of the diffuse flux to the fluence as dictated by the partial-current boundary condition. However, the dipole approximation, which is based on the extrapolated boundary condition, has been shown (Chapter 4) to deviate from the partial-current boundary condition more substantially under index-mismatched conditions. In particular, the ratio of the fluence to the flux at the boundary does not increase linearly with the internal reflection parameter, A. To get a better understanding of the effect these factors have on the estimated optical properties, Monte Carlo simulations were conducted using a planar semi-infinite turbid medium as described in Section 5.2, but under various index-mismatched boundary conditions. The index-mismatch is expressed in both model solutions in terms of the internal reflection parameter described in detail in Chapter 4. Previously Groenhuis *et al.* (1983b) have derived an empirical relationship connecting the degree of the mismatch with this parameter. This was expressed in terms of the following relationship:

$$A = \frac{1 + r_d}{1 - r_d}, \tag{5.2}$$

where

$$r_d = -\frac{1.44}{n^2} + \frac{0.71}{n} + 0.668 + 0.0636n \tag{5.3}$$

and n is the ratio of the index of refraction of the turbid medium to that of the surrounding medium. Farrell *et al.* (1992) have indicated that this relationship provides the best agreement with Monte Carlo though systematic errors were observed. For both model solutions, A does not appear to be a worthwhile fitting parameter, so Equations (5.2) and (5.3) were used to obtain values of A appropriate for the indices of refraction used in the Monte Carlo simulations.

Figures 5.8 and 5.9 illustrate the dependence of the estimated optical properties on the minimum source-detector separation used in the analysis. Either the dipole or the exact photo-diffusion reflectance expressions were used to analyze the data. While the analysis based on the exact expression is virtually identical to that obtained under index-matched conditions (Figure 5.2), the mismatch is seen to have a significantly deleterious effect on the optical properties estimated by the dipole fit. Two trends are apparent in Figure 5.8. First, the minimum distance at which the two curves cross has been moved out to ≈ 1.75 mfp$'$, one mfp$'$ further than was observed under index-matched conditions. Second, the disagreement between the returned and actual optical properties is much more significant with the index-mismatch. For ρ_{min} greater than two mfp$'$ the scattering coefficient is overestimated by approximately 40% while the absorption coefficient is systematically underestimated by an equal margin. This differs from the index-matched scenario where the optically properties were seen to differ by no more than 20%. In addition, the goodness of fit is much worse for the dipole model with a mismatched boundary condition than with a matched boundary condition.

Previously, it was shown that adjusting A had a diminished effect on the true extrapolation distance (Chapter 4). While the location where the fluence rate is set to zero moves away from the boundary linearly with increasing A, the actual distance to where the fluence rate extrapolates to zero has a much weaker dependence. Furthermore, excellent results were obtained when index-matched data

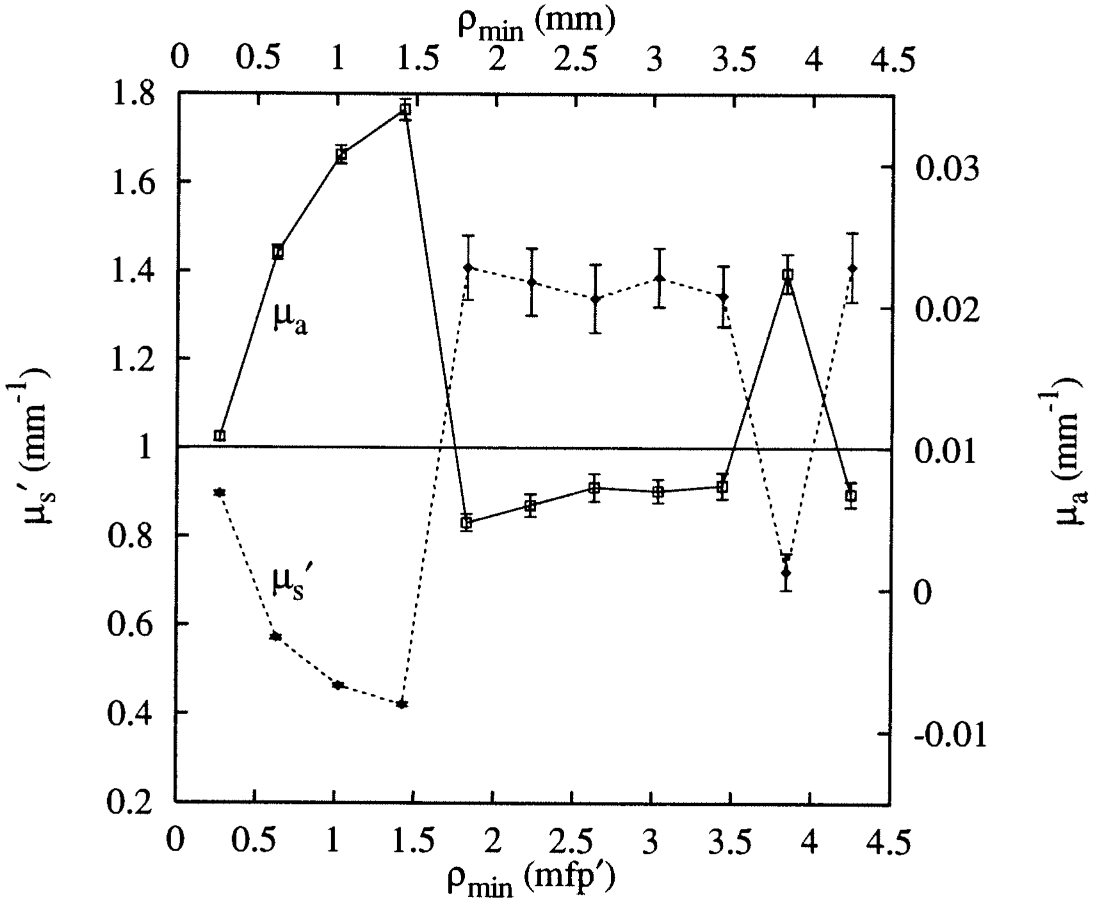

Figure 5.8: The optical coefficients μ_s' (solid diamonds) and μ_a (open squares) estimated by fitting index-mismatched Monte Carlo diffuse reflectance data generated as described in Figure 5.1, but with an index-mismatch of 1.4 at the air/medium boundary. The points reflect the results of several dipole fits with the scattering and absorption coefficients used as fitting parameters while the internal reflection coefficient, A, is held constant at 3.25, as specified by Equation (5.2).

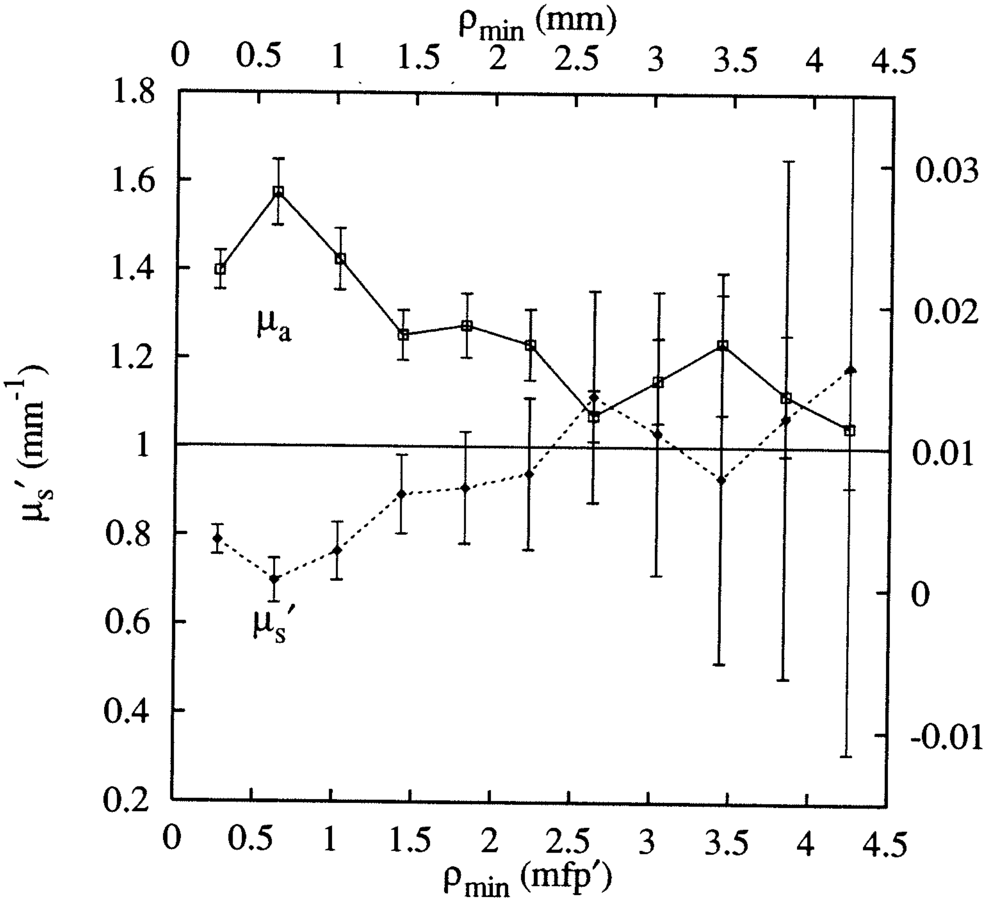

Figure 5.9: The optical coefficients μ_s' (solid diamonds) and μ_a (open squares) estimated by fitting the index-mismatched Monte Carlo diffuse reflectance data described in Figure 5.8. The data reflect the results of several fits using the exact photo-diffusion reflectance expression with the scattering and absorption coefficients used as fitting parameters while the internal reflection coefficient, A, is held constant at 3.25.

sets were analyzed using $A = 1$. To see if better results could be obtained with the dipole solution, fits were done holding this parameter constant at 1.0, 1.25 and 1.75. The resulting variation in the optical properties reported from the fit is given as a function of the minimum source-detector separation, ρ_{min}, in Figures 5.10 - 5.12. The goodness of fit for these values of A, as well as the correct value of 3.25, is depicted in Figure 5.13. It is evident that the dipole fits conducted with erroneously low values of A provide a better representation of the Monte Carlo data sets for all values of ρ_{min}. In contrast, the exact expression better describes the reflectance near the source. At a quarter of a mfp′, χ^2/ν is a factor of ten lower than any of the dipole fits, although again, the exact fits improve more gradually with increasing source detector separation than do the dipole fits with small A. For larger A, the exact reflectance expression produces a much better fit to the data. As for the dipole model's predictive capability using erroneously small values of A, it is clear that the mismatch noticeably impacts the determination of both optical coefficients. As A is increased from 1 to 1.75, the returned optical properties for large ρ_{min} ($>$ 2 mfp′) move closer to the true optical properties, while introducing a much larger discrepancy for smaller ρ_{min}. The fact that the small value of $A = 1.75$ produces both a better fit and a better agreement with the true optical properties suggests that this parameter does not play the same role in the dipole model as it does for the exact diffusion model. This is evidenced by its diminished role in manipulating the extrapolation length.

Since the diffusion approximation is premised on the assumption that the fluence rate is much larger than the diffusive flux, it is anticipated that the predictive

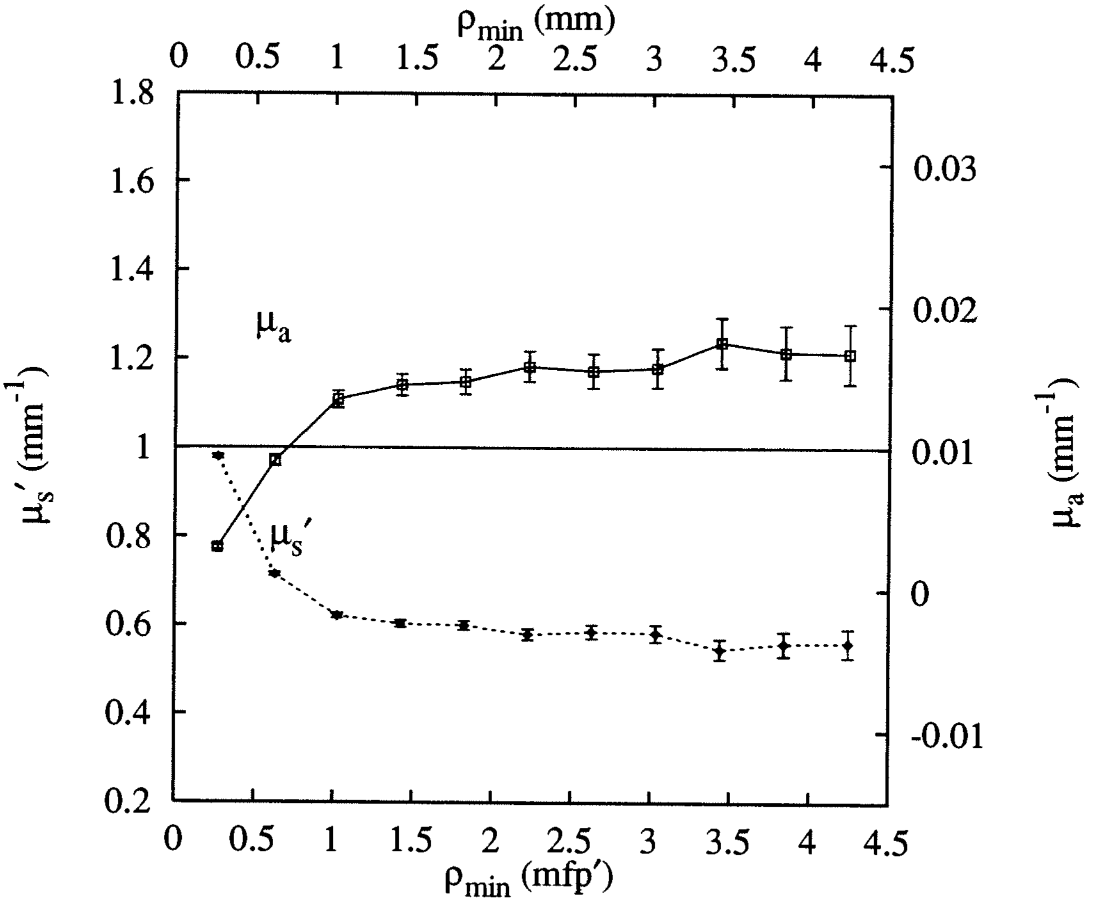

Figure 5.10: The optical coefficients μ_s' (solid diamonds) and μ_a (open squares) estimated by fitting index-mismatched Monte Carlo diffuse reflectance data described in Figure 5.8. As in that figure, the points reflect the results of several two-parameter dipole fits, with the internal reflection coefficient, A, held constant at a low value of 1.0.

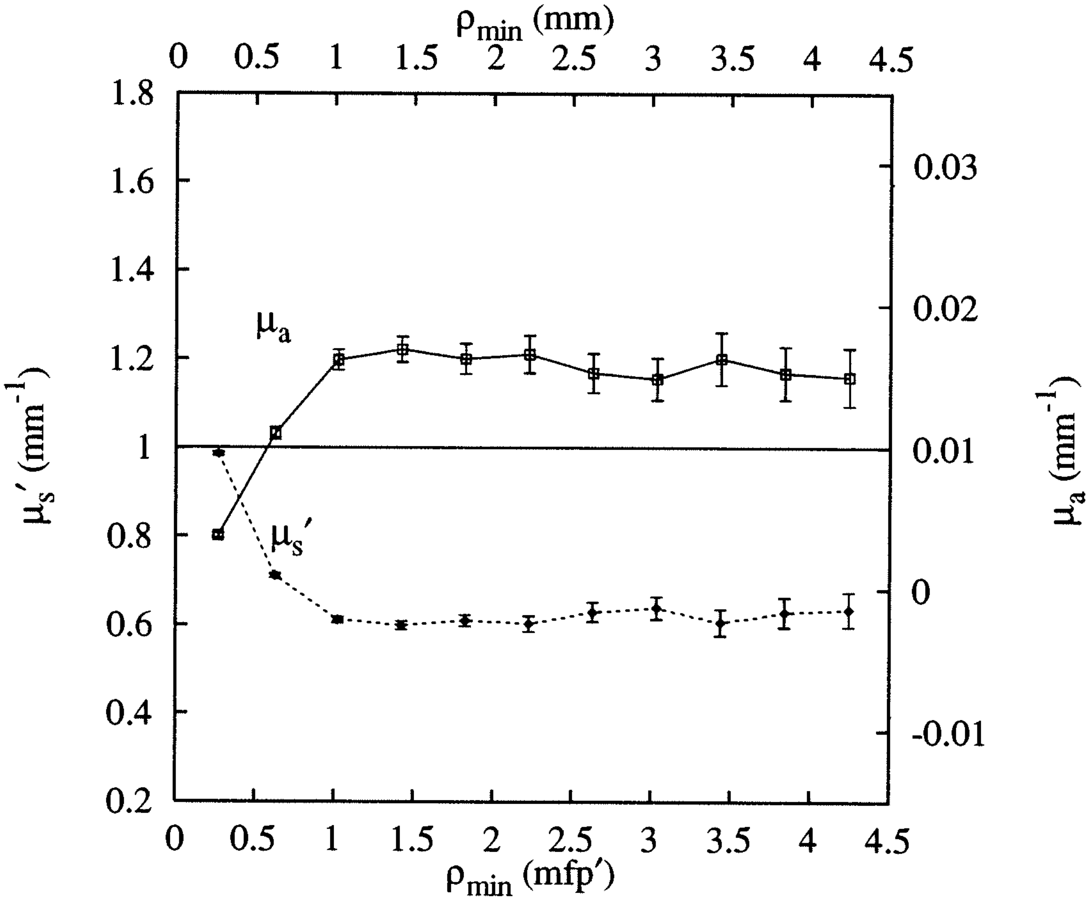

Figure 5.11: The optical coefficients μ_s' (solid diamonds) and μ_a (open squares) estimated by fitting index-mismatched Monte Carlo diffuse reflectance data described in Figure 5.8. As in that figure, the points reflect the results of several two-parameter dipole fits, with the internal reflection coefficient, A, held constant at a low value of 1.25.

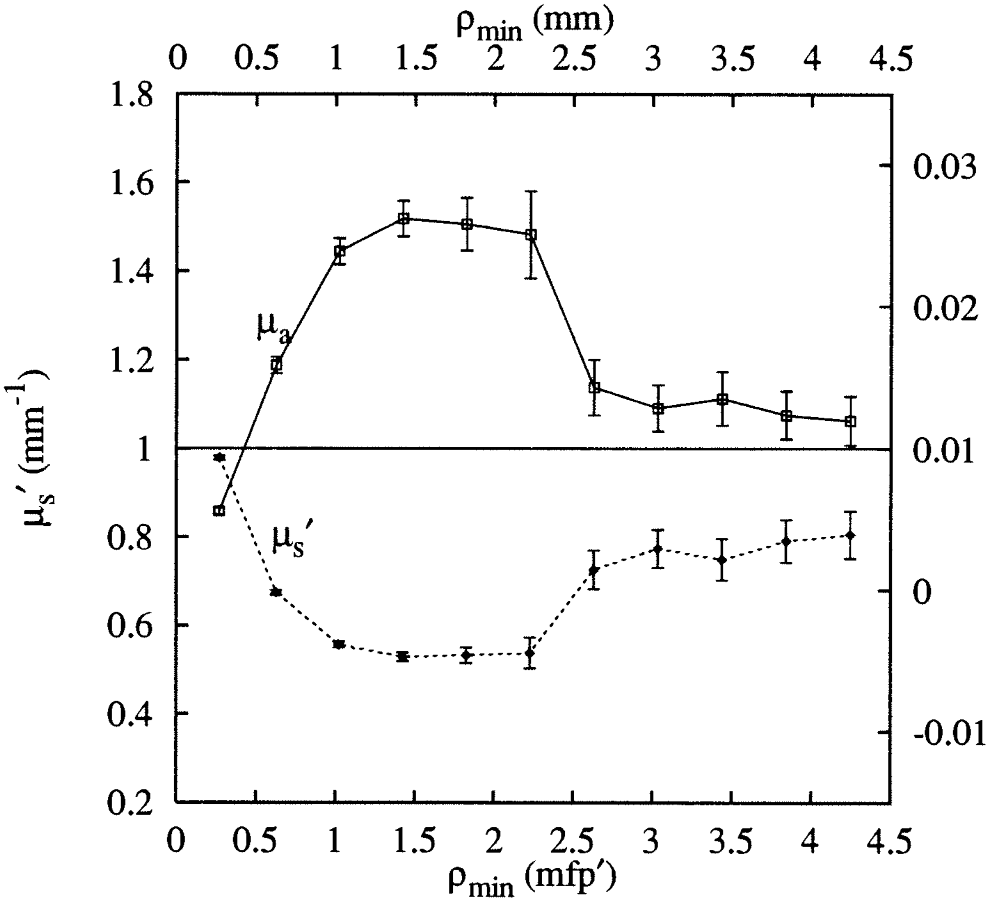

Figure 5.12: The optical coefficients μ_s' (solid diamonds) and μ_a (open squares) estimated by fitting index-mismatched Monte Carlo diffuse reflectance data described in Figure 5.1. As in that figure, the points reflect the results of several two-parameter dipole fits, with the internal reflection coefficient, A, held constant at a low value of 1.75.

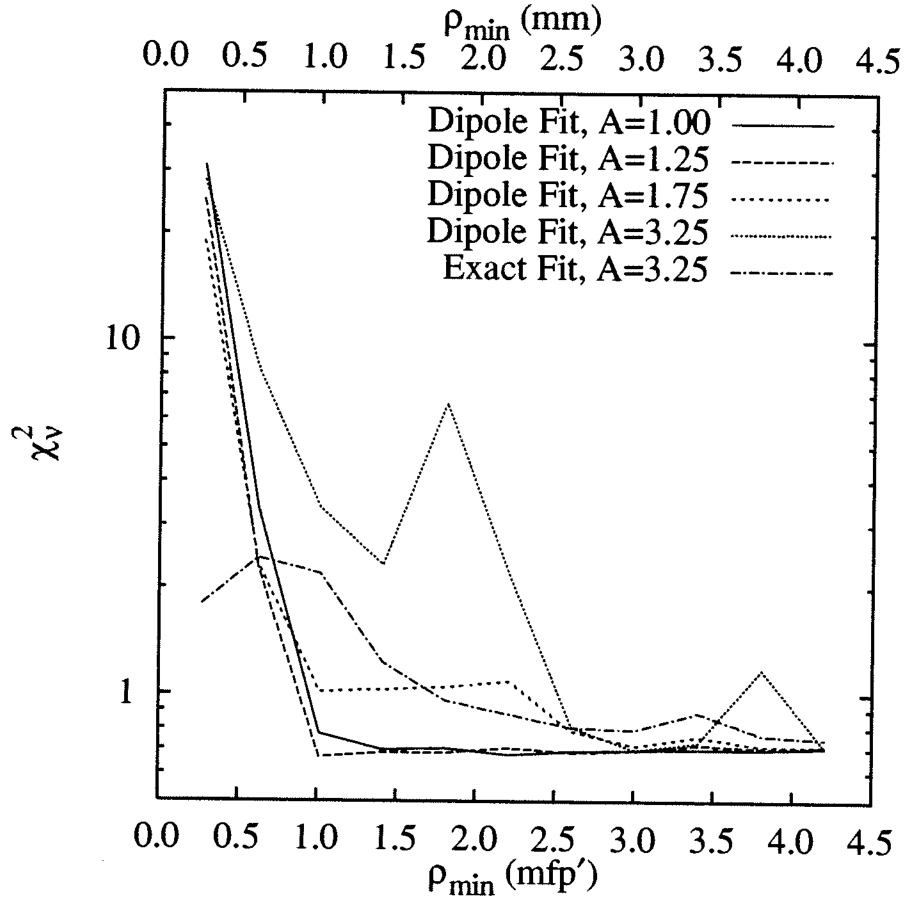

Figure 5.13: The χ^2/ν goodness of fit parameter corresponding to fits of index-mismatched Monte Carlo data described in Figures 5.8 - 5.12. The various lines give the dependence of the quality of fit on the minimum source detector separation, ρ_{min}. To optimize the fit, the internal reflectance parameter, A, was varied from 1 to 3.25, which should be the correct value. The best fits are obtained with erroneously low values of A, however. The results are compared with the quality of fit obtained using the exact reflectance expression as the merit function.

power of diffusion theory should improve as the index mismatch at the boundary of the turbid medium increases. A larger mismatch would result in more internal reflection at the boundary which would increase the fluence rate relative to the flux. In fact, since A increases approximately as the third or forth power of the index-mismatch, the ratio of the fluence rate to the flux at the boundary increases substantially with the index of refraction.

Figures 5.14 and 5.15 indicate that the predictive powers of the dipole approximation progressively worsen as the index-mismatch increases from 1 to 2, while the predictions based on the exact diffusion theory do, in fact, improve. The fits in these figures were obtained using a minimum source detector separation of 1 mfp$'$, which was previously seen to be sub-optimum for the exact diffusion theory model. As the index of refraction increases the goodness of fit also improves slightly for the exact expression when using Equation (5.2) to determine the proper value for the internal reflection parameter. This indicates that this parameter appears to be serving its function in the exact expression. Unfortunately, the increased reflectivity expected for biological tissues with an index of refraction of approximately 1.4 does not seem to have a strong effect on the returned optical properties when such short source-detector separations are used.

The results for the dipole approximation indicate the inability of this expression to properly account for changes in diffuse reflectance due to internal reflections at the interface. This is most obvious in the scattering coefficient, which progressively worsens as the mismatch increases; the estimated value for the absorption coefficient also exhibits a pronounced dependence on the index-mismatch. Once

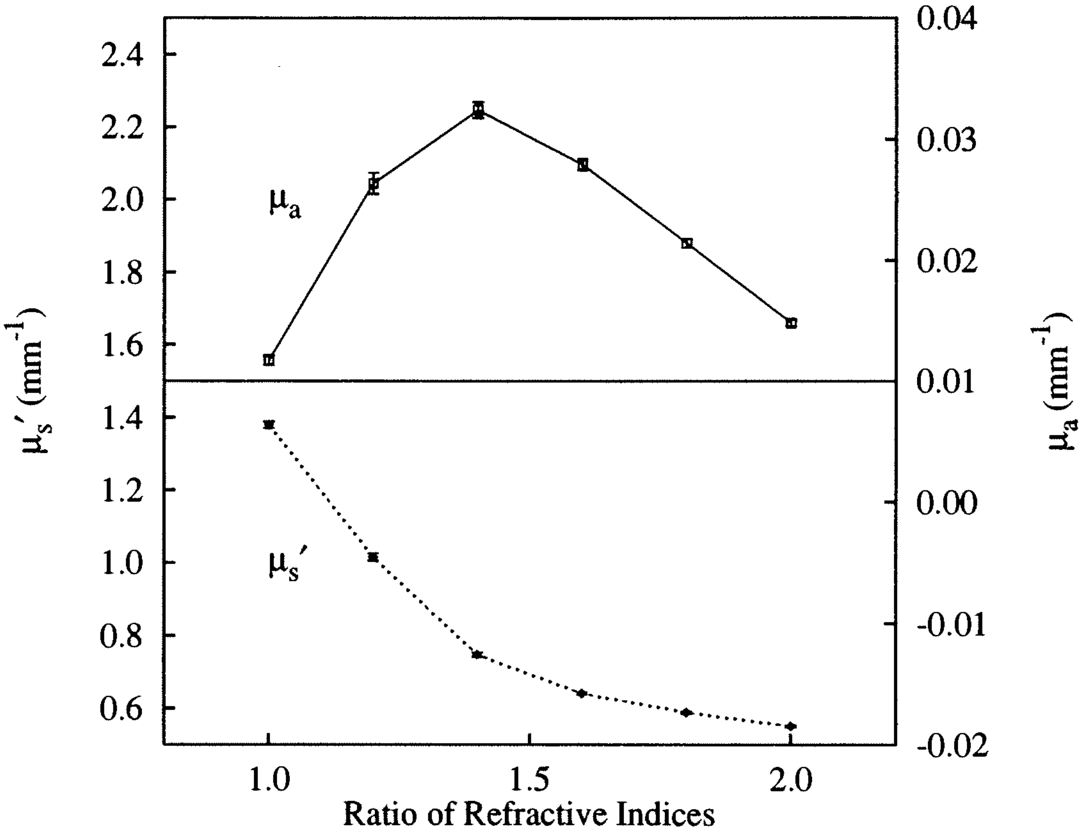

Figure 5.14: The optical coefficients μ_s' (solid diamonds) and μ_a (open squares) estimated by fitting index-mismatched Monte Carlo diffuse reflectance data with the dipole reflectance expression. The value of the internal reflection parameter, A, was determined by Equation (5.2) for each fit according to the index of refraction used in the Monte Carlo simulation. The minimum source-detector separation was approximately 1 mfp′ for each fit.

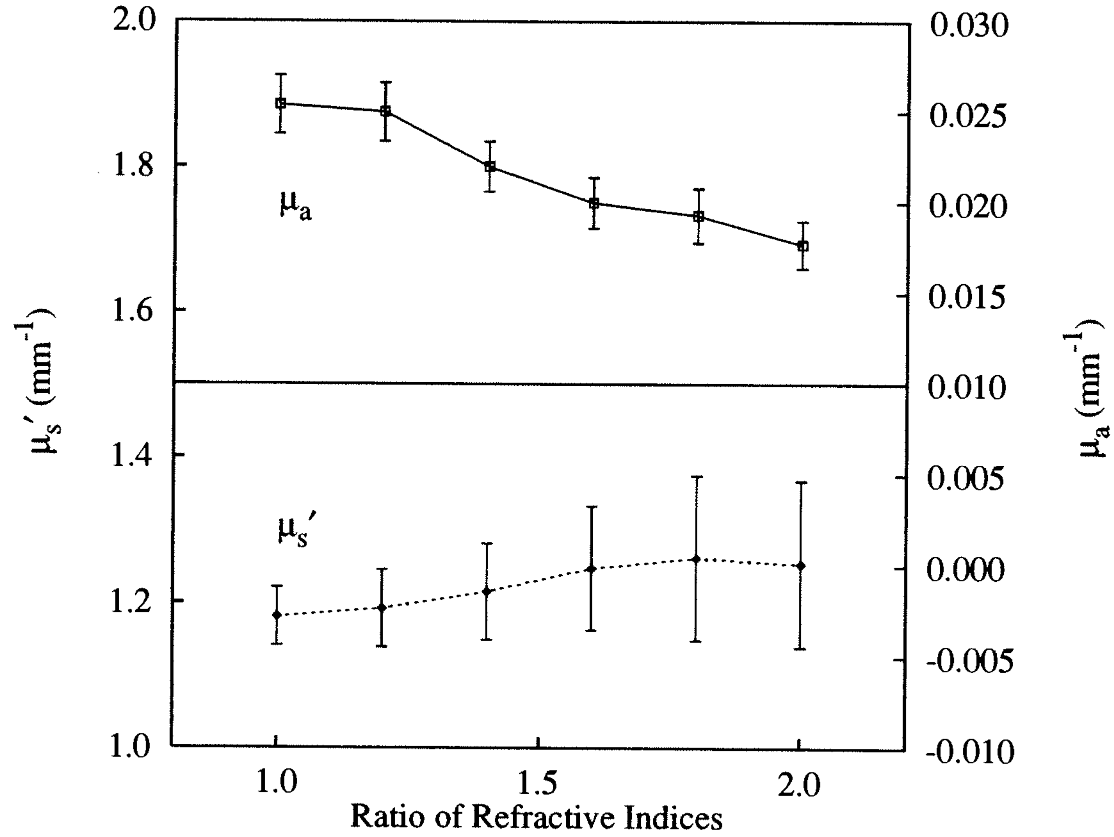

Figure 5.15: The optical coefficients μ_s' (solid diamonds) and μ_a (open squares) estimated by fitting index-mismatched Monte Carlo diffuse reflectance data with the exact photo-diffusion reflectance expression. The value of the internal reflection parameter, A, was determined by Equation (5.2) for each fit according to the index of refraction used in the Monte Carlo simulation. The minimum source-detector separation was approximately 1 mfp$'$ for each fit.

again, Equation (5.2) was used to determine the proper value of A to use in the fits. In addition to the observed dependence of the estimated optical properties on the index of refraction, the quality of the dipole fits progressively worsened as well. While χ^2/ν was less than 1 for index-matched boundary conditions, this increased to over 21 when a mismatch of 2 was used. The disagreement occurs most notably in the reflectance near the source. As ρ_{min} is increased to greater than 2 mfp′ the optical properties are still seen to be highly dependent on the index-mismatch, but χ^2/ν doesn't exceed 2.5.

5.4 Conclusions

Fitting model expressions for the diffuse reflectance emitted from a semi-infinite turbid medium to Monte Carlo reflectance data sets allows one to test the ramifications of certain model assumptions on an idealized system. Monte Carlo simulations provide a direct analog to optical transport in turbid media, so the analysis described in this chapter should be applicable to biological tissue provided the geometrical configuration is appropriate.

We have fit the dipole and exact diffusion theory expressions for the radially-resolved diffuse reflectance to Monte Carlo simulated data sets obtained with typical values of the visible and near-infrared optical properties of tissues. In either case, μ_s' and μ_a were used as fitting parameters and the statistical error associated with each diffuse reflectance point was used as a measure of the uncertainty. Both the quality of fit and the accuracy of the optical properties returned by the fitting algorithms were investigated. Since neither expression was expected to accurately model the non-diffuse reflectance near the incident beam, these characteristics were obtained as a function of the minimum source-detector separation used in the data set.

It is clear that the dipole approximation results in a reliable fitting function when index-matched conditions exist. In order to take full advantage of the approximation experimentally, care must be taken to measure reflectance near and far from the source to extract sufficient information to uniquely determine μ_a and μ_s'. Optimally, the first detection fiber should be situated at a radial distance approximately 0.75 - 1.0 mfp′ from the source, while more remote fibers should sample diffuse reflectance as far away as measurement sensitivity requires. Monte Carlo analysis indicates that the absorption coefficients obtained from an optimal diffuse reflectance measurement will generally be correct to within 10-13%, while transport scattering coefficients obtained from these measurements will be correct to within 5-8%, provided the transport albedo is sufficiently high.

While the dipole expression results from an approximation, it is a better predictor of optical properties than the exact diffusion theory expression when reflectance data near the source is analyzed. The exact expression actually fits the data better, but the estimated optical properties are less accurate; the absorption coefficient is overestimated by a factor of two and the fits are insensitive to absorption coefficients less than 0.001 mm^{-1}. Censoring data within 2 mfp′ of the source results in estimations comparable to that made by the dipole model, but the estimated uncertainty in the predictions is significantly larger.

The dipole model is less accurate in modeling diffuse reflectance from an index-mismatched boundary, however. When Monte Carlo simulations were conducted with various mismatches in the index of refraction, both the quality of the dipole fits and the accuracy of the predictions decreased significantly with increasing mismatch. This is likely to be a direct consequence of the approximate extrapolated boundary condition used by the model, as discussed in Chapter 4. Unlike the dipole expression, both the quality of fit and the accuracy of the exact reflectance expression improved with increased mismatch, as expected for diffusion theory.

It has been our experience that matched boundary conditions can be assumed when using a flat black detection probe placed in contact with the turbid medium, as suggested initially by Farrell *et al.*. It is likely, however, that mismatched boundary conditions may also arise. One such example would be when optical fibers are placed on the surface of a tumor during photodynamic treatment, as will be discussed in Chapter 8.

Chapter 6

The Design and Testing of a White-Light Steady-State Diffuse Reflectance Spectrometer for the Determination of Tissue Optical Properties

6.1 Introduction

The importance of the accurate assessment of tissue optical properties has long been recognized. Chance (1991) has recently reviewed the progress in applications of the optical method to probe biochemical indicators of physiological status.

Quantitative visible and near-infrared spectroscopy would provide a non-invasive means of probing structural as well as biochemical status of tissues *in vivo* for a variety of important applications. The quantitative monitoring of tissue oxygenation status, for example, has been the subject of a great deal of research since Jöbsis (1977) reported the use of near-infrared spectroscopy of hemoglobin and cytochrome aa_3 to observe shifts in the oxygenation status of the cat brain. The photodynamic therapy of cancer (PDT) also relies on a knowledge of tissue optical properties to properly assess the optical dose distribution in an irradiated tumor. PDT is a particularly intriguing application for *in vivo* spectroscopy because, as discussed in Chapter 2, therapeutic efficacy has been linked to the local oxygen supply in the tumor. Currently, there is no reliable means of non-invasively assessing this critical parameter in the small rodent tumors used in cancer research.

As discussed in Chapter 4, to perform quantitative optical spectroscopy *in vivo*, an appropriate model of photon transport must be used to eliminate the distortion of the absorption spectrum by wavelength-dependent scattering. Many approaches to this problem have been made for a variety of applications. Perhaps one of the most influential has been the determination of tissue oxygenation in the brain or muscle. It has been well established that optical transmission through the brain or leg muscles can be understood in terms of a modified form of Beer's law. But due to the large distances between the source and detector, scattering cannot be separated from absorption by a continuous-wave transmission measurement. Recently, techniques based on time- and frequency-domain solutions of the photo-diffusion equation first published by Patterson *et al.* (1989, 1991) have been shown to be effective in absolute measurements of tissue optical properties under these configurations. As a consequence, continuous-wave techniques have been used as qualitative trend indicators while time- and frequency-domain techniques are primarily relied on for accurate quantitation. Nevertheless, a steady-state optical technique capable of absolutely measuring tissue optical properties is highly desirable due to the decreased cost and simplicity that are characteristic of this approach.

In Chapter 5, index-matched and mismatched diffuse reflectance from a semi-infinite turbid slab was analyzed using two different solutions to the photo-diffusion equation. While the exact solution satisfying the partial-current boundary conditions can be used as a merit function in a fitting algorithm to determine tissue optical properties based on observed reflectance from a surface, the solution is quite complicated and not ideally suited for this task. However, the simpler dipole approximation of Farrell *et al.* (1992) provides an excellent alternative, and, in fact, this solution is a better predictor of optical properties than the exact solution when index-matched boundary conditions are used.

In this chapter, we present experimental results related to the implementation of spatially-resolved steady-state diffuse reflectance spectroscopy based on the theory of Farrell *et al.*. We describe details of a white-light diffuse reflectance spectrometer, designed on principles first suggested by (Wilson *et al.*, 1990), that is capable of simultaneous acquisition of spatially-resolved diffuse reflectance data over a variable 160 nm wavelength range in the visible and near-infrared spectral regions. The ability of the technique to accurately separate and report absorption and transport scattering coefficients is assessed through a series of experiments performed on tissue-simulating phantoms. From these phantom studies and the Monte Carlo evaluation of the dipole expression (Chapter 5), we conclude that a steady-state technique based on the dipole approximation is capable of reporting optical properties of turbid media to within 10% of the true values.

6.2 System Description

6.2.1 Instrument

Our steady-state diffuse reflectance spectrometer is based on a design first proposed by Wilson *et al.* (1990). A schematic diagram of the instrument is given in Figure 6.1. White light from a 250 W quartz tungsten halogen bulb is coupled into a 400-μm diameter optical fiber (NA = 0.22). Present coupling efficiency enables throughput of approximately 200-250 μW of optical power in a 10 nm bandpass in the wavelength range 550 - 850 nm. This source fiber is mounted in a circular probe containing fifteen 200 μm diameter detection fibers located at radial distances of 1.0 mm to 20.0 mm from the source fiber as shown in Figure 6.2. The source fiber and the fifteen detection fibers are arranged in a 2.0 cm diameter circle. At the center of this circular probe is mounted another 400 μm source fiber, which, because it is equidistant from all other fibers, can be used to calibrate the spectral response and throughput of the detection fibers. The flat surface of the probe is placed in contact with the surface of the phantom or tissue under investigation,

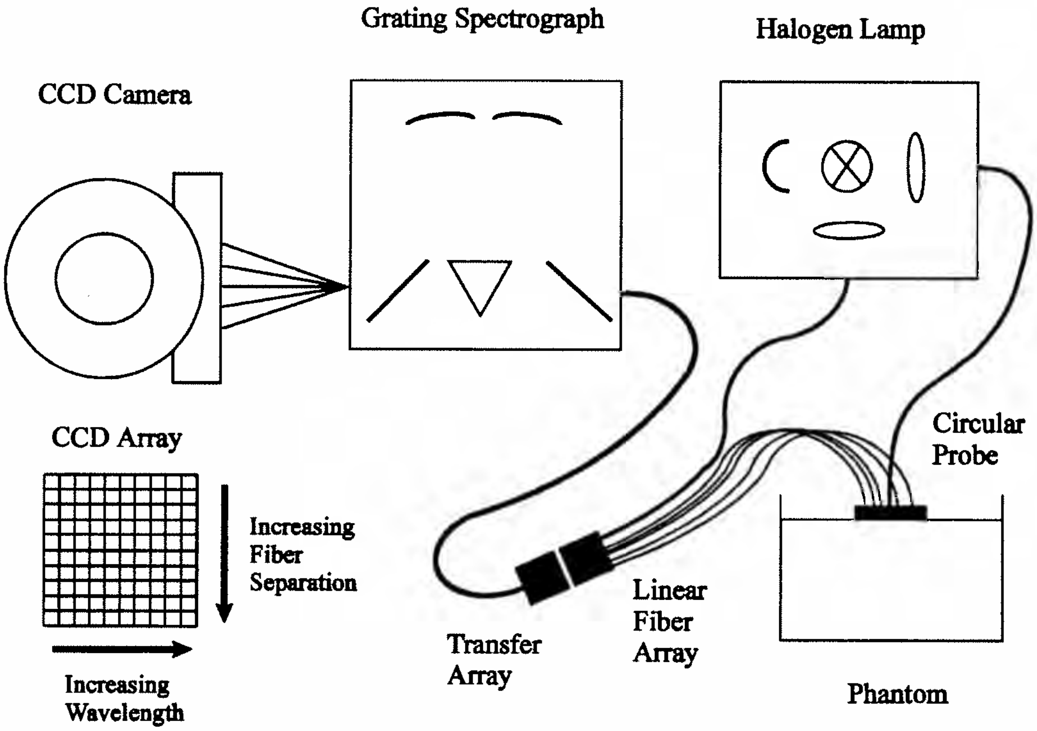
Grating Spectrograph
Halogen Lamp
CCD Camera
CCD Array
Increasing Fiber Separation
Increasing Wavelength
Circular Probe
Transfer Array
Linear Fiber Array
Phantom

Figure 6.1: The white-light steady-state spatial-resolved diffuse reflectance spectrometer

allowing white light from the source fiber to be injected into the sample surface. Since the optical properties μ_a and μ_s' are, in general, wavelength dependent, the use of a broadband source enables sampling of the medium's optical properties within a selected range of the visible to near-infrared spectrum. A portion of the light which propagates back to and escapes from the surface is collected as diffuse reflectance at well-defined distances from the source fiber by the detection fibers. The probe is constructed of Delron, a black plastic material, so that its surface approximates a perfectly absorbing boundary. As a result, the effective internal reflection coefficient (A) is assumed to be equal to unity.

The detection fibers and a reference fiber that monitors the lamp intensity are gathered together and terminated in a linear fiber array. This linear array of 200 μm detection fibers is connected to a transfer array of 400 μm fibers (see Figure 6.2), which transmits the signal of the individual detection fibers to a grating spectrograph. The coupling between arrays is such that each 400 μm transfer fiber is aligned with a single 200 μm detection fiber. The two fiber arrays can be connected such that each detection fiber physically contacts its respective transfer fiber. Because of the large dynamic range inherent in radial reflectance data (the signals from the detection fibers nearest to and most remote from the source typically differ by about four orders of magnitude), it is convenient to attenuate the output of the fibers carrying the strongest signals using a gradient neutral density filter. Such a filter was created by exposing a clear piece of radiographic film (Kodak Ektascan C EC-1) to x-rays through an aluminum step wedge. Placing the exposed film between the detection and transfer fibers increases the uniformity of

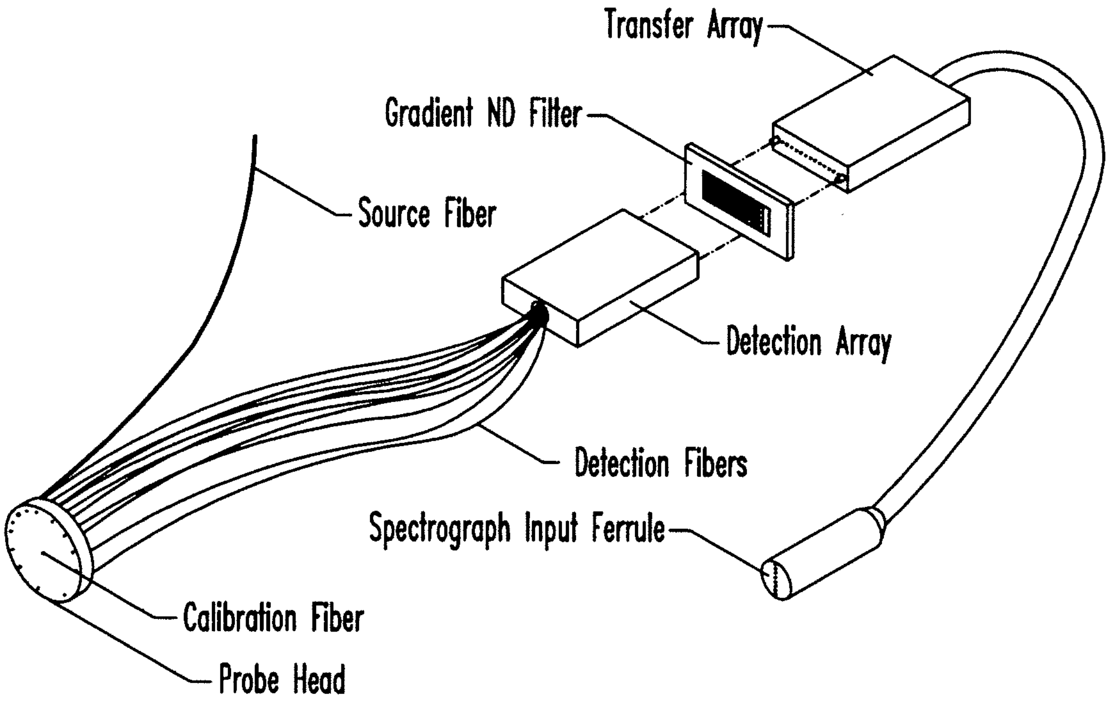
Transfer Array
Gradient ND Filter
Source Fiber
Detection Array
Detection Fibers
Spectrograph Input Ferrule
Calibration Fiber
Probe Head

Figure 6.2: An optical probe for detecting spatially-resolved diffuse reflectance.

signal intensities arriving at the CCD, which decreases the dynamic range required of the detector and reduces the influence of stray light that scatters through the spectrograph.

The transfer fibers are gathered into a bundle that terminates in a ferrule. At the end of the ferrule the fibers are arranged in a row and positioned in the focal plane of a 0.275 m imaging spectrograph (Acton Research Corporation, Acton, Mass.). The spectrograph was modified slightly by the addition of several baffles in order to maximize stray light rejection. Presently, approximately 0.5% of the signal from any given fiber is present as stray light in the signal of the adjacent fibers. The fibers are imaged through a low resolution, high dispersion grating (300 g/mm) onto the surface of a liquid nitrogen cooled, 512x512, 16 bit CCD camera (Princeton Instruments, Princeton, NJ). The dispersion of the grating and the useful flat field of the spectrograph are such that 170 nm of spectra may be collected in a single acquisition. The signal at the detector is thus the spectrally-resolved diffuse reflectance collected at several distinct distances from the source fiber, oriented such that the signals from the individual optical fibers lie in non-overlapping regions of the CCD array perpendicular to the slit axis. Imaging of the fibers is 1:1 through the spectrograph, so the signal from a given 400 μm transfer fiber is distributed over approximately sixteen 25 μm pixels along the axis of the spectrometer slit. To optimize the signal-to-noise ratio, regions of approximately 10 pixels along the slit axis and 3 pixels along the wavelength axis are binned to create a single super-pixel. Pixel binning in the wavelength direction limits resolution to 0.95 nm. The binned pixels are read from the CCD with the software provided by the manufacturer (CSMA, Princeton Instruments, Princeton, NJ) and later analyzed on a Sparc LX microcomputer.

6.2.2 Data Reduction

The first stage of data analysis constructs a diffuse reflectance curve for each of the binned wavelengths obtained by the apparatus. To do this, the raw reflectance data must first be corrected for individual fiber throughput differences as well as for fluctuations in the lamp output. Calibration data are acquired over the wavelength range of interest by injecting white light into a tissue-simulating phantom through the center fiber of the detector probe and collecting reflectance through each of the detection fibers. Since each detection fiber is equidistant from the center source fiber and the tissue-simulating phantom is presumed to be homogeneous, any differences in the spectra obtained in this configuration are due to individual variation in the detection fibers or variation of the throughput of the apparatus along different sections of the light path. It should be emphasized that the phantom is used in the calibration procedure only because it provides a convenient method for providing a uniform signal to each detection fiber. The technique described here is in no way dependent upon obtaining a calibration standard with known optical properties (Liu *et al.*, 1995a). Calibration signal intensities from the highest and lowest throughput fibers are typically within a factor of two of each other. For this reason, the calibration data are collected without the gradient neutral density filter, as the dynamic range of the CCD is adequate. Since it is possible that the lamp output may vary between acquisition of the calibration and radial reflectance data sets, a reference fiber monitors the lamp output during each data acquisition to allow for later correction. In order to correct for the possibility of background light leakage through the system, a second reflectance data set is acquired after removing the source fiber. While the background thus obtained is typically negligible, this procedure allows subtraction of any constant offset counts added to the analog-to-digital converter by the CCD controller in order to facilitate data acquisition.

After obtaining these calibration and background reflectance data sets, the diffuse reflectance curve, $R_d(\rho,\lambda)$, can be computed for each binned wavelength on the CCD from the following equation:

$$R_d(\rho,\lambda) = \left(\frac{R_s(\rho,\lambda) - B_s(\rho,\lambda)}{L_s(\lambda) - B_{L_s}(\lambda)}\right)\left(\frac{L_c(\lambda) - B_{L_c}(\lambda)}{R_c(\rho,\lambda) - B_c(\rho,\lambda)}\right)\frac{1}{T(\rho,\lambda)}, \tag{6.1}$$

where R, L, and T denote reflectance, lamp emission, and transmittance of the gradient neutral density filter, respectively; B denotes the measured background signal which, in general, can vary across the CCD (hence the dependence on ρ and λ); the subscripts s and c denote signals obtained during experiment and calibration runs, respectively; ρ is the source-detector separation and λ is the wavelength. B_{L_c} and B_{L_s} designate the background signal on that portion of the CCD which monitors the lamp emission for experiment and calibration acquisitions, respectively. The parameters ρ and λ correspond to binned locations parallel and perpendicular to the spectrometer slit axis, respectively (see Figure 6.1). We have found this calibration procedure to effectively eliminate systematic deviations due to variations in the throughput of the individual fibers and lamp fluctuations between data and calibration measurements. The reciprocal of the transmittance acknowledges the fact that we are filtering individual detection fibers to various degrees when obtaining radial reflectance data but not when calibration data are acquired. Finally, after calculating $R_d(\rho, \lambda)$ for all ρ and λ used in a given experiment, each radial reflectance curve generated at a particular wavelength is normalized to the diffuse reflectance from the detection fiber nearest the source fiber at that wavelength. By doing this, the experimental data are cast into a form suitable for analysis with Equation (5.1) as a fitting function.

The second stage of the data analysis involves successively fitting Equation (5.1) to each of the 170 normalized diffuse reflectance profiles to determine the absorption and transport scattering coefficients at each wavelength represented in the data set. Completing this fitting process and printing the results to a monitor typically takes 12 seconds or less on our Sun Sparc LX microcomputer. In this manner, the absorption and transport scattering spectra are effectively reconstructed from the radially-resolved diffuse reflectance profiles.

6.3 Phantom Studies

We have conducted a series of experiments in order to calibrate the instrument and determine its accuracy and sensitivity to changes in sample absorption and scattering. In these trials, we have prepared optical phantoms consisting of a scattering solution and known quantities of chromophore. The phantoms were prepared to simulate tissue scattering properties reported in the literature (Wilson and Jacques, 1990; Duck, 1990). The porphyrin manganese meso-tetra (4-sulfanatophenyl) porphine (MnTPPS) was used as an absorber because of its high water solubility and lack of fluorescence.

Absorption spectra of a phantom consisting of 1.25% Liposyn-II® (Abbott Laboratories, North Chicago, IL) and varying concentrations of MnTPPS are shown in Figure 6.3. Data for each spectrum were collected over the wavelength range 510 nm to 670 nm in a single 30 second acquisition. The points are the absorption coefficients (μ_a) estimated by fitting Equation (5.1) to radially-resolved diffuse reflectance measurements following subtraction of the background absorption of the lipid emulsion, which was obtained prior to the addition of MnTPPS. The error bars in Figure 6.3 represent the estimated standard deviation of the fitted values of μ_a. Absorption spectra acquired from samples of MnTPPS in non-scattering aqueous solution in a conventional spectrometer were then fit to the data points with the amplitude of the spectrum as a linear fitting parameter. The solid lines in Figure 6.3 indicate the best fits of these "cuvette" spectra to the absorption coefficients calculated from diffuse reflectance measurements. Since the concentration of the solution used to obtain the cuvette spectrum is known, the fitting parameter enables the determination the absolute concentration of MnTPPS in the phantom. This method was used to quantitatively evaluate the absorption coefficients estimated by fitting Equation (5.1) to the diffuse reflectance data over the range of concentrations used in these experiments. A total of 34 measurements were made with MnTPPS concentrations ranging from 7.8 nM to 13.8 μM.

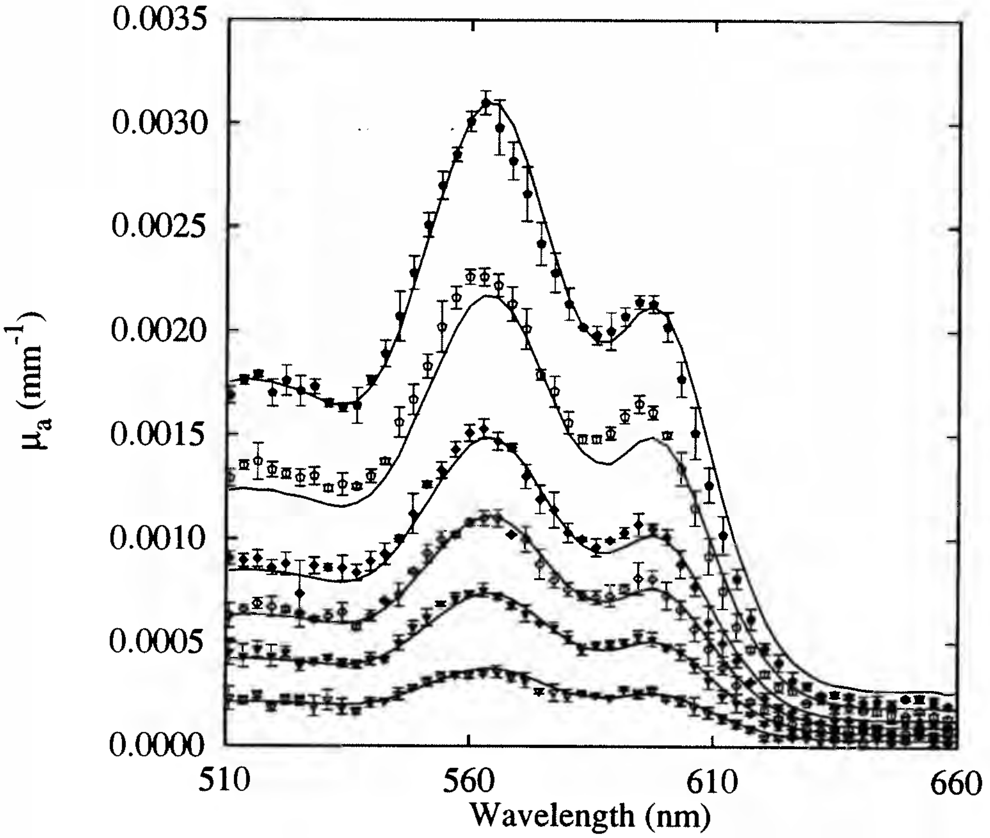

Figure 6.3: Background-subtracted absorption spectra (data points) of several concentrations of MnTPPS in 1.25% Liposyn-II® reconstructed from diffuse reflectance measurements. The error bars represent the standard deviation of the fitted values of μ_a. The standard deviation in the diffuse reflectance data points used in the fitting algorithm resulted from assuming Poisson counting statistics for the counts read from the CCD camera. The lines are absorption spectra from spectrophotometer measurements of non-scattering samples with amplitudes scaled to provide the best fit to the data. The actual concentrations of MnTPPS range from 0.15 μM to 1.25 μM.

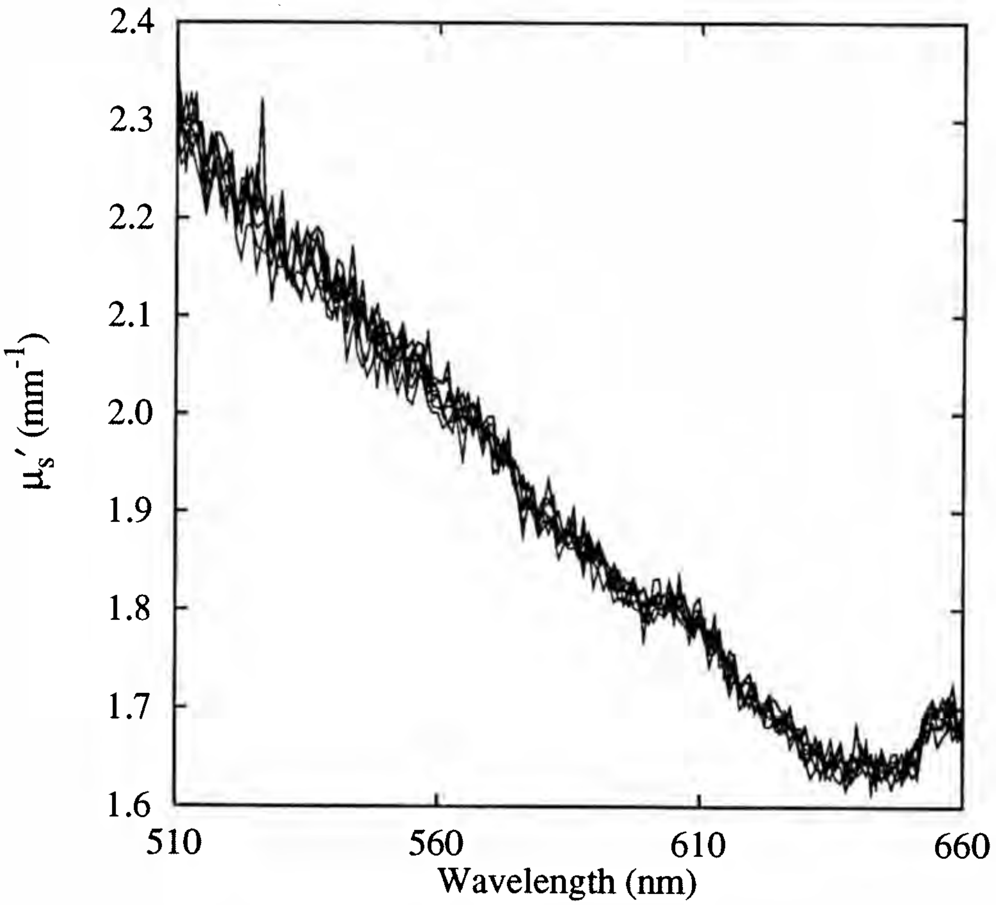

Figure 6.4: Scattering spectra of a 500 ml 1.25% Liposyn-II® phantom corresponding to the absorption spectra of Figure 6.3. The spectra are all within experimental uncertainty of one another.

Figure 6.4 illustrates the transport scattering (μ_s') spectra of the same phantom used to obtain the absorption spectra in Figure 6.3. As described earlier, these spectra are obtained simultaneously with the absorption spectra through the fitting process. Since a molecular absorber was being added to the phantom in this experiment the scattering properties of the phantom should not change. Indeed, all of the scattering spectra in Figure 6.4 are within experimental uncertainty of one another. This is an indication that the independent effects of scattering and absorption have been isolated in analyzing the diffuse reflectance spectrum.

The accuracy of the MnTPPS concentration determined by this procedure is illustrated in Figure 6.5. In this plot, the data points represent the concentrations of MnTPPS in the phantom obtained by fitting the cuvette spectrum to the absorption spectra reconstructed from radial diffuse reflectance measurements, such as those in Figure 6.3. The solid line indicates the actual MnTPPS concentration in the phantom as determined by the volume of 0.780 mM MnTPPS stock added to the phantom.

The smallest concentrations, for which the fits are most inaccurate, correspond to changes in μ_a less than or equal to 0.0001 mm^{-1} above the background absorption of the Liposyn-II® phantom near the 560 nm absorption maximum of MnTPPS. This appears to be the approximate limit of the sensitivity of the current instrument to changes in μ_a. After this threshold is exceeded, the estimated concentration is quite accurate.

It is interesting to compare the trends observed in Figure 6.5 with the predictions of the Monte Carlo analysis depicted in Figure 5.1. The characteristic

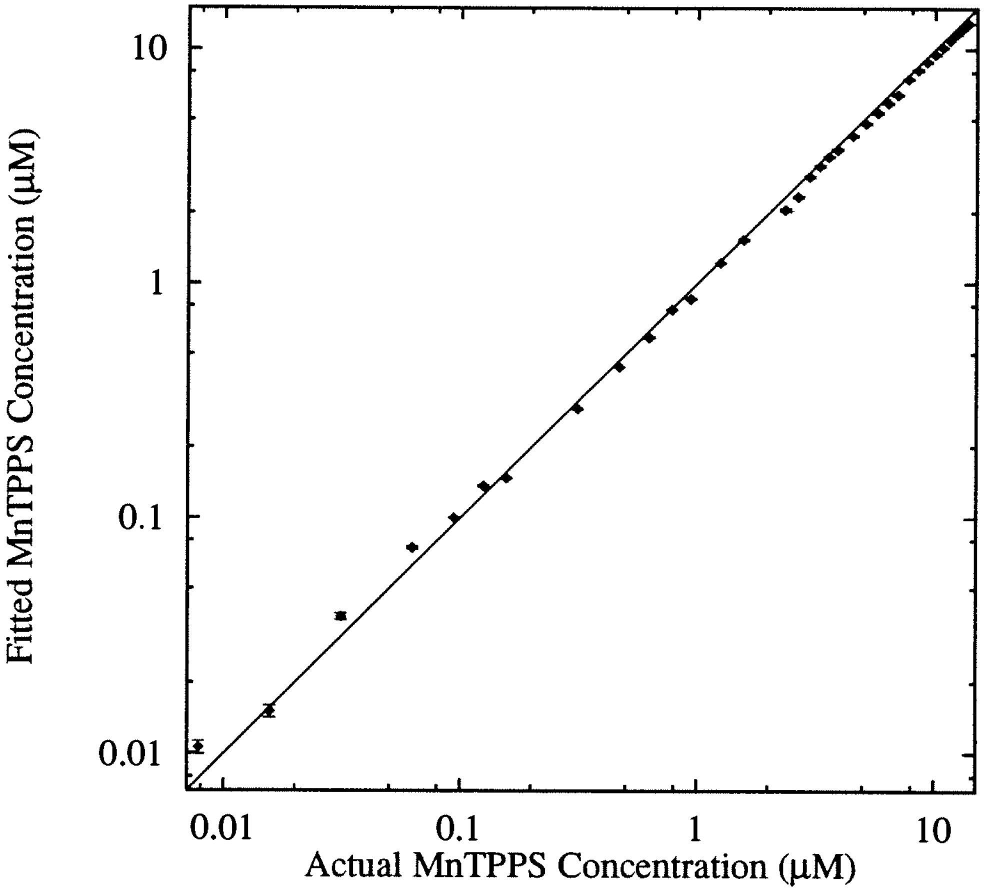

Figure 6.5: The actual (line) and fitted concentrations (data points) of MnTPPS in a 1.25% Liposyn-II® phantom. The fitted concentrations were determined using the scaling parameter obtained from fits of cuvette spectra from non-scattering MnTPPS solutions to absorption spectra reconstructed from diffuse reflectance measurements. The maximum value of μ_a (at approximately 560 nm) in the reconstructed absorption spectra ranges from 2.5×10^{-5} to 3.5×10^{-2} mm^{-1}.

transport mean free path of each of the phantoms was approximately 0.5 mm at 560 nm. While it is true that absorption was changed for each experiment, the change in absorption is slight compared to experimental noise in the scattering coefficient. The smallest source-detector fiber separation used in the fitting process was 1.0 mm, or 2 transport mean free paths. Given this configuration, the Monte Carlo analysis would predict that the absorption coefficient should be overestimated by approximately 13%. This is seen to occur only for the smallest concentrations of MnTPPS. Indeed, the majority of the experiments appeared to underestimate the actual concentration by approximately 10%. It is possible that this discrepancy may be explained by the fact that our source and detection fibers have finite diameters of 0.4 and 0.2 mm, respectively. In addition, the optical fibers have a numerical aperture of 0.22, rather than the idealized pencil beam assumed for the Monte Carlo simulations. These factors may combine to yield an effective minimum source-detection fiber separation of less than 1.00 mm, thus placing our experiment in the regime where estimated values for μ_a are systematically low. Our data indicate that estimated values for μ_a are accurate to within 10% for transport albedos ≥ 0.983, provided a threshold change in absorption over background of approximately 0.0001 mm^{-1} is exceeded. These errors compare favorably with those observed by others using a variety of techniques (Patterson *et al.*, 1991; Madsen *et al.*, 1994; Matcher *et al.*, 1995a).

In an effort to evaluate the quantitative accuracy of the scattering coefficients estimated by fitting Equation (5.1) to radially-resolved diffuse reflectance data, phantoms were prepared consisting of 500 ml distilled water and varying amounts of an aqueous suspension of 0.519 μm diameter polystyrene microspheres (Duke

Scientific, Palo Alto, CA). The density of scatterers was varied from 1.58×10^{10} ml^{-1} to 2.79×10^{10} ml^{-1} in these experiments. It is well known that the scattering spectrum of a spherical scatterer can be determined by Mie theory (van de Hulst, 1981). Figures 6.6 through 6.9 illustrate the transport scattering spectra predicted by Mie theory for four suspensions of 0.519 μm diameter non-absorbing spheres in the wavelength range of 500-825 nm, along with the measured values of μ_s' obtained from the phantom using our diffuse reflectance spectroscopy system. In Figure 6.6, the experimental and theoretical spectra possess the same wavelength dependence and are in excellent quantitative agreement. This corresponds to the maximum density of scatterers used in this experiment. As the density of scatterers is decreased (Figures 6.7 - 6.9), the fitted transport scattering coefficients are overestimated with respect to the theoretical prediction. This may again be understood in terms of the minimum source-detector separation used in the acquisition and analysis of these data. For each of these experiments, ρ_{min} was equal to 1.0 mm. In Figure 6.6, the actual transport scattering coefficients are in the range of 0.75 - 1.0 mm^{-1}, corresponding to transport mean free paths of approximately 1.3 - 1.0 mm. Thus, since ρ_{min} is on the order of 0.75 - 1.0 mfp$'$ one would expect the experimental data to yield the correct optical coefficients. As the density of scatterers decreases, the transport mean free path associated with the phantom increases to as high as 2.4 mm (Figure 6.9). As a result, ρ_{min} becomes increasingly small with respect to the transport mean free path, and the transport scattering coefficient is correspondingly overestimated. This agrees qualitatively with the Monte Carlo results shown in Figure 5.1.

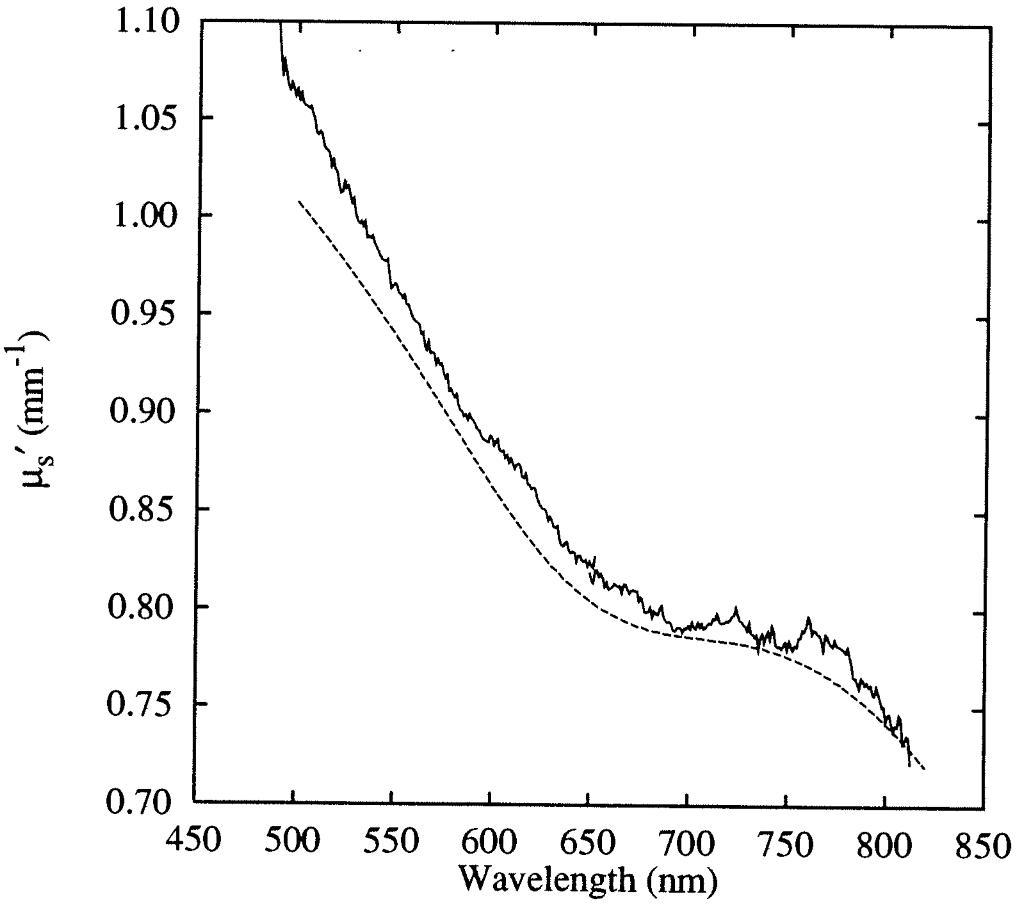

Figure 6.6: The scattering spectrum of a phantom consisting of 0.519 μm diameter polystyrene microspheres in aqueous suspension at a density of 2.79×10^{10} spheres ml^{-1}. The dashed line indicates the transport scattering coefficient as predicted by Mie theory. The solid line is the estimated value of μ_s' from experimental diffuse radial reflectance data.

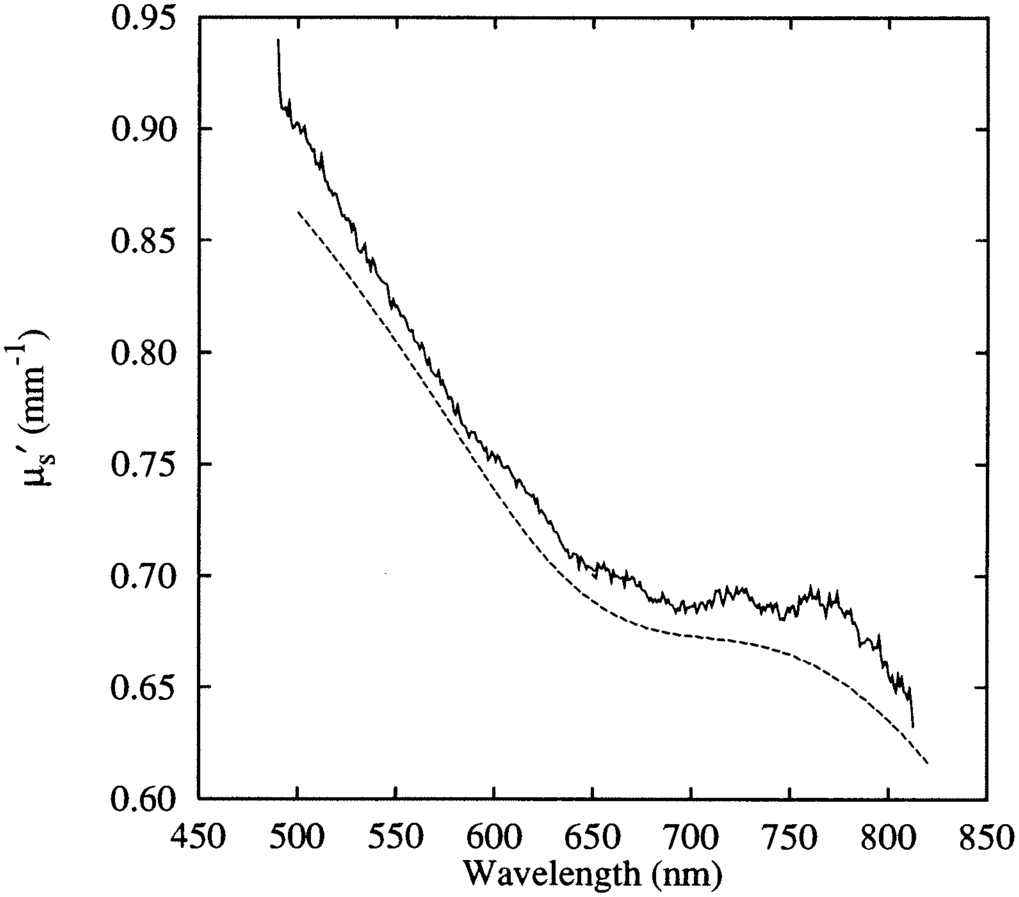

Figure 6.7: The scattering spectrum of a phantom consisting of 0.519 μm diameter polystyrene microspheres in aqueous suspension at a density of 2.39×10^{10} spheres ml^{-1}. The dashed line indicates the transport scattering coefficient as predicted by Mie theory. The solid line is the estimated values of μ_s' from experimental diffuse radial reflectance data.

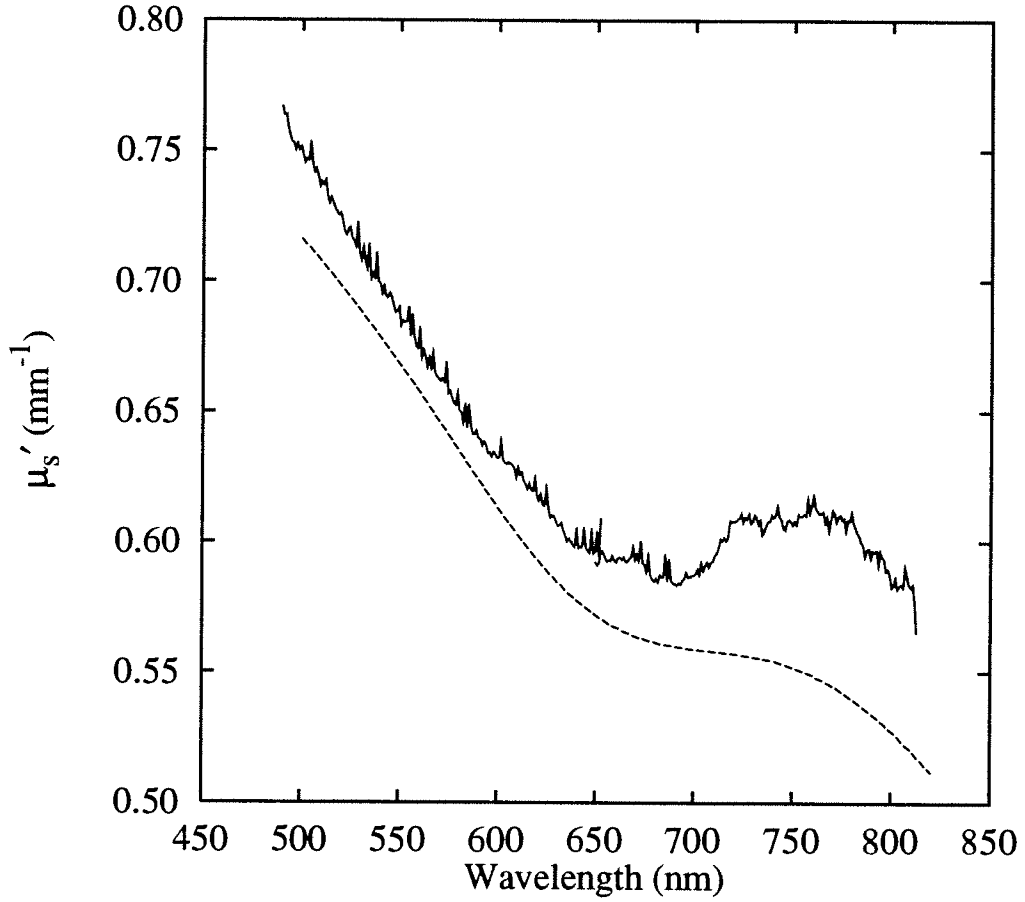

Figure 6.8: The scattering spectrum of a phantom consisting of 0.519 μm diameter polystyrene microspheres in aqueous suspension at a density of 1.98×10^{10} spheres ml^{-1}. The dashed line indicates the transport scattering coefficient as predicted by Mie theory. The solid line is the estimated value of μ_s' from experimental diffuse radial reflectance data.

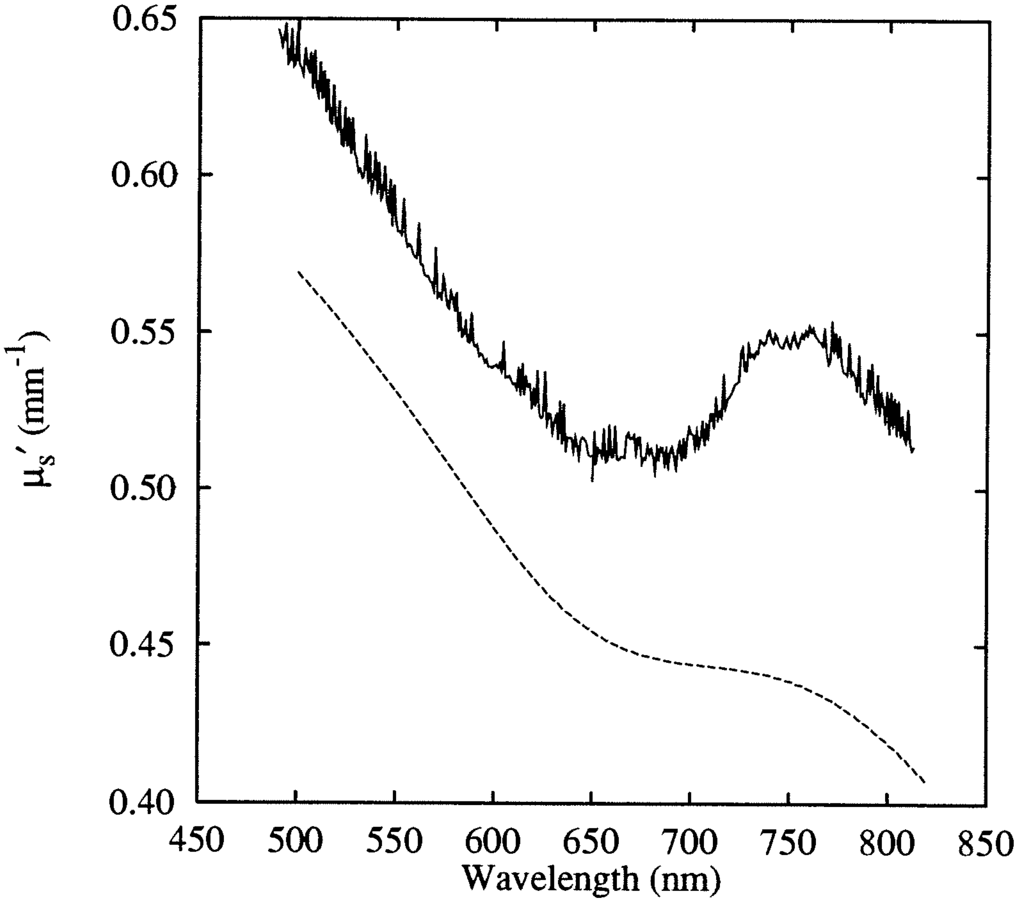

Figure 6.9: The scattering spectrum of a phantom consisting of 0.519 μm diameter polystyrene microspheres in aqueous suspension at a density of 1.58×10^{10} spheres ml^{-1}. The dashed line indicates the transport scattering coefficient as predicted by Mie theory. The solid line is the estimated value of μ'_s from experimental diffuse radial reflectance data.

An interesting effect can be observed when performing diffuse reflectance absorption spectroscopy in the presence of fluorescent chromophores. Since fluorescence emission cannot be discriminated from diffusely reflected light originating with the source beam, the diffuse reflectance data will be contaminated by the presence of increased signal in the wavelength range where fluorescence emission is appreciable. As a result, the fitting procedure returns an artificially low absorption coefficient in these regions. We have observed this phenomenon in diffuse reflectance experiments conducted with the fluorophore Nile Blue A (NBA), which has a fluorescence quantum yield of approximately 0.2 and a peak in its fluorescence emission at approximately 680 nm. Various amounts of NBA were added to a 1.25% Liposyn-II® phantom in a manner similar to the MnTPPS experiment described earlier in this chapter. The NBA absorption spectra obtained in this manner are illustrated in Figure 6.10, where the data points indicate the absorption coefficients reconstructed from diffuse reflectance measurements at each wavelength. Solid lines are the best fit of the known absorption spectrum to these reconstructed absorption coefficients. Note that in the regions of the spectrum where there is significant fluorescence emission, the fitted absorption coefficient is much too low to obtain accurate fits to the data. In fact, the reconstructed absorption coefficient is negative in the wavelength region where fluorescence emission dominates absorption.

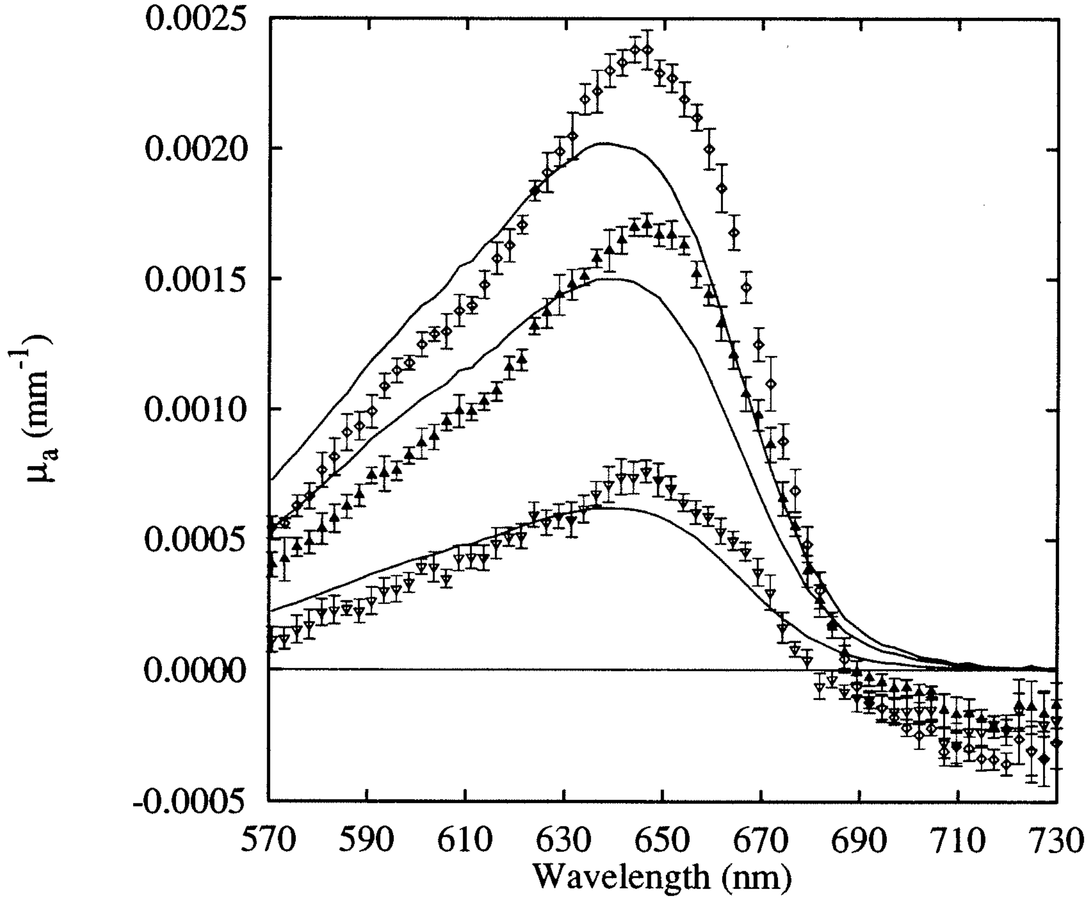

Figure 6.10: Background-subtracted absorption spectra (data points) of several concentrations of Nile Blue A (NBA) in 1.25% Liposyn-II® reconstructed from diffuse reflectance measurements. The lines are absorption spectra from spectrophotometer measurements of non-scattering samples with amplitudes scaled to provide the best fit to the data. The presence of fluorescence emission causes the estimated absorption coefficient to be artificially low.

6.4 Conclusions

The white-light steady-state diffuse reflectance spectrometer is capable of obtaining diffuse reflectance spectra possessing signal-to-noise levels sufficient for quantitative analysis using signal integration times as small as 4 seconds in systems with biologically relevant optical properties. The range of absorption coefficients which may be accurately measured with this instrument has an apparent lower limit of approximately 0.0001 mm^{-1} over the background phantom absorption, while absorption coefficients as large as 0.035 mm^{-1} have been measured to within 10% of the true value in scattering emulsions with transport albedos as low as 0.983. It has been observed that chromophores with appreciable fluorescence quantum yields are not good candidates for quantitative analysis by the methods described here because fluorescence emission creates artificially elevated diffuse reflectance measurements at wavelengths corresponding to the fluorescence emission spectrum. As a result, the estimated absorption coefficients in this spectral region are artificially low.

For the analysis described in this chapter we were able to assume that index-matched conditions were present at the interface because of the experimental situation; a flat black detector probe was placed in contact with the surface of a liquid phantom. This is the ideal situation for the implementation of Farrell's dipole approximation. The fact that the phantom studies agreed quite well with the Monte Carlo evaluation of this solution under matched boundary conditions seems to support our assumptions, though the analysis of Chapter 5 indicated that even when an index-mismatch exists, the dipole approximation gives better predictions when A is arbitrarily reduced. It is quite conceivable that with other detector probes and/or solid tissue or tissue-simulating phantoms this assumption may not be appropriate. In this case the analysis of Chapter 5 indicates that less accurate results may be expected.

The results presented here are very encouraging with respect to the possibility of quantifying the absorption of certain biologically relevant chromophores *in vivo*. Of particular interest to us is the eventual measurement of hemoglobin oxygen saturation in the small, spherical rodent tumors which are commonly used in many pre-clinical studies of cancer treatment modalities. The small source-detector separations required for accurate quantitation using steady-state radially-resolved diffuse reflectance spectroscopy may be ideally suited for probing the small volumes encountered with tumors such as these.

Chapter 7

Visible and Near-Infrared Radially-Resolved Diffuse Reflectance Spectroscopy of Hemoglobin

7.1 Introduction

The goal of tissue spectroscopy is to accurately measure the absorption of tissue chromophores as a means of monitoring a physiological quantity of interest. The Optical Method, as referred to in a recent review article by Chance (1991), has been used as an analysis tool to measure a variety of physiological absorbers since the 1930's, when it was developed for *in vitro* studies. It has continued to be refined over the years, and recently there has been substantial interest in optical techniques to non-invasively measure physiological status *in vivo.* Examples of potential applications include the identification and localization of exogenously administered photosensitizers for use in the photodynamic therapy of cancer (Patterson *et al.*, 1987, 1989; Wilson *et al.*, 1990), the use of the tissue scattering spectrum as a means of monitoring glucose concentration in the diabetic (Maier *et al.*, 1994; Kohl *et al.*, 1994), as well as the measurement of hemoglobin oxygen saturation for tissue oximetry and identification of certain mitochondrial disorders (Ferrari *et al.*, 1995; Liu *et al.*, 1995a; Chance *et al.*, 1988a,b; Bank and Chance, 1995).

The spectral shift of the hemoglobin absorption spectrum upon oxygenation has been used qualitatively as a means of assessing blood oxygenation for many years. In 1977, Jöbsis was able to measure oxygen-dependent changes in transillumination spectra of the cat brain and identify cytochrome aa_3 and hemoglobin as the primary near-infrared chromophores (Jöbsis, 1977). Organometallic molecules such as these are ideal indicators of environmental oxygen concentration because while the oxygen affinity can depend on a variety of factors (pH, pCO_2, inorganic phosphates, temperature, *etc.*), the characteristic spectroscopic shifts in absorption depend only upon the oxygen tension (Benesch and Benesch, 1974; Kilmartin and Rossi-Bernardi, 1973). Several techniques have been developed that make use of this shift to quantitatively determine the oxygen status of tissue.

Continuous-wave transmission measurements have functioned primarily as trend indicators because of the inability of these techniques to properly separate the effect of absorption and scattering in the attenuation measurement. This problem was recognized in Jöbsis' first measurements. In contrast, while more costly than steady-state techniques, time- and frequency-domain techniques have proven to be able to do this. Time-domain measurements, for example, can be used to predict the effective photon pathlength of light injected into multiply scattering tissue by monitoring the temporal delay in the arrival of an optical pulse. Naturally, steady-state techniques do not have recourse to this information. Continuous-wave techniques can and have been used to monitor the trend in absorption provided the scattering spectrum is assumed to be constant or is otherwise known. This assumption must be cautiously applied, however, since tissue scattering is dependent upon a variety of factors such as temperature, water concentration, and red blood cell density. Furthermore, there are several potential applications of tissue oximetry for which this assumption will likely be invalid. One example is monitoring tumor oxygenation during or immediately following cancer treatment. In these circumstances, the structural characteristics of the tissue can change dramatically and the effects of scattering and absorption must be properly separated for meaningful analysis. Since treatment efficacy of a variety of modalities has been linked to the local oxygen concentration in the tumor, non-invasive tumor oximetry is a very attractive application of tissue spectroscopy (Stone *et al.*, 1993).

In Chapter 6, we described a reflectance-mode steady-state technique based on an analytic solution of the photo-diffusion equation presented by Farrell *et al.* (1992) which indicates that the spatial distribution of the radially-resolved diffuse reflectance is dependent only on the reflectivity of the air-tissue interface, the reduced scattering coefficient (μ_s'), and the absorption coefficient (μ_a), as described in Chapter 4. This technique was shown to be capable of accurately determining the tissue scattering and absorption spectrum, typically with an accuracy of better than 10% in tissue-simulating phantoms and with full spectrum acquisition times as short as 4 s with our experimental system.

In this chapter, we present the use of the steady-state diffuse reflectance technique to measure the absolute hemoglobin absorption spectrum in tissue-simulating phantoms consisting of a scattering emulsion (Liposyn-II®) and red blood cells. Yeast is added to deoxygenate the phantom and cause the characteristic spectral shift of oxyhemoglobin. By fitting the entire measured absorption spectrum to published molar extinction spectra, the absolute concentration of hemoglobin as well as the oxygen saturation can be measured. Simultaneous measurements of the dissolved oxygen concentration permit the construction of Hill plots which can be used to correlate hemoglobin oxygen saturation with local oxygen concentration. This is demonstrated at visible as well as at near-infrared wavelengths. Finally, since this procedure is likely to be highly dependent on an accurate knowledge of chromophore extinction spectra and the background spectrum of the tissue or tissue-simulating phantom, the consequences of inadequate knowledge of these factors are discussed.

7.2 Experimental Methods

The instrument used to acquire radially-resolved reflectance spectra from tissue simulating phantoms is based on a design first proposed by Wilson *et al.* (1990)

and is described in detail in Chapter 6. In this section we discuss the technique by which realistic hemoglobin-containing tissue-simulating phantoms are produced and monitored.

7.2.1 Phantom Preparation

The phantoms used in this study consisted of a scattering emulsion, 0.91% Liposyn-II® (Abbott Laboratories, North Chicago, IL), suspended in a pH-buffer solution consisting of 0.9% saline and 0.05 M Trizma (Sigma, pH 7.3). The phantoms were approximately 500 ml in volume and were placed in a glass beaker. A magnetic stirring rod was placed in the beaker and the phantom was stirred for all of the studies discussed here. To simulate various blood volume fractions expected to be encountered *in vivo*, human red blood cells were obtained either from post-dated blood-bank blood or from a volunteer immediately prior to the experiment. With samples directly drawn from volunteers the red blood cells were separated from the plasma by centrifugation (2500 g) and replacement of the plasma with 0.9% saline. This process was repeated several times until the supernatant was clear. The stock solution was then obtained by resuspending the red blood cells in saline. To deoxygenate the phantom, a small amount of dry baker's yeast was added. Typically a 1:1000 volume fraction was sufficient to deoxygenate the phantom in approximately 1 hour.

7.2.2 Determination of Oxygen Saturation and Total Hemoglobin Concentration

Before addition of the red blood cells and yeast, diffuse reflectance spectra were obtained for the Liposyn-II® phantom to characterize the oxygen-independent background. Then red blood cells were added to the phantom and spectra were again obtained. To determine the amount of hemoglobin and the oxygenated fraction, the background spectrum was subtracted from the phantom spectrum. Since hemoglobin was the only absorber used in this study, the absorption of the phantom, $\mu_a(\lambda)$, can be represented by a linear combination of oxy- and deoxyhemoglobin spectra,

$$\mu_a(\lambda) = C_{Hb}\epsilon(\lambda)_{Hb} + C_{HbO_2}\epsilon(\lambda)_{HbO_2}, \tag{7.1}$$

where $\epsilon(\lambda)_{HbO_2}$ and $\epsilon(\lambda)_{Hb}$ are the molar extinction spectra of oxy- and deoxyhemoglobin, respectively, and C_{HbO_2} and C_{Hb} represent the concentrations of these two species. By fitting Equation (7.1) to the measured red blood cell spectrum, the concentration of oxy- and deoxyhemoglobin can be independently determined from the best-fit values of the fitting parameters. Having obtained C_{Hb} and C_{HbO_2}, the total concentration of hemoglobin, C_{Tot}, as well as the oxygen saturation, S, can easily be computed from

$$C_{Tot} = C_{Hb} + C_{HbO_2} \tag{7.2}$$

and

$$S = \frac{C_{HbO_2}}{C_{Tot}}. \tag{7.3}$$

Diffuse reflectance spectra of Liposyn-II®-red blood cell-yeast phantoms were obtained periodically as the yeast deoxygenated the phantom to monitor hemoglobin oxygenation.

To correlate hemoglobin oxygenation saturation with the concentration of dissolved oxygen, spectra were obtained simultaneously with oxygen partial pressure (pO_2), as determined by a 3 mm tip-diameter Clark-style oxygen electrode (Microelectrodes, Inc., Londonderry, N.H.). At the beginning of a given experiment, the electrode was calibrated in air-saturated Liposyn-II® and Liposyn-II® deoxygenated with $Na_2S_2O_4$. Oxygen partial pressure was then determined from the electrode current assuming a linear response. The calibration procedure was also repeated at the end of an experiment to help control for electrode drift. The temperature of the phantom was also periodically recorded. The studies reported here were conducted between 28.0 °C and 30.0 °C. During the experiment the electrode was placed approximately 5 mm below the surface of the phantom near the wall of the beaker to avoid interference with the measurement of the diffuse reflectance.

7.3 Phantom Oxygenation Status Assessment

To test the ability of the steady-state diffuse reflectance technique to measure absolute hemoglobin absorption spectra in tissue-simulating phantoms, a Liposyn-II®-red blood cell-yeast phantom was prepared as described in Section 7.2.1. Prior to adding red blood cells the absorption spectrum of the Liposyn-II® phantom was obtained to allow for background subtraction. Human red blood cells were then added to the phantom and allowed to mix thoroughly. This was repeated several times, and a spectrum was obtained after each addition until a desirable absorption coefficient had been reached. The typical Liposyn-II® background spectrum is shown along with several red blood cell absorption spectra for the visible and near infrared in Figures 7.1 and 7.2, respectively.

In the near infrared, the background peak at approximately 740 nm can be attributed to an overtone of the OH absorption of water (Kou *et al.*, 1993). This feature dominates the background spectrum in the wavelength range investigated here. With each addition of red blood cells absorption increases above background as expected. Subtracting the background spectrum from each of the absorption spectra resulted in the red blood cell spectra. Each of these spectra were then fit to a linear superposition of oxygenated and deoxygenated extinction spectra for the visible and near infrared. The extinction spectra used in this fit were obtained from the literature and are reproduced as Figures 7.3 and 7.4. The linear fitting coefficients provided the best-fit estimates of the concentration of oxy- and deoxyhemoglobin, which were then added together to obtain the total hemoglobin concentration. For each of the spectra shown, the red blood cells were estimated to be completely saturated with oxygen. The fit results indicate that the total hemoglobin concentrations for each of the red blood cell spectra shown in Figure 7.1 are 2.19 ± 0.16 μM (first aliquot), 4.37 ± 0.16 μM (second aliquot), and 6.50 ± 0.19 μM (third aliquot). The corresponding oxygen saturations are 105.5 ± 8.7 %, 102.0 ± 4.8 %, and 100.0 ± 3.7 %. Similar results were obtained for the near-infrared assessment of the spectra shown in Figure 7.2. In this experiment,

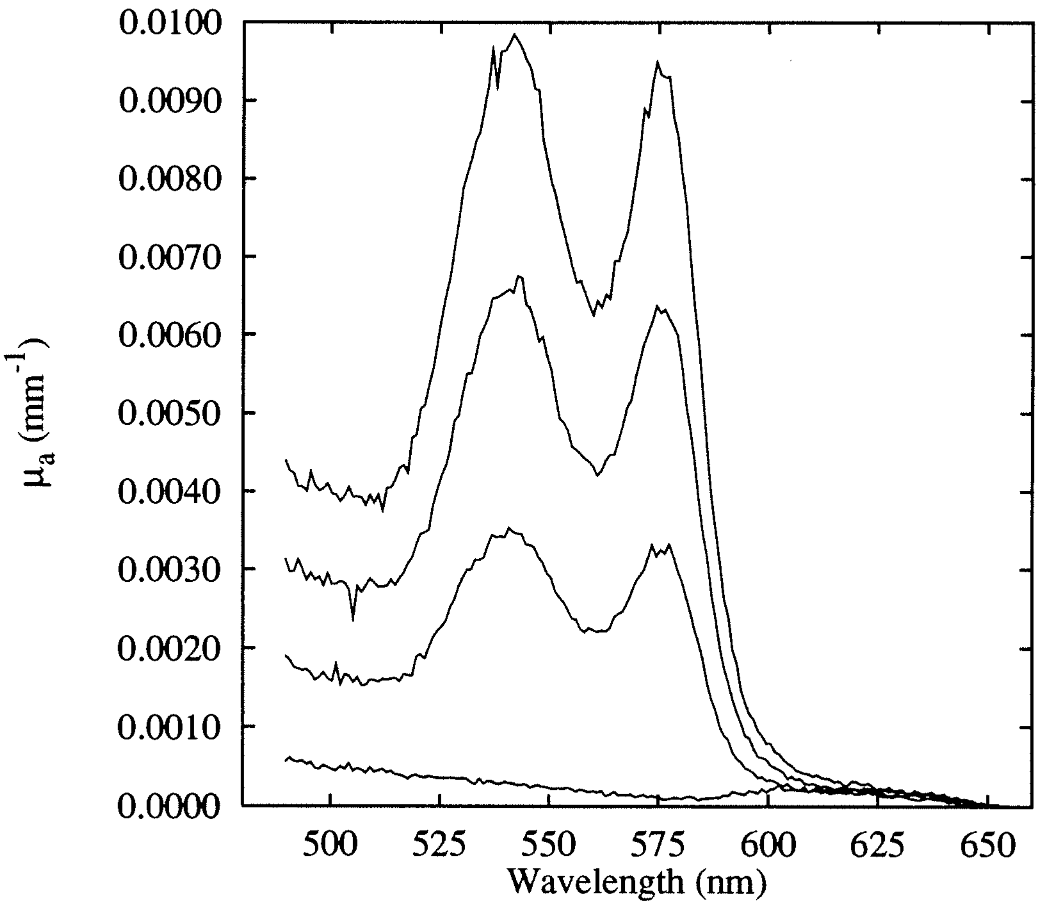

Figure 7.1: Absorption spectra of a 0.91% Liposyn-II® phantom with human red blood cells measured with the steady-state diffuse reflectance spectrometer. The bottom curve is a typical Liposyn-II® absorption spectrum, while the remaining three curves were obtained after adding aliquots of red blood cells. The center wavelength of the spectrometer was set to 560 nm.

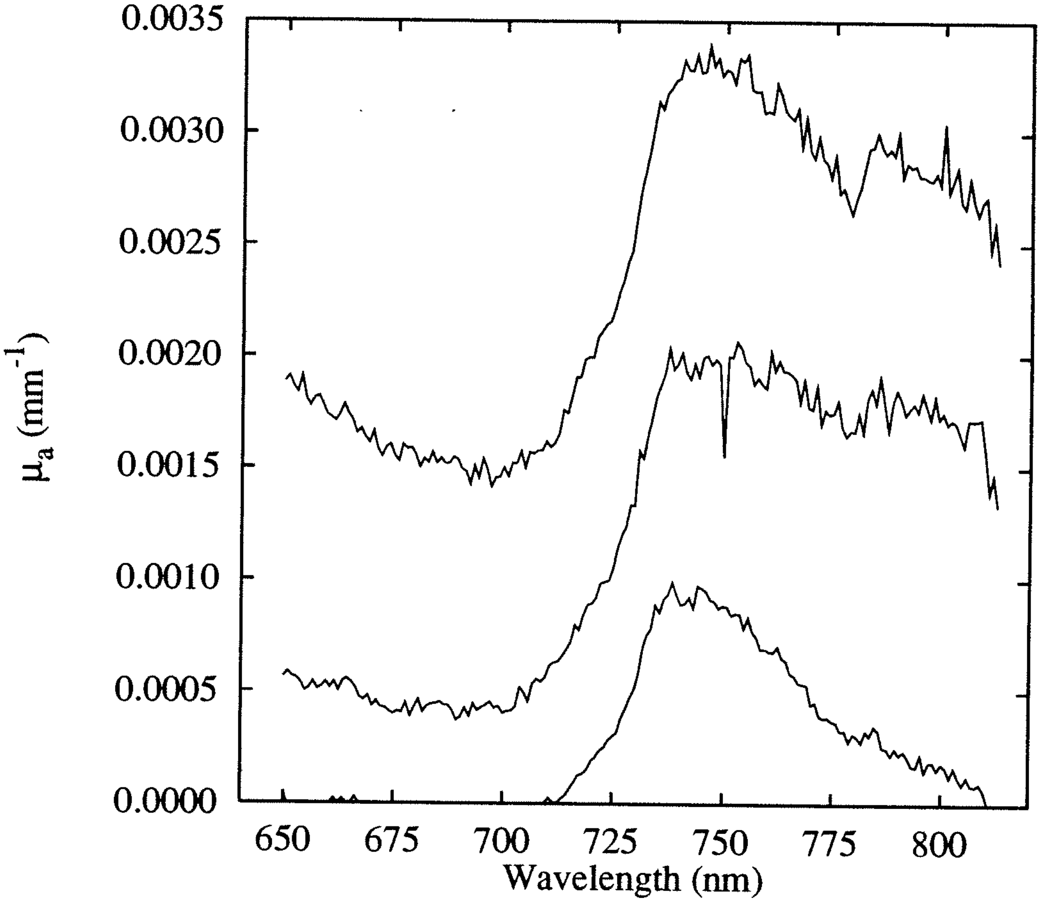

Figure 7.2: Absorption spectra of a 0.91% Liposyn-II® phantom with human red blood cells measured with the steady-state diffuse reflectance spectrometer. The bottom curve is a typical Liposyn-II® absorption spectrum, while the remaining two curves were obtained after adding aliquots of red blood cells. The center wavelength of the spectrometer was set to 740 nm. The peak in the Liposyn-II® absorption at this wavelength is due to an overtone of the OH absorption of water.

the total hemoglobin concentrations for each of the spectra shown in Figure 7.2 are 39.72 ± 3.00 μM (first aliquot) and 124.0 ± 4.0 μM (second aliquot), with corresponding oxygen saturations of 109.8 ± 11 % and 97.1 ± 4.4 %. When the total hemoglobin concentration is plotted as a function of the concentration of red blood cells in the phantom, a linear relationship is found. This is shown in Figure 7.5. With the exception of a single point, a line with zero intercept fits the data very well. The single discrepancy was probably a result of insufficient mixing before acquiring the data, since the subsequent point falls on the best-fit line.

It was shown in Chapter 6 that the predicted concentration obtained from fitting to radial-reflectance spectra of MnTPPS phantoms is typically within 10% of the true concentration over a wide range of absorption coefficients. Therefore, it can be assumed that the returned hemoglobin concentration will also differ from the true value by no more than this amount. Of course, the mapping from absorption coefficient to concentration is dictated by the extinction spectra. In this analysis, extinction spectra from two independent sources were used for visible and near-infrared wavelengths. Any systematic errors in these spectra could also translate into errors in the hemoglobin concentration.

After an appropriate amount of red blood cells had been added a small amount of yeast was mixed in to gradually deoxygenate the phantom. Previous attempts at removing oxygen with $Na_2S_2O_4$ resulted in an undesirable oxidation of hemoglobin as was readily apparent from the absorption spectrum. An oxygen electrode placed near the surface of the phantom was used to monitor the oxygen partial pressure as deoxygenation occurred, and spectra were obtained at regular inter-

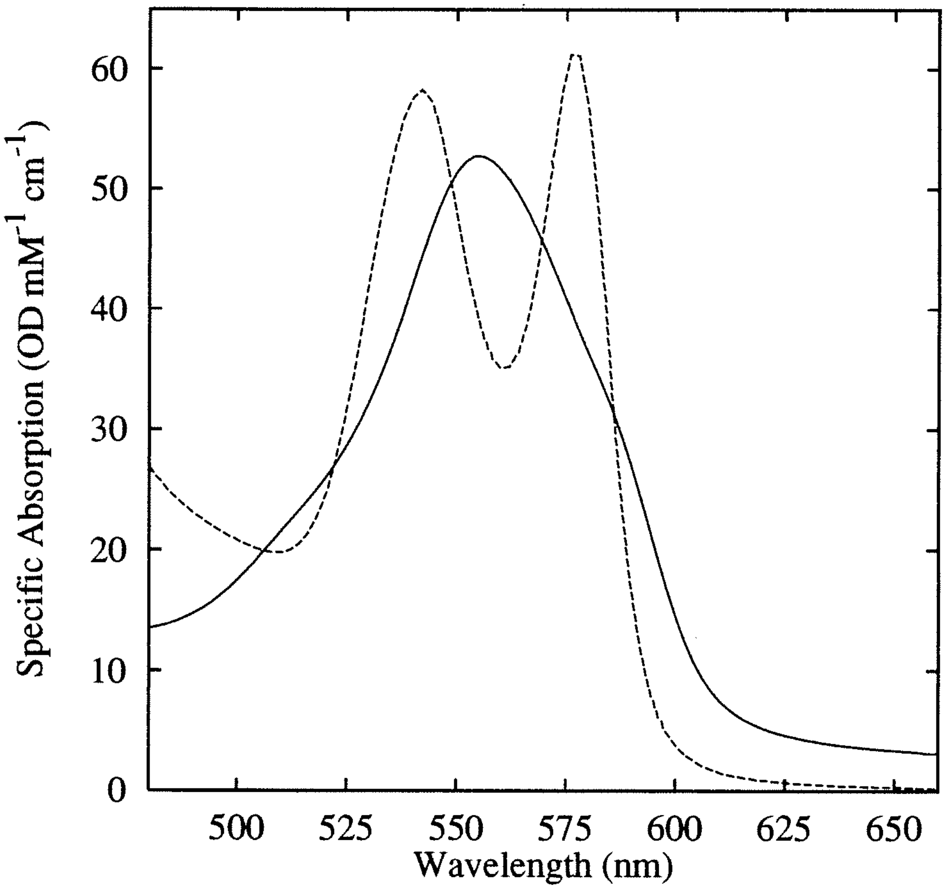

Figure 7.3: The visible absorption spectra of oxy- and deoxyhemoglobin. The dashed and solid lines represent the absorption spectrum for 100% oxygenated and 0% oxygenated hemoglobin, respectively. Data were obtained by Zijlstra and Buursma (1987) in carefully prepared non-scattering solutions. The values of the specific absorption have been multiplied by a factor of four from that reported by Zijlstra and Buursma to convert the absorption per heme unit to absorption per hemoglobin molecule.

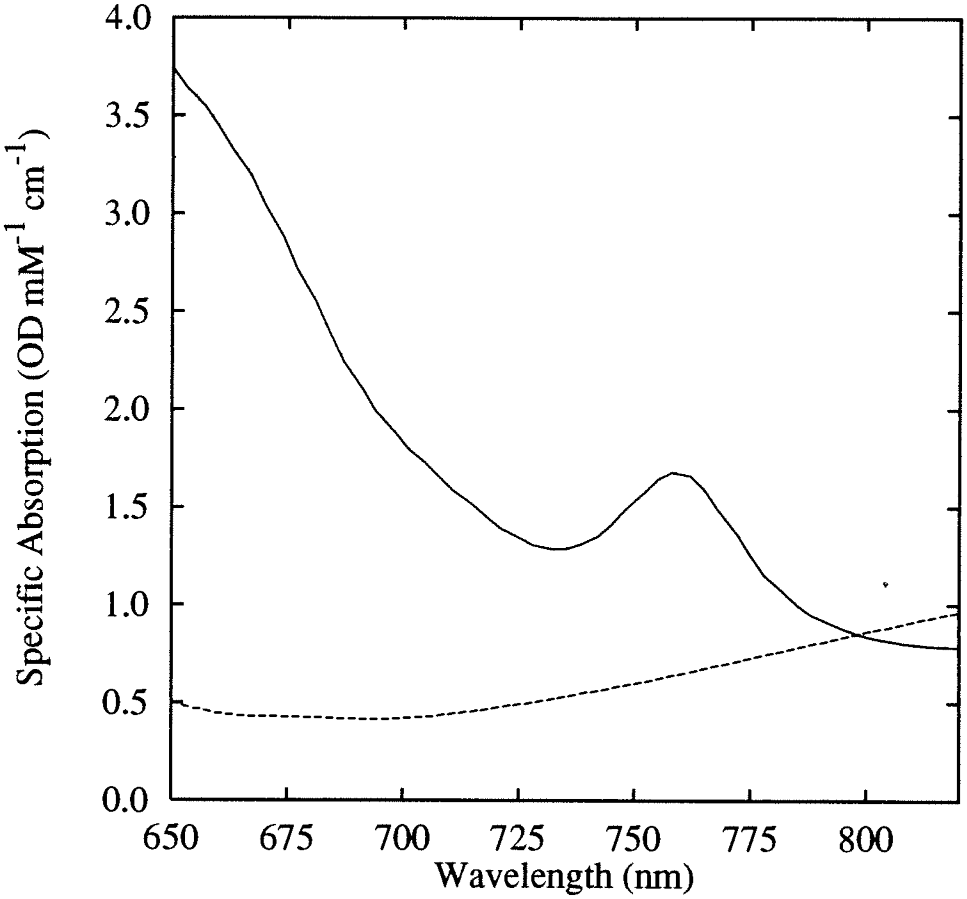

Figure 7.4: The near-infrared absorption spectra of oxy- and deoxyhemoglobin. The dashed and solid lines represent the absorption spectrum for 100% oxygenated and 0% oxygenated hemoglobin, respectively. Data were obtained by Wray *et al.* (1988) in carefully prepared non-scattering solutions.

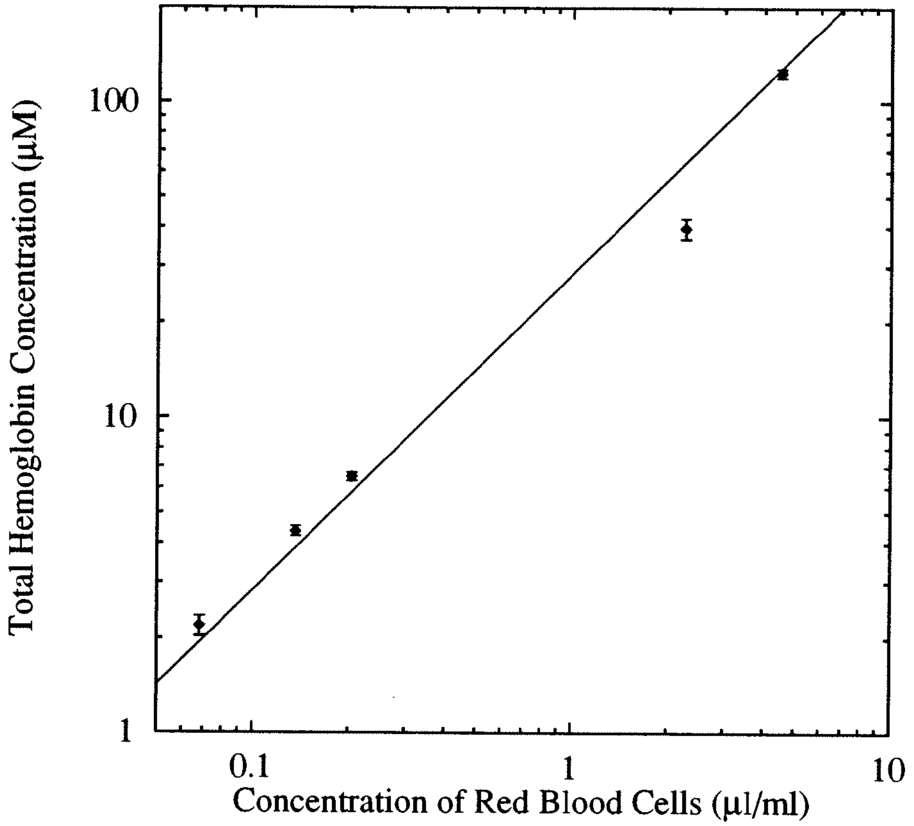

Figure 7.5: The total hemoglobin concentration, determined spectroscopically at visible and near-infrared wavelengths, is plotted against the red blood cell concentration of the phantom. The three lowest concentrations were obtained at visible wavelengths, while the higher concentrations were obtained at infrared wavelengths. The red blood cell concentration is the volume of red blood cells added to the phantom divided by the total volume of the phantom. The error bars are the standard deviations returned from the fitting process, and the line is the best one parameter fit to the data points (slope = 28.3 ± 5.6 mM $(\mu l/ml)^{-1}$).

vals to monitor the shift in the oxyhemoglobin absorption spectra as a function of oxygen partial pressure. Spectra were obtained soon after mixing in the yeast to determine if the yeast absorption was a significant addition to the background. This did not seem to occur unless excessive amounts of yeast were added. As deoxygenation occurred, spectra were obtained using both 4 s and 45 s integration times. Experiments were conducted at a central wavelength of 560 nm to obtain the visible deoxygenation spectra and repeated using approximately thirty times the red blood cell concentration at a central wavelength of 740 nm to obtain the near-infrared deoxygenation spectra. Figures 7.6 and 7.7 illustrate the characteristic spectral shifts of oxyhemoglobin which were observed as the oxygen partial pressure was lowered from approximately 160 to 0 torr. The data obtained in the visible, shown in Figure 7.6, were obtained with a 45 s integration time, while the near-infrared data, shown in Figure 7.7, were obtained with a 4 s integration time. The characteristic isosbestic points in the visible occur at wavelengths of 506, 522, 548, 568 and 585 nm, while the peaks of oxyhemoglobin appear at 542 and 577 nm, and the deoxyhemoglobin peak appears at 552 nm. The near-infrared peak of deoxyhemoglobin is observed at approximately 758 nm and the near-infrared isosbestic point occurs near 800 nm, though a precise determination of these last two wavelengths is difficult due to the reduced signal-to-noise ratio characteristic of the data acquired with a 4 s integration time. With a 45 s integration time, these spectra have a similar signal-to-noise ratio as the visible spectra in Figure 7.6, and a more precise determination of these wavelengths should be possible. Near-infrared spectra obtained with a 45 s integration time are shown for comparison in Figure 7.8. In both Figure 7.7 and 7.8 the oxygenated and deoxygenated spectra are nearly identical for wavelengths greater than 790 nm, so a still longer integration may be needed to locate the isosbestic point near 804 nm. The majority of the observed peaks and isosbestic points agree to within 1 nm of those obtained in carefully prepared extinction measurements of non-scattering hemoglobin solutions, as reported, for example, by Zijlstra and Buursma (1987).

The reconstructed scattering spectra obtained simultaneously with the absorption spectra in Figures 7.6, 7.7, and 7.8 are shown in Figures 7.9, 7.10, and 7.11, respectively. In both visible and near-infrared experiments, while absorption changed consistently with the local oxygen partial pressure, no trends in the scattering coefficient were observed. This is an indication that the steady-state diffuse reflectance technique is capable of separating changes in absorption from changes in scattering as discussed previously in Chapter 6. In these two experiments, the variation in the scattering coefficient determined at visible wavelengths was smaller than that at near-infrared wavelengths. It is unclear exactly why this is so, though it is likely due to the stability of the phantom. While the experiment in the visible was completed in approximately 45 minutes, deoxygenation in this near-infrared experiment took three times as long. Nevertheless, no systematic variation in scattering was observed in either experiment.

Once the absorption spectra had been obtained, the background spectrum was subtracted and Equation (7.1) was fit to the resulting red blood cell spectra. Air-saturated and deoxygenated data sets are shown in Figures 7.12 and 7.13 for the visible and near-infrared, respectively, along with the best-fit spectra. The error

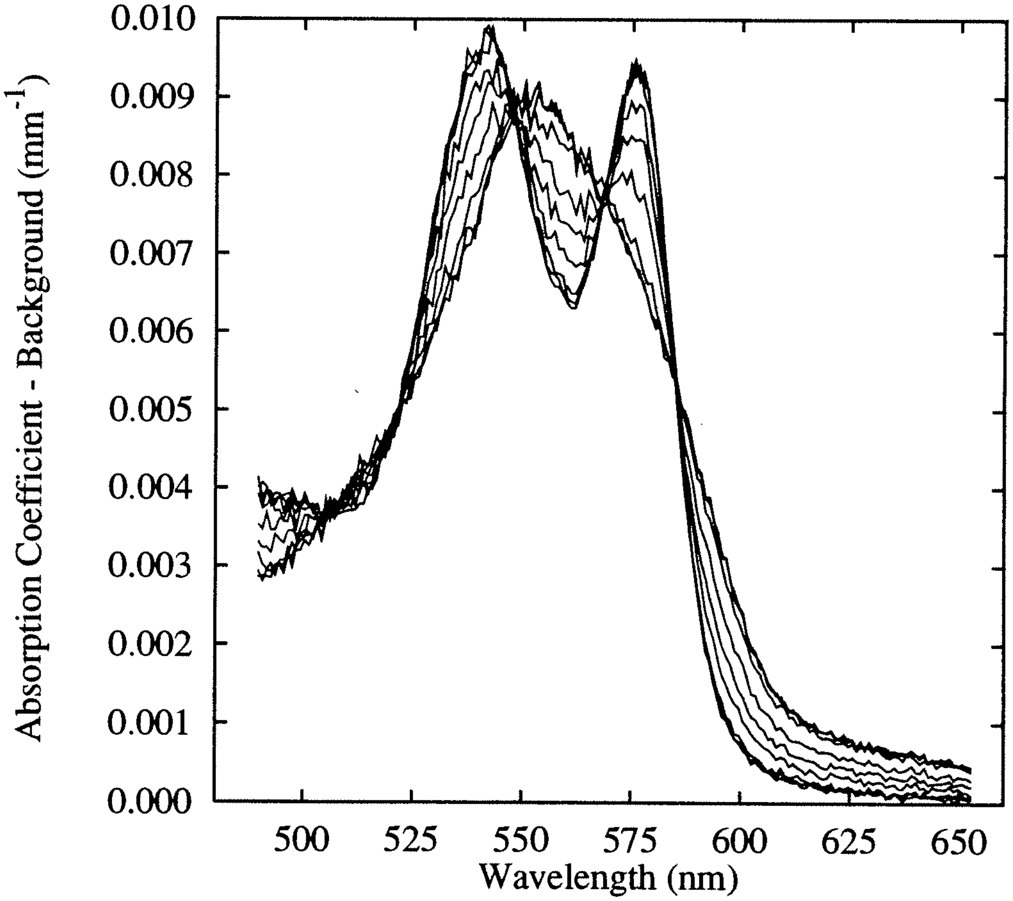

Figure 7.6: Several background-subtracted visible wavelength absorption spectra obtained from a Liposyn-II®-red blood cell-yeast phantom as the yeast deoxygenated the phantom. Data were obtained with a 45 s integration time. The error bars have been removed for clarity.

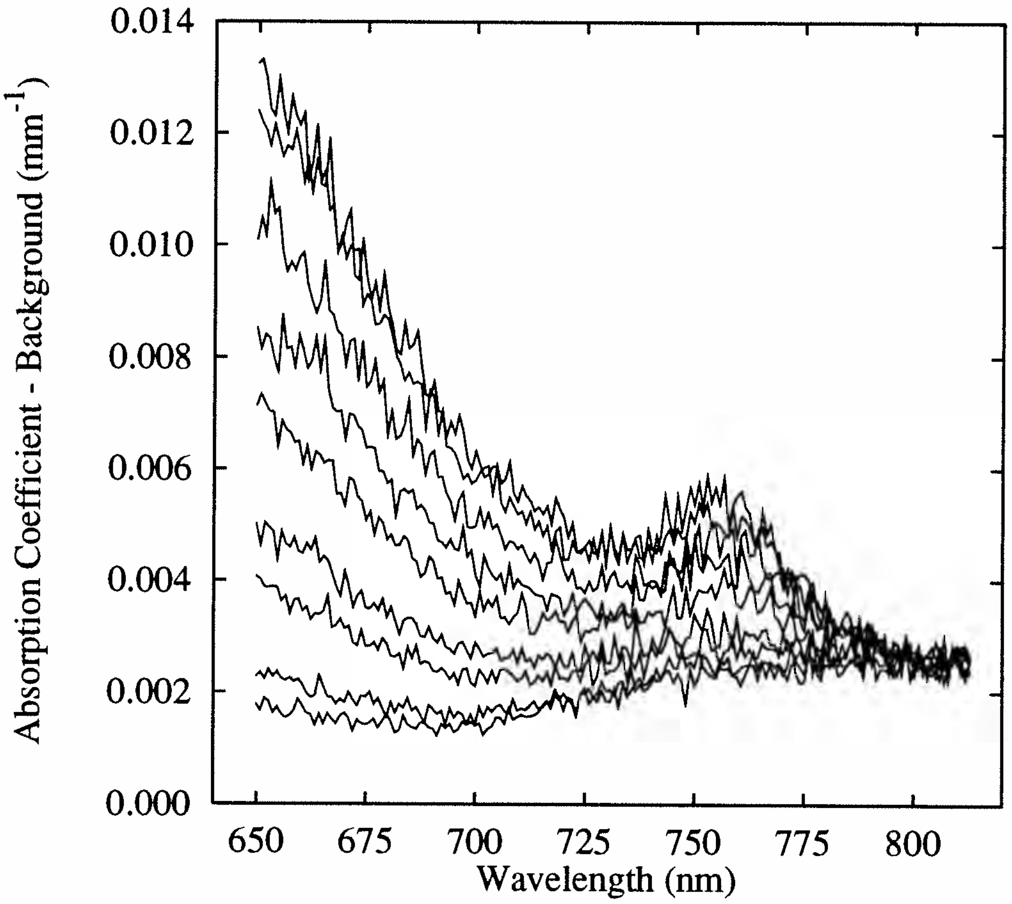

Figure 7.7: Several background-subtracted near-infrared absorption spectra obtained from a Liposyn-II®-red blood cell-yeast phantom as the yeast deoxygenated the phantom. Data were obtained with a 4 s integration time. The error bars have been removed for clarity.

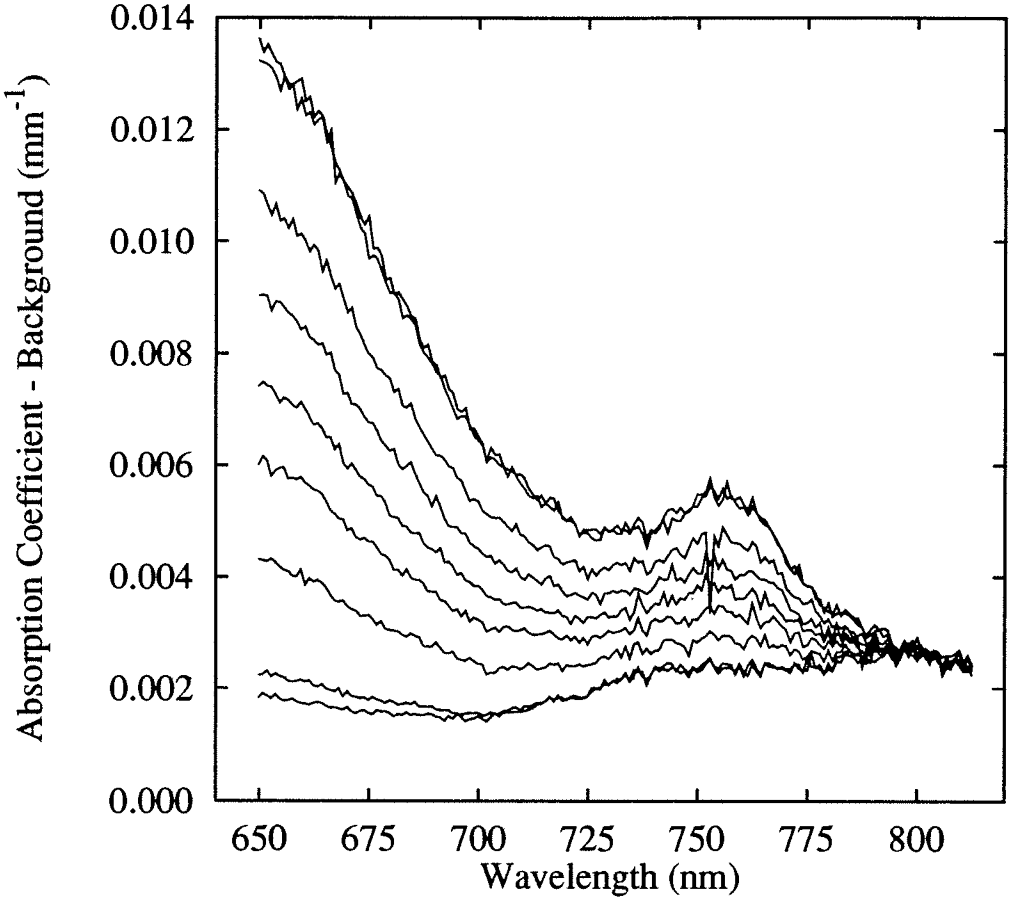

Figure 7.8: Several background-subtracted near-infrared absorption spectra obtained from a Liposyn-II®-red blood cell-yeast phantom as the yeast deoxygenated the phantom. Data were obtained with a 45 s integration time. These spectra were obtained from the same phantom as the spectra of Figure 7.7.

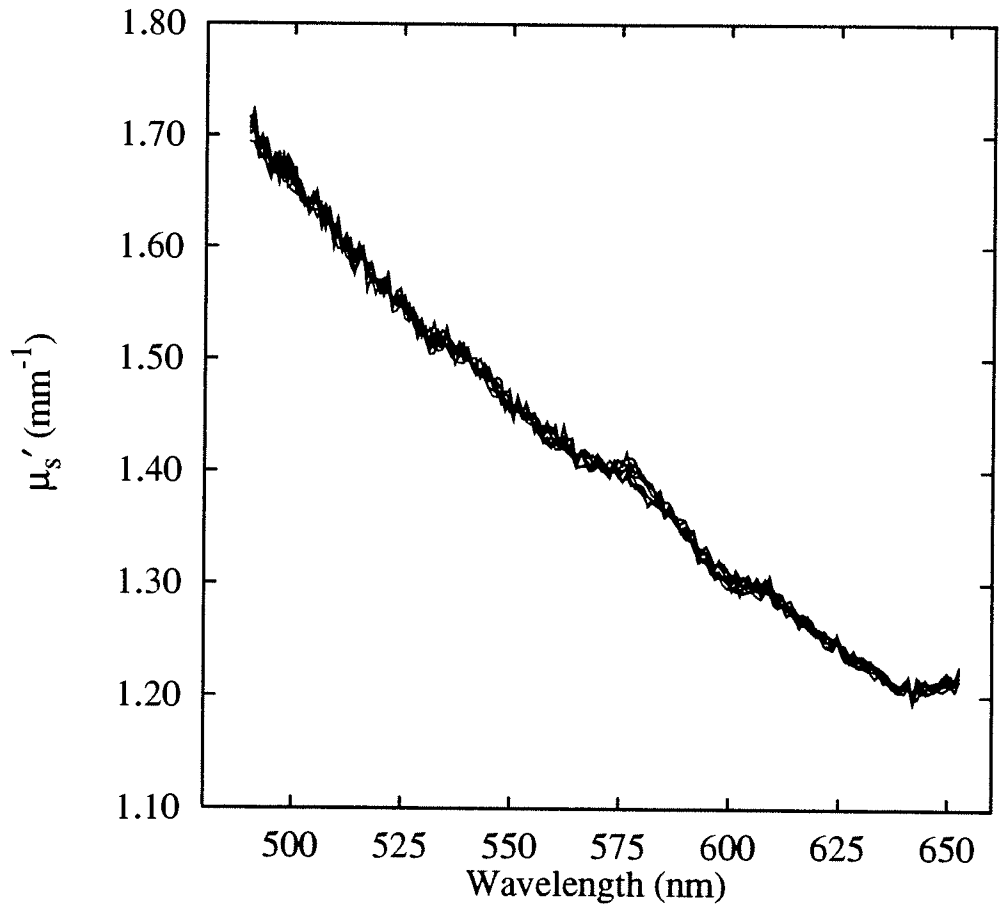

Figure 7.9: Several scattering spectra from a Liposyn-II®-red blood cell-yeast phantom obtained simultaneously with the absorption spectra of Figure 7.6. No statistically significant changes in scattering were observed during deoxygenation.

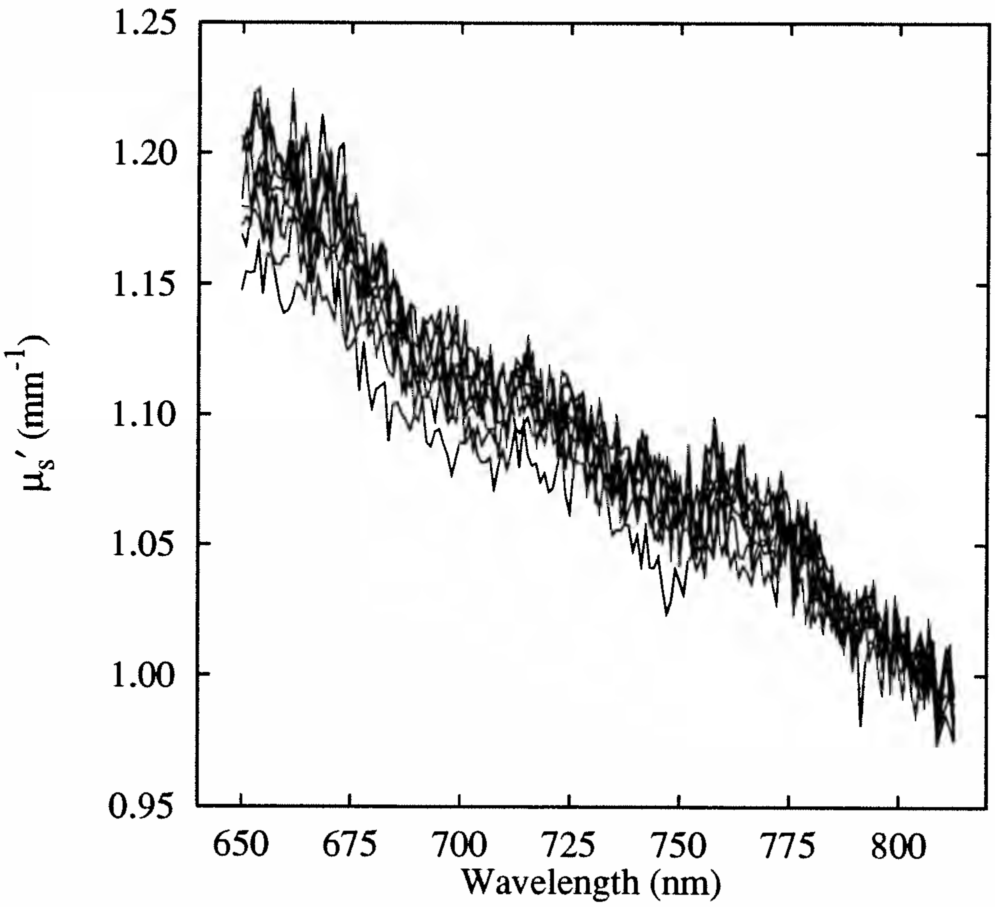

Figure 7.10: Several scattering spectra from the Liposyn-II®-red blood cell-yeast phantom obtained simultaneously with the absorption spectra of Figure 7.7. No statistically significant changes in scattering were observed during deoxygenation.

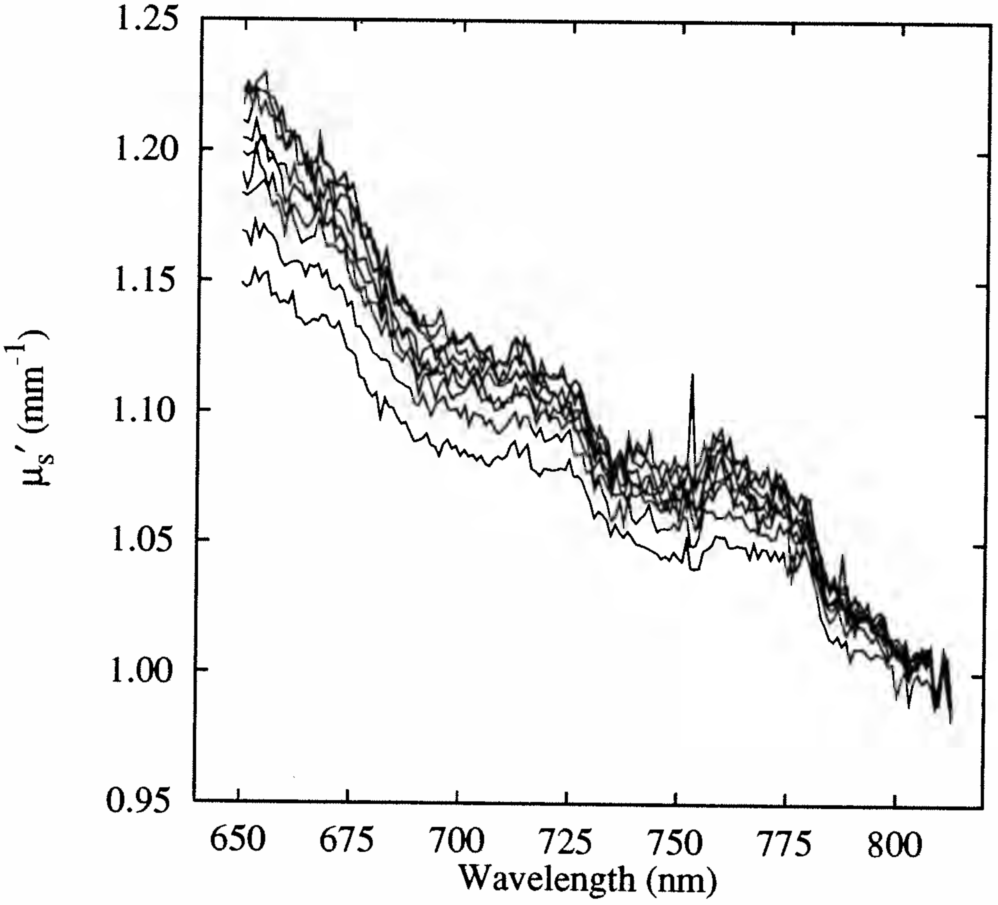

Figure 7.11: Several scattering spectra from the Liposyn-II®-red blood cell-yeast phantom obtained simultaneously with the absorption spectra of Figure 7.8. These spectra were obtained from the same phantom used to obtain the spectra of Figure 7.10, but a 45 second integration time was used.

bars have been omitted for clarity. Excellent fit results are obtained in the visible for both the intense absorption bands and the low absorption tail. This indicates that the subtracted absorption spectrum is well characterized by the oxygenated and deoxygenated components of hemoglobin. The best-fit near-infrared spectra deviate slightly from the observed spectra between 710 and 760 nm for both the oxygenated and deoxygenated spectra. This disagreement has been reproduced in several experiments so it is not expected to be a spurious effect or due to improper background subtraction. It is more likely that the discrepancy is due to real differences between the extinction spectra used in the fitting process and the near-infrared absorption spectra obtained from human red blood cells. This seems reasonable given the difficulty of obtaining accurate extinction spectra.

The linear fitting coefficients C_{HbO_2} and C_{Hb} estimated from fits such as those shown in Figures 7.12 and 7.13 report the best estimate of the concentration of oxy- and deoxyhemoglobin, respectively. In Figures 7.15 and 7.16 these values are plotted as a function of time since the addition of yeast to the phantom for measurements made at visible (Figure 7.15) and near-infrared (Figure 7.16) wavelengths. The oxygen partial pressures measured by an oxygen electrode during each of these experiments are shown for reference in Figures 7.17 and 7.18, respectively. While the pressure decays monotonically after the addition of yeast, no significant change in the relative concentration of oxy- and deoxyhemoglobin is apparent until the local partial pressure is reduced below 60 torr in each case. This is expected since hemoglobin has a high affinity for oxygen, and the partial pressure at which 50% is deoxygenated does not occur until approximately 20-30 torr, depending on

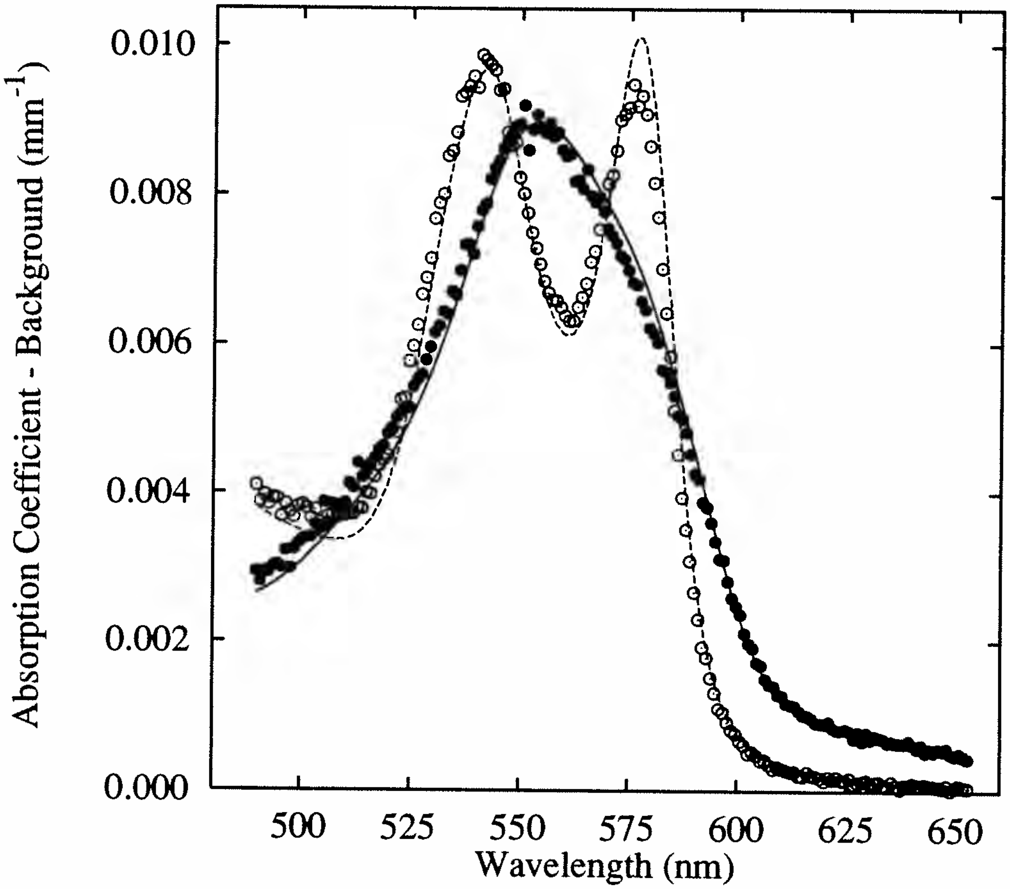

Figure 7.12: The best-fit visible spectra obtained from an oxygenated and a deoxygenated Liposyn-II®-red blood cell-yeast phantom. The data points were obtained by steady-state diffuse reflectance spectroscopy using a 45 s data acquisition interval, and the line is the best linear combination of oxy- and deoxyhemoglobin extinction spectra of Figure 7.3 . The error bars have been omitted for clarity.

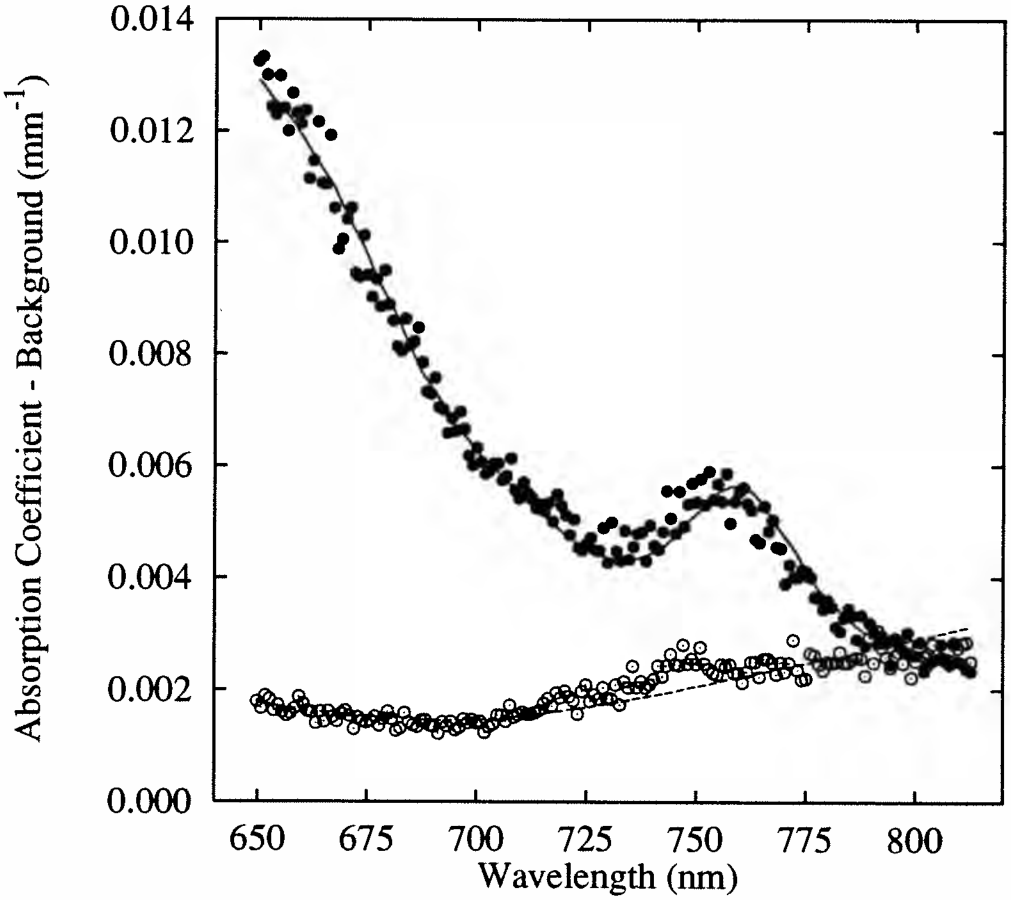

Figure 7.13: The best-fit near-infrared spectra obtained from an oxygenated and a deoxygenated Liposyn-II®-red blood cell-yeast phantom. The data points were obtained by steady-state diffuse reflectance spectroscopy using a 4 s data acquisition interval, and the line is the best linear combination of oxy- and deoxyhemoglobin extinction spectra of Figure 7.4. The error bars have been omitted for clarity.

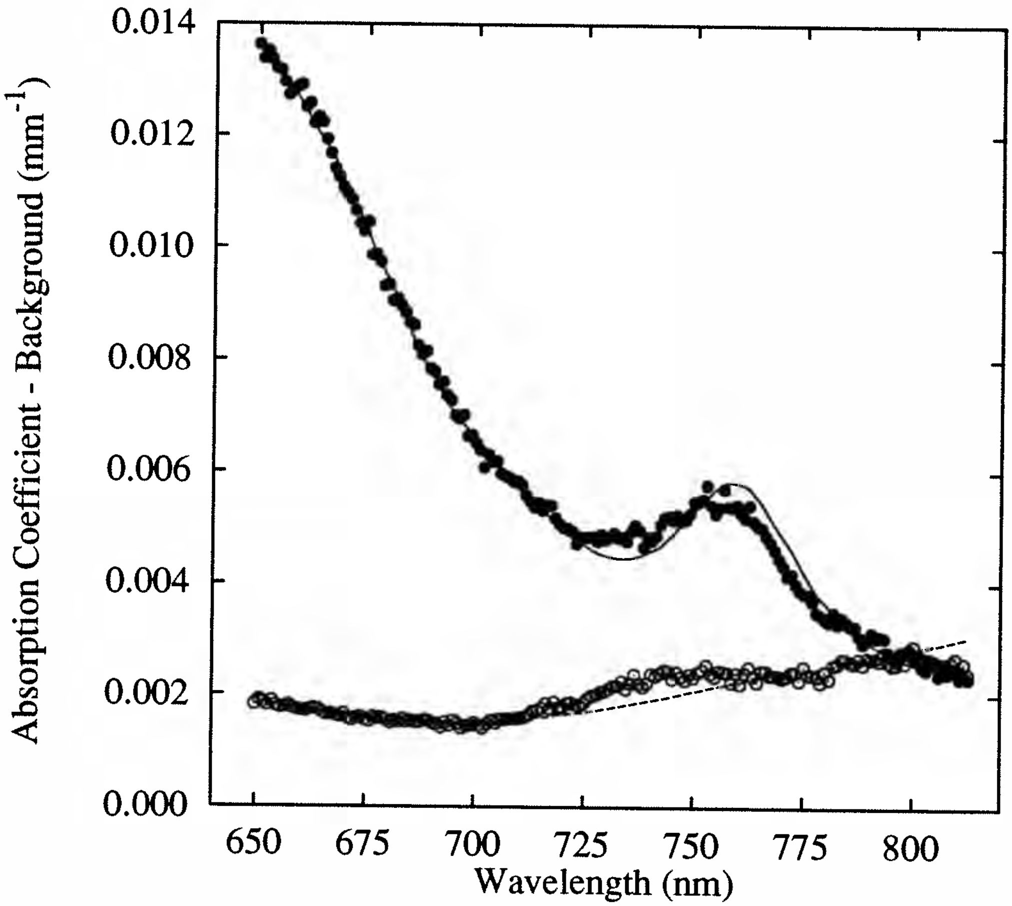

Figure 7.14: The best-fit near-infrared spectra obtained from an oxygenated and a deoxygenated Liposyn-II®-red blood cell-yeast phantom. The data points were obtained by steady-state diffuse reflectance spectroscopy using a 45 s data acquisition interval, and the line is the best linear combination of oxy- and deoxyhemoglobin extinction spectra of Figure 7.4. These spectra were obtained from the same phantom used to obtain the spectra of Figure 7.13.

a variety of parameters including organic phosphate concentration and pH (Benesch and Benesch, 1974). Below approximately 60 torr the relative proportions of oxy- and deoxyhemoglobin change quickly until at 0 torr they have inverted completely. The solid lines in Figures 7.15 and 7.16 indicate the total hemoglobin concentration measured during each experiment. With the exception of an early apparently artificial rise during the near infrared experiment, the lines are constant in keeping with experimental conditions.

For the experiment conducted in the visible, the concentrations of oxy- and deoxyhemoglobin are always positive, but this is not true for the near-infrared experiment. As the oxygen partial pressure approaches zero in this experiment, the oxyhemoglobin concentration is returned negative and a corresponding increase in the deoxyhemoglobin concentration occurs to guarantee no net increase in hemoglobin. This evidently is related to the poor fit of the deoxyhemoglobin curve depicted in Figure 7.13. The experimental data deviate enough from the extinction data of Wray *et al.* (1988) that to compensate for the discrepancy deoxyhemoglobin is overestimated and oxyhemoglobin is effectively subtracted.

If one plots the hemoglobin oxygen saturation, S, from Figures 7.15 and 7.16 against the oxygen partial pressure from Figures 7.17 and 7.18, the data points in Figures 7.19 and 7.20 are obtained. Hemoglobin oxygen saturation is known to be well described by the Hill equation,

$$S = \frac{{P_{O_2}}^n}{{P_{O_2}}^n + {P_{50}}^n}, \tag{7.4}$$

where n is the Hill constant, indicating the oxygen binding cooperativity of the

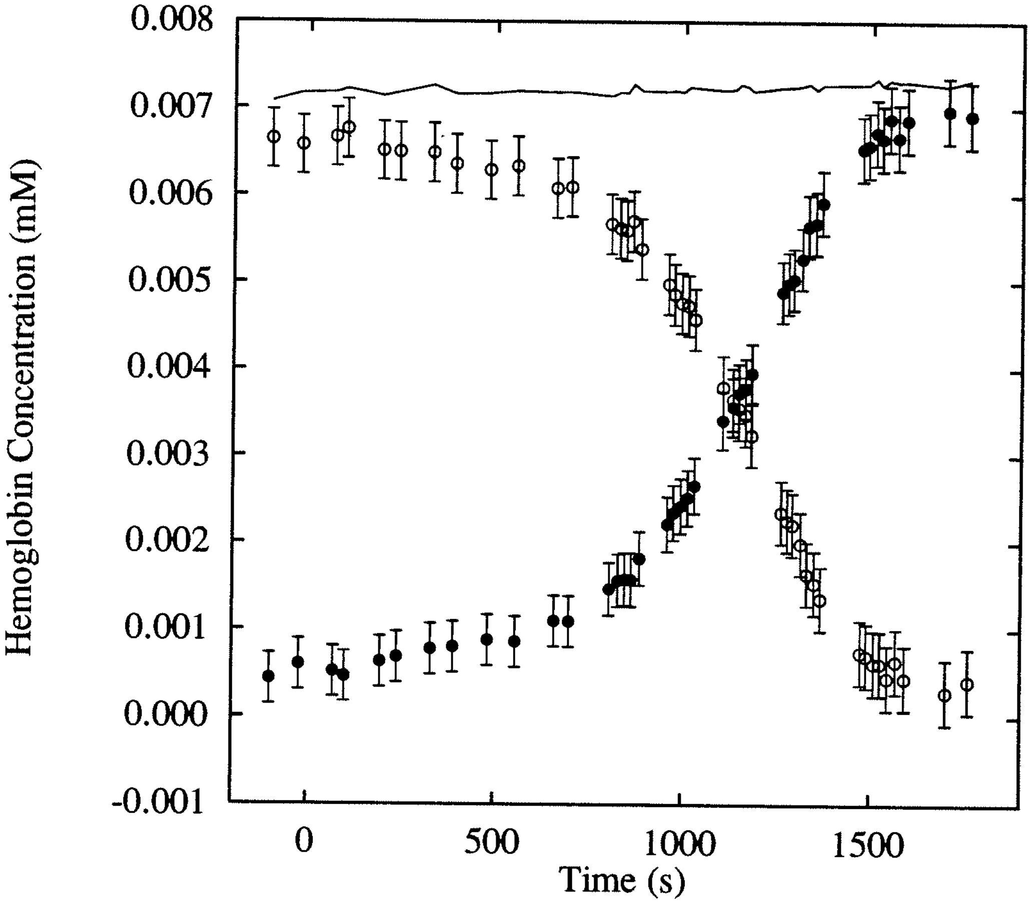

Figure 7.15: The concentrations of oxy- and deoxyhemoglobin in the Liposyn-II®-red blood cell-yeast phantom as determined by steady-state diffuse reflectance spectroscopy in the visible. The data points were determined as the best-fit coefficients from spectra such as those shown in Figure 7.12. Spectra were obtained periodically as yeast deoxygenated the phantom. The data acquisition time was 4 s for each data pair. The error bars are the returned standard deviations in the fitting parameters, and the solid line is the sum of the oxy- and deoxyhemoglobin concentrations. Yeast was added to the phantom at the zero time point.

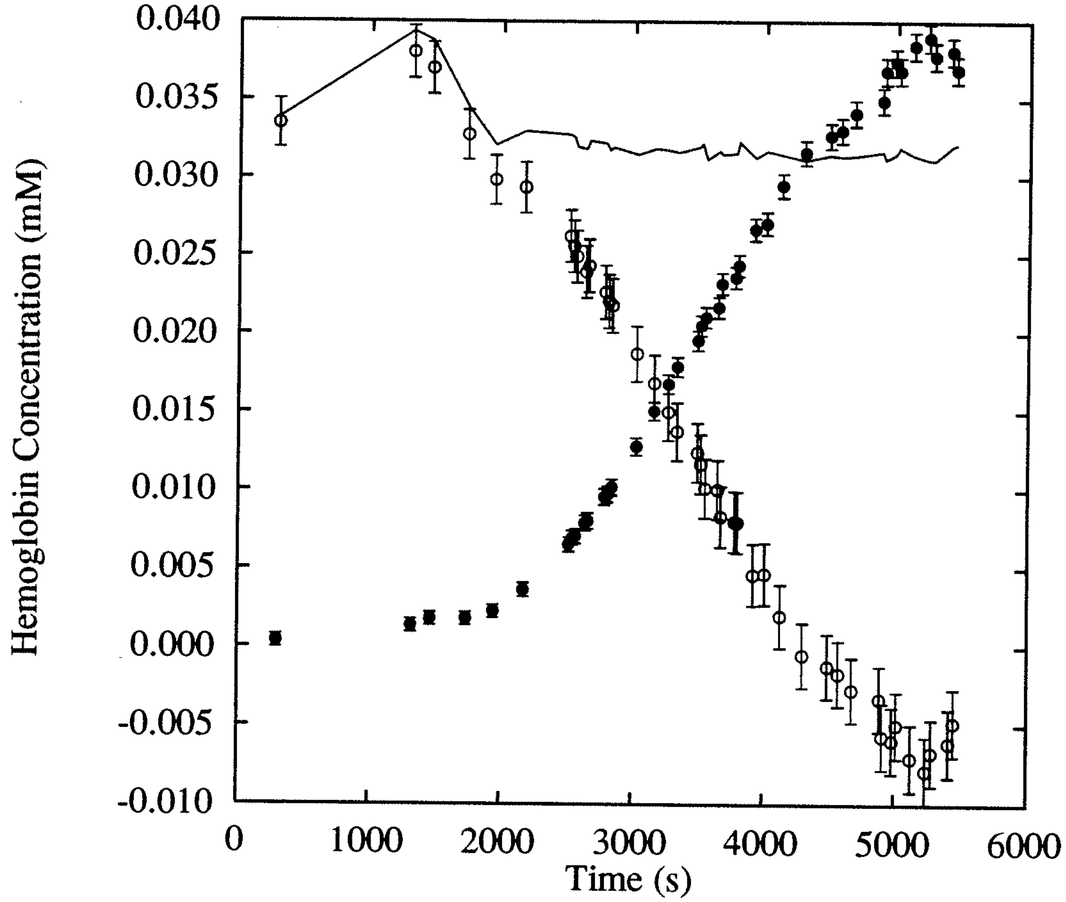

Figure 7.16: The concentrations of oxy- and deoxyhemoglobin in the Liposyn-II®-red blood cell-yeast phantom as determined by steady-state diffuse reflectance spectroscopy in the near infrared. As in Figure 7.15, the data acquisition time was 4 s.

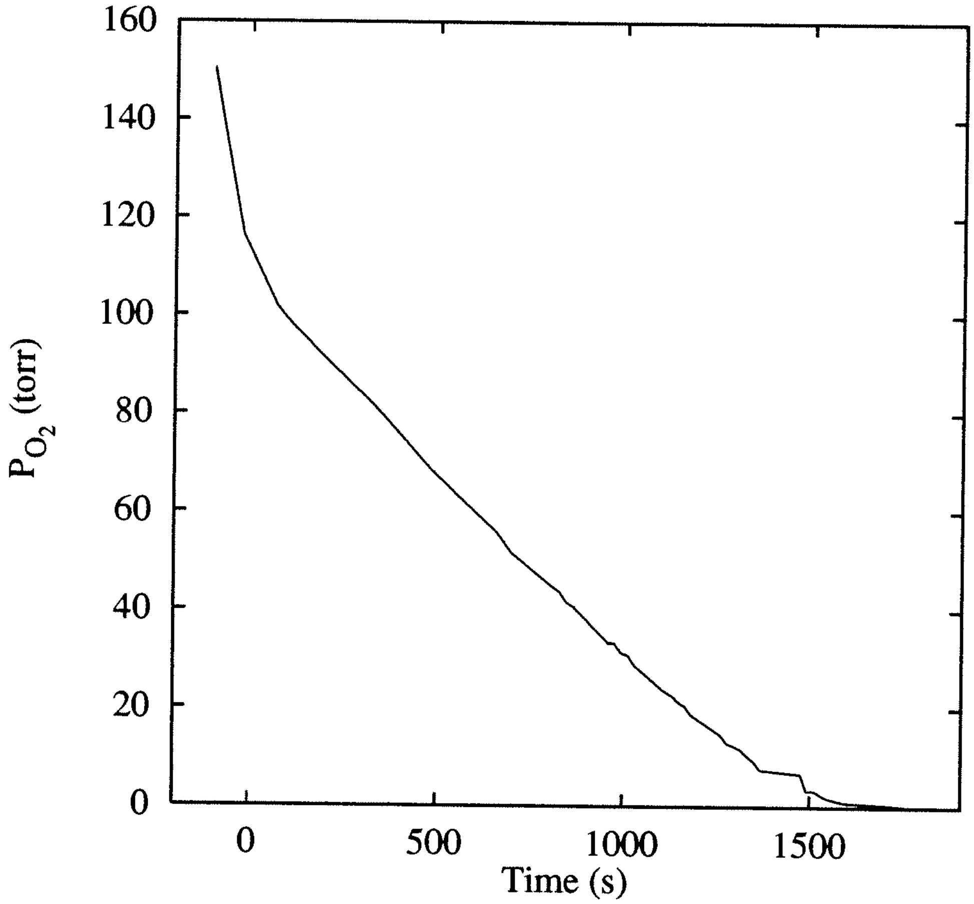

Figure 7.17: The oxygen partial pressure measured in the Liposyn-II®-red blood cell-yeast phantom with a Clark oxygen electrode (3 mm tip diameter) during the experiment depicted in Figure 7.15.

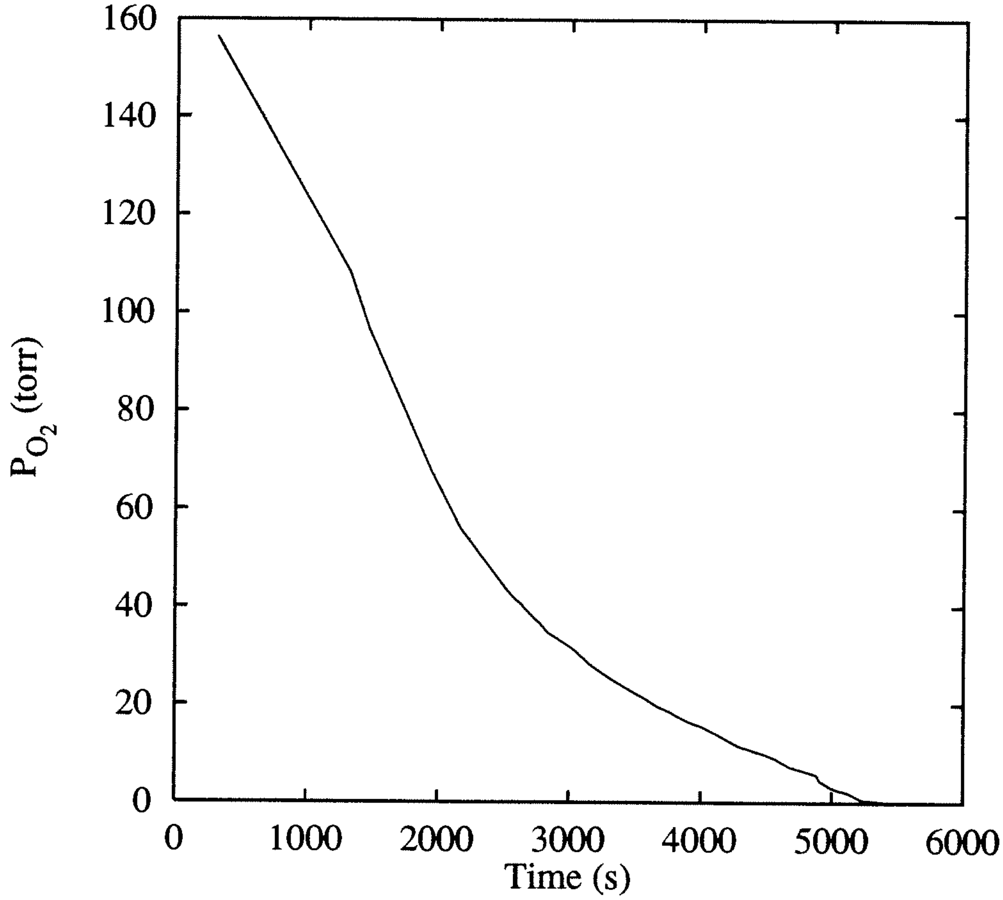

Figure 7.18: The oxygen partial pressure measured in the Liposyn-II®-red blood cell-yeast phantom with a Clark oxygen electrode (3 mm tip diameter) during the experiment depicted in Figure 7.16.

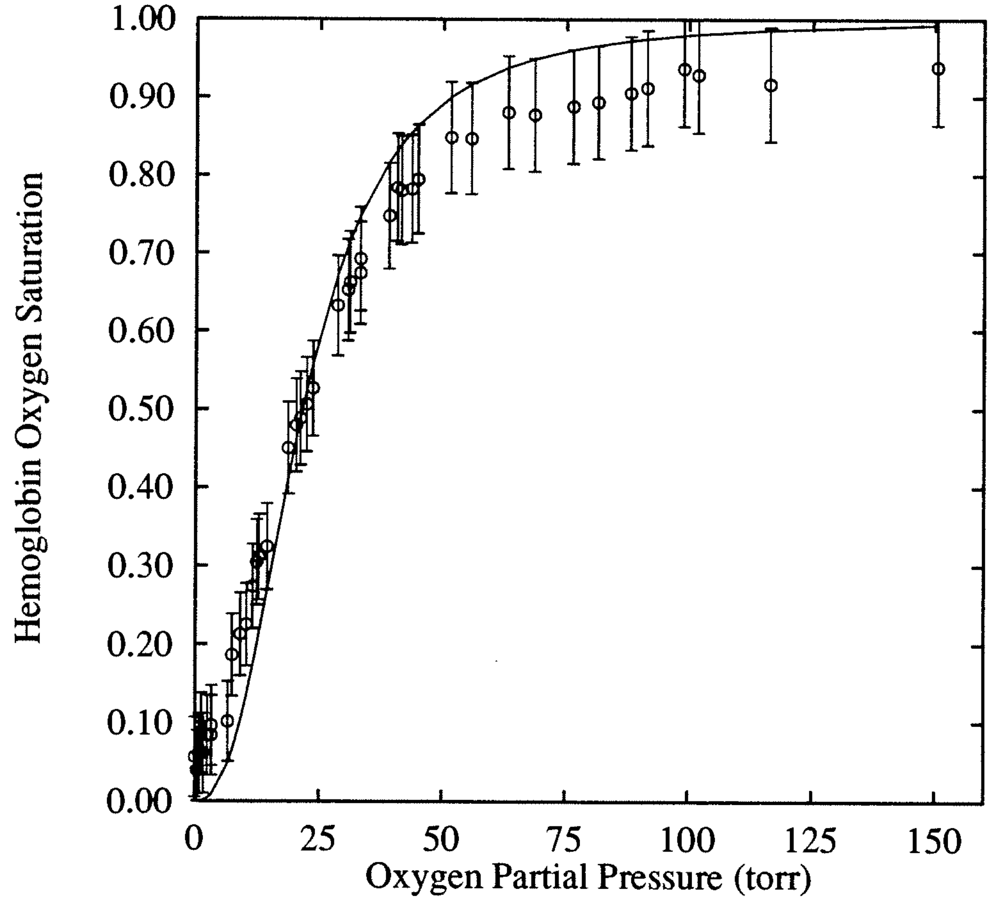

Figure 7.19: The fractional hemoglobin oxygen saturation, obtained from spectra in Figure 7.15, is plotted as a function of the measured oxygen partial pressure of the Liposyn-II®-red blood cell-yeast phantom, obtained from data in Figure 7.17. The error bars represent the standard deviation, and the line is the best two-parameter fit of Equation (7.4) to the data. A Hill coefficient of 2.53 ± 0.03 and a P_{50} of 21.6 ± 0.2 torr were obtained.

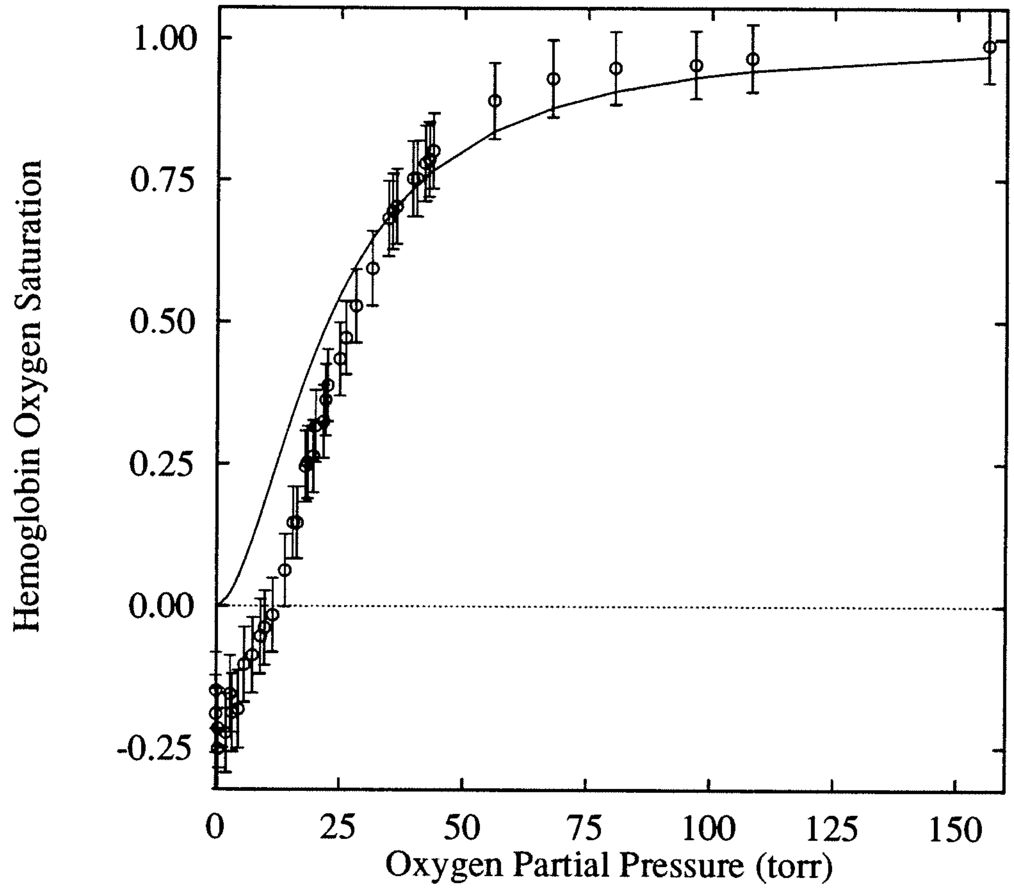

Figure 7.20: The fractional hemoglobin oxygen saturation, obtained from spectra in Figure 7.16, is plotted as a function of the measured oxygen partial pressure of the Liposyn-II®-red blood cell-yeast phantom, obtained from data in Figure 7.18. The error bars represent the standard deviation, and the line is the best two-parameter fit of Equation (7.4) to the data. A Hill coefficient of 1.79 ± 0.04 and a P_{50} of 22.5 ± 0.5 torr were obtained.

four binding sites of the hemoglobin molecule, P_{50} is the oxygen partial pressure at which 50% of the binding sites are deoxygenated and P_{O_2} is the local oxygen partial pressure. The lines in Figures 7.19 and 7.20 represent the best fits of Equation (7.4) to the data points. This yields Hill coefficients of 2.53 ± 0.03 and 1.79 ± 0.04, and a P_{50} of 21.6 ± 0.2 and 22.5 ± 0.5 torr for the visible and near-infrared cases, respectively. The fit results from the experiment conducted in the visible are close to the expected Hill constant (2.8-3.0 for normal human blood (Bunn and Forget, 1983), and 20-30 torr for P_{50} (Benesch and Benesch, 1974), though the fitted data for the near-infrared experiment are likely to be incorrect because of the erroneous oxygen saturation at low oxygen partial pressures.

7.4 The Effects of Additional Chromophores

While we have been successful in using this technique with Liposyn-II®-red blood cell-yeast phantoms, the ability to absolutely characterize oxy- and deoxyhemoglobin concentrations is expected to be dependent upon characterizing the background absorption spectrum. The hemoglobin absorption spectrum was reconstructed because it was possible to measure the absorption spectrum of the Liposyn-II® phantom *prior* to adding red blood cells. Naturally, the situation is much more complex *in vivo* due to the presence of additional chromophores, especially in the visible but also in the near infrared. Melanin and water, for example, add an oxygen independent background, while cytochrome aa_3, present in the mitochondria, provides an oxygen dependent background. Matcher *et al.* (1995b) have recently reviewed several near-infrared algorithms which seek to separate the effects of oxy- and deoxyhemoglobin as well as cytochrome aa$_3$ by monitoring several discrete wavelengths in the near-infrared attenuation spectrum. Since these species are expected to be the only significant oxygen-dependent chromophores in the near infrared, it is possible to determine changes in absorption due to these chromophores if one assumes that the background is unchanging. With optical techniques that are incapable of separating the effects of absorption from scattering, additional assumptions regarding the shape and dynamics of the scattering spectrum are also needed. Typically, these assumptions are that the scattering coefficient is constant and stationary such that the ratio of two attenuation coefficients measured at different wavelengths can be interpreted as the ratio of the actual absorption coefficients (Liu *et al.*, 1995a). These assumptions are likely to be justified if the wavelength range is narrow enough, since the wavelength dependence of scattering is slight. Taking the scattering spectrum of Liposyn-II® in the infrared as an example, the ratio of the measured transport scattering coefficients at 760 nm and 800 nm is approximately 1.06. Therefore, ignoring this wavelength dependence should result in a 6 percent systematic error in the ratio of the absorption coefficients determined for two wavelengths, since the measured attenuation, μ_{eff}, depends on the product of the absorption and transport scattering coefficients (Equation (4.28). Since the wavelength dependence of scattering is more severe in the visible, one would expect the error to increase accordingly. A more sophisticated approach described by Matcher *et al.* (1995b) actually corrects for the wavelength dependence of the scattering spectrum, but a separate measurement is necessary to obtain these correction factors.

It is conceivable, using the technique outlined here, that one could increase the number of extinction spectra to measure the other chromophores absolutely without the need for any assumptions regarding the scattering spectrum. In general, reflectance must be obtained for at least one wavelength per independent absorber. Given the number of wavelengths which are simultaneously sampled, one could easily do this with this technique provided that accurate extinction spectra are known. As we have discovered, this can be quite a challenging requirement given the complex dependence on the micro-environment and sample variation which is likely to occur. Wray *et al.* have suggested, for example, that *in vitro* cytochrome aa_3 extinction spectra may be unreliable and instead obtained the tissue background spectrum *in vivo* by replacing the blood with a fluorocarbon-based substitute which would not interfere with cytochrome aa_3. This same procedure has been followed by other investigators (Hazeki and Tamura, 1987). While this technique may in fact offer the best solution to a difficult problem, a less invasive technique would certainly be preferred.

We have chosen to use a white-light source rather than more intense laser sources because of the additional information provided by a high bandwidth source. While two-, three- and four-wavelength techniques using bright monochromatic sources can be used to identify a discrete number of tissue chromophores with optimal signal-to-noise levels and data acquisition rates, these techniques are vulnerable to unanticipated changes in tissue absorption. For example, an optimized two-wavelength technique would incorrectly correlate the presence of methemoglobin, which has increased near-infrared absorption compared to oxyhemoglobin and a pronounced peak at 630 nm, with decreased oxygen saturation and increased blood volume. Only when additional wavelengths are analyzed would it become clear that the assumption that absorption changes were due only to oxy- and deoxyhemoglobin was invalid. Generally, the penalty for using a white-light source is reduced intensity due to poor fiber-optic coupling and transmission, but this is offset by the additional data that is obtained at wavelengths that are difficult to obtain with current lasers. In practice, however, we have found that it is possible to obtain a brightness in the near infrared that is comparable to that reported by researchers using laser sources. Figures 7.15, 7.16, 7.19, and 7.20 were obtained with four second data acquisition rates, and the observed fluctuations in the determined concentrations are approximately 5%. By fitting the entire spectral range (170 data points) the effective signal-to-noise is increased by almost a factor of 10 compared to a similar two-wavelength measurement provided the data are randomly distributed about the actual absorption coefficients.

Figures 7.13, 7.16, and 7.20 illustrate a potential weakness of this technique, though it applies to any technique which relies on accurate extinction spectra. When the extinction spectra disagree systematically with background-subtracted absorption spectra, as is evident in Figure 7.14, anomalous fitting results can occur. In the case of the near-infrared data which we have collected, the deoxyhemoglobin peak appears to be blue-shifted by several nanometers compared to the extinction spectra. It is interesting to note that the shift in this peak is in the direction of the near-infrared water peak at 740 nm and may be associated with an increased water background. This effect has been reproduced on several occasions, however, so it is not anticipated that the shift is due to an improper background subtraction. Rather, it appears as though the concentration of water has increased after the addition of red blood cells and yeast. Equally plausible is that the hemoglobin extinction spectra are in disagreement with the red blood cell spectra. Regardless of the cause, the effect results in the erroneous determination of the oxyhemoglobin concentration as is evident in Figures 7.16 and 7.20. Since the oxyhemoglobin spectrum increases approximately linearly in the 710 to 760 nm spectral region, it is possible to produce the necessary blue-shift in the extinction spectra by overestimating the contribution due to deoxyhemoglobin and subtracting an appropriate amount of oxyhemoglobin. Hence, the best-fit oxyhemoglobin concentration is negative, and a negative saturation results in the Hill plot. This is purely artificial as is evidenced by the more agreeable visible spectra and Hill plot depicted in Figures 7.15 and 7.19. We are currently collecting additional extinction spectra to rule out the latter of the two proposed scenarios. Nevertheless, this is an important consideration which needs to be addressed by any technique which attempts to resolve the various chromophores that constitute the measured absorption spectrum.

7.5 Conclusions

The experiments outlined here demonstrate that the steady-state diffuse reflectance apparatus based on original designs by Wilson, Patterson and Farrell can be used to monitor hemoglobin oxygen saturation and total concentration in tissue simulating phantoms non-invasively with data acquisition rates as fast as 0.25 Hz with our present equipment. Unlike previous steady-state methods, the technique described here can be used to absolutely quantify hemoglobin absorption in the presence of a changing scattering environment without any assumptions regarding the scattering spectrum or additional measurements needed to uncouple scattering from absorption in attenuation measurements. Furthermore, the technique is based upon reflectance measurements which should enable it to be used in situations where transmission measurements are difficult or impossible.

Chapter 8

Optical Spectroscopy *In Vivo*

8.1 Introduction

In Chapters 6 and 7, it was established that steady-state radially-resolved diffuse reflectance spectroscopy was capable of independently measuring the transport scattering (μ_s') and absorption (μ_a) coefficients of a variety of tissue-simulating phantoms consisting of aqueous solutions of Liposyn-II® and chromophores of interest. While these phantoms have been chosen with optical properties that are characteristic of the biological tissues in which we are interested (Cheong *et al.*, 1990; Duck, 1990; Wilson and Jacques, 1990), they do not adequately mimic the structural characteristics of biological tissue. It may be the case that the tissue of interest may be considered flat on the optical length scales typical of tissues, but this has yet to be demonstrated. In particular, studies conducted on the head or extremities of human children may be influenced by the curved nature of the boundary (Pogue and Patterson, 1994). Furthermore, in studies conducted on rodent tumor models, which account for the majority of cancer research studies, the assumption of a planar boundary is clearly questionable.

Another simplification that has been appropriate for the phantom studies in previous chapters but must be carefully considered for biological tissues is the assumption of homogeneity. While micro-inhomogeneity is responsible for the high scattering cross sections encountered in turbid media, biological tissues are also characterized by heterogeneity on much longer length scales. Structures such as the layers of tissue that constitute skin (epidermis, dermis, subcutaneous fat) and the various branches of the circulatory system (capillaries, venules, arterioles, veins, arteries) exemplify the possible complexity of the problem. For example, in an attempt to determine the optical properties of a tumor, injected photons are likely to encounter both the high albedo cellular space as well as the capillaries which have a much lower albedo. In order to interpret measurements made in such an environment, it is necessary to develop computational models capable of capturing the fundamental features of the physical system.

Recently, Liu *et al.* (1995b) have developed a heterogeneous resin-tube phantom to study the effect that blood vessels can have on the apparent absorption coefficient of a tissue measured with time-domain reflectance spectroscopy. A series of experiments on phantoms constructed with regular arrays of hollow tubes with specified diameters embedded in a scattering resin indicated that the apparent absorption coefficient is dependent not only on the volume fraction of absorber added to the tubes, but also on the tube radius. These results hold for phantoms with tube diameters between 1.6 mm and 6.4 mm when the absorption coefficient of the absorber added to the tubes was in the range of 0.1 mm^{-1} to 0.5 mm^{-1}. This is appropriate for simulating the effect of large blood vessels given the fact that the blood hemoglobin concentration is approximately 2 mM (150 g/L at 67000 g/mol) and the extinction coefficient for hemoglobin in the near infrared can range from 0.151 mM^{-1} mm^{-1} to 0.530 mM^{-1} mm^{-1}. Extrapolation of the results from these phantoms further indicated, however, that in tissues with vessels less than 1.0 mm in diameter the apparent absorption coefficient should only be dependent on the blood volume fraction in the tissue. This is likely to be the case for the majority of tissues.

This study demonstrates the expectation that the measured absorption coefficient for a heterogeneous tissue will be dependent on the tissue optical properties encountered by photons, weighted by the pathlength taken in distinct optical regions. When the optical properties are not too disparate and the optical regions are equally accessible, measurements will likely lead to an estimation of the spatially averaged optical properties. However, if a single optical region is primarily probed by the technique, one would expect the optical properties of that region to be determined.

In this chapter, Monte Carlo simulations of steady-state radially-resolved diffuse reflectance spectroscopy are conducted for a variety of physical situations which are likely to be encountered *in vivo*. I begin by describing a subcutaneous tumor geometry, to be used in OOMC calculations, in which the effects of a curved interface as well as distinct heterogeneous regions – namely skin, tumor and nontumorous tissue – are explored. Simulations conducted in this geometry are analyzed with the reflectance expressions obtained *via* the dipole approximation which was thoroughly investigated in Chapters 5 and 6 for a planar interface and a semi-infinite turbid medium. The goal of tumor spectroscopy *in vivo* will be to accurately obtain tumor optical properties, though this will be complicated by both geometry and the heterogeneous layered nature of the subcutaneous tumor. Although the dipole expression for the diffuse reflectance was derived for a planar interface in a semi-infinite half space, it is useful to investigate the extent to which this simple model can be used in more complex situations.

8.2 Considerations for Non-Planar Air-Tissue Boundaries

Often the tissue of interest is of limited extent and the air-tissue boundary is curved. In this case, the geometry for photo-diffusion may not be a semi-infinite half space, but may be modeled more appropriately as a sphere or an infinite or finite cylinder. The time-dependent Green's functions for the photo-diffusion equation (Equation 4.18) have recently been compiled by Arridge *et al.* (1992) for a variety of geometries such as these. In principle, these Green's functions can be used to obtain analytic expressions for the diffuse reflectance and fluence rate in the tissue, but due to the complexity of these solutions they are a less than desirable starting point when attempting to ascertain the optical properties of a turbid medium experimentally. Alternatively, since the length scale of scattering interactions is typically much smaller than the radius of curvature of tissue boundaries or the geometrical extent, it is worthwhile to determine the degree to which the dipole-source approximation described in Chapter 4 can be successfully applied to certain practical situations.

One application of considerable interest is the determination of the optical properties of a subcutaneous tumor in a rodent model. Tumors which are considered to be of treatable size for PDT are typically 7 mm in diameter or less. Figure 8.1 is a histological section of the R3230AC adenocarcinoma tumor which was grown in the Fischer rat. The pronounced curvature of the boundary is typical of subcutaneous tumors that are grown in this animal model. This histological section is of a tumor that has been removed from the animal; *in vivo*, it would be found on the chest or abdomen. As can be seen in the figure, a subcutaneous tumor will have a layer of skin above the actual tumor. Thus, another issue to consider is the effect of the skin layer on the diffuse reflectance. Furthermore, surrounding the tumor in the animal will be normal tissue, particularly below the actual tumor. In general, the skin, the tumor, and the normal tissue may all have distinct optical properties, and photons injected into the tumor will likely encounter all three of these distinct regions.

To ascertain the effect of these complications on the diffuse reflectance from a subcutaneous tumor, Monte Carlo simulations of photo-diffusion were conducted in a geometrically realistic heterogeneous environment. To mimic the actual physical situation, a sphere of a given diameter was embedded some distance below a

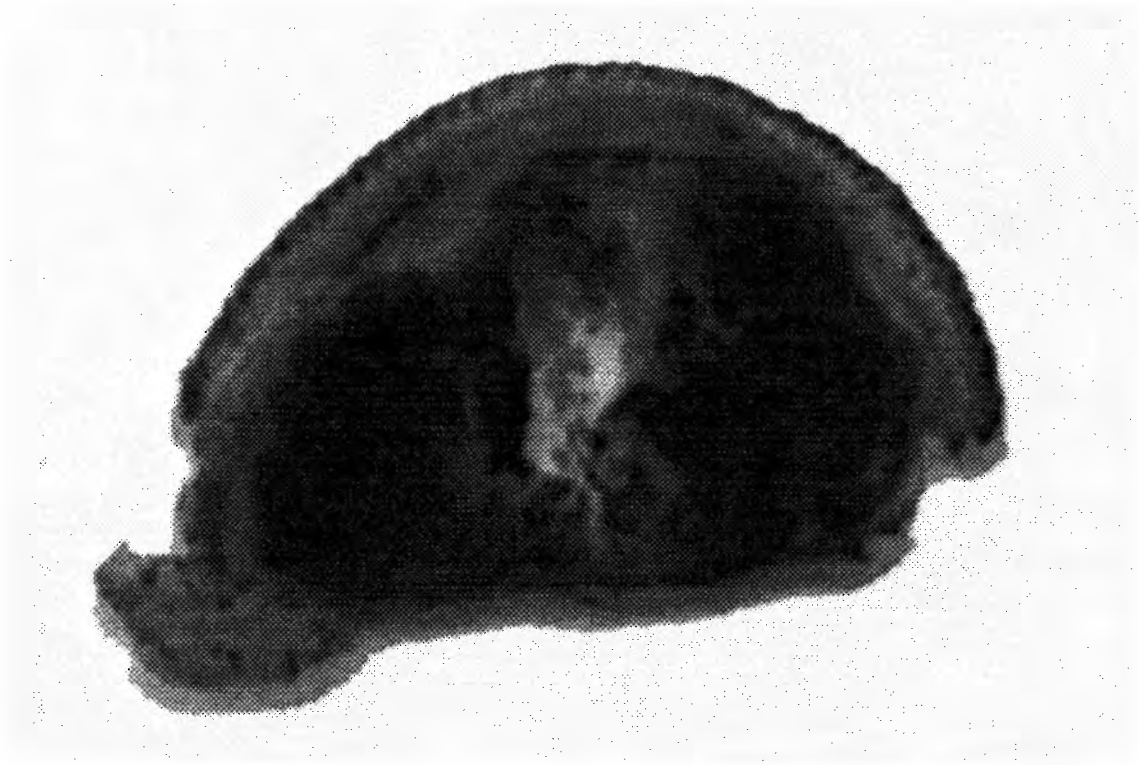

Figure 8.1: A histological section of an R3230AC tumor excised from a Fischer rat. The width of this tumor is approximately 1 cm, and a layer of skin can be seen above the tumor itself.

hemisphere placed atop a semi-infinite half space. This is illustrated schematically in Figure 8.2. In this figure, each shaded region represents a distinct optical region, specified by a scattering coefficient (μ_s), a scattering anisotropy (g), an absorption coefficient (μ_a), and an index of refraction (n). Photons are injected into the skin layer at the top of the tumor and are detected as they exit the skin layer along the arc of the hemisphere. In order to obtain the best Monte Carlo statistics, a single collection bin is used for each discrete azimuthal angle. This is equivalent to conducting a diffuse reflectance experiment with rings of detectors, with each detector in a ring being equidistant from the entry point. To make the best comparison with the dipole reflectance expression for the semi-infinite planar geometry, the chord length from the entry point to the exit point is used as the "radial" distance for radially-resolved diffuse reflectance.

Figures 8.3 and 8.4 depict the diffuse reflectance assuming matched or mismatched air- tissue boundaries, respectively, for tumors ranging in size from 3 to 12 mm in radius. In these figures the skin layer and the normal tissue surrounding the tumor have the same optical properties as the tumor, and the radius quoted includes the thickness of the skin. Also included in these figures for reference is the diffuse reflectance from a semi-infinite planar turbid medium with optical properties identical to that of the tumor. Clearly, the largest difference in reflectance occurs with the smallest radius of curvature, as photons downstream from the entry point are able to exit the hemisphere. This is unlike the situation for a planar boundary where a return trip to the surface is required. But this disagreement appears to be severe only in the case of mismatched boundary conditions

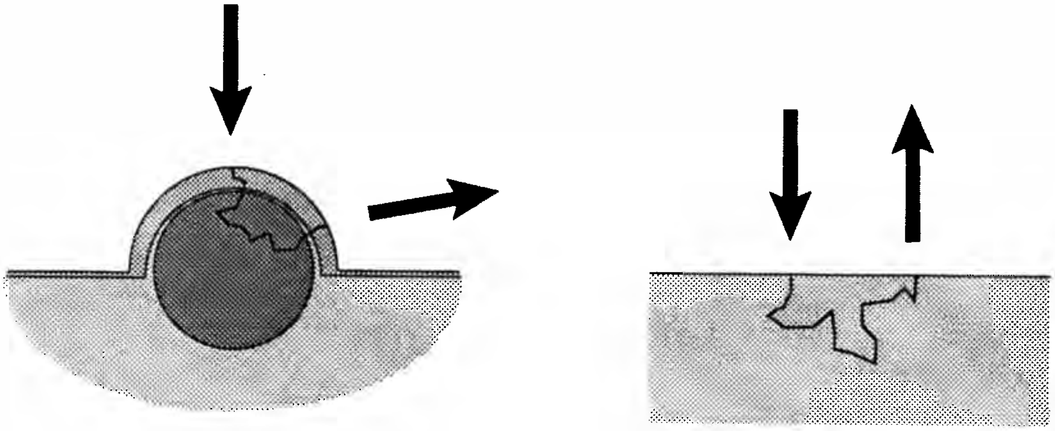

Figure 8.2: A schematic representation of the the two geometric models used for simulating light propagation in tissue simulating turbid media. To the right, the arrangement for detecting the radially resolved diffuse reflectance from a homogeneous semi-infinite slab is depicted. The arrow pointing into the turbid medium (shaded) is the source beam, while the arrow pointing away from the medium is the reflectance remote from the source. The line in the turbid medium represents a possible photon path as it travels from the source and is reemitted from the medium. To the left, a similar arrangement is depicted for the subcutaneous tumor model. In this schematic, light is injected into a skin layer and propagates into a spherical tumor below. The medium below the tumor represents possible normal tissue.

(Figure 8.4). The extreme curvature tends to increase the diffuse reflectance relative to the planar geometry. This is most likely due to a relative decrease in total internal reflection which accompanies a decreased angle of incidence. Under matched boundary conditions the disparity between reflectance at curved boundaries and planar boundaries is slight.

To discern the impact on the determination of optical properties when using the dipole approximation with a curved interface, the Monte Carlo data for matched and mismatched boundary conditions were analyzed with the reflectance equations derived from the dipole approximation (Equation (4.33)) and the exact solution of the photo-diffusion equation (Equation (4.26)). From the Monte Carlo analysis conducted in Chapter 5, it is known that the dipole approximation of the photo-diffusion equation is in good agreement with photon transport provided a minimum distance between source and detector is maintained and matched boundary conditions are assumed. When matched boundary conditions cannot be assumed, the exact solution appears to provide a more accurate description of the diffuse reflectance. For the exact fit, the predicted optical coefficients converge to the proper values when the source-detector separation is greater than 2 mfp$'$ for a typical index mismatch of 1.4, whereas the dipole fit does not appear to converge to the correct optical properties at all. For both matched and mismatched boundary conditions the exact solution is in better agreement with the Monte Carlo diffuse reflectance near the source, as is evident in the dependence of the goodness of fit summarized in Figure 5.13. With this in mind, a minimum source-detector separation of $\approx$ 1 mfp$'$ was used in analyzing the data sets of Figures 8.3 and

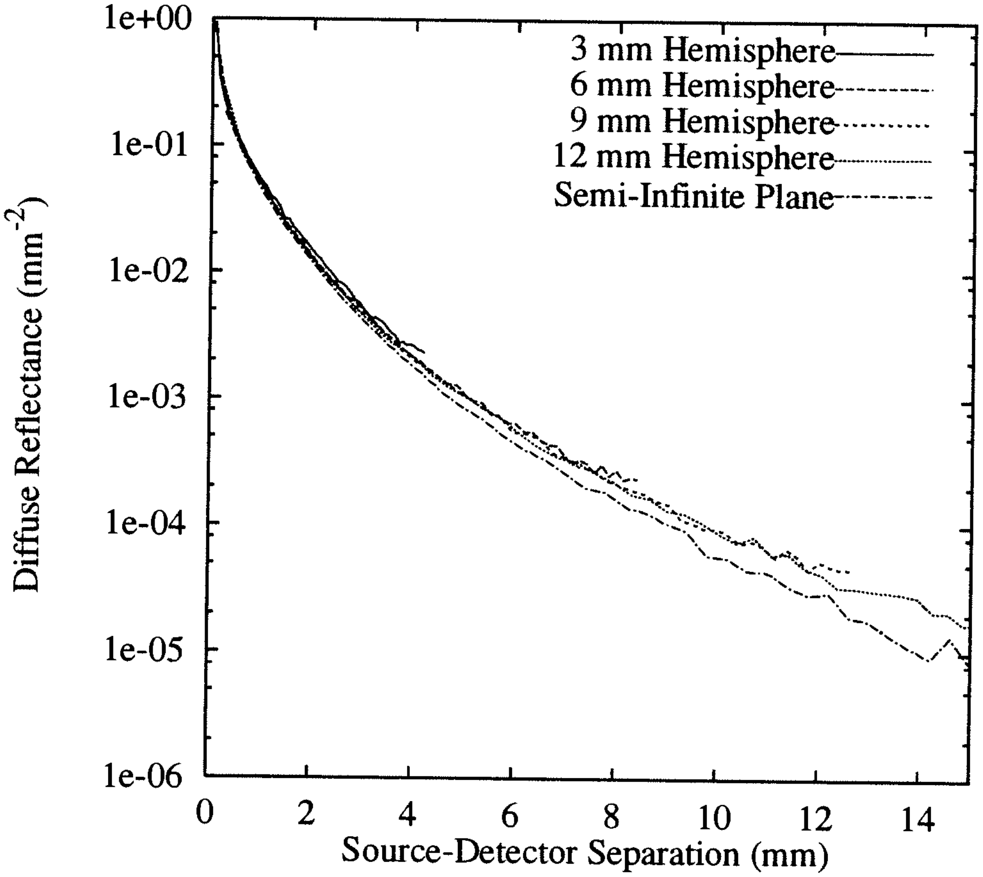

Figure 8.3: The diffuse reflectance from the hemispherical subcutaneous tumor model illustrated in Figure 8.2. Monte Carlo reflectance from homogeneous tumors with radii 3, 6, 9 and 12 mm are shown along with the diffuse reflectance from a semi-infinite plane. The optical properties used in each simulation were μ_s = 15 mm^{-1}, μ_a = 0.01 mm^{-1}, g=0.90 and n=1.0 (matched). A one micron wide collimated beam of photons is incident at the top of the tumor, and the source-detection separation represents the chord length from the entry point to the exit point located somewhere on the curved surface.

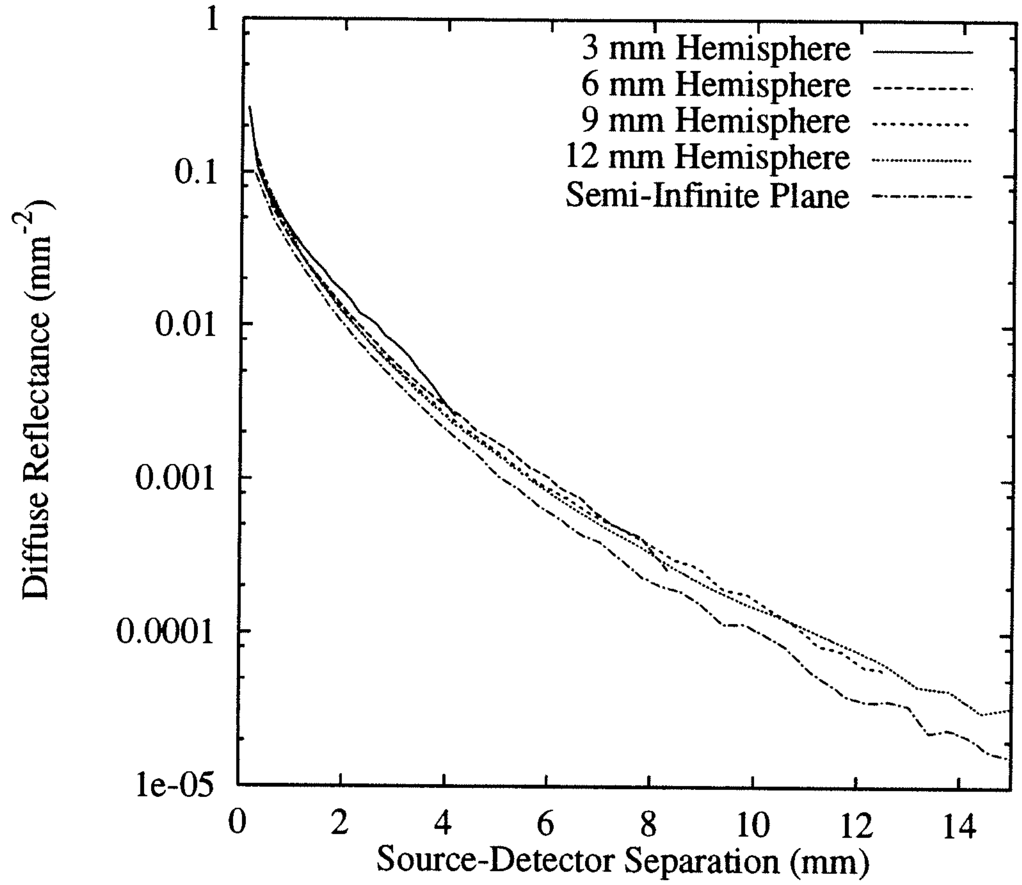

Figure 8.4: The diffuse reflectance from the hemispherical subcutaneous tumor model illustrated in Figure 8.2. Monte Carlo reflectance from the homogeneous tumors described in Figure 8.3 is shown along with the diffuse reflectance from a semi-infinite plane. The only difference in the optical properties is an index mismatch at the air-skin layer of 1.4.

8.4. The optical properties determined from each of these fits for the matched and mismatched data sets are summarized in Tables 8.1 and 8.2.

For matched boundary conditions, the optical properties estimated from the dipole fit vary only slightly with increasing radius of curvature. In each simulation, the scattering coefficient (μ_s') is underestimated as was seen previously in analyzing planar reflectance. This is understandable given the fact that the first radial data point is approximately 1 mfp′ from the source. An artifact from the curvature, however, is the underestimated absorption coefficient which was previously seen to be overestimated. As is evident from Figure 8.3, there are more photons exiting the hemisphere at a given chord length than there are exiting the plane at an equal radial distance. Hence, the apparent absorption coefficient is reduced. The fit indicates that the absorption coefficient is most underestimated with the largest radius of curvature.

This result seems counterintuitive since the plane has an infinite radius of curvature and the absorption coefficient is *overestimated* for the plane. In all of the fits of the curved surface reflectance, however, data was obtained from the entire extent of the hemisphere above the planar surface. The maximum source-detector separation increased with increasing radius of curvature, so the curvature was always apparent in the data. If data points are censored at large chord lengths to maintain a fixed maximum separation, then the apparent curvature will be reduced as the radius of curvature increases. In this case, the fit results converge to the planar results as the radius is increased, as expected. This approach can be effective when large radii tumors are investigated or when the absorption coefficient

	Dipole Approximation (Equation 4.33)			Exact Diffusion Theory (Equation 4.26)		
Radius (mm)	μ_s' (mm^{-1})	μ_a (mm^{-1})	χ_ν^2	μ_s' (mm^{-1})	μ_a (mm^{-1})	χ_ν^2
3.0	1.318 ± 0.020	0.0077 ± 0.0019	1.27	0.923 ± 0.107	0.0450 ± 0.0100	1.94
6.0	1.346 ± 0.012	0.0063 ± 0.0006	1.20	1.083 ± 0.049	0.0240 ± 0.0027	3.43
9.0	1.387 ± 0.010	0.0062 ± 0.0004	1.08	1.207 ± 0.039	0.0176 ± 0.0012	3.49
12.0	1.440 ± 0.008	0.0054 ± 0.0002	0.96	1.221 ± 0.031	0.0159 ± 0.0009	4.53
∞	1.379 ± 0.009	0.0117 ± 0.0004	0.97	1.181 ± 0.040	0.0254 ± 0.0016	4.10

Table 8.1: Comparison of fits to Monte Carlo diffuse reflectance from a hemispherical boundary with index-matched boundary conditions. The optical properties used in each simulation are $\mu_s = 15$ mm^{-1}, $\mu_a = 0.01$ mm^{-1}, g=0.90 and n=1.0 (matched). The radius of the hemispherical part of the medium is given in the table along with the results of two parameter fits using the normalized diffuse reflectance expression from both the dipole approximation and the exact solution of the photo-diffusion equation. In addition, the fit results obtained when analyzing a semi-infinite planar medium are given for reference (radius = ∞). In all of these fits, the minimum source detector separation used in the data sets was 1 mfp′, while the maximum source detector separation was 4.2, 8.5, 12.7, 17.0 and 20.0 mm for the 3, 6, 9, 12 and ∞ mm radius simulations, respectively. The internal reflection parameter, A, was held constant at 1.00.

	Dipole Approximation (Equation 4.33)			Exact Diffusion Theory (Equation 4.26)		
Radius (mm)	μ_s' (mm^{-1})	μ_a (mm^{-1})	χ_ν^2	μ_s' (mm^{-1})	μ_a (mm^{-1})	χ_ν^2
3.0	0.647 ± 0.008	0.021 ± 0.002	10.4	0.170 ± 0.889	0.227 ± 0.336	6.6
6.0	0.733 ± 0.005	0.022 ± 0.001	16.8	0.936 ± 0.070	0.030 ± 0.003	2.4
9.0	0.671 ± 0.006	0.027 ± 0.001	5.8	1.278 ± 0.070	0.013 ± 0.001	1.9
12.0	0.970 ± 0.007	0.016 ± 0.001	11.4	1.505 ± 0.050	0.010 ± 0.001	1.5
∞	0.747 ± 0.006	0.032 ± 0.001	3.9	1.215 ± 0.066	0.022 ± 0.001	2.9

Table 8.2: Comparison of fits to Monte Carlo diffuse reflectance from a hemispherical boundary with index-mismatched boundary conditions. The simulations were conducted as described in Table 8.1, except for an index mismatch of 1.4 at the air-media interface. In all of these fits, the internal reflection parameter, A, was held constant at 3.25.

is large enough that small source-detector separations are sufficient. The issue of measurement sensitivity will be discussed in Section 8.3.

Optical coefficients predicted by the exact diffusion theory expression for the diffuse reflectance have similar behavior with increasing radius of curvature as those predicted from the dipole fit. However, the absorption coefficient predicted by the exact fit is strongly dependent on the radius of curvature, with a 450% overestimate from the 3 mm radius tumor compared to a 59% overestimate from a 12 mm radius tumor. A similar increase in the absorption coefficient with decreasing radius was reported by Pogue and Patterson (1994) for frequency-domain spectroscopy conducted on spheres and cylinders when analyzed with a slab diffusion model. The scattering coefficient is also more strongly dependent on the radius of curvature than was observed for the dipole fit.

With an index mismatch of 1.4 present at the air-tumor interface, the dependence of the estimated optical coefficients on the radius of curvature is strengthened for both fitting functions, though again the exact fit seems to be more sensitive to the geometry of the boundary. It is interesting to note that while the quality of the fit deteriorates dramatically for the dipole fit, the exact fit actually improves with the index mismatch and the estimated optical properties show a similar improvement.

The results of the Monte Carlo analysis of diffuse reflectance from a curved surface indicate that curvature can have a significant effect on the estimated optical properties, especially when a realistic index mismatch is present. Many of the trends, however, are the same as were observed for planar boundaries. The analysis was conducted using Monte Carlo reflectance as close as 1 mfp′ from the beam, which is more suited to the dipole fit than the exact fit. Previously, it was found that the exact diffusion theory reflectance expression performed better with data sets containing points further from the source, and it is likely that a similar improvement would be seen on curved boundaries as well. With small tumor diameters, however, the extent over which reflectance may be measured is tightly constrained. Both algorithms would likely fair better under mismatched boundary conditions if the minimum source detector distance was increased to 2-3 mfp′, *i.e.* 1.2 to 1.8 mm, but this could only be done for fairly large tumors greater than 1 cm in diameter.

8.3 Indications of Limited Measurement Sensitivity in Monte Carlo Diffuse Reflectance from the Subcutaneous Tumor Model

Since the tumor is of limited extent, another concern is the range of absorption coefficients which can be measured. This can be seen, in the case of the dipole model, to be limited by the minimal falloff of the diffuse reflectance curve which can be observed when detection is limited to the hemisphere above the plane. In the case of the 1 cm diameter tumor, for example, the maximum source-detector separation that can be used when injecting photons at the top of the tumor is about 7.2 mm. Larger separations could be obtained if the photons were injected on the side of the tumor and directed radially towards the center, but this interesting configuration has yet to be investigated. An inspection of Equation (4.33) reveals that the determination of the absorption coefficient, μ_a, is only possible through a determination of μ_{eff}, which appears in the exponent multiplied by ρ, the source-detector separation. These exponentials are the only parts of the expression which depend on absorption. A conservative requirement for an accurate estimation by an exponential fit is that one decay length must be measured. A less stringent criteria might only require the measured quantity to decay to $e^{-0.3}$. As this exponent is decreased, the significance of the exponential term is diminished relative to the inverse-square decay term in the reflectance expression. Consequently, the accuracy of the fit determination of the exponential decay constant will suffer unless the data is characterized by a high signal-to-noise ratio to adequately distinguish the decay terms. Beyond a decay length an exponential can easily be distinguished from an inverse-square decay, but the two functions have quite similar features within a third of a decay length. The different decay mechanisms can be separated, however, provided the signal-to-noise ratio is sufficient. Regardless of the criteria, the sensitivity to the absorption coefficient is seen to be limited by the maximum source-detector separation. This makes intuitive sense, since by increasing this separation, the photon pathlength and the probability of absorption will likewise be increased. Alternatively, the effective photon pathlength can also be increased by turbidity, hence one would expect the sensitivity of the measurement to absorption to also increase with μ_s'. By these criteria then, the minimal absorption coefficient that can be accurately measured by the diffuse reflectance technique will be given approximately by

$$\mu_a^{min} = \frac{\mu_s'}{2}\left(\sqrt{1+\frac{4c}{3\left(\mu_s'\rho_{max}\right)^2}}-1\right) \tag{8.1}$$

where c is 1.0 by a conservative estimation or perhaps as small as 0.3 if signal-to-noise permits. These relations are depicted in Figures 8.5 and 8.6. The lines in these figures indicate the minimum values of ρ_{max} and μ_s' necessary to accurately measure a given μ_a.

As a practical test of this analysis, one would predict that the minimum measurable value for μ_a for a 12 mm diameter tumor with $\mu_s' = 1.0$ mm^{-1} will be between 0.0025 and 0.005 mm^{-1} ($c = 1$) or potentially as small as 0.001 ($c = 0.3$) if the signal-to-noise ratio is sufficiently high. To test these predictions, Monte Carlo simulations in 1.2 cm diameter tumors were conducted with absorption coefficients varying from 0.0001 to 0.1 mm^{-1}. Once again, the optical properties of all three regions were equal for a given simulation, and the transport scattering coefficient, μ_s', was 1.0 mm^{-1} ($\mu_s = 10$ mm^{-1}, $g = 0.90$). The diffuse reflectance curves are plotted in Figures 8.7 and 8.8 for index-matched and mismatched (n=1.4) conditions, respectively. Since the reflectance is detected on a 12 mm diameter hemisphere, the maximum source-detector separation is limited to approximately 8.5 mm. For both matched and mismatched cases, the reflectance from the hemisphere appears to be insensitive to absorption coefficients less than 0.001 mm^{-1}, as expected by the more liberal estimate.

The lack of sensitivity can readily be seen when these diffuse reflectance curves are analyzed with the dipole or exact reflectance expressions. Figures 8.9 and 8.10

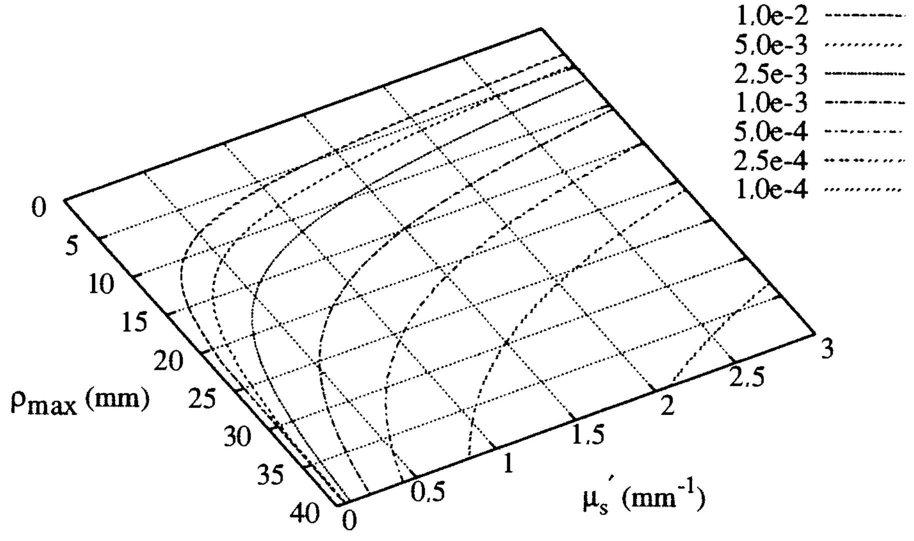

Figure 8.5: Contour map indicating the approximate sensitivity of radially-resolved diffuse reflectance measurements to small absorption coefficients for a given value of ρ_{max} and μ_s'. Increasing either of these parameters allows for a smaller μ_a to be measured when using the reflectance expression for the dipole model. The legend indicates the approximate minimum value of μ_a that can be reliably measured. The more conservative requirement that the exponential decay by at least one decay length has been assumed.

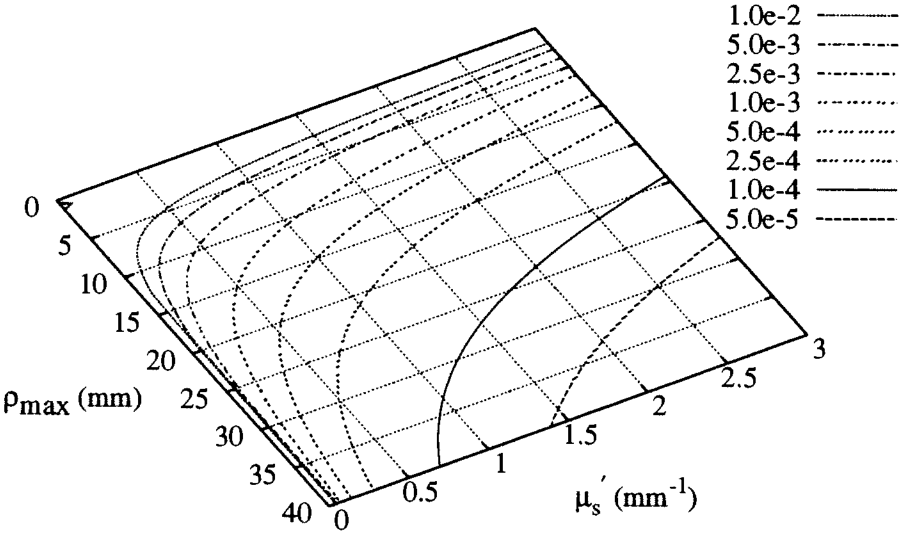

Figure 8.6: Contour map indicating the approximate sensitivity of diffuse reflectance measurements to small absorption coefficients, as described in Figure 8.5. The more liberal requirement that the exponential decay by at least 0.3 decay lengths has been assumed.

summarize the fit-estimates of the absorption coefficient when these two models are used to analyze the index-matched data shown in Figure 8.7. In these fits the minimum source detector separation is approximately 0.7 mfp. Under matched conditions the dipole fit is, in fact, insensitive to changes in absorption less than 0.001 mm^{-1}. The returned values are systematically low by a fairly uniform factor of 2-3, hence the lowest estimated absorption coefficient is 0.00033 mm^{-1}. Though systematically low, the estimated absorption coefficient does increase linearly with the actual value. Thus, while the technique may be inaccurate in absolute terms, relative changes in this regime may be determined more accurately.

Although the reflectance data appear to be changing when absorption is increased beyond 0.001 mm^{-1}, Figure 8.10 indicates that the exact expression is insensitive to absorption coefficients that are an order of magnitude greater than this. It is not until $\mu_a = 0.01$ mm^{-1} that the exact algorithm begins to respond. This behavior was seen to a more limited extent under matched conditions for the planar geometry. In this case, it is as though the curved boundary itself results in an apparent absorption coefficient of approximately 0.03 mm^{-1}. With an index mismatch of 1.4, the sensitivity of either algorithm is unchanged, and the trends are very similar to that depicted in Figures 8.9 and 8.10.

A minimum sensitivity to absorption of 0.001 mm^{-1} in the 12 mm diameter tumor is likely to be acceptable for measurements *in vivo*, but may be insufficient under certain circumstances. For near-infrared tissue oximetry, for example, a 4% blood volume fraction and a hemoglobin concentration of 2 mM would result in a fully oxygenated absorption coefficient on the order of 0.01 mm^{-1}, while the

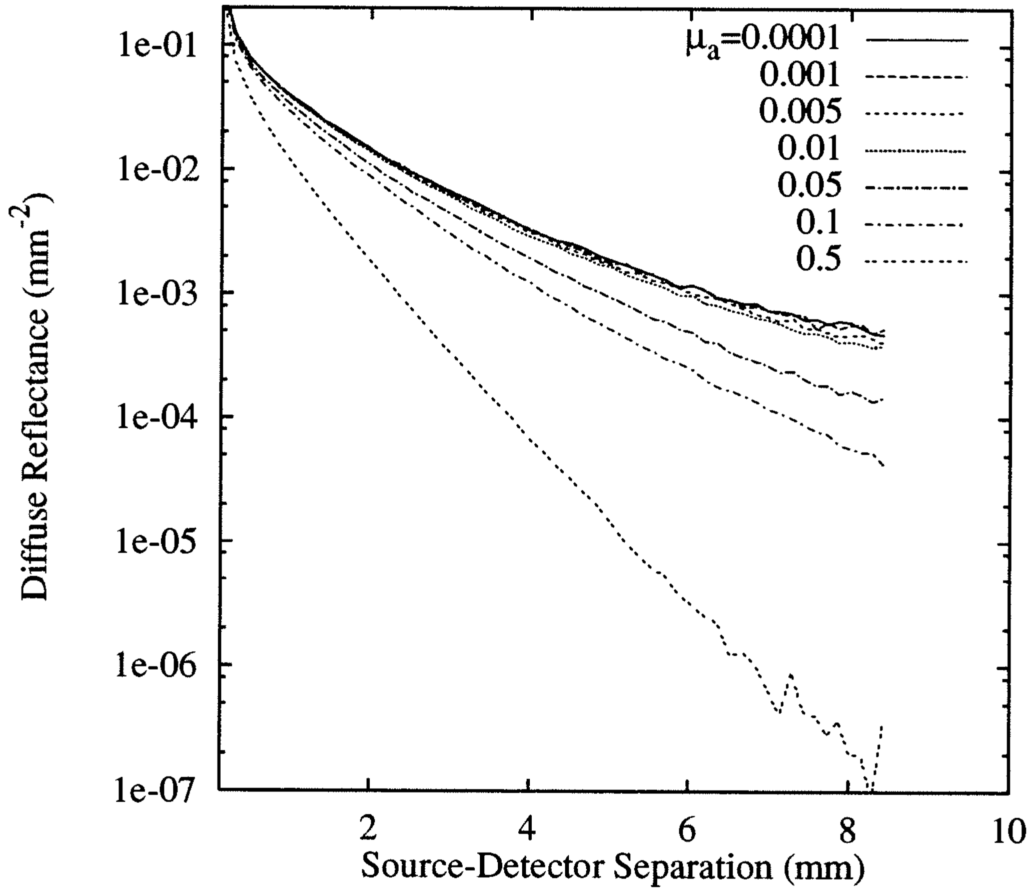

Figure 8.7: Radially-resolved diffuse reflectance from a 6 mm radius subcutaneous tumor geometry. The optical properties of the skin, tumor, and normal regions are the same for each simulation. Several simulations are shown using various values for the absorption coefficient, μ_a, while the remaining optical properties are held constant (μ_s = 10 mm^{-1}, g = 0.9, n=1.0).

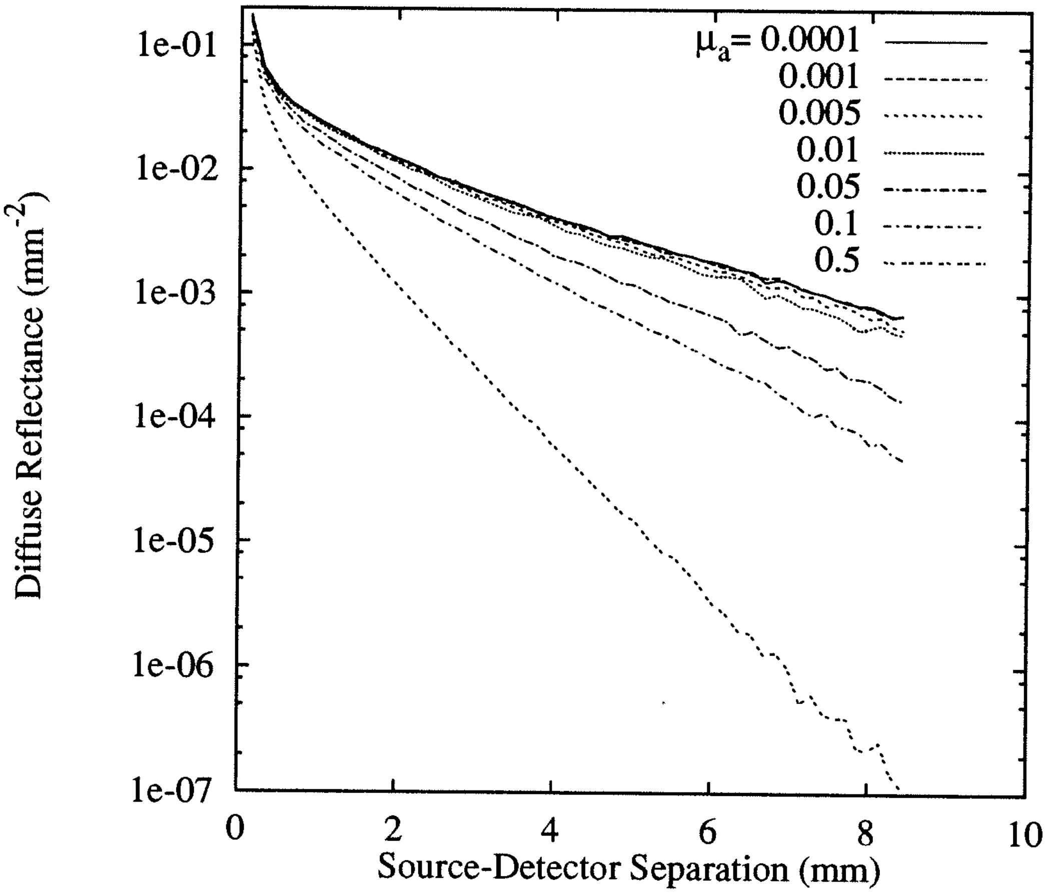

Figure 8.8: Radially-resolved diffuse reflectance such as that described in Figure 8.7, except that an index mismatch of 1.4 was used at the air-skin boundary. The absorption coefficient was varied for each simulation and the value used is shown in the legend.

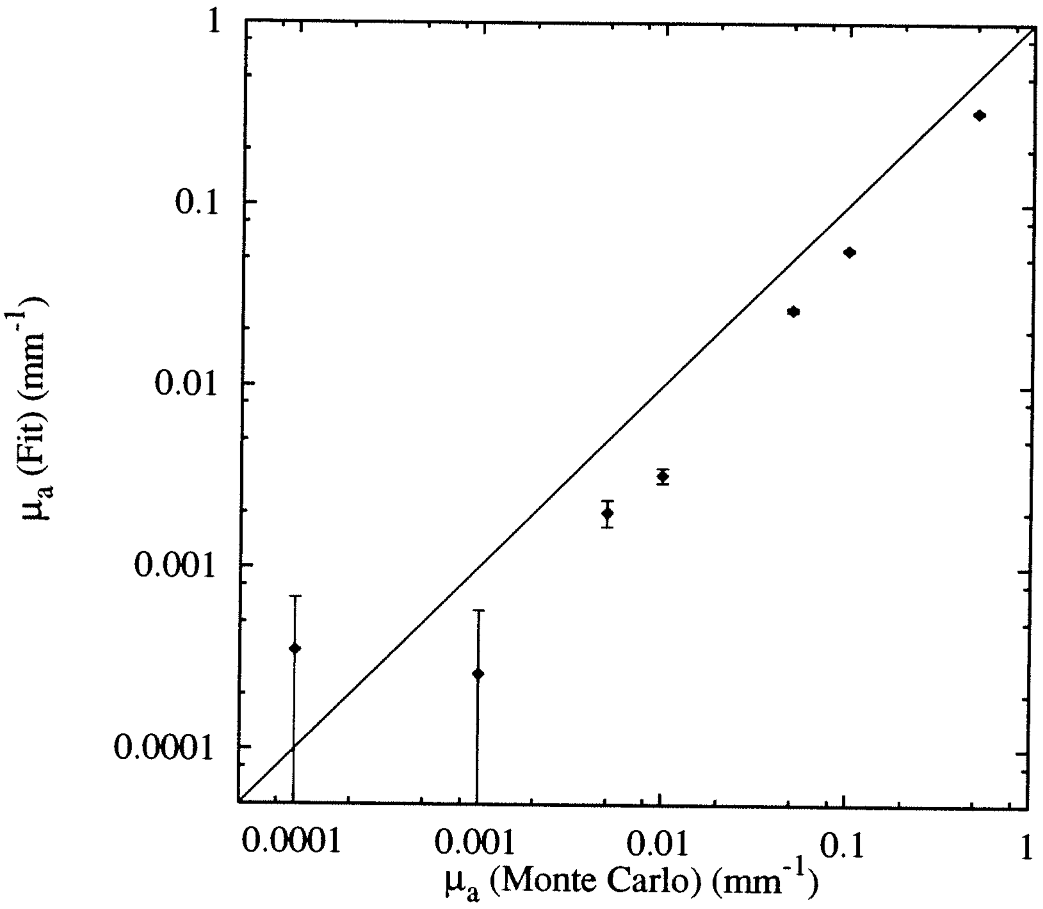

Figure 8.9: Summary of the absorption coefficients estimated from dipole fits of Monte Carlo diffuse reflectance from a 6 mm radius tumor (Figure 8.7). The line represents the true value used in the simulation, and the error bars are the estimated standard deviations from the fits. In each simulation the optical properties of the skin, normal and tumor regions were equivalent. The scattering properties were the same for all simulations ($\mu_s = 10$ mm^{-1}, $g = 0.9$, n=1.0).

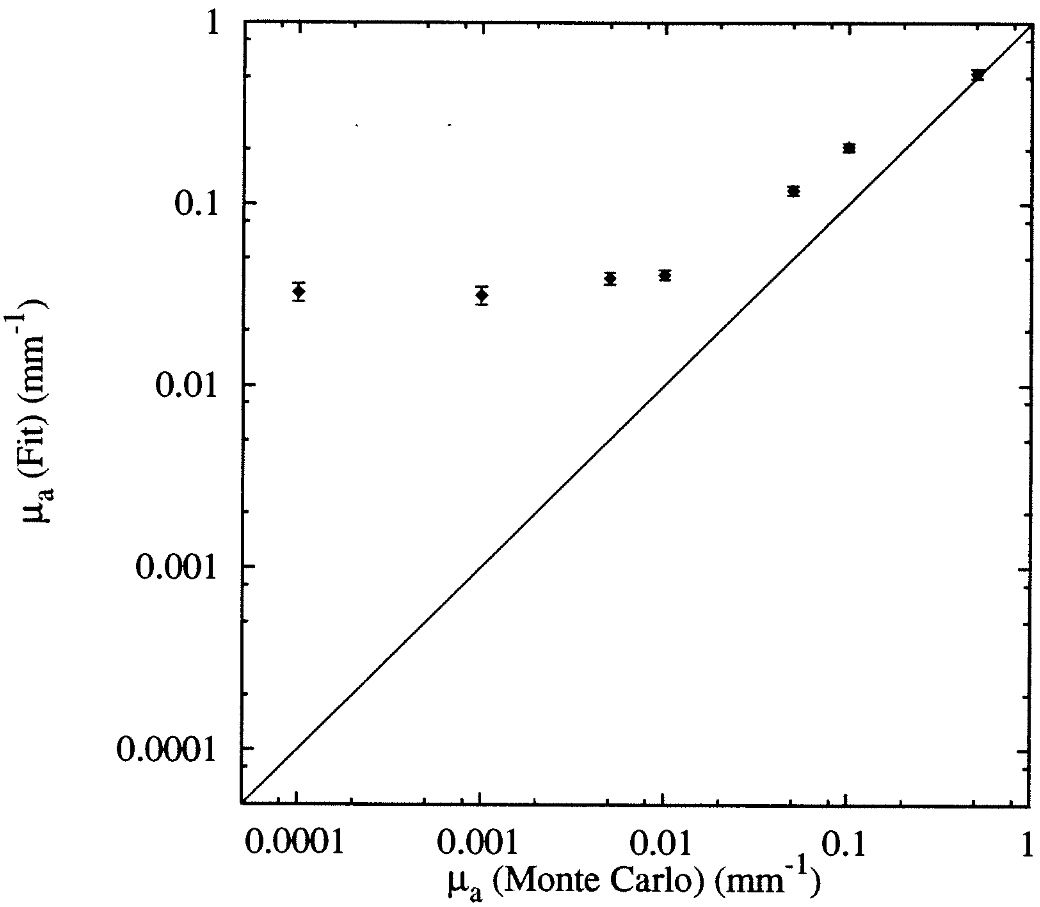

Figure 8.10: Summary of the absorption coefficients estimated from fits using the exact diffusion theory reflectance expression to analyze Monte Carlo diffuse reflectance from a 6 mm radius tumor (Figure 8.7). The line represents the true value used in the simulation, and the error bars are the estimated standard deviations from the fits. In each simulation the optical properties of the skin, normal and tumor regions were equivalent. The scattering properties were the same for all simulations (μ_s = 10 mm^{-1}, $g = 0.9$, n=1.0).

deoxygenated absorption coefficient may be a factor of five higher than this. For tissues with blood volume fractions significantly less than this, or for tumors of much smaller radii of curvature, the apparent absorption coefficient due to the geometry of the tumor may preclude hemoglobin spectroscopy. The results for the exact fit indicate that this model is not likely to be useful in the presence of a curved boundary, and perhaps a better approach would be to solve the photodiffusion equation under a more appropriate geometry.

8.4 Layered Geometries: The Subcutaneous Tumor Model

Since it is likely that the steady-state diffuse reflectance technique will most often be applied to study tissues which lie just below the skin, such as for studying oxygenation in muscle during exercise or subcutaneous tumors during cancer therapy, it is important to characterize the effect of the skin layer on the measurement.

Nossal *et al.* (1988) have previously studied the effect on the radially-resolved reflectance from a two-layer semi-infinite medium in which the absorption coefficients of the two layers are different. When the surface layer had an absorption coefficient twenty times that of the lower layer, it was found that the diffuse reflectance close to the source decayed as it would within a semi-infinite medium with an absorption coefficient equal to that of the uppermost layer. In contrast, for distances large compared to the scattering length, the diffuse reflectance decayed exponentially with a decay constant proportional to the absorption coefficient of the bottom layer. This was reported to occur independently of the thickness of the surface layer, though the distance from the source at which the absorption of the lower layer could be determined from the reflectance increased with this thickness. For intermediate distances, the radial reflectance appeared to decay according to an absorption coefficient between that of the two layers.

When the absorption of the upper layer was taken to be twenty times smaller than that of the lower layer, it was found that the diffuse reflectance was quite sensitive to the thickness of the upper layer. This is understandable when the upper layer is relatively thick, since photons can remain in the low absorption region for considerable distances from the source with relatively high probability, while photons entering the lower region are absorbed after relatively shorter distances. One would expect the diffuse reflectance to be more sensitively dependent on the lower layer when the surface layer is so thin that the photon pathlength in this layer is negligible.

Using similar discrete lattice models, both Nossal *et al.* and Taitelbaum *et al.* (1989) reported observable differences in the calculated radially-resolved diffuse reflectance with the addition of a surface layer of thickness as small as one scattering length. Given that the scattering was isotropic in their calculations and typical tissue transport scattering coefficients are approximately 1 mm^{-1}, one would expect to see a difference experimentally with an upper layer as thin as approximately 1 mm. Their results were obtained with a surface layer absorption coefficient of 0.01 mfp'^{-1} and a lower layer absorption coefficient of 0.20 mfp'^{-1} at distances as large as 24 mfp′. One very nice feature of the exact enumeration approach used in these studies is that it is possible to obtain the diffuse reflectance for large distances from the source, even with extremely high absorption coefficients. Similar Monte Carlo simulations would require many days to compile similar statistics under these conditions due to the extremely low probability of photons taking such long random walks without being absorbed. As the authors caution, however, the discrete nature of the lattice model is not analogous to the physical situation, and the results should be validated with a more realistic model.

We potentially face a similar layered problem in the subcutaneous tumor. As was indicated in Figure 8.1, the subcutaneous tumor has a skin layer approximately 0.5 mm thick which lies above the tumor. Early experiments with this tumor model led us to suspect that the skin layer has little effect on the measured diffuse reflectance. Radially-resolved diffuse reflectance at 632 nm was measured from a 1 cm diameter R3230AC tumor in the Fischer rat. A commercial depilatory agent was used to remove the hair from the skin lying above the tumor to minimize surface roughness. The rat was anesthetized and seven detector fibers were placed at various radial distances from the source fiber, which injected light into the skin layer above the top surface of the hemispherical tumor. A sample radial-reflectance curve is shown in Figure 8.11. Later, the skin layer was surgically removed and the reflectance measurement was repeated. Analysis of the two reflectance curves indicated an overall decrease in the reflectance when the skin layer was removed, probably due to a layer of blood covering the tumor. The estimated optical properties of the tumor, however, were not statistically different when obtained with a dipole fit. At least in this instance, the skin layer appeared to have a negligible impact, either because the optical properties of the skin and tumor were quite similar, or because there were sufficiently few photon interactions in the skin layer. In light of Nossal *et al.*'s findings, however, the latter possibility would only be possible if the skin layer was more highly absorbing than the tumor, since they observed differences with an upper layer thickness as small as 1 mfp′ when the upper layer was less absorbing than the lower layer. Due to the discrete nature of their enumeration technique, they could not examine the effects of skin layers that were a fraction of a mfp′ thick.

Literature values for human skin and tumor lend some support to this interpretation, although the range of optical properties of skin vary widely. Duck (1990) tabulates human skin scattering (μ_s) and absorption (μ_a) coefficients measured at at 630 nm that range from 2.5 to 39.4 mm^{-1} and 0.18 to 24 mm^{-1}, respectively. Jacques *et al.* (1987) have reported the absorption coefficient, scattering coefficient and anisotropy (g) of human dermis to be 0.27 mm^{-1}, 18.7 mm^{-1} and 0.82, respectively, at 633 nm. These values can be cautiously compared to the optical properties of human tumors (breast cancer, cutaneous and subcutaneous nodules) at 630 nm reported by Driver *et al.* (1991). They measured the distribution of fluence in tumors resulting from either superficial or interstitial illumination and found $\mu_a = 0.031 \pm 0.016$ mm^{-1} and $\mu_s' = 0.9 \pm 0.7$ mm^{-1}. Although a wide variation exists in these values, the skin does appear to be roughly an order of magnitude more absorbing than the tumors investigated by Driver *et al.*.

To model the effect of the skin on the diffuse reflectance and the estimation

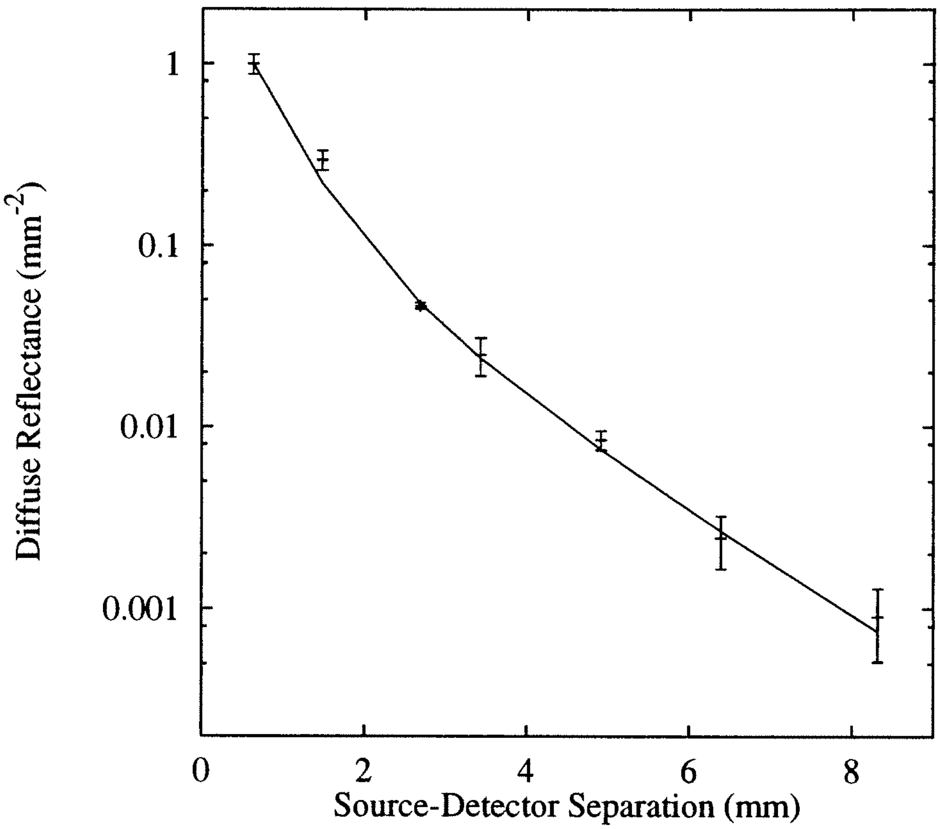

Figure 8.11: Measured radially-resolved 632.8 nm diffuse reflectance from a 1 cm diameter R3230AC tumor in a Fischer rat. The hair above the tumor was removed, but the skin was intact. The error bars represent one standard deviation assuming Poisson (counting) statistics and an appropriate uncertainty in the detector location. The data have been normalized to the reflectance measured at the closest detector, and the line represents the best two-parameter dipole fit. The estimated optical coefficients of the tumor are $\mu_s' = 1.17 \pm 0.15$ mm^{-1} and $\mu_a = 0.057 \pm 0.016$ mm^{-1}, assuming mismatched boundary conditions with $A = 3.25$ (n=1.4).

of optical coefficients by a dipole fit, subcutaneous tumor simulations using a 500 μm thick skin layer and a 5.0 mm radius tumor were conducted for various skin absorption coefficients. For all of the simulations, the scattering properties of all three regions were equal (n = 1.4, $\mu_s' = 10$ mm^{-1}, g=0.90), and the tumor and normal regions had equivalent absorption coefficients of 0.02 mm^{-1}. These values were chosen so that a range of absorption coefficients could be investigated in a regime of adequate measurement sensitivity, as discussed in Section 8.3.

Absorption of the skin layer was varied from 1/20th of that of the tumor to 20 times that of the tumor. The resulting Monte Carlo diffuse reflectance curves are shown in Figure 8.12. Notice that there is no change in the diffuse reflectance until the skin absorption exceeds the tumor absorption. When this occurs, the overall reflectance is diminished, but starting approximately 2 mm beyond the source the decay of the reflectance is the same for all curves. This is in agreement with Nossal *et al.*'s findings for highly absorbing upper layers, but is contrary to their findings for less absorbing upper layers. Note, however, that in this case the skin layer is 0.5 mfp′ thick, and this could not be investigated with their discrete model. When the upper layer is more absorbing, the reflectance curve could be divided into two regimes: near the source, where the decay is primarily determined by the skin layer; and far from the source, where the optical properties of the tumor dictate the shape of the curve. It would be interesting to determine if a multipole expression for the reflectance, satisfying two boundary conditions, would be able to capture these features and successfully discern the optical properties of the lower layer.

When these curves were analyzed with a dipole fit, the estimated optical coef-

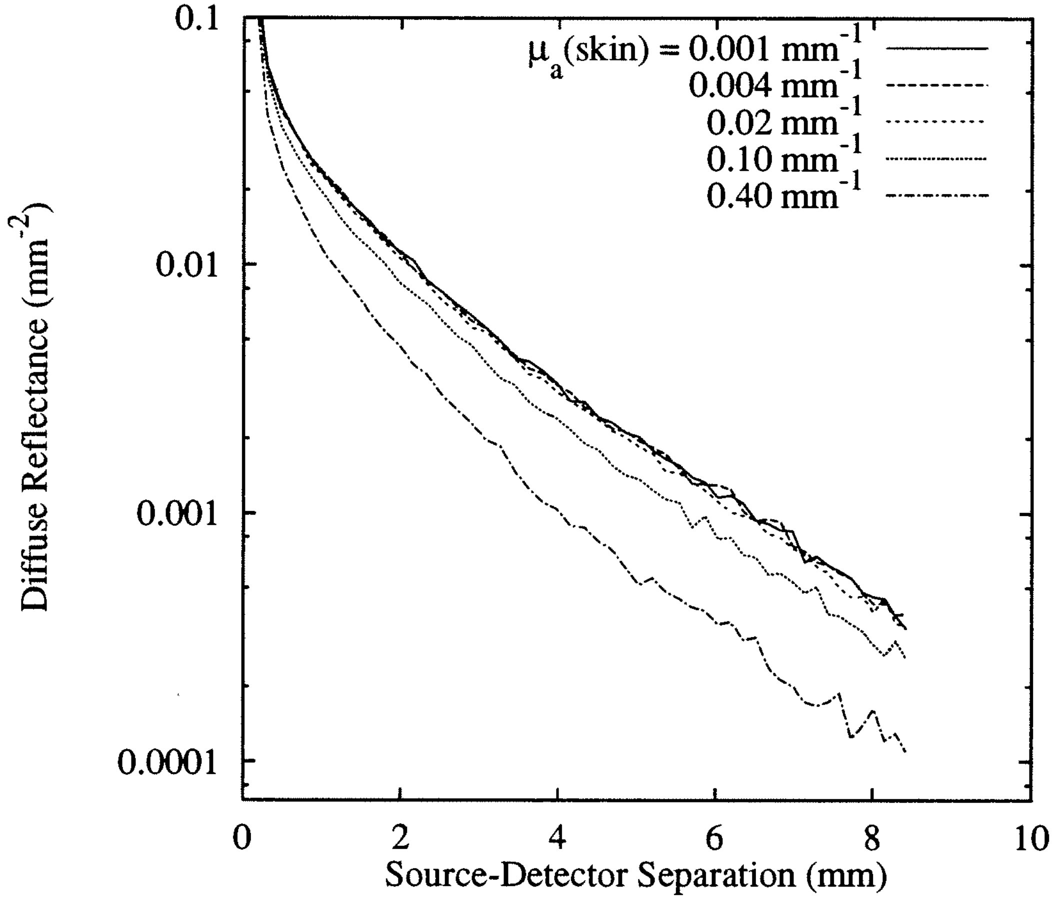

Figure 8.12: Monte Carlo diffuse reflectance data from a heterogeneous 12 mm diameter tumor. The various curves represent the effect of increasing the skin absorption coefficient from 1/20th (top curve) to 20 times (bottom curve) that of the tumor. The scattering properties used in the three regions shown in Figure 8.2 are n = 1.4, $\mu_s' = 10$ mm^{-1} and $g = 0.90$. The absorption coefficient of the tumor and normal tissue is 0.02 mm^{-1}.

ficients were unperturbed by less absorbing skin layers and only significantly affected by the most highly absorbing skin layer. For that simulation, the scattering coefficient was perturbed by approximately +18%, while the absorption coefficient increased by +50%. Oddly enough, as the absorption of the skin layer increased beyond that of the tumor, the quality of the dipole fits improved substantially. This may be a consequence of a decreasing mfp′ in the skin layer relative to the tumor layer while using a minimum source-detector separation of 1 mfp′ (tumor).

Another possible source of contamination may come from the scattering properties of the skin layer. Since the reflectance in the vicinity of the source carries the most information about both the scattering coefficient and the skin layer, it is likely that disparate scattering properties of the skin will have an adverse effect on the estimation of the optical properties of the subcutaneous tumor. The spread in the literature values indicates that the scattering coefficient of skin could either be smaller or greater than that of the tumor, so both of these possibilities are investigated. To get a feeling for the effect of disparate skin scattering coefficients, Monte Carlo simulations in the subcutaneous tumor with a 0.5 mm thick skin layer were conducted over a wide range of possible skin scattering coefficients, from transparent ($\mu_s = 0$ mm^{-1}, $g = 0.90$) to twice that of the underlying tumor ($\mu_s = 20$ mm^{-1}, $g = 0.90$). As before, the remaining optical properties were held fixed for all simulations, with the scattering coefficient and anisotropy of normal and tumor regions equal to 10 mm^{-1} and 0.90, respectively. An absorption coefficient of 0.02 mm^{-1} and an index of refraction of 1.4 were used in all regions. The resulting Monte Carlo diffuse reflectance curves are shown in Figure 8.13.

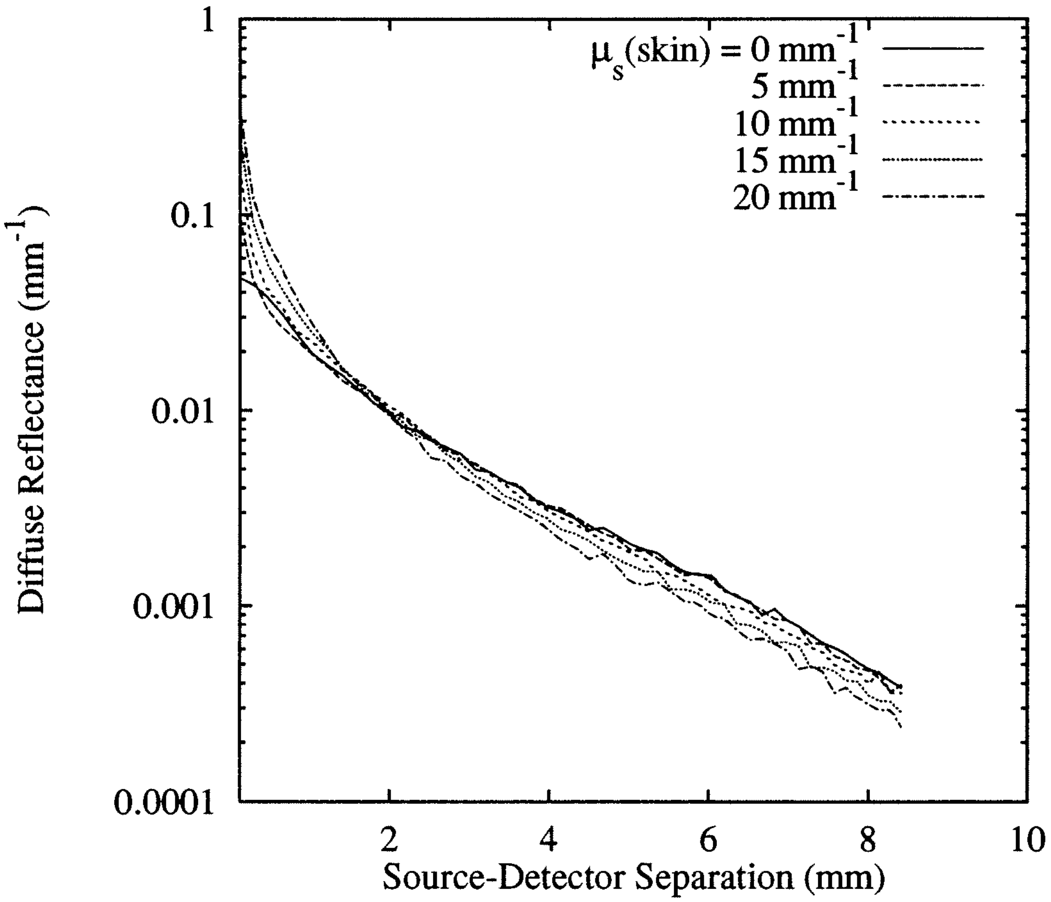

Figure 8.13: Monte Carlo diffuse reflectance data from a heterogeneous 12 mm diameter tumor. The various curves represent the effect of increasing the skin scattering coefficient from zero (transparent) to twice that of the tumor. The optical characteristics of the tumor and normal tissue were the same for all simulations (n = 1.4, $\mu_s' = 10$ mm^{-1}, g=0.90, $\mu_a = 0.02$ mm^{-1}). Absorption of the skin layer was equal to that of the tumor and normal tissue.

As expected, changes in the scattering coefficient have the most significant effect in the reflectance in the vicinity of the source. With an increase in the scattering coefficient, the probability of backscatter increases and both the fluence and reflectance increase within 2 mm of the source. The increasing decay far from the source indicates that scattering in the skin layer affects the entire diffuse reflectance curve. When these curves are fit with the dipole expression for the diffuse reflectance, the severity of the perturbation is seen to increase with the disparity of the scattering properties of the skin and tumor. The estimated absorption coefficient is depressed for both transparent and highly scattering skin, while the estimated scattering coefficient scales with the skin scattering coefficient. As with the estimated absorption coefficient, the quality of fit worsens with the disparity in the scattering coefficients.

Scattering in the skin layer has a more pronounced effect than absorption because the scattering length scale is sufficiently short to allow for a relatively high scattering probability within the skin layer, even for layers as thin as 0.5 mm. For this reason, the accurate determination of tumor optical properties requires either that the skin be extremely thin ($\ll$ 1 mfp$'$) or that the scattering properties of the skin be closely matched to that of the underlying tumor. When the scattering of the 0.5 mm skin layer is matched to that of the tumor, variations in the tumor absorption coefficient have a pronounced impact on the diffuse reflectance. Figure 8.14 depicts the Monte Carlo diffuse reflectance obtained when the absorption of the tumor is varied, while the skin and normal tissue absorption coefficients are held at 0.02 mm^{-1} and all regions have the same scattering properties ($\mu_s = 10.0$

mm^{-1}, $g = 0.90$, n=1.4). When the skin layer is more highly absorbing than the tumor, the estimated absorption coefficient is intermediate to that of either region, and no perturbation of the scattering coefficient is observed, as expected. The reflectance is unperturbed, however, by the three region heterogeneity when the tumor is more highly absorbing than the skin layer.

Yet another complexity that could conceivably effect the estimation of tumor optical properties is the normal tissue which surrounds the tumor. Photons injected into the skin layer may traverse the tumor and enter the normal tissue. One would then expect that the diffuse reflectance would also be affected by the optical properties in this layer, much as the tumor itself affects the diffuse reflectance. For this to be the case, however, photons entering the normal region would have to return to the surface and be emitted as diffuse reflectance. One would expect that if the tumor was sufficiently thick or if the normal tissue was highly absorbing, the probability of reflectance being affected by normal tissue would be quite remote. This is in fact seen to be the case when Monte Carlo simulations are conducted with a wide range of absorption coefficients for the normal layer, as depicted in Figure 8.15.

The parameters for this simulation were chosen as described for the other simulations presented in this chapter and are summarized in the figure caption. The simulations clearly indicate that as the absorption coefficient of the normal tissue changes from 1/20th to 20 times that of the tumor, the reflectance above the tumor is unaffected. The tumor absorption coefficient was held at a reasonably high value of 0.02 mm^{-1} for these simulations, but similar results have been obtained

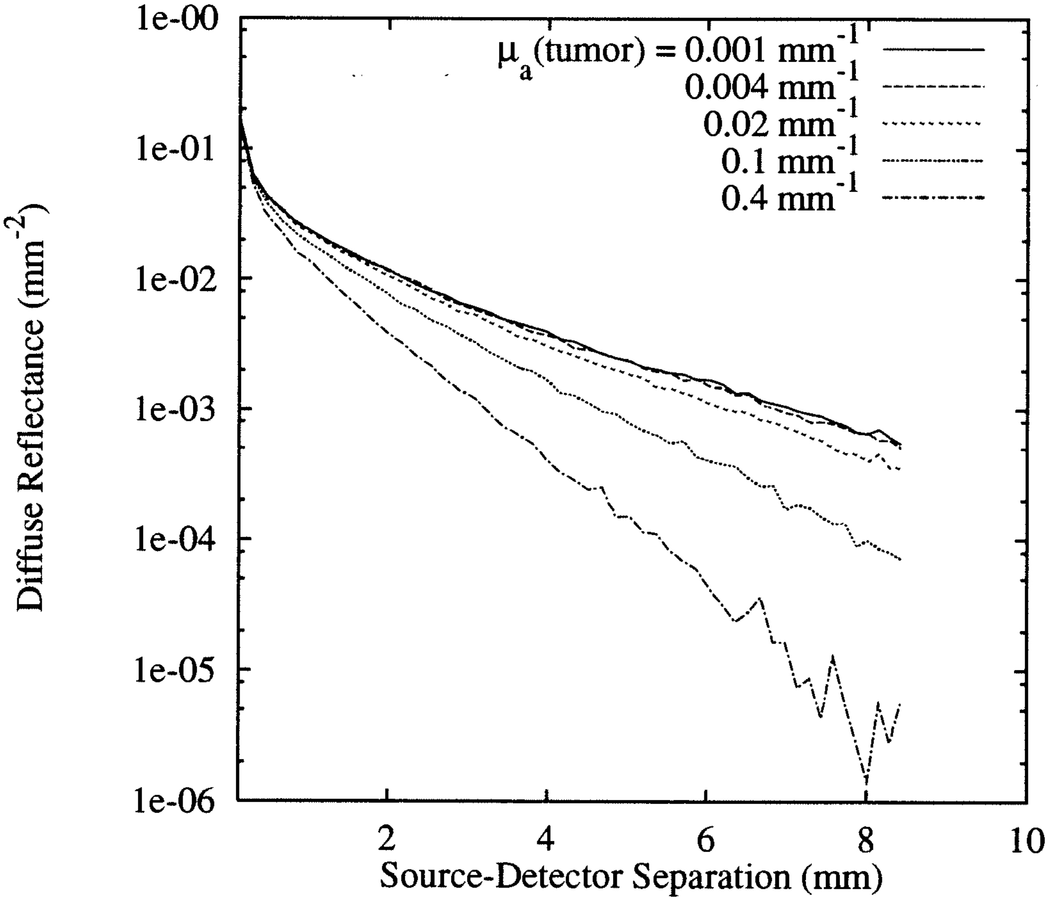

Figure 8.14: Monte Carlo diffuse reflectance data from a heterogeneous 12 mm diameter tumor. The various curves represent the effect of increasing the tumor absorption coefficient. The optical characteristics of the skin and normal tissue were the same for all simulations (n = 1.4, $\mu_s' = 10$ mm^{-1}, g=0.90, $\mu_a = 0.02$ mm^{-1}). The scattering properties of the tumor were equal to that of the skin and normal tissue.

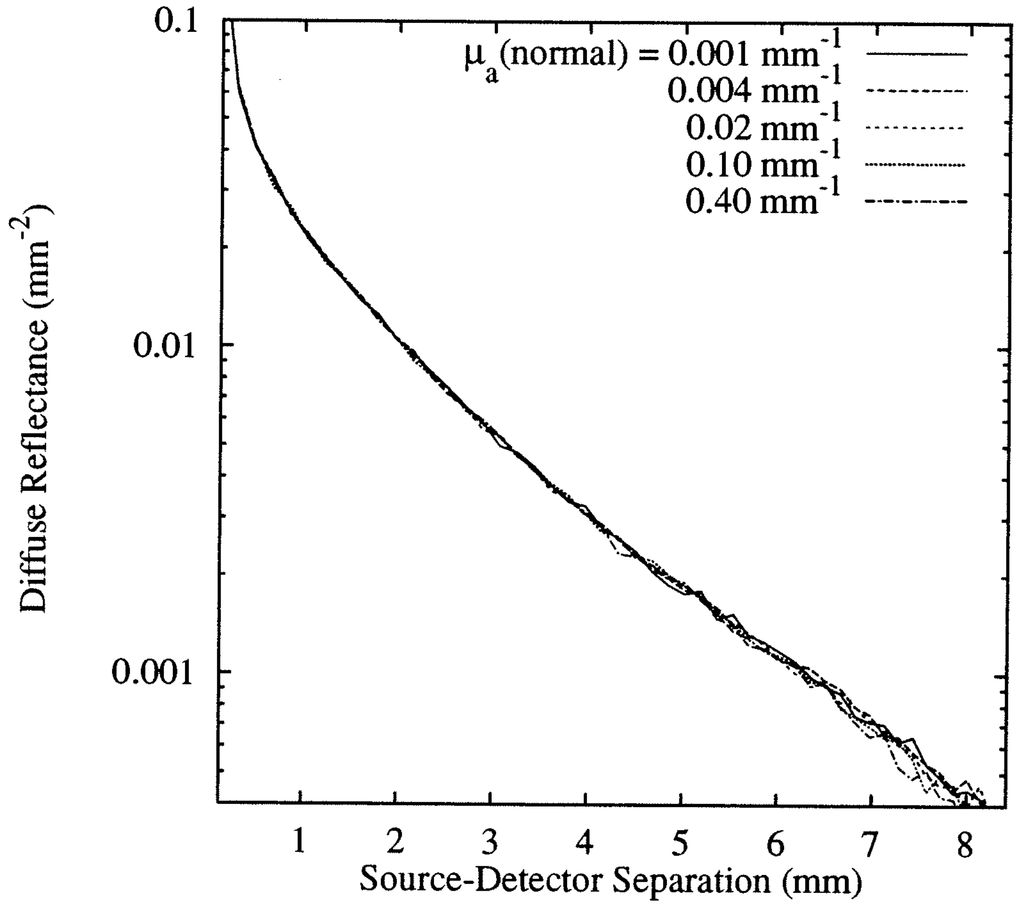

Figure 8.15: Monte Carlo diffuse reflectance data from a heterogeneous 12 mm diameter tumor. The various curves represent the effect of increasing the absorption coefficient in the normal tissue layer. The optical characteristics of the skin and tumor tissue were the same for all simulations (n = 1.4, $\mu_s' = 10$ mm^{-1}, g=0.90, $\mu_a = 0.02$ mm^{-1}). The scattering properties of the normal tissue were equal to that of the skin and tumor.

for 12 mm diameter tumors with absorption coefficients as low as 0.001 mm^{-1}. In both cases, it seems that the tumor is sufficiently thick to prevent contamination from the normal layer below. If reflectance was monitored on the plane beside the tumor, the slightly absorbing normal tissue would be discernible since photons emitted from the plane will almost certainly have traveled a considerable distance in the normal tissue.

8.5 Conclusions

In this chapter, the ramifications of using planar diffuse reflectance expressions to analyze data obtained from non-planar and heterogeneous tissues have been presented. Due to the geometric complexity that realistic tumors present, the appropriate solution of the photo-diffusion equation is likely to be ineffective when used to analyze diffuse reflectance data. These simpler models present an attractive analysis tool, though their applicability must be carefully considered.

While excellent agreement was found between predicted and actual optical properties for semi-infinite turbid media bounded by a planar matched boundary, the dipole fit performed less well when analyzing reflectance from a curved surface. For both matched and mismatched boundary conditions, the estimated absorption coefficient increases with decreasing radius. For radii greater than 3 mm, the reflectance from the curved surface at a given chord length was greater than that from a planar surface at an equivalent radial distance. This led to an overall underestimation of the true absorption coefficient for matched boundary conditions.

As with planar boundary conditions, an index mismatch of 1.4 on a curved interface led to a gross underestimation of the scattering coefficient and a corresponding overestimation of absorption, though not as severe as was seen for the plane. In contrast, the exact expression for the diffuse reflectance appears to be much more resilient to a mismatch in the index of refraction, but its sensitivity to non-diffuse reflectance near the source renders this solution inadequate for many small tumors.

Both expressions for the diffuse reflectance demonstrated a lack of sensitivity to small absorption coefficients when only reflectance above the tumor was analyzed. The dipole expression can be used to predict absorption coefficients as small as 0.001 mm^{-1} on a 12 mm diameter tumor, which is an order of magnitude smaller than can be estimated by the exact solution. The inability of the exact solution to measure tumor absorption coefficients less than 0.01 mm^{-1} on a 12 mm diameter tumor limits its usefulness for *in vivo* spectroscopy, though the exact solution for a spherical boundary would be expected to fare better.

Monte Carlo simulations of the diffuse reflectance from the subcutaneous tumor model with three-layer heterogeneity have indicated the consequences of not properly accounting for heterogeneity in the light propagation model. The skin layer does not appear to offer any additional perturbation of the estimated tumor optical properties when the scattering properties of the skin are matched to that of the tumor and absorption is equal to or less than that of the tumor. When the absorption of the skin layer is greater than that of the tumor, the reflectance near the source is primarily characterized by the upper skin layer, while the reflectance remote from the source contains information from the lower tumor region.

This is in agreement with the results presented by Nossal *et al.* for a layered slab geometry. Since the reflectance for small source-detector separation distances primarily determines the scattering coefficient in the dipole fit, a highly absorbing skin layer ultimately contaminates the characterization of the tumor absorption coefficient. The goodness of fit parameter cannot be used as an indicator of the presence of this kind of heterogeneity, however, since a highly absorbing skin layer seems to diminish the systematic deviations that accompanied an index mismatch. The goodness of fit does deteriorate, however, when the scattering of the skin layer is not the same as that of the tumor layer.

Variations in the absorption coefficient in the normal tissue did not appear to perturb the estimated optical properties of the tumor at all. This is consistent with Monte Carlo fluence calculations which indicate that the primary tissue volume probed by the diffuse reflectance technique is the volume immediately beneath the source beam. Since the probability for photons traveling through a 12 mm diameter tumor and returning to be emitted as diffuse reflectance is so slight, the optical properties of the normal tissue are not probed by the measurement. The tumor below the skin is adequately probed, however, and diffuse reflectance curves with various tumor absorption characteristics are consistent with the homogeneous curved boundary reflectance curves, provided the tumor is at least as absorbing as the skin layer.

Due to the complexity of creating tissue-simulating phantoms with curved boundaries and/or layered structures, the analysis here has been limited to Monte Carlo modeling. Recently, Firbank *et al.* (1995) have described a technique for making solid tissue-simulating phantoms that could be cast in various geometrical forms, such as the subcutaneous tumor model described here. It would be interesting to employ Firbank *et al.*'s techniques to verify these Monte Carlo results through experimental trials.

Finally, while it seems that under certain circumstances models of light propagation derived for planar boundaries and homogeneous turbid media can be used to estimate the optical properties of a more complex medium, it would clearly be more desirable to derive models which more closely represent the physical situation. Ultimately, it is important to weigh the merits of a given model by its predictive capabilities if it is to be used to study biological response *in vivo.*

Bibliography

S.R. Arridge, M. Cope, and D.T. Delpy. The theoretical basis for the determination of optical pathlengths in tissue: Temporal and frequency analysis. *Phys. Med. Biol.*, **37**(7):1531–1560, 1992.

S.R. Arridge, M. Hiraoka, and M. Schweiger. Statistical basis for the determination of optical pathlength in tissue. *Phys. Med. Biol.*, **40**:1539–1558, 1995.

W. Bank and B. Chance. Diagnosis of mitochondrial diseases by near infrared spectroscopy (NIRS). In B. Chance and R.R. Alfano, editors, *Optical Tomography, Photon Migration, and Spectroscopy of Tissue and Model Media: Theory, Human Studies, and Instrumentation*, volume 2389, pages 829–834, Bellingham, WA, 1995. SPIE.

J.L. Barton and L.R. Nackman. *Scientific and Engineering C++*. Addison-Wesley Publishing Company, Inc, Reading, Mass., 1994.

B. Beauvoit, S.M. Evans, T.W. Jenkins, E.E. Miller, and B. Chance. Correlation between the light scattering and the mitochondrial content of normal tissues and transplantable rodent tumors. *Anal. Biochem.*, **226**:167–174, 1995.

R.E. Benesch and R. Benesch. The mechanism of interaction of red cell organic phosphates with hemoglobin. *Adv. Protein Chem.*, **28**:211–235, 1974.

P.R. Bevington and D.K. Robinson. *Data Reduction and Error Analysis for the Physical Sciences.* McGraw-Hill, New York, 2nd edition, 1992.

J.W. Boag. Oxygen diffusion and depletion problems in radiobiology. In M. Erbert and A. Howard, editors, *Current topics in radiation research*, volume 5, pages 141–195. North Holland, Amsterdam, 1969.

D.G. Boyle and W.R. Potter. Photobleaching of Photofrin II as a means of eliminating skin photosensitivity. *Photochem. Photobiol.*, **46**(6):997–1001, 1987.

H.F. Bunn and B.G. Forget. *Hemoglobin: Molecular, Genetic and Clinical Aspects.* W.B. Saunders Company, Philadelphia, 1983.

J. Carlsson and H. Acker. Relations between pH, oxygen partial pressure and growth in cultured cell spheroids. *Int. J. Cancer*, **42**:715–720, 1988.

K.M. Case and P.F. Zweifel. *Linear Transport Theory.* Addison-Wesley, Reading, Mass., 1967.

B. Chance, J.S. Leigh, H. Miyake, D.S. Smith, S. Nioka, R. Greenfeld, M. Finander, K. Kaufmann, W. Levy, M. Young, P. Cohen, H. Yoshioka, and R. Boretsky. Comparison of time-resolved and -unresolved measurements of deoxyhemoglobin in brain. *Proc. Natl. Acad. Sci. USA*, **85**:4971–4975, 1988a.

B. Chance, S. Nioka, J. Kent, K. McCully, M. Fountain, R. Greenfedl, and G. Holtom. Time-resolved spectroscopy of hemoglobin and myoglobin in resting and ischemic muscle. *Anal. Biochem.*, **174**:698–707, 1988b.

B. Chance. Optical method. *Annu. Rev. Biophys. Biophys. Chem.*, **20**:1–28, 1991.

S. Chandrasekhar. *Radiative Transfer.* Dover, New York, 1960.

W. Cheong, S.A. Prahl, and A.J. Welch. A review of the optical properties of biological tissues. *IEEE J. Quant. Elec.*, **26**(12):2166–2185, 1990.

L. Cincotta, J.W. Foley, T. MacEachern, E. Lampros, and A.H. Cincotta. Novel photodynamic therapy of a benzophenothiazine on two different murine sarcomas. *Cancer Res.*, **54**:1249–1258, 1994.

M. Cope and D.T. Delpy. System for long-term measurement of cerebral blood and tissue oxygenation on newborn infants by near infra-red transillumination. *Med. & Biol. Eng. & Comput.*, **26**:289–294, 1988.

P.A. Cowled and I.J. Forbes. Photocytotoxicity *in vivo* of haematoporphyrin derivative components. *Cancer Lett.*, **28**:111–118, 1985.

J. Crank. *The Mathematics of Diffusion.* Oxford University Press, New York, 1975.

T.J. Dougherty, C.J Gomer, and K.R. Weishaupt. Energetics and efficiency of photoinactivation of murine tumor cells containing hematoporphyrin. *Cancer Res.*, **36**:2330–2333, 1976.

T.J. Dougherty. Photodynamic therapy. *Photochem. Photobiol.*, **58**:895–900, 1993.

I. Driver, C.P. Lowdell, and D.V. Ash. *In vivo* measurement of the optical interaction coefficients of human tumors at 630 nm. *Phys. Med. Biol.*, **36**(6):805–813, 1991.

F. A. Duck. *Physical Properties of Tissue: A Comprehensive Reference Book.* Academic Press Ltd., London, 1990.

R.E. Durand. Oxygen enhancement ratio in V79 spheroids. *Radiat. Res.*, **96**:322–334, 1983.

R.L. Fante. Relationship between radiative-transport theory and Maxwell's equations in dielectric media. *J. Opt. Soc. Am.*, **71**(4):460–468, 1981.

T.J. Farrell, B.C. Wilson, M.S. Patterson, and R. Chow. The dependence of photodynamic threshold on treatment parameters in normal rat liver *in vivo.* *Proc. SPIE*, **1426**:146–155, 1991.

T.J. Farrell, M.S. Patterson, and B. Wilson. A diffusion theory model of spatially resolved, steady-state diffuse reflectance for the noninvasive determination of tissue optical properties *in vivo.* *Med. Phys.*, **19**(4):879–888, 1992.

R.H. Feins, R. Hilf, H. Ross, and S.L. Gibson. Photodynamic therapy for human malignant mesothelioma in the nude mouse. *J. Surg. Res.*, **49**:311–314, 1990.

M. Ferrari, R.A. De Blasi, S. Fantini, M.A. Franceschini, B. Barbieri, V. Quaresima, and E. Gratton. Cerebral and muscle oxygen saturation measurement by a frequency-domain near-infrared spectroscopic technique. *Proc. SPIE*, **2389**:868–874, 1995.

V.H. Fingar, W.R. Potter, and B.W. Henderson. Drug and light dose dependence of photodynamic therapy: A study of tumor cell clonogenicity and histological changes. *Photochem. Photobiol,*, **45**:643–650, 1987.

M. Firbank, M. Oda, and D.T. Delpy. An improved design for a stable and reproducible phantom material for use in near-infrared spectroscopy and imaging. *Phys. Med. Biol.*, **40**:955–961, 1995.

C.S. Foote. Photosensitized oxygenations and the role of singlet oxygen. *Acct. Chem. Res.*, **1**:104–110, 1967.

T.H. Foster and L. Gao. Dosimetry in photodynamic therapy: Oxygen and the critical importance of capillary density. *Radiat. Res.*, **130**:379–383, 1992.

T.H. Foster, R.S. Murant, R.G. Bryant, R.S. Knox, S.L. Gibson, and R. Hilf. Oxygen consumption and diffusion effects in photodynamic therapy. *Radiat. Res.*, **126**:296–303, 1991.

T.H. Foster, D.F. Hartley, M.G. Nichols, and R. Hilf. Fluence rate effects in photodynamic therapy of multicell tumor spheroids. *Cancer Res.*, **53**:1249–1254, 1993.

A.J. Franko and R.M. Sutherland. Oxygen diffusion distance and development of necrosis in multicell spheroids. *Radiat. Res.*, **79**:439–453, 1979.

J.P. Freyer and R.M. Sutherland. Determination of diffusion constants for metabolites in multicell tumor spheroids. In H.I. Bicher and D.F. Bruley, editors, *Advances in Experiments in Medicine and Biology*, volume 159, pages 463–475. Plenum Press, 1983.

D. Fried, R.E. Glena, J.D.B. Featherstone, and W. Seka. Nature of light scattering in dental enamel and dentin at visible and near-infrared wavelengths. *Appl. Opt.*, **34**(7):1278–1285, 1995.

I. Georgakoudi, M.G. Nichols, and T.H. Foster. The mechanism of Photofrin photobleaching and its consequences for photodynamic dosimetry. *J. Photochem. Photobiol.*, , 1996. Submitted.

S.L. Gibson, T.H. Foster, R.H. Feins, R.F. Raubertas, M.A. Fallon, and R. Hilf. Effects of photodynamic therapy on xenografts of human mesothelioma and rat mammary carcinoma in nude mice. *Br. J. Cancer*, **69**:473–481, 1994.

R.G. Giovanelli. Reflection by semi-infinite diffusers. *Optica Acta*, **2**(4):154–162, 1955.

C.J. Gomer. Preclinical examination of first and second generation photosensitizers used in photodynamic therapy. *Photochem. Photobiol.*, **54**:1093–1107, 1991.

R.A.J. Groenhuis, H.A. Ferwerda, and J.J Ten Bosch. Scattering and absorption of turbid materials determined from reflection measurements. 1: Theory. *Appl. Opt.*, **22**(16):2456–2462, 1983a.

R.A.J. Groenhuis, H.A. Ferwerda, and J.J Ten Bosch. Scattering and absorption of turbid materials determined from reflection measurements. 2: Measuring method and calibration. *Appl. Opt.*, **22**(16):2463–2467, 1983b.

U. Grossmann. Profiles of oxygen partial pressure and oxygen consumption inside multicellular spheroids. In H. Acker, J. Carlsson, R. Durand, and R.M. Sutherland, editors, *Spheroids in Cancer Research*, volume 95, pages 150–161. Springer–Verlag, 1984.

J Grote, R Susskind, and P Vaupel. Oxygen diffusivity in tumor tissue (DS-carcinosarcoma) under temperature conditions within the range of 20-40 °C. *Pflugers Arch.*, **372**:37–42, 1977.

R.C. Haskell, L.O. Svaasand, T. Tsay, T. Feng, M.S. McAdams, and B.J. Tromberg. Boundary conditions for the diffusion equation in radiative transfer. *J. Opt. Soc. Am. A*, **11**(10):2727–2741, 1994.

O. Hazeki and M. Tamura. Near-infrared spectroscopic monitoring of hemoglobin and cytochrome aa_3 *in situ*. *Adv. Exp. Med. Biol.*, **215**:283–289, 1987.

B.W. Henderson and T.J. Dougherty. How does photodynamic therapy work? *Photochem. Photobiol.*, **55**:145–157, 1992.

L.G. Henyey and J.L. Greenstein. Diffuse radiation in the galaxy. *Astrophys. J.*, **93**:70–83, 1941.

Z. Hua, S.L. Gibson, T.H. Foster, and R. Hilf. Effectiveness of δ-Aminolevulinic acid-induced protoporphyrin as a photosensitizer for photodynamic therapy. *Cancer Res.*, **55**:1723–1731, 1995.

A. Ishimaru. *Wave Propagation and Scattering in Random Media*, volume 1. Academic, New York, 1978.

S.L. Jacques, C.A. Alter, and S.A. Prahl. Angular dependence of HeNe laser light scattering by human dermis. *Lasers Life Sci.*, **1**:309–333, 1987.

F.F. Jöbsis. Noninvasive infrared monitoring of cerebral and myocardial oxygen sufficiency and circulatory parameters. *Science*, **198**:1264–1267, 1977.

M.H. Kalos and P.A. Whitlock. *Monte Carlo Methods I: Basics.* John Wiley and Sons, Inc, New York, 1986.

J.C. Kennedy and R.H. Pottier. Endogenous protoporphyrin IX, a clinically useful photosensitizer for photodynamic therapy. *J. Photochem. Photobiol. B: Biol.*, **14**:275–292, 1992.

J.V. Kilmartin and L. Rossi-Bernardi. Interaction of hemoglobin with hydrogen ions, carbon dioxide and organic phosphates. *Physiol. Rev.*, **53**(4):836–890, 1973.

S. Kimel, B.J. Tromberg, W.G. Roberts, and M.W. Berns. Singlet oxygen generation of porphyrins, chlorins and pthalocyanines. *Photochem. Photobiol.*, **50**:175–183, 1989.

M. Kohl, M. Cope, M Essenpreis, and D. Böker. Influence of glucose concentration on light scattering in tissue-simulating phantoms. *Opt. Lett.*, **19**(24):2170–2172, 1994.

K. König, H. Schneckenburger, H. Walt, T. Leemann, M. Wyss-Desserich, A. Rück, and B. Tromberg. Microscopic studies on ALA-incubated tumor cells and tumor spheroids. *Proc. SPIE*, **2133**:238–248, 1994.

L. Kou, D. Labrie, and P. Chylek. Refractive indicies of water and ice in the 0.65- to 2.5-μm spectral range. *Appl. Opt.*, **32**(19):3531–3540, 1993.

H. Liu, D.A. Boas, Y. Zhang, A.G. Yodh, and B. Chance. Determination of optical properties and blood oxygenation in tissue using continuous nir light. *Phys. Med. Biol.*, **40**:1983–1993, 1995a.

H. Liu, B. Chance, A.H. Hielscher, S.L. Jacques, and F.K. Tittel. Influence of blood vessels on the measurement of hemoglobin oxygenation as determined by time-resolved reflectance spectroscopy. *Med. Phys.*, **22**(8):1209–1217, 1995b.

S.J. Madsen, E.R. Anderson, R.C. Haskell, and B.J. Tromberg. Portable high-bandwidth frequency-domain photon migration instrument for tissue spectroscopy. *Opt. Lett.*, **19**:1934–1936, 1994.

J.S. Maier, S.A. Walker, S. Fantini, M.A. Franceschini, and E. Gratton. Possible correlation between blood glucose concentration and the reduced scattering coefficient of tissues in the near infrared. *Opt. Lett.*, **19**(24):2062–2064, 1994.

T.S. Mang, T.J. Dougherty, W.R. Potter, D.G. Boyle, S. Somer, and J. Moan. Photobleaching of porphyrins used in photodynamic therapy and implications for therapy. *Photochem. Photobiol.*, **45**(4):501–506, 1987.

S. J. Matcher, P. Kirkpatrick, K. Nahid, M. Cope, and D. T. Delpy. Absolute quantification methods in tissue near infrared spectroscopy. *Proc. SPIE*, **2389**:486–495, 1995a.

S.J. Matcher, C.E. Elwell, C.E. Cooper, M. Cope, and D.T. Delpy. Performance comparison of several published tissue near-infrared spectroscopy algorithms. *Anal. Biochem.*, **227**:54–68, 1995b.

J. Moan and S. Sommer. Oxygen dependence of the photosensitizing effect of hematoporphyrin derivative in NHIK 3025 cells. *Cancer Res.*, **45**:1608–1610, 1985.

J. Moan. Effect of bleaching of porphyrin sensitizers during photodynamic therapy. *Cancer Lett.*, **33**:45–53, 1986.

J. Moan. On the diffusion length of singlet oxygen in cells and tissues. *J. Photochem. Photobiol. B:*, **6**:343–344, 1990.

W.F. Mueller-Klieser and R.M. Sutherland. Oxygen tensions in multicell spheroids of two cell lines. *Br. J. Cancer*, **45**:256–264, 1982.

W. Mueller-Klieser, J.P. Freyer, and R. M. Sutherland. Evidence for a major role of glucose in controlling development of necrosis in EMT6/Ro multicell tumor spheroids. In H.I. Bicher and D.F Bruley, editors, *Advances in Experiments in Medicine and Biology*, volume 159, pages 487–495. Plenum Press, 1983.

W. Mueller-Klieser. Method for the determination of oxygen consumption rates and diffusion coefficients in multicellular spheroids. *Biophys. J.*, **46**:343–348, 1984.

K. Razi Naqvi, A. El-Shahat, and S.A. El-Wakil. Alternative to the Pomraning-Eddington approach to radiative transfer. *Phys. Rev. A.*, **46**(8):4697–4703, 1992.

M.G. Nichols and T.H. Foster. Oxygen diffusion and reaction kinetics in the photodynamic therapy of multicell tumour spheroids. *Phys. Med. Biol.*, **39**:2161–2181, 1994.

R. Nossal, J. Kiefer, G.H. Weiss, R. Bonner, H. Taitelbaum, and S. Havlin. Photon migration in layered media. *Appl. Opt.*, **27**(16):3382–3391, 1988.

M.S. Patterson and B.C. Wilson. A theoretical study of the influence of sensitizer photobleaching on depth of necrosis in photodynamic therapy. *Proc. SPIE*, **2133**:208–219, 1994.

M.S. Patterson, B.C. Wilson, W. Feather, D.M. Burns, and W. Pushka. The measurement of dihematoporphyrin ether concentration by reflectance spectrophotometry. *Photochem. Photobiol.*, **46**:337–343, 1987.

M.S. Patterson, E. Schwartz, and B.C. Wilson. Quantitative reflectance spectrophotometry for the noninvasive measurement of photosensitizer concentration in tissue during photodynamic therapy. *Proc. SPIE*, **1065**:115–122, 1989.

M.S. Patterson, B.C. Wilson, and R. Graff. *In-vivo* tests of the concept of photodynamic threshold dose in normal rat liver photosensitized by aluminum chlorosulphonated phthalocyanine. *Photochem. Photobiol.*, **51**:343–349, 1990.

M.S. Patterson, J.D. Moulton, B.C. Wilson, K.W. Berndt, and J.R. Lakowicz. Frequency-domain reflectance for the determination of the scattering and absorption properties of tissue. *Appl. Opt.*, **30**:4474–4476, 1991.

B.W. Pogue and M.S. Patterson. Frequency-domain optical absorption spectroscopy of finite volumes using diffusion theory. *Phys. Med. Biol.*, **39**:1157–1180, 1994.

W.R. Potter, T.S. Mang, and T.J. Dougherty. The theory of photodynamic therapy dosimetry: Consequences of photodestruction of sensitizer. *Photochem. Photobiol.*, **46**:97–101, 1987.

S.A. Prahl, M. Keijzer, S.L. Jacques, and A.J. Welch. A Monte Carlo model of light propagation in tissue. *Proc. SPIE*, **IS 5**:102–111, 1989.

W.H. Press, S.A. Teukolsky, W.T. Vetterling, and B.P. Flannery. *Numerical Recipes in C: The Art of Scientific Computing.* Cambridge University Press, New York, 2nd edition, 1992.

A.E. Profio and D.R. Doiron. Dosimetry considerations in phototherapy. *Med. Phys.*, **8**:190–196, 1981.

L. Reynolds, C. Johnson, and A. Ishimaru. Diffuse reflectance from a finite blood medium: Applications to the modeling of fiber optic catheters. *Appl. Opt.*, **15**(9):2059–2067, 1975.

I.S. Saidi, S.L Jacques, and F.K Tittel. Mie and Rayleigh modeling of visible-light scattering in neonatal skin. *Appl. Opt.*, **34**(31):7410–7418, 1995.

E.M. Sevick, B. Chance, J. Leigh, S. Nioka, and M. Maris. Quantitation of time- and frequency-resolved optical spectra for the determination of tissue oxygenation. *Anal. Biochem.*, **195**:330–351, 1991.

J.D. Spikes. Quantum yields and kinetics of the photobleaching of hematoporphyrin , Photofrin II, tetra(4-sulfonatophenyl)-porphine and uroporphyrin. *Photochem. Photobiol.*, **55**(6):797–808, 1992.

C.E. St-Denis and C.J.D. Fell. Diffusivity of oxygen in water. *Can. J. Chem. Eng.*, **49**:885, 1971.

H.B. Stone, J.M. Brown, T.L. Phillips, and R.M. Sutherland. Oxygen in human tumors: Correlations between methods of measurement and response to therapy. *Radiat. Res.*, **136**:422–434, 1993.

R.M. Sutherland, J.A. McCredie, and W.R. Inch. Growth of multicell spheroids in tissue culture as a model of nodular carcinomas. *J. Natl. Cancer Inst.*, **46**:113–120, 1971.

L.O. Svaasand, P. Wyss, M-T. Wyss, Y. Tadir, B.J. Tromberg, and M.W. Berns. Dosimetry model for photodynamic therapy with topically administered photosensitizers. *Lasers Surg. Med.*, **18**:139–149, 1996.

H. Taitelbaum, S. Havlin, and G.H. Weiss. Approximate theory of photon migration in a two-layer medium. *Appl. Opt.*, **28**(12):2245–2249, 1989.

B.J. Tromberg, A. Orenstein, S. Kimel, S.J. Barker, J. Hyatt, J.S. Nelson, and M.W. Burns. *In vivo* tumor oxygen tension measurements for the evaluation of the efficiency of photodynamic therapy. *Photochem. Photobiol.*, **52**:375–385, 1990.

V. Twersky. Propagation in pair-correlated distributions of small-spaced lossy scatters. *J. Opt. Soc. Am.*, **69**(11):1567–1572, 1979.

H.C. van de Hulst. *Multiple Light Scattering*, volume II. Academic Press, New York, 1980.

H.C. van de Hulst. *Light Scattering by Small Particles.* Dover Publications, Inc., New York, 1981.

J.C. van Gemert, M.C. Berenbaum, and G.H.M. Gijsbers. Wavelength and light-dose dependence in tumour phototherapy with hematoporphyrin derivative. *Br. J. Cancer*, **52**:43–49, 1985.

R. van Hillegersberg, W.J. Kort, and J.H.P. Wilson. Current status of photodynamic therapy in oncology. *Drugs*, **48**(4):510–527, 1994.

H.J. van Staveren, C.J.M. Moes, J. van Marle, S.A. Prahl, and M.J.C. van Gemert. Light scattering in Intralipid-10% in the wavelength range of 400-1000 nm. *Appl. Opt.*, **30**(31):4507–4514, 1991.

L. Wang and S.L. Jacques. *Monte Carlo Modeling of Light Transport in Multi-layered Tissues in Standard C.* The University of Texas M.D. Anderson Cancer Center, Houston, Texas, 1992.

L. Wang and S.L. Jacques. Hybrid model of Monte Carlo simulation and diffusion theory for light reflectance by turbid media. *J. Opt. Soc. Am. A*, **10**(8):1746–1752, 1993.

K.R. Weishaupt, C.J. Gomer, and T.J. Dougherty. Identification of singlet oxygen as the cytotoxic agent in the photo-inactivation of a murine tumor. *Cancer Res.*, **36**:2326–2329, 1976.

C.M.L West. Size–dependent resistance of human tumour spheroids to photodynamic treatment. *Br. J. Cancer*, **59**:510–514, 1989.

W.J. Whalen, J. Riley, and P. Nair. A microelectrode for measuring intracellular PO_2. *J. Appl. Physiol.*, **23**(5):798–801, 1967.

B.C. Wilson and G. Adam. A Monte Carlo model for the absorption and flux distributions of light in tissue. *Med. Phys.*, **10**(6):824–830, 1983.

B.C. Wilson and S.L. Jacques. Optical reflectance and transmittance of tissues: Principles and applications. *IEEE J. Quant. Elec.*, **26**(12):2186–2199, 1990.

B.C. Wilson, T.J. Farrell, and M.S. Patterson. An optical fiber-based diffuse reflectance spectrometer for non-invasive investigation of photodynamic sensitizers *in vivo*. *Proc. SPIE*, **IS 6**:219–232, 1990.

E. Wolf. New theory of radiative energy transfer in free electromagnetic fields. *Phys. Rev. D.*, **13**(4):869–886, 1976.

S. Wray, M. Cope, D.T. Delpy, J.S. Wyatt, E. Osmund, and R. Reynolds. Characterization of the near infrared absorption spectra of cytochrome aa_3 and haemoglobin for the non-invasive monitoring of cerebral oxygenation. *Biochim. Biophys. Acta*, **933**:184–192, 1988.

G. Yoon, S.A. Prahl, and A.J. Welch. Accuracies of the diffusion approximation and its similarity relations for laser irradiated biological media. *Appl. Opt.*, **28**(12):2250–2255, 1989.

W.G. Zijlstra and A. Buursma. Spectrophotometry of hemoglobin: A comparison of dog and man. *Comp. Biochem. Physiol.*, **88B**:251–255, 1987.

Appendix A

Derivation of the Exact Diffusion Theory Expression for the Radial Reflectance from a Semi-Infinite Turbid Medium

Previously, Reynolds *et al.* (1975) have presented the rigorous solution of the steady-state photo-diffusion equation (Equation (4.12)) for the case of a beam of light of radius b incident on a turbid slab of depth d. The solution was obtained by constructing the appropriate Green's function satisfying the partial-current boundary conditions (Equation (4.23)). Here, Reynolds *et al.*'s derivation is modified for the case of a pencil beam incident on a semi-infinite medium. Due to the nature of the original solution, this configuration cannot be easily modeled by setting the beam radius to zero and the depth of the slab to a very large number. Instead, one must construct a Green's function which reflects the assumption that the far boundary of the slab is removed to infinity. To do this, it is convenient to start with the Green's function for the finite slab as presented by Reynolds *et al.*, $G_{slab}(\rho, z|\rho', z')$, and obtain the limit of an infinitely thick slab.

By construction, the Green's function of the photo-diffusion equation represents the fluence at field point (ρ,z) due to a photon source at (ρ',z'). Since the medium that we are interested in is turbid, the net fluence at a specified field point can arrive there by following an infinite number of paths. However, since there are constraints on the fluence at *both* the upper and lower interfaces of the slab, the energy density in the medium is consequently limited to a discrete number of distributions. The overall fluence is therefore a sum of the fluence of any possible distribution weighted by the likelihood of the particular distribution. This is accomplished by an eigenfunction solution for the axial part of the Green's function.

Thus, the axially symmetric Green's function, G_{slab}, may be written

$$G_{slab}(\rho, z|\rho', z') = \frac{2}{\pi} \sum_{n=1}^{\infty} \Gamma_n f_n(z) f_n(z') G_n(\rho|\rho') \tag{A.1}$$

where

$$f_n(z) = \sin(k_n z + \gamma_n) \tag{A.2}$$

is an eigenfunction with normalization

$$\Gamma_n = \frac{k_n}{2k_n d + \sin 2\gamma_n - \sin 2\left(k_n d + \gamma_n\right)}, \tag{A.3}$$

eigenvalues, k_n, determined by the transcendental equation

$$\tan k_n d = \frac{2z_b k_n}{z_b^2 k_n^2 - 1}, \tag{A.4}$$

and phase

$$\gamma_n = \arctan(z_b k_n), \tag{A.5}$$

where $z_b = 2AD$ is the distance from the real boundary to the extrapolated boundary that was discussed in Chapter 4.

The form of the radial component of the slab Green's function, $G_n(\rho|\rho')$, is dependent on whether the radial field coordinate, ρ, is closer to the beam axis than the radial source coordinate ρ',

$$G_n(\rho|\rho') = \begin{cases} I_0(\lambda_n \rho) K_0(\lambda_n \rho') & (\rho' > \rho) \\ I_0(\lambda_n \rho') K_0(\lambda_n \rho) & (\rho' < \rho) \end{cases} . \tag{A.6}$$

Here, I_0 and K_0 are modified zeroth order Bessel functions, and λ_n is related to the eigenvalues of the axial solution by

$$\lambda_n = \sqrt{k_n^2 + \frac{\mu_a}{D}}. \tag{A.7}$$

The appropriate semi-infinite Green's function, G_{SI}, can be obtained by taking the limit of the slab Green's function as the depth is removed to infinity,

$$G_{SI}(\rho, z|\rho', z') = \lim_{d \to \infty} G_{slab}(\rho, z|\rho', z'). \tag{A.8}$$

In taking this limit, the eigenvalues of the axial solution obtained by Equation (A.4) become continuous, since the spacing between eigenvalues, δk, is approximately,

$$\delta k \approx \frac{\pi}{d}. \tag{A.9}$$

Furthermore, the normalization term must also become a differential, as can be seen by taking the appropriate limit,

$$\lim_{d\to\infty} \Gamma_n = \frac{1}{2d} = \frac{\delta k}{2\pi}. \tag{A.10}$$

Upon taking the limit in Equation (A.8) we find

$$G_{SI}(\rho, z|\rho', z') = \frac{1}{\pi^2}\int_0^\infty \rho(z)\rho(z')G(\rho|\rho')dk, \tag{A.11}$$

where the subscripts have been removed to reflect the fact that the functions are now of a continuous variable, k. This equation has the same interpretation as Equation (A.1), but one of the constraints on the photon density has been relaxed by removing the far boundary to infinity.

Having found the Green's function appropriate for photo-diffusion in a semi-infinite half space, the fluence rate at any point in the medium can be obtained by integrating the fluence rate due to the diffuse sources in the medium,

$$\phi(\rho, z) = \frac{1}{D}\int S(\rho', z')G_{SI}(\rho, z|\rho', z')(2\pi\rho' d\rho' dz'), \tag{A.12}$$

where $S(\rho', z')$ represents the strength of diffuse sources. For an arbitrary beam incident along the z-axis, the strength term is given by

$$S(\rho', z') = \mu_s\left(1 + 3g\mu_t D\right)F(\rho')\exp(-\mu_t z') \tag{A.13}$$

where $F(\rho')$ specifies the radial distribution of the incident beam. This equation expresses the fact that point sources of diffuse fluence in the medium will be established along the beam profile, but the strength of the sources are exponentially damped with depth as a result of both scattering and absorption. The strength term is composed of an isotropic term as well as a term that depends on the scattering anisotropy, g. In media with a high degree of scattering anisotropy, such as biological tissue, this anisotropic component can be more than an order of magnitude stronger than the isotropic component.

For a pencil beam of unit fluence incident, the radial distribution of incident fluence can be written as

$$F(\rho') = \frac{\delta(\rho')}{2\pi\rho'}, \tag{A.14}$$

where $\delta(\rho')$ is the Dirac delta function. Inserting Equations (A.8), (A.13) and (A.14) into Equation (A.12) and performing the volume integration, the following expression is obtained for the diffuse fluence rate in the semi-infinite medium:

$$\phi(\rho, z) = \frac{\mu_s}{\pi^2}\left(\frac{1}{D} + 3g\mu_t\right)(1 + z_b\mu_t)\int_0^\infty \frac{(\sin kz + z_b k \cos kz)\, K_0(\sqrt{k^2 + \frac{\mu_a}{D}}\rho)}{(1 + z_b^2 k^2)(\mu_t^2 + k^2)} k dk. \tag{A.15}$$

While this integral is not easily solved analytically, it can be solved numerically for $\rho > 0$ by using Romberg integration.

To obtain the radial reflectance, the flux exiting the medium is computed from the distribution of the fluence rate according to

$$J_z^-(\rho) = \frac{1}{2}\left(\frac{1}{2}\phi(\rho, 0) + D\frac{\partial\phi(\rho, z)}{\partial z}\Big|_{z=0}\right) \tag{A.16}$$

(Reynolds *et al.*, 1975). This indicates that the fluence rate exiting the medium depends on both the fluence rate and the gradient of the fluence rate at the boundary. Since it is expected that the fluence rate will extrapolate to zero, it will not be zero at the boundary. Furthermore, according to the assumptions of the diffusion approximation, the fluence rate should be greater than the gradient of the fluence rate. Inserting Equation (A.15) into Equation (A.16) immediately yields the diffuse reflectance,

$$R_d(\rho) = \frac{\mu_s}{2\pi^2}\left(1 + 3g\mu_t D\right)\left(1 + z_b\mu_t\right)\left(1 + A\right)\int\limits_0^\infty \frac{K_0(\sqrt{k^2 + \frac{\mu_a}{D}}\rho)}{\left(1 + z_b^2 k^2\right)\left(\mu_t^2 + k^2\right)} k^2 dk. \quad \text{(A.17)}$$

Appendix B

Characterization of the Radially-Resolved Diffuse Emittance from a Fluorescent Source Embedded in a Semi-Infinite Turbid Medium

B.1 Introduction

To determine the diffuse reflectance that results when a laser beam enters a turbid medium, the photo-diffusion equation (Equation (4.12)) was rigorously solved by the method of Green's functions (Appendix A) and by a dipole approximation suggested by Farrell *et al.* (1992). Farrell *et al.*'s approach was to replace the incident laser beam with a pair of fluence sources that were positioned relative to the physical boundary in such a way that an extrapolated boundary condition could be satisfied. The fluence at a position $\vec{r}$ resulting from a spherically symmetric point source located at $\vec{r'}$ is given by the Green's function of the Helmholtz equation, which can be written

$$G(\vec{r}|\vec{r'}) = \frac{1}{4\pi D}\frac{e^{-\mu_{eff}|\vec{r}-\vec{r'}|}}{|\vec{r}-\vec{r'}|} \tag{B.1}$$

where μ_{eff} and D depend on the optical properties of the medium, as defined by Equations (4.28) and (4.13).

This Green's function can also be used to describe the fluence that would result at $\vec{r}$ from a fluorescent point source located at $\vec{r'}$ in a turbid medium. This situation arises, for example, when a PDT photosensitizer localized in a tumor embedded in normal tissue is excited by an external beam. Depending on the degree to which the photosensitizer localizes in the tumor, this fluorescent signal may provide valuable quantitative information about the location and size of the tumor. Therapeutic ratios of photosensitizer concentration in the tumor to that in the surrounding normal tissue are sensitizer and tumor specific, but typical values reported in the literature can range anywhere from 2 to 10. This may be significant enough to use fluorescence as a quantitative tumor characterization modality. In this appendix, calculations of diffuse fluorescence are presented for localized and uniformly distributed fluorophores in infinite and semi-infinite turbid media.

B.2 Calculation of the Fluorescence from a Localized Extended Spherical Inhomogeneity in an Infinite Medium

In electrostatics, Gauss's law indicates that the electric field exterior to a spherical distribution of charge is identical to that of a point located at the center of the sphere with an equivalent charge. Here we demonstrate that the same principle can be used to simplify the diffuse fluence emitted from a fluorescent spherical inhomogeneity in a turbid medium.

The fluence at a location $\vec{r}$ in a turbid medium due to an extended source can be found by integrating the Green's function given by Equation (B.1) weighted by the strength of the source over the source volume

$$\psi(\vec{r}) = \int_{\text{Source Volume}} S(\vec{r'})G(\vec{r}|\vec{r'})dV', \tag{B.2}$$

where $S(\vec{r'})$ indicates the strength of the source located at $\vec{r'}$. This integral is readily evaluated for the case of a uniform spherical source in an infinite medium to yield

$$\psi(\vec{r}) = \mathcal{C}\frac{1}{4\pi D}\frac{e^{-\mu_{eff}r}}{r} \tag{B.3}$$

where r is the distance from the center of the source to the field point and. The constant, $\mathcal{C}$, is

$$\mathcal{C} = \frac{4\pi}{\mu_{eff}^3}\left(\mu_{eff}r_s\cosh\left(\mu_{eff}r_s\right) - \sinh\left(\mu_{eff}r_s\right)\right), \tag{B.4}$$

where r_s is the radius of the fluorescent source. This is the same fluence that would be obtained from a point source of strength C located at the origin

$$\psi(\vec{r}) = CG(\vec{r}|0), \tag{B.5}$$

where the strength is seen to depend on both the optical properties of the medium and the size of the source. Hence, by adjusting the strength of the source, an extended spherical inhomogeneity can be collapsed to a point located at the center of the sphere.

While the fluence may depend on r_s, it only enters into the expression in the form of a constant. This is less than ideal from an experimental standpoint if the intended goal is to obtain information about the extent of a tumor, for example. Equation (B.5) could be used to locate the tumor, however. Furthermore, depending on the size of the tumor and the optical properties of the medium, the excitation fluence of a probe beam might change rapidly enough that some information pertaining to the size might be available in the radial distribution of the fluence or reflectance.

B.3 Calculation of the Fluence in an Infinite Turbid Medium when Absorption Can Lead to Fluorescence

While it may be the case that exogenously administered fluorophores become localized in tumorous tissue, it is likely that they will be somewhat distributed throughout the surrounding tissue as well. In this case the distribution of the excitation fluence will result in non-uniform fluorescence excitation. Here we calculate the distribution of fluence in an infinite turbid medium due to an excitation source located at the origin. Fluorescence results naturally from absorption by the chromophores within the medium, so we will approach it similarly. To simplify the problem, we consider an isotropic monochromatic source and assume that fluorescence will be emitted at one wavelength that is longer than the excitation wavelength. This eliminates the complication of fluorescence excitation which would affect the distribution of fluence.

Figure B.1 illustrates the propagation of fluence of wavelength λ_1 from an excitation source (S) to secondary fluorescent sources (S') distributed throughout the medium. The fluence from the primary source is given by Equation (B.1) where $\vec{r'}$ is taken to be the origin. Fluorescence is excited at wavelength λ_2 everywhere in the medium according to the quantum yield for fluorescence, ϕ_f, and the absorption coefficient, $\mu_a^{\lambda_1}$, of the fluorophores. While fluorescence only occurs for λ_1 absorption, in general the fluorescence can be absorbed by other non-fluorescent absorbers in the medium (such as hemoglobin, for example) as specified by the absorption coefficient $\mu_a^{\lambda_2}$. We also allow for wavelength-dependent scattering. Irradiation at λ_1 will scatter according to the transport scattering coefficient $\mu_{s1}'^{\lambda}$, while fluorescence of wavelength λ_2 will be given by $\mu_{s2}'^{\lambda}$. Given this, the photo-diffusion coefficient for wavelengths λ_1 and λ_2 will be denoted D^{λ_1} and D^{λ_2}, respectively.

The resulting two-color fluence distribution at $\vec{r_1}$ is the sum of the contributions

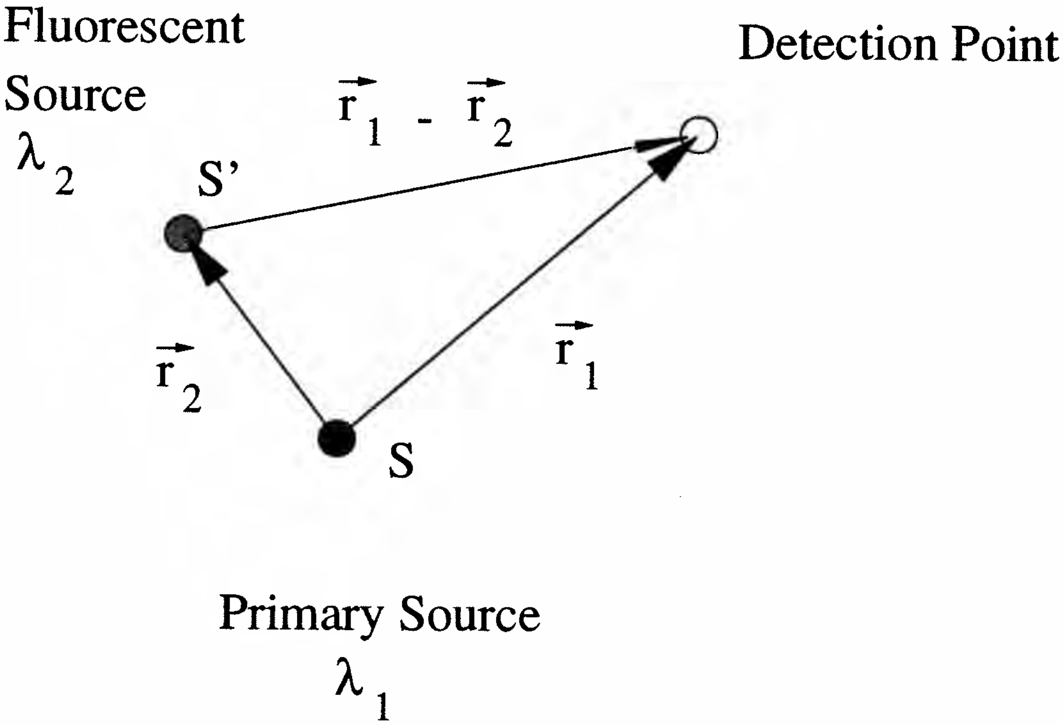
Fluorescent Source
λ 2
S'
r 1 - r 2
Detection Point
r 2
r 1
S
Primary Source
λ 1

Figure B.1: Illustration of the generation and propagation of primary and fluorescent fluence in an infinite turbid medium. The primary excitation source (black circle) excites fluorophores (grey circle) distributed throughout the medium. The fluence from both primary (S) and secondary (S') sources are detected (open circle).

from the primary and secondary sources,

$$\psi(\vec{r_1}) = \psi_{S'}^{\lambda_1}(\vec{r_1}) + \int_{S'} F_{S'}^{\lambda_2}(\vec{r_1}|\vec{r_2})dV, \tag{B.6}$$

where

$$F_{S'}^{\lambda_2}(\vec{r_1}|\vec{r_2}) = \phi_f \mu_a^{\lambda_1} \psi_{S'}^{\lambda_1}(\vec{r_2}) \psi_{S'}^{\lambda_2}(\vec{r_2} - \vec{r_1}) \tag{B.7}$$

is the fluence density at $\vec{r_1}$ due to fluorescent emission at $\vec{r_2}$. Using the infinite space Green's functions to determine the individual fluence distributions, Equation (B.6) evaluates to

$$\psi(r_1) = \frac{1}{4\pi D^{\lambda_1}} \frac{e^{-\mu_{eff}^{\lambda_1} r_1}}{r_1} + \frac{\phi_f \mu_a^{\lambda_1}}{4\pi D^{\lambda_1} D^{\lambda_2} \left(\left(\mu_{eff}^{\lambda_1}\right)^2 - \left(\mu_{eff}^{\lambda_2}\right)^2 \right)} \left(\frac{e^{-\mu_{eff}^{\lambda_2} r_1} - e^{-\mu_{eff}^{\lambda_1} r_1}}{r_1} \right). \tag{B.8}$$

The first term of Equation (B.8) represents the λ_1 emission from the primary point source, and the second term represents the effect of the distributed fluorophores at a wavelength λ_2. The fluorescence term is similar in form to the fluence from a point source. It again appears as though the fluorescent fluence is concentrated at the origin, but instead of a single point source, the fluorescent fluence is the difference of two weighted point sources; one that is characterized by the optical properties at the excitation wavelength, λ_1, and another characterized by the optical properties at the fluorescent wavelength, λ_2. Both of these point sources are weighted equally by a combination of factors including the optical properties of the medium at both wavelengths. Once again, there is no information regarding the extent of the fluorescent source.

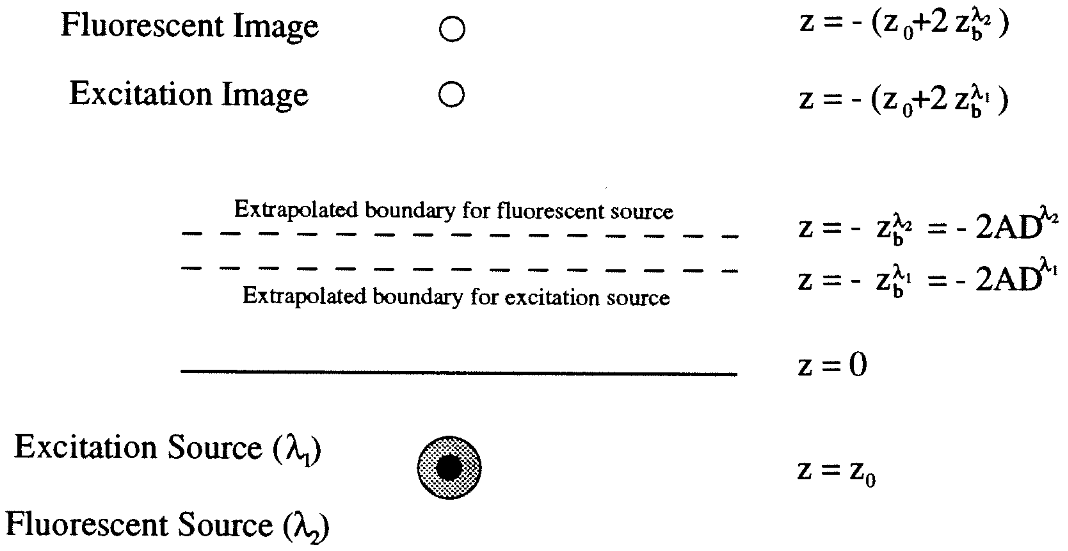
Fluorescent Image
Excitation Image
$z = -(z_0+2z_b^{\lambda_2})$
$z = -(z_0+2z_b^{\lambda_1})$
Extrapolated boundary for fluorescent source
Extrapolated boundary for excitation source
$z = -z_b^{\lambda_2} = -2AD^{\lambda_2}$
$z = -z_b^{\lambda_1} = -2AD^{\lambda_1}$
$z = 0$
Excitation Source (λ_1)
Fluorescent Source (λ_2)
$z = z_0$

Figure B.2: The arrangement of fluence point sources used to obtain the radially-resolved diffuse fluorescence emitted from a semi-infinite medium. The approach is a straightforward extension of Farrell *et al.* (1992). A point excitation source and a fluorescence source are located a distance z_0 from the planar boundary. Images corresponding to each of these sources are placed a distance above the physical boundary to force the fluence to zero on their respective extrapolated boundaries located at distances of $z_b^{\lambda_1}$ and $z_b^{\lambda_2}$ from the physical boundary. A is the internal reflection coefficient, and D^{λ_1} and D^{λ_2} are the photo-diffusion coefficients for wavelengths λ_1 and λ_2, respectively.

B.4 Calculation of the Radially-Resolved Diffuse Fluorescent Emittance from the Surface of a Semi-Infinite Medium

Having obtained the two-color diffuse fluence from a point excitation source in a medium with distributed fluorophores, we can follow the approach of Farrell *et al.* and obtain the semi-infinite Green's function for fluorescence. This can then be used to obtain the radially resolved fluorescence that would be emitted from a planar boundary.

Figure B.2 depicts the arrangement of excitation and fluorescence sources and their images relative to a planar boundary. Farrell *et al.* demonstrated that a laser beam incident on a semi-infinite turbid medium could be replaced by a pair of isotropic fluence sources placed on either side of the physical boundary. As shown in the previous section, the distributed fluorescence also appears to emanate from a point source located at the site of the excitation irradiation. Therefore, to find the diffuse fluence in a semi-infinite medium containing distributed fluorophores irradiated with a pencil beam, both a point excitation source and a fluorescence source are positioned a distance z_0 from the planar boundary. As described in Section 4.3, this is 1 mfp′ of the excitation irradiation. To approximately satisfy the partial-current boundary conditions, images corresponding to each of the sources are placed a distance above the physical boundary to force the fluence to zero on their respective extrapolated boundaries, $z_b^{\lambda_1}$ and $z_b^{\lambda_2}$. For convenience we make the simplification that the internal reflection parameter, A, has no wavelength dependence. Summing the contributions from the sources and their images, the following two-color fluence is obtained:

$$\begin{aligned}\psi(\rho, z) &= \frac{1}{4\pi D^{\lambda_1}}\left(\frac{e^{-\mu_{eff}^{\lambda_1} r_1(\rho,z)}}{r_1(\rho, z)} - \frac{e^{-\mu_{eff}^{\lambda_1} r_2(\rho,z)}}{r_2(\rho, z)}\right) + \frac{\phi_f \mu_a^{\lambda_1}}{4\pi D^{\lambda_1} D^{\lambda_2}\left(\left(\mu_{eff}^{\lambda_1}\right)^2 - \left(\mu_{eff}^{\lambda_2}\right)^2\right)} \\ &\left(\frac{e^{-\mu_{eff}^{\lambda_2} r_1(\rho,z)} - e^{-\mu_{eff}^{\lambda_1} r_1(\rho,z)}}{r_1(\rho, z)} - \frac{e^{-\mu_{eff}^{\lambda_2} r_3(\rho,z)} - e^{-\mu_{eff}^{\lambda_1} r_3(\rho,z)}}{r_3(\rho, z)}\right) \end{aligned} \tag{B.9}$$

where

$$r_1(\rho, z) = \sqrt{(z - z_0)^2 + \rho^2}, \tag{B.10}$$

$$r_2(\rho, z) = \sqrt{\left(z + z_0 + 2z_b^{\lambda_1}\right)^2 + \rho^2}, \tag{B.11}$$

and

$$r_3(\rho, z) = \sqrt{\left(z + z_0 + 2z_b^{\lambda_2}\right)^2 + \rho^2}. \tag{B.12}$$

Again, the first term represents the fluence due to the irradiation beam, as derived by Farrell *et al.* while the second term is the fluorescence at λ_2 in the semi-infinite medium.

The two-color radial reflectance can then be obtained by evaluating the flux leaving the medium at $z = 0$. Following the derivation of Farrell *et al.*, this can be obtained by substituting each term of Equation (B.9) into Equation (4.14), taking care to use the appropriate photo-diffusion coefficient for each wavelength. The reflectance for the excitation wavelength was specified previously by Equation (4.33), the corresponding fluorescent diffuse reflectance is

$$R_d(\rho) = \frac{\phi_f \mu_a^{\lambda_1}}{4\pi D^{\lambda_1}\left(\left(\mu_{eff}^{\lambda_1}\right)^2 - \left(\mu_{eff}^{\lambda_2}\right)^2\right)}$$

$$\left[z_0\left(\left(\mu_{eff}^{\lambda_2}+\frac{1}{r_1(\rho,0)}\right)\frac{e^{-\mu_{eff}^{\lambda_2}r_1(\rho,0)}}{r_1^2(\rho,0)}-\left(\mu_{eff}^{\lambda_1}+\frac{1}{r_1(\rho,0)}\right)\frac{e^{-\mu_{eff}^{\lambda_1}r_1(\rho,0)}}{r_1^2(\rho,0)}\right)\right.$$
$$+\left(z_0+2z_b^{\lambda_2}\right)$$
$$\left.\left(\left(\mu_{eff}^{\lambda_2}+\frac{1}{r_3(\rho,0)}\right)\frac{e^{-\mu_{eff}^{\lambda_2}r_3(\rho,0)}}{r_3^2(\rho,0)}-\left(\mu_{eff}^{\lambda_1}+\frac{1}{r_3(\rho,0)}\right)\frac{e^{-\mu_{eff}^{\lambda_1}r_3(\rho,0)}}{r_3^2(\rho,0)}\right)\right]. \tag{B.13}$$

This derivation has made several assumptions that must be considered before considering experimental verification. First, in general, a spectrum of fluorescence will result from a monochromatic excitation. To use Equation (B.13) the reflectance would need to be spectrally resolved. Since the fluorescence yield enters only as a constant, it would not need to be known provided the shape of Equation (B.13) was evaluated. We have also ignored the possibility of fluorescence excitation, *i.e.* $\lambda_1 \rightarrow \lambda_i \rightarrow \lambda_2$, where λ_i is an intermediate fluorescence wavelength. Since fluorescence yields are typically quite low, ignoring these contributions is probably well justified.